Topological Formulation of Beam Dynamics

A Study of Quasiperiodic Motion in Hamiltonian Systems

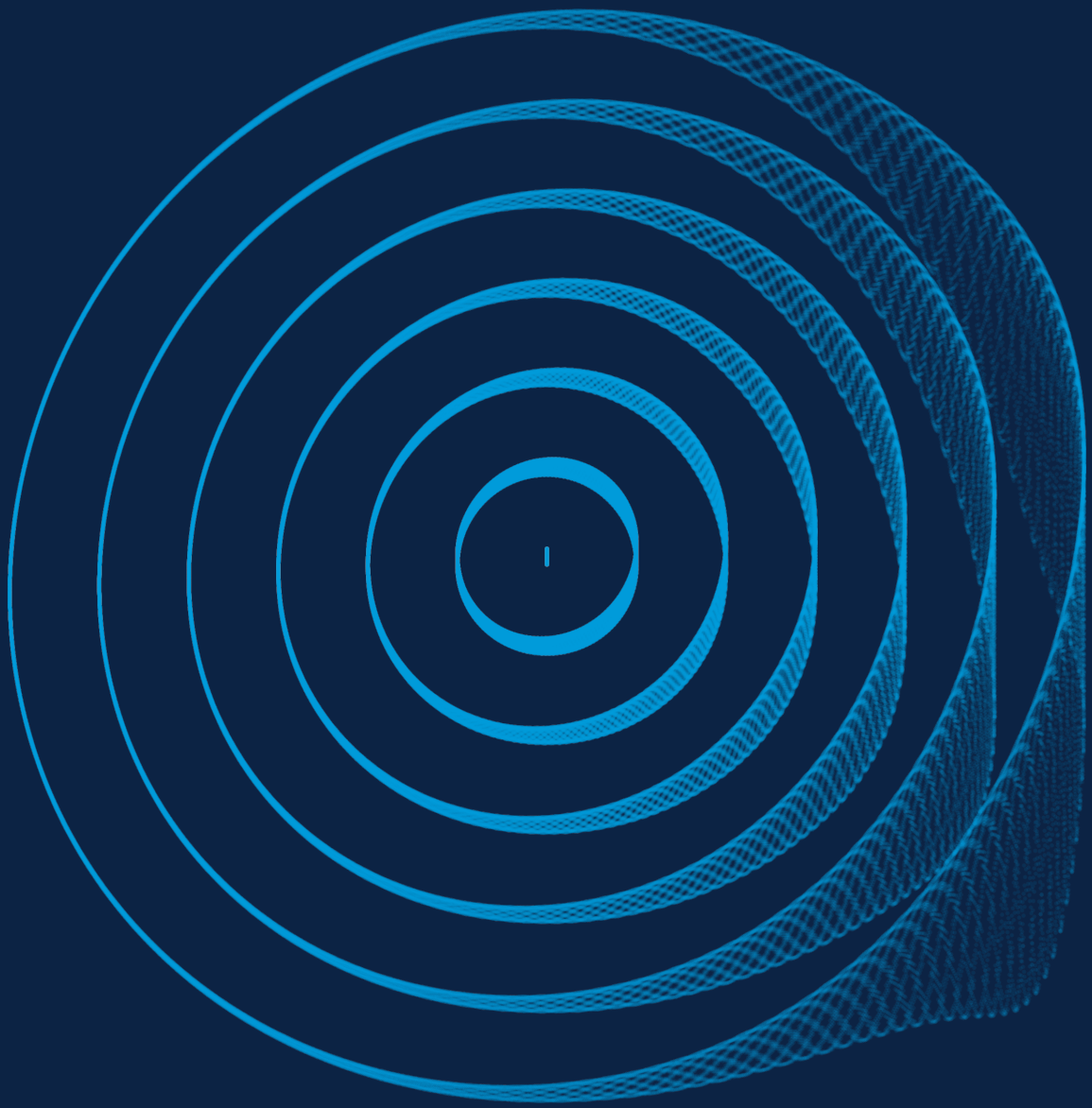

Philippe Bélanger

Ph.D. Thesis (2025)

Topological Formulation of Beam Dynamics

A Study of Quasiperiodic Motion in Hamiltonian Systems

by

Philippe Bélanger

B. Eng., Polytechnique Montréal, 2018

M. Sc., The University of British Columbia, 2020

A THESIS SUBMITTED IN PARTIAL FULFILLMENT
OF THE REQUIREMENTS FOR THE DEGREE OF

Doctor of Philosophy

in

THE FACULTY OF GRADUATE AND POSTDOCTORAL STUDIES
(Physics)

The University of British Columbia
(Vancouver)

December 2025

The following individuals certify that they have read, and recommend to the Faculty of Graduate and Postdoctoral Studies for acceptance, the thesis entitled:

Topological Formulation of Beam Dynamics:
A Study of Quasiperiodic Motion in Hamiltonian Systems

submitted by Philippe Bélanger in partial fulfillment of the requirements for

the degree of Doctor of Philosophy

in Physics

Examining Committee:

Reiner Kruecken, Division Director, Lawrence Berkeley National Laboratory (also UBC)

Supervisor

Richard Baartman, Head of Beam Physics/Senior Research Scientist, TRIUMF

Co-supervisor

Aaron Boley, Professor, Astronomy and Astrophysics, UBC

University Examiner

Stephen Gustafson, Professor, Mathematical physics, UBC

University Examiner

Andrei Seryi, Associate Director for Accelerator Operations, R&D, Jefferson Lab

External Examiner

Additional Supervisory Committee Members:

Colin Gay, Professor, Particle and Nuclear Physics, UBC

Supervisory Committee Member

Ludovic Van Waerbeke, Professor, Astronomy and Astrophysics, UBC

Supervisory Committee Member

Abstract

The stability of particle motion is a central concern of beam dynamics for the optimal design of particle accelerators. Linear effects are generally well under control, allowing us to store beams for more than 50 hours in machines like the Large Hadron Collider, at CERN. Non-linear effects, on the other hand, introduce complications that must be controlled to enhance the region of stable motion. In such complex systems, the emergence of chaos forces us to integrate the motion element-by-element to study the complete picture of beam dynamics. This establishes particle tracking as a fundamental tool required to probe non-linear effects. Yet despite the successes of the field, the ubiquity of the linear picture leads to a framework which often appears fragmented. In this respect, this dissertation proposes a formalism which can naturally describe linear, non-linear, analytic and numerical experiments alike using a self-consistent framework. To do so, we take an epicycle approach (in the spirit of the ancient Greeks) and place a general quasiperiodic expansion as the central object of study.

Critically, this choice ensures close contact with empirical observables and enables a detailed spectral analysis of the particle's motion. After providing a visual interpretation of KAM tori, we show how the integrals of motion can be recovered for arbitrary Hamiltonian flows, including fully coupled six-dimensional systems such as the LHC. Using Lie algebraic methods, we investigate the transport and deformation of these tori, establishing a foundation for describing coupled linear motion as a stepping stone toward a more complete non-linear treatment. Although closed-form solutions remain generally inaccessible, we demonstrate that the compensation of non-linear effects can be rigorously studied through the non-linear residual, a quantity shown to correlate strongly with dynamic aperture. Ultimately, the framework connects naturally with the Normal Form approach, which relies on the same quasiperiodic expansions.

Lay Summary

The stability of particle motion is a central concern in the design of particle accelerators. In the Large Hadron Collider, protons can travel billions of times around the machine without significant loss — just as the Earth has revolved around the Sun for billions of years. Describing accurately this delicate motion requires strong conceptual foundations, which are still being refined.

This dissertation introduces a framework that can naturally describe both simple and complex systems alike, in a unified and self-consistent way. It also provides practical methods for interpreting experimental measurements. By building a bridge between mathematical theory and empirical observations, this work allows us to probe (as best as we can) elusive concepts such as *chaos* by deepening our understanding of its counterpart: stable motion.

Preface

This dissertation is an original intellectual work from the author, P. Bélanger. All figures were made by the author. Unless specified otherwise, the figures were generated from tracking codes and represent realistic physical scenarios. To do so, XSUITE [1], NAFFLIB [2] (from the author) and PYTORI [3] (from the author) were used.

Intellectual property of previous authors is identified throughout the text when needed, and "quotation marks" are used when exact wording is kept. This dissertation introduces a novel formalism to describe elements of common knowledge in beam dynamics. Because of this, every chapter (introduction included) is considered to be an integral part of this intellectual work, aiming to build towards a deeper understanding of beam dynamics by the end of the dissertation.

The ideas presented in this thesis are the result of many years of work and discussions. Naturally, the credit should be shared with numerous collaborators, mentors and friends. In particular, the contribution from G. Sterbini cannot be overstated; both in terms of time (cumulating several hundreds of hours of personal discussions) and in terms of impact on the content of the thesis (and on the author). Additionally, discussions with R. Baartman, T. Planche, D. Kaltchev and K. Paraschou were foundational to cultivate the understanding of the author; and ultimately foundational for the global results achieved in this work.

Chapter 1 presents common concepts of beam dynamics, mostly inspired by A. Wolski [4], but oriented towards tracking codes such as XSUITE [1]. The perspective presented comes from the author, with an important inspiration from J. Moser [5].

Chapter 2 presents a view of Hamiltonian mechanics taken from J.D. Meiss [6] which follows naturally from the seminal work of J. Laskar [7]. The global approach, the formalism and the interpretation of the results come from the author. The calculation of the integrals of motion was the subject of a publication from the author [8].

Chapter 3 presents a topological interpretation of Lie algebra following the results of Chapter 2. The intellectual approach was importantly inspired by the work of É. Forest [9]. The equations obtained throughout the chapter are the work of the author.

Chapter 4 presents a topological description of linear dynamics based on the results of Chapter 3. Parts of the approach were importantly inspired (and in a sense justified) by the work of A. Chao [10]. The novel formalism and the ensuing interpretations are the work of the author.

Chapter 5 presents a topological description of non-linear dynamics based on the results of the author in Chapter 3 and 4. The numerical experiments presented are the fruits of the author's work, importantly inspired by J. Laskar's numerical methods [11].

GenAI tools : For this dissertation, the use of Generative AI was limited to ChatGPT; used as an enhanced search engine and as a programming aid. All texts and figures were made by the author without any direct involvement of Generative AI.

Published Work

Papers & Proceedings, (Papers P. I to P. V can be found in appendix.)

- P. I (2023) — P. Belanger, R. Baartman, D. Kaltchev, G. Sterbini, **"Beam-Beam Long-Range Wire Compensators in LHC Run 3"**, *JACoW Publishing: IPAC*, 2023.
- (2023) — G. Iadarola, A. Abramov, P. Belanger *et al.*, **"Xsuite: An Integrated Beam Physics Simulation Framework"**, *JACoW Publishing: ICFA Advanced Beam Dynamics Workshop*, 2023.
- P. II (2024) — P. Belanger, R. Baartman, D. Kaltchev, G. Iadarola, G. Sterbini, **"Bunch-by-Bunch Simulations of Beam-Beam Driven Particle Losses in the LHC"**, *JACoW Publishing: IPAC*, 2024.
- P. IV (2024) — P. Belanger, R. Baartman, D. Kaltchev, G. Sterbini, **"A Topological Approach to the Problem of Beam-Beam Compensation"**, *CERN Yellow Reports: Beam-Beam Workshop*, 2024.
- P. III (2025) — P. Belanger and G. Sterbini, **"Numerical Evaluation of the Integrals of Motion in Particle Accelerator Tracking Codes"**, *arXiv*, 2025.
- P. V (2025) — P. Belanger, R. Baartman, D. Kaltchev, G. Sterbini, **"The Beam Dynamics Case of Beam-Beam Wire Compensators for the HL-LHC Era"**, *JACoW Pub.: HIAT*, 2025.

Presentations

- CERN (2022) — Implementation of the wire compensator in MAD-X, Xsuite and pymask
- CERN (2022) — BBCW results during Run 3 operation
- Hi-Lumi (2022) — Results of BBCW operation in LHC Run 3
- CERN (2022) — Results from BBCW MD8043 and footprint studies
- Hi-Lumi (2023) — BBLR compensation in Run 3: b-by-b losses and wire operation
- CERN (2024) — Back to Laskar: KAM tori in particle tracking codes
- CERN (2024) — The integrals of motion: a topological adventure
- BB'24 (2024) — A topological approach to the problem of beam-beam compensation
- TRIUMF (2024) — A topological description of accelerator beam dynamics
- CERN (2024) — The beam dynamics case of the BBWC in HL era
- CERN (2024) — From tracking codes to topology: integrals of motion and non-linearity
- HIAT (2025) — The beam dynamics case of the BBWC in HL era

Table of Contents

List of Tables

List of Figures

Acknowledgements

First and foremost, I wish to express my deepest gratitude to my mentor and CERN supervisor, Guido Sterbini, without whom none of these results would have been possible. The role that he played in shaping the character of this research was foundational and needs to be recognized. I am deeply grateful for the trust and openness he expressed towards my ideas, as well as the constant stream of honest challenges he brought forth to push me forward (and upward). His willingness to challenge agreed-upon concepts while simultaneously ensuring that we reach practical results was invaluable and most certainly elevated this research to what it is today. I am grateful to have found in him a source of inexhaustible wisdom and an inspiring figure to look up to.

I want to extend my gratitude to Rick Baartman, from TRIUMF, who also acted as an important mentor, both during my Master's degree and my Ph.D. His guidance and vast experience in the field often opened my eyes to the limitations and problems of the ideas I was proposing. Over the years, I have never doubted his support towards my work, which helped create a rich environment where all ideas could be discussed and examined in good faith. I wish to recognize here his invaluable contribution to the success of this work.

I also wish to thank Dobrin Kaltchev, from TRIUMF, who has been a brilliant source of knowledge over the years, informing and guiding my research towards the rigorous and complete mathematical treatment it ultimately achieved. Similarly, T. Planche has been an important source of knowledge, and his enthusiasm for the work most certainly helped me believe in the strength of the approach.

Finally, I wish to express my gratitude to my colleagues from TRIUMF and CERN with whom I had the pleasure of learning, working, and growing over the many years abroad. In particular, I wish to thank E. Lamb, K. Paraschou, L. Giacomel, A. Fornara, B. Lindström and many others for their precious friendship. The years spent by their side are a gift that I will cherish forever.

CHAPTER 1

Introduction: Beam Lines and Storage Rings

Particle accelerators are built with the purpose of bringing nuclei, ions and elementary particles (like protons and electrons) to high velocities, typically close to the speed of light. Thereafter, the particles can serve as projectiles directed at some fixed target — to probe and alter nuclei — or at some moving target, like other particles in the case of a collider [12]. The energy of the accelerated particles depends on the research objectives and dictates, in counterpart, the design characteristics of the required accelerator. Due to the variety of existing machines (linacs, cyclotrons, synchrotrons, etc.) and the vast range of achievable energies (from a few eV to several TeV), it would be difficult to present concepts of beam dynamics general enough to apply to all. As such, the present thesis will be implicitly working under the heuristics of high energy storage rings such as the Large Hadron Collider (LHC). That being said, the formalism introduced and developed throughout this work shall be applicable — implicit assumptions aside — to a wide range of dynamical systems reaching even outside of the field of beam dynamics, as long as they can be described with an appropriate Hamiltonian.

After introducing the LHC for general context, this chapter presents a generic description of beam lines, storage rings and of the basic components that are used to build them. From there, fundamental ideas pertaining to the study of beam dynamics are introduced and the general problem of particle stability is discussed.

1.1 General Context

The aim of this work is to clarify the foundations of beam dynamics within the broader context of modern accelerator physics. While the success of the field is undeniable (with groundbreaking technological achievements such as the Large Hadron Collider) the theoretical framework often appears fragmented and ambiguous — at least from the perspective of newcomers. Compared to older fields (*e.g.* Optics), the conceptual language of beam dynamics remains unsettled. There are good historical reasons for this situation, as discussed in Chapter 3, but the resulting ambiguities motivate a re-examination of the formalism. A central issue is the treatment of generic Hamiltonian flow (see Chapter 2). Standard introductions reduce the dimensionality step-by-step (from 6D to 4D to 2D) in order to simplify the concepts. While pedagogically useful, this reduction obscures the fundamental principles and ultimately limits our ability to interpret the complete 6-dimensional motion. This limitation is the motivation behind the fundamental research question at the heart of the dissertation:

> "Can we find a *natural* and *effective* way to describe non-linear motion in the full 6-dimensional Hamiltonian flow of beam dynamics?"

Addressing this question requires revisiting some of the most basic notions of the field. The first one concerns the *action*, a supposed invariant of motion. In practice, the "action" is often taken as either a linear approximation or an abstract formal construct that cannot be measured. In Chapter 2, we show — inspired by J. Laskar's work [13] — that one can construct a topological description of the dynamics in which the action becomes a measurable area. This area can be *visualized*, but also *computed* numerically using particle tracking codes (see Chapter 3). Moreover, this approach connects naturally with standard experimental diagnostics (*i.e.* spectral analysis and Resonance Driving Terms [14]), as well as advanced theoretical frameworks (*i.e.* Normal Form Analysis [15]).

The aim of the dissertation, therefore, is to assemble a consistent and unified picture of beam dynamics, valid from the simplest linear models to the highly non-linear regimes (even "hopelessly complex" [16]). Although the underlying motivation is to clarify our understanding of complex simulations and experimental observations, the strategy adopted consists in developing an analytic framework. From Chapter 1 onwards, key concepts of beam dynamics are discussed in terms of topology (*i.e.* the study of *shapes*, in phase space). Chapter 4 introduces a linear formalism to describe fully coupled systems; and Chapter 5 extends these concepts to non-linear dynamics, even when closed-form expressions are unavailable. The strength of this approach lies in its ability to bridge linear and non-linear regimes seamlessly; and to connect the analytic theory with computational and experimental observations.

Throughout, the reader is invited to challenge some common notions: are particles ever truly confined to *ellipses*? How is particle *smearing* different from *chaos*? Can there be *tune modulation*? *Coupling resonance* in linear systems? Are there any surviving *KAM tori* in complex machines like the LHC? Although these questions are not necessarily all answered, we believe that a reframing of the formalism is an important step towards a deeper understanding of beam dynamics.

1.2 The Large Hadron Collider

The Large Hadron Collider is made of two interlaced rings — each 27 km in circumference — buried 100 m underground at the European Organization for Nuclear Research (CERN) on the border of Switzerland and France. Protons extracted from a bottle of hydrogen gas are accelerated through a chain of accelerators before being injected in the LHC in two counter-rotating beams (beam 1 and beam 2), where they are further accelerated to an energy of 7 TeV. To guide these high energy protons, more than 1200 dipole magnets and 400 quadrupole magnets are used, respectively bending and focusing the beams around the machine. Most of the magnets are made of superconductive material, kept at a temperature of about 2 K. Bringing the beams into collisions takes about an hour of operation, during which the protons simply circulate around the machine. Even then, only a small fraction of the protons successfully collide together — given the small interaction cross-section — while the rest simply remain on course. Hence, the LHC is first a *storage ring* for the majority of the protons, and a *collider* only for some. Its primary goal is to successfully store the beams for several hours (57 h achieved in a single fill in 2022), losing as few protons as possible, while maximizing the number of collisions over time.

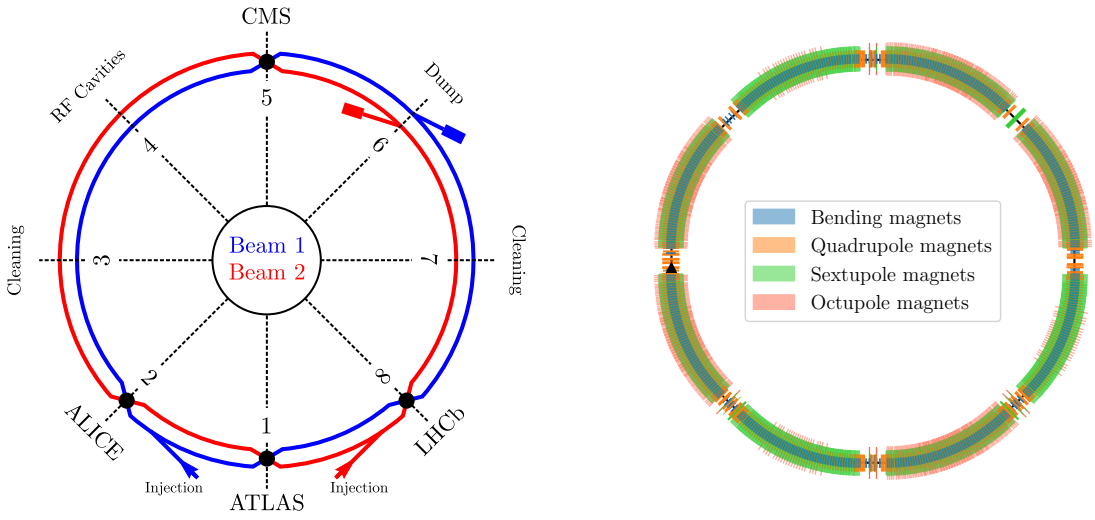

(a) LHC sectors layout

(b) LHC beam 1 magnets

Figure 1.1: The Large Hadron Collider. (a) LHC layout showing the 8 sectors and the 4 IPs. (b) The LHC magnets distribution (up to octupoles) for beam 1.

The two interlaced rings of the LHC are not perfectly circular, but are instead made of eight *arcs* and eight *insertions* (straight sections) as shown in Fig. 1.1. The insertions are used for specific tasks: beam collisions for the four big experiments (ATLAS, ALICE, CMS and LHCb), beam injection, beam cleaning, beam acceleration, beam diagnostics and beam dumping. The arcs on the other hand, mainly guide and focus the beam along its circular trajectory. The two cleaning IRs (3 and 7) contain the LHC collimation system, which protects the accelerator equipment against beam losses by removing protons from the beam halo. Finally, the beam dumping system (IR 6), is designed to extract the circulating beams from each ring and send them to an external dump block, located at the end of a 700 m long beam line.

The two beams are not made of a continuous stream of protons, but are instead bunched into groups of $1.0 - 1.8 \times 10^{11}$ protons separated by 25 ns gaps. Longitudinally, each bunch is about 1 ns long. The bunched structure is fixed by the accelerating radiofrequency (RF) cavities, which divide the machine into 35,640 stable RF buckets. During regular LHC operation, protons are injected in the machine in a given arrangement of filled and unfilled buckets, which forms the so-called filling pattern. Typical filling patterns contain around 2500 bunches, for a total beam intensity in the order of 10^{14} p^+.

The nominal velocity achieved by the protons at top energy is very close to the speed of light, *i.e.* $\beta_r = v/c = 0.999999991017$ (with "r" standing for "relativistic"), bringing the LHC beam in an *ultrarelativistic* regime. At 7 TeV, the Lorentz factor reaches a value of $\gamma_r = 7460.5$, which has important implications for the protons. In particular, the electric field lines around each proton are confined in the plane perpendicular to the direction of motion, as shown in Fig. 1.2. This entails that neighbouring protons do not produce any significant force on each other, which reduces collective effects such as *space charge* [4]. Another way of understanding this phenomenon is to consider the length contraction between the reference frame of the protons and the reference frame of the laboratory. As the speed of the protons increases closer to the speed of light, the distance between neighbouring protons (in the moving frame) stretches by a factor γ_r. As a result, any single proton is essentially isolated from its neighbours. This condition shall be satisfactory to justify the study — for the rest of the thesis — of *single-particle* dynamics.

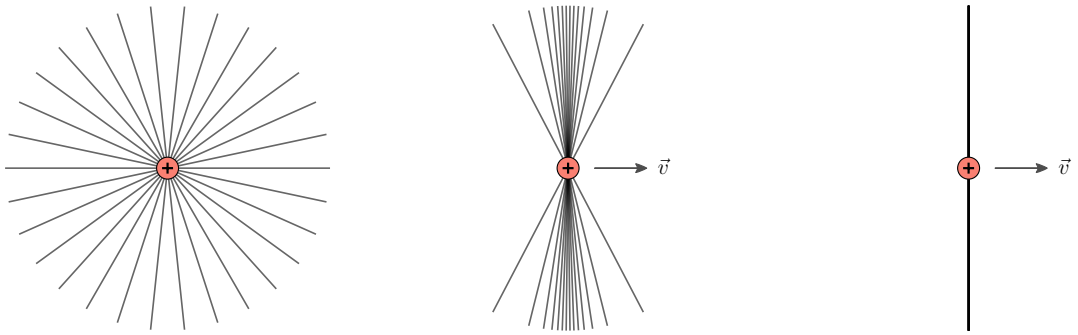

(a) $\gamma_r = 1$ (b) $\gamma_r = 3$ (c) $\gamma_r = 7460.5$

Figure 1.2: Field lines for a moving proton with increasing velocity [17]. (a) At rest, $\gamma_r = 1$. (b) Relativistic velocity, $\gamma_r = 3$. (c) Ultrarelativistic velocity, $\gamma_r = 7460.5$. The field lines are compressed towards the plane perpendicular to the velocity. In the ultrarelativistic limit, the field lines are essentially confined to the plane.

Following this brief overview of the Large Hadron Collider and of the energy range at which it operates, the main considerations for a simple model of storage rings should be highlighted. For the purpose of our work, the LHC shall indeed be reduced to a storage ring enabling the study of single-particle dynamics: a periodic system in which 10^{14} p^+ are forced to circulate in a beam pipe of 5 cm of diameter for several hours and billions of turns.

1.3 Building a Storage Ring

Consider that we wish to build a simple storage ring. Since the trajectory of charged particles in motion can be bent with the help of magnetic fields — following the Lorentz force — one is required to design a magnetic lattice in order to guide particles through a *beam line*. To ensure that particles are stored efficiently, the beam line needs to eventually close onto itself in the shape of a ring. Let us introduce the coordinate system used for such a task.

1.3.1 Coordinate System

Starting with a single particle — the reference particle — uniform dipolar fields can be used to guide it through any generic circular arc. This is done with the help of dipolar magnets (bending magnets), as discussed below. By distributing such magnets appropriately around the ring, the reference particle can be made to loop back to its original position, thereby forming the *reference orbit*, illustrated in Fig. 1.3. To follow the reference particle along its orbit, only the longitudinal location, s, is needed. Provided that all magnets are properly aligned with the reference orbit, the reference particle will remain stable and circulate indefinitely.

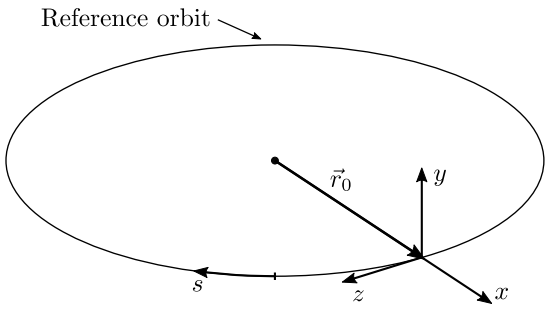

Figure 1.3: Curvilinear coordinate system for the description of accelerator beam dynamics. The longitudinal position along the reference trajectory is given by s and the deviation from the reference particle is given by the co-moving frame (x, y, z).

Let us now consider a second particle, slightly displaced with regard to the reference particle. Its position can be described, at any point, with the displacement from the reference particle in the transverse plane (x, y) — perpendicular to s — and along the longitudinal axis, z. Before developing the tools allowing us to describe the equations of motion for this particle, let us look at the fundamental accelerator components used in the making of a storage ring.

1.3.2 Fundamental Lattice Elements

The minimal set of elements required to guide particles through a storage ring consists of a quartet: drift sections (to connect magnets together), dipoles (to bend the reference trajectory), quadrupoles (to focus the beam transversely) and RF cavities (to focus the beam longitudinally). Let us first consider a series of test particles which are *on-momentum*, meaning that they travel at the same speed as the reference particle. In the field-free space between magnets, these particles will simply drift along the beam line following their initial transverse momentum, as shown in Fig. 1.4(a). To bend the reference trajectory, dipoles (dipolar magnets) are used, providing a uniform kick to all particles independently of their position, as shown in Fig. 1.4(b). Finally, to ensure stable bounded motion around the lattice, quadrupoles (quadrupolar magnets) are used to focus and defocus the beam as shown in Fig. 1.4(c).

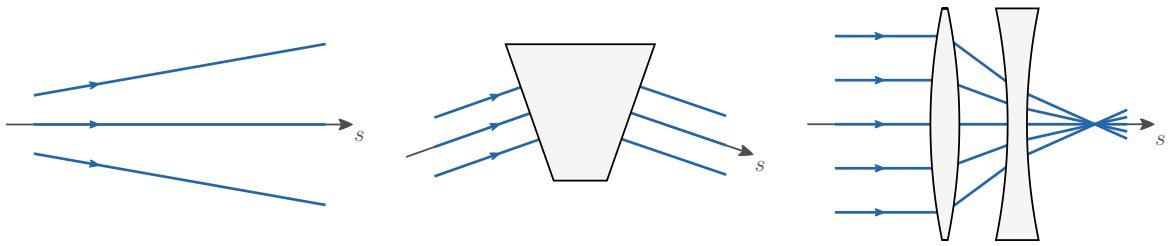

(a) Drift (b) Dipole (c) Quadrupole

Figure 1.4: Trajectory of on-momentum particles traveling through common elements. (a) A drift, where particles keep their original transverse momentum. (b) A dipole, where particles receive a uniform kick, independent of their position. (c) A focusing quadrupole followed by a defocusing quadrupole, where particles are focused towards the magnetic axis. In all cases, traveling along the s-axis corresponds to a drift and the magnetic elements only provide an instantaneous kick, changing the momentum of the particles.

By virtue of Maxwell's equations ($\nabla \cdot \boldsymbol{B} = 0$ and $\nabla \times \boldsymbol{B} = 0$), a quadrupole magnet which focuses the beam in the horizontal plane must defocus it in the vertical plane, and vice versa. Following conventions, quadrupoles are named based on their effect in the horizontal plane. It can be shown that a combination of focusing and defocusing quadrupoles — appropriately spaced — allows for stable motion in both planes simultaneously (see Chapter 4). Since dipoles provide a uniform kick which is independent of the position (in straight sections) and quadrupoles provide a kick which scales linearly with the position, both are known as *linear elements*.

The description of the motion — positions and momenta — of particles travelling through a beam line is at the core of the fundamental *transport* problem of beam dynamics. Several heuristics and physical models have been adopted throughout the years [9] in an attempt to improve tracking codes (such as XSUITE [1]) and improve the analytic description of beam dynamics [15]. The reader shall be made aware that for the present thesis, all magnetic elements are considered to be *thin* (zero length) and that any progress along the s-axis requires the presence of drift sections of finite length. As will be shown in later chapters, complicated dynamics arise from the presence of drifts due to unavoidable coupling effects between the longitudinal motion and the transverse one. To illustrate this claim, let us return to the few elements discussed previously but considering, this time, particles of varying energy (*off-momentum* particles).

Chromatic Effects

Assuming a reference particle traveling with a longitudinal reference momentum $\mathrm{p}_0 = \beta_{r_0}\gamma_{r_0}mc$, slight variations in the energy can be described using $\delta_\mathrm{p} = \Delta\mathrm{p}/\mathrm{p}_0$, which is typically in the order of 10^{-4} within the bunches of the LHC. In the drift regions between magnets, particles with different longitudinal momenta — but otherwise identical transverse momenta — travel at different angles along the s-axis, as shown in Fig. 1.5(a). This simple phenomenon leads to a multitude of *chromatic* effects, which arise due to the energy dependence of the beam dynamics. When passing through dipoles, particles with higher energy ($\delta_\mathrm{p} > 0$) are bent less — an effect known as *beam rigidity* — and conversely for particles with lower energy ($\delta_\mathrm{p} < 0$), as shown in Fig. 1.5(b).

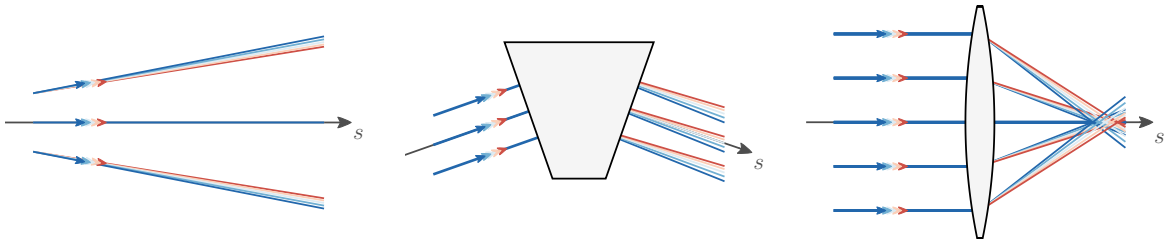

(a) Drift (b) Dipole (c) Quadrupole

Figure 1.5: Trajectory of off-momentum particles traveling through common elements. (a) A drift, where the spread in energy develops into a position deviation. (b) A dipole, where particles are bent more or less depending on their momentum deviation. (c) A quadrupole, where the effective focal length depends on δ_p due to the necessary drifts around the magnet. The trajectories have been computed via tracking using $\delta_p \in [-10^{-1}, 10^{-1}]$, a deviation 1000 times higher than typical LHC values.

As a result, particles entering a dipole parallel to the magnetic axis exit with small transverse momentum based on their momentum deviation, δ_p. This spread of energy and transverse momentum then develops into a position deviation over the length of the following drift sections. For a thin quadrupole and fixed reference momentum, the instantaneous kick only depends on the transverse amplitude. But in the necessary drift sections surrounding said quadrupole, the behaviour discussed earlier applies: particles with different energy travel at different angles along the s-axis, and the effective focal length of the quadrupole is being impacted, as shown in Fig. 1.5(c). A physically thick quadrupole — of finite length — therefore has a focal length which depends on the momentum deviation, an effect known as the *chromatic aberration*. Whether we consider a thick quadrupole or a thin quadrupole surrounded by drift sections makes no difference; both approaches equivalently capture the essential physics of the problem.

Longitudinal stability

As a final point of discussion, RF cavities need to be added in order to to maintain longitudinal stability, provide longitudinal focusing and compensate for energy loss (although negligible in hadron storage rings). Their effect depends on the time of arrival of each particle with regards to the reference particle, which can be described with the longitudinal position $\zeta = s - \beta_{r_0} ct$. Above the so-called *transition* energy, particles entering a cavity earlier than the reference particle ($\zeta > 0$) are accelerated, and particles entering later than the reference particle ($\zeta < 0$) are decelerated, as illustrated in Fig. 1.6(a). This is because above transition (like in the LHC), particles with higher momentum take longer paths around the circular trajectory of the machine.

To further improve longitudinal stability, it is required to reduce chromatic effects as much as possible. As discussed earlier, the presence of dipoles in the magnetic lattice introduces an important energy-dependence leading to *dispersion*, which is the variation of the closed-orbit with energy. As such, in dispersive regions, particles with $\delta_p \neq 0$ tend to be off-centered with regard to the magnetic axis, leading to chromatic aberrations, as shown in Fig. 1.6(b). To correct

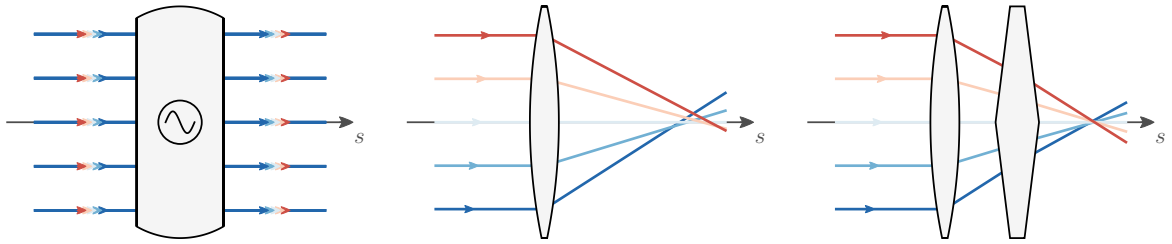

(a) RF Cavity (b) Chromatic aberration (c) Sextupolar correction

Figure 1.6: Trajectory of off-momentum particles traveling through common elements. (a) An RF cavity, where particles with $\zeta > 0$ are accelerated and particles with $\zeta < 0$ are decelerated. (b) A quadrupole in a dispersive region, which leads to chromatic aberration. (c) A sextupole corrector in a dispersive region — from (b) — which corrects the chromatic aberration, but introduces non-linear effects. The trajectories have been computed via tracking using $\delta_{\mathrm{p}} \in [-10^{-1}, 10^{-1}]$ and $D_x = 18$ m (dispersion).

for this undesirable effect and reduce the overall energy-dependence of the beam dynamics, sextupoles (sextupolar magnets, with a quadratic kick) are required, as shown in Fig. 1.6(c). By doing so, the chromatic aberration is corrected, but non-linear effects are introduced, leading to several additional complications in the beam dynamics — the topic of Chapter 5.

Following this introduction of common beam dynamics elements, let us now look, in the next section, at the mathematical tools required for the study of the equations of motion for particles in an accelerator beam line. This shall be done using Hamiltonian mechanics.

1.3.3 Hamiltonian

The Hamiltonian for a relativistic particle of mass m and charge q_e moving in an electromagnetic field is given by:

$$\mathcal{H} = c\sqrt{(\vec{\mathrm{p}} - q_e\vec{A})^2 + m^2c^2} + q_e\phi \ , \tag{1.1}$$

where $\vec{\mathrm{p}}$ is the canonical momentum of the particle, ϕ is the scalar potential and $\vec{A}$ is the vector potential. From there, the equations of motions can be found as a function of time by integrating Hamilton's equations. However, the usual form given in eq. (1.1) is not ideal for the study of particle accelerators: "in general, it is difficult to work out the time at which a particle enters a particular magnet, but we know immediately how far along the beam line it has travelled when it does so" [A. Wolski, 4]. To work around this, it is convenient to change the independent variable, from the time t to the path length s, such that the equations of motion can be integrated from one accelerator component to the next. We therefore change the Hamiltonian $\mathcal{H}(x_i, \mathrm{p}_i; t)$ to a new one, $H(x_i, p_i; s)$, and Hamilton's equations become:

$$\frac{dx_i}{dt} = \frac{\partial \mathcal{H}}{\partial \mathrm{p}_i} \quad \mapsto \quad \frac{dx_i}{ds} = \frac{\partial H}{\partial p_i} \ , \tag{1.2}$$

$$\frac{d\mathrm{p}_i}{dt} = -\frac{\partial \mathcal{H}}{\partial x_i} \quad \mapsto \quad \frac{dp_i}{ds} = -\frac{\partial H}{\partial x_i} \ . \tag{1.3}$$

To ensure that H properly describes the equations of motion following Hamilton's equations, a careful canonical transformation is required. The reader is referred to the complete treatment from A. Wolski [4] for the details (namely a rescaling by the reference momentum and a change of the longitudinal variables). For the purpose of this work, we simply recall the final pairs of conjugate variables [18]: (x, p_x), (y, p_y) and (ζ, p_ζ). Assuming that the reference particle travels with a longitudinal reference momentum $\mathrm{p}_0 = \beta_{r_0}\gamma_{r_0}mc$, the transverse canonical momenta are normalized such that in the end:

$$p_x = \mathrm{p}_x/\mathrm{p}_0 \quad \text{and} \quad p_y = \mathrm{p}_y/\mathrm{p}_0 \ , \tag{1.4}$$

which yields the unitless momenta p_x and p_y considered for H. The transverse position, x and y, are unchanged. As for the longitudinal variables, the longitudinal deviation from the reference particle, ζ, is considered together with the energy deviation, p_ζ, following:

$$\zeta = s - \beta_{r_0}ct \quad , \quad p_\zeta = \frac{1}{\beta_{r_0}^2}\frac{E - E_0}{E_0} \ . \tag{1.5}$$

Note that the energy deviation, p_ζ, and the momentum deviation, δ_p, are closely related via $(1+\delta_\mathrm{p})^2 = 1+2p_\zeta+\beta_{r_0}^2p_\zeta^2$, which leads to $\delta_\mathrm{p} \approx p_\zeta$ for small energy deviations ($p_\zeta \ll 1$, $\delta_\mathrm{p} \ll 1$) or ultrarelativistic velocities, $\beta_{r_0} \approx 1$. In the absence of electric fields ($\phi = 0$), the final Hamiltonian reads:

$$H = p_\zeta - (1 + hx)\left[\sqrt{(1 + 2p_\zeta + \beta_{r_0}^2p_\zeta^2) - (p_x - a_x)^2 - (p_y - a_y)^2} - a_s\right] \ , \tag{1.6}$$

where $\vec{a} = q_e\vec{A}/\mathrm{p}_0$ is the scaled vector potential and h is the curvature of the reference trajectory ($h = 1/R$ for a circular arc of radius R). For most magnets, the magnetic field can be taken to be purely transverse ($a_x = a_y = 0$) and piecewise constant, in which case eq. (1.6) can be simplified. These considerations will be made clear in the following chapters. Moreover, typical drift sections will be assumed to be straight ($h = 0$) with curvature only arising as a sequence of small instantaneous dipolar kicks in bending magnets (see Chapter 3).

1.4 The Stability Problem

As we have already established, storage rings are a challenging environment for particle survival: any slight deviation from the design orbit — transverse, or longitudinal — needs to be carefully controlled using different magnets to ensure stability. Moreover, these conditions have to hold for many hours as the particles circulate around the machine for several billions (10^9) of turns. As a direct comparison, the Earth has also revolved around the Sun — autonomously — for several billions of years. It seems therefore natural to draw parallels between these two periodic Hamiltonian systems, and more generally, between the fields of Accelerator Physics and Celestial Mechanics, as did J. Laskar [19], A. Chao [20] and J. Moser [5].

Celestial Mechanics has been, for a long time, the emblem of ultimate stability, periodicity and regularity; concerned with the project of describing with absolute precision the motion of celestial bodies. Significant progress was already established by the *epicycle* theory of the Greeks [21], formalized in the Almagest of Ptolemy (100–175 AD), which is to say that the motion can be decomposed into a finite number of uniform circular motions. However, following Newton's Principia (1687), it has been made clear that this apparent regularity was not so easy to describe mathematically, especially for the case of the famous three-body problem. In 1885,

King Oscar II of Sweden formulated the question as an open challenge, looking for a solution [5]:

> "For an arbitrary system of mass points which attract each other according to Newton's laws, assuming that no two points ever collide, give the coordinates of the individual points for all time as the sum of a uniformly convergent series whose terms are made up of known functions."

The prize from the challenge was awarded to H. Poincaré, who showed in the following years (1892-1899) that no general closed form solutions exist to describe the motion — a behaviour now known as *chaos*. Finally, half a century later (1954-1963), Kolmogorov, Arnold and Moser demonstrated — in a joint theorem (KAM) — that despite the result of Poincaré, some converging solutions are guaranteed to exist in restricted regions of the system. Aside from all this theoretical work, the first "striking example of chaotic behaviour in the solar system" [J. Laskar, 19] was given by the chaotic tumbling of Hyperion, a satellite of Saturn observed in 1984 by the Voyager spacecraft. Clearly, as highlighted throughout 2000 years of history, the question of stability is a complicated one. This is what led J. Moser to ask [5]: *Is the Solar System stable?* And similarly, one could reasonably ask: *Is the LHC beam stable?*

1.4.1 Chaotic systems

Let us emphasize where the problem lies. In the simplest formulation of the n-body problem, two masses orbit each other and the motion remains stable for all eternity — the classical Kepler Problem. Adding additional masses, say by considering Jupiter alongside the Earth and the Sun, brings us into the three-body problem, which has no general closed-form solution. Poincaré himself noted that trajectories can then be separated into two categories: those for which the series expansion converges (stable) and those for which the series diverges (unstable). Moreover, most systems are mixed and admit cases from the first category, and cases from the second [22, 23].

To understand this behaviour, M. Hénon showed that the dynamics of the three-body problem could be reduced to the study of a simple mathematical *map* — which transforms a set of initial coordinates into a set of final coordinates — iterated many times [24]. He noted that *regular* trajectories "seem to lie on a curve", whereas *chaotic* ones behave in a completely different way: "it is clearly impossible to draw any curve through them. They seem to be distributed at random, in an area left free between the closed curves. Most striking is the fact that this change of behaviour seems to occur abruptly" [M. Hénon, 25]. An example of both trajectories can be seen in Fig. 1.7(b), for the Hénon map. As we now know, there is no stochasticity in chaoticity, which is a perfectly deterministic phenomenon. Instead, the problem lies in the non-existence of closed form expressions to describe the motion. S. Wolfram, creator of WolframAlpha, eloquently puts it this way: "From all the successes of Science, we've come to believe that there would be formulas to predict everything. But computational irreducibility [of chaotic systems] shows us that that isn't true. And in fact, to find out what a system will do, we have to go through the same irreducible computational steps as the system itself. Yes it is a weakness of Science, but it is also why the passage of time is significant and meaningful: we cannot jump ahead and get the answer, we have to live the steps." [S. Wolfram, 26]

As it turns out, the Hénon map also finds a direct application in Accelerator Physics, where it models the transverse motion of particles in a simple non-linear system with 1 degree of freedom (see Chapter 5). Starting from a purely linear lattice and considering on-momentum

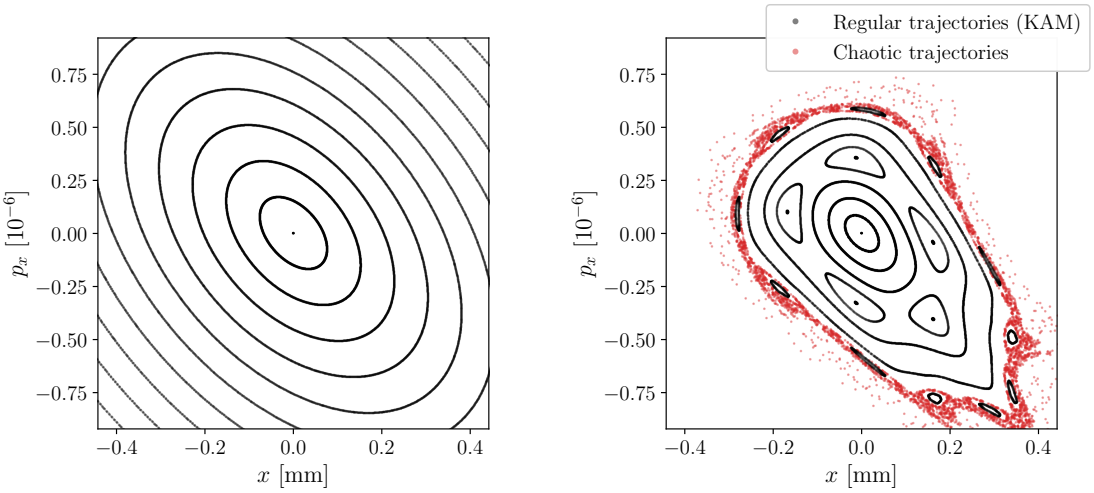

(a) Linear lattice

(b) Non-Linear lattice

Figure 1.7: Phase space portrait of the simplest 2D system of Accelerator Physics. (a) A linear lattice, composed of quadrupoles, dipoles and drifts. (b) A non-linear lattice, where a single thin sextupole is added, leading to amplitude-dependent dynamics. In the non-linear case, the dynamics follows the Hénon map, originally used to study the famous three-body problem of Celestial Mechanics.

particles, the motion remains stable for all eternity at all amplitudes, as shown in Fig. 1.7(a) — a direct analog to the Kepler problem. When a single sextupolar kick is added to the lattice, one obtains the simplest non-linear system of Accelerator Physics, which follows the Hénon map, as shown in Fig. 1.7(b). The dynamics then appears drastically different from the linear case: chaos, resonance islands, high-order fixed points and amplitude-dependent behaviour emerge, in accordance with the observations from Poincaré and Hénon. Therein lies the fundamental question: how then is the stability impacted by the introduction of non-linearities? The KAM theorem, ultimately, provides an answer which guarantees the *existence* of some stable solutions:

KAM Theorem

Consider a Hamiltonian system with n degrees of freedom that is *integrable*, meaning that it admits n independent integrals of motion I_j, also called *actions*, which commute under the Poisson bracket $\{I_j, I_k\} = 0$ $(j, k = 1, 2, \ldots, n)$. Such a Hamiltonian, H_0, can be written as a function of the actions only (*e.g.* for $n = 3$ degrees of freedom):

$$H_0(x, p_x, y, p_y, \zeta, p_\zeta) \mapsto H_0(I_x, I_y, I_\zeta) \tag{1.7}$$

Suppose the system is perturbed by a small term in some region of the phase space. Then, under suitable assumptions (*e.g.*, the non-degeneracy and smoothness of the frequency map $\partial H_0/\partial I_j$), the following claim holds: most of the invariant tori of the integrable system survive the perturbation and the corresponding motion remains quasiperiodic [11, 27, 28]. These surviving KAM tori correspond to frequency vectors that satisfy a diophantine condition [8]. (Additional context shall be found in Chapter 2.)

1.4.2 Quasiperiodic Expansions in Beam Dynamics

Chaos, as it stands, is both a physical phenomenon limiting our ability to describe the motion of realistic non-linear systems; and a mathematical problem emerging from the iteration of simple maps such as Hénon's. In the latter case, convergent solutions require the mathematician to provide formal stability proofs, ensuring a proper description of the motion for all eternity [5]. That being said, most practical applications do not require us to know if the motion is stable for all eternity, but simply for a limited meaningful period of time, which lifts a lot of mathematical subtleties and opens the door for numerical methods to be used.

Oftentimes, chaotic motion may appear to be regular over long periods of time before diverging [22]. If this characteristic time length is longer than the lifetime of the circulating beams, then such a trajectory might be, by all practical accounts, indistinguishable from a stable one. One can therefore understand the interest that was put, over the years, towards the development of *symplectic* particle tracking codes [9], driven by the need to accurately investigate the complex dynamics of non-linear systems beyond the reach of analytic calculations; element by element. As S. Wolfram puts it, "we have to go through the same irreducible computational steps as the system itself". This simple fact establishes particle tracking as the fundamental tool to be used in order to better our understanding of complex machines like the LHC.

But through this process of continuous development on the numerical front, one is at risk of eventually losing the ability to describe, analyse and understand the final particle motion. Let us therefore recall the challenge posed by King Oscar II and seek out the proper series to describe the motion. The natural format for such series was already given by the Greeks — the epicycles — and is nothing else than a generalized Fourier series. This *quasiperiodic* expansion, used by Poincaré for his demonstration and later by Kolmogorov, Arnold and Moser for their theorem, can be written as:

$$\psi_x(N) = \sum_{\vec{n}} A_{\vec{n}} \; e^{i(2\pi(\vec{n}\cdot\vec{Q})N)} \tag{1.8}$$

where $\mathrm{Re}\{\psi_x\}$ is the position — see Chapter 2 — as a function of the turn number, N, which depends on some frequencies, $\vec{Q}$, and integer linear combinations thereof, $\vec{n}\cdot\vec{Q}$. Equation (1.8), the "prize equation", is at the heart of this thesis work, where we aim to show that a profound understanding of beam dynamics can be built around this representation of the motion, building on the success of our predecessors.

In Chapter 2 the distinction between particle dynamics and energy manifold is presented, with important geometrical results pertaining to eq. (1.8). The use of quasiperiodic expansions to describe tracking results is also presented. In Chapter 3, the transformation of eq. (1.8) through a given Hamiltonian flow is described using Lie algebra, which serves as a basis for analytic calculations. In Chapter 4, coupled and uncoupled linear dynamics is presented in this formalism, leading to an effective and unified description of 2D, 4D and 6D linear motion. In Chapter 5, non-linear effects are introduced, showing the importance of eq. (1.8) in this context, allowing for visual interpretations of non-linearities and measurements of the non-linear residual. Finally, the Appendix presents experimental studies that motivated and guided the development of this formalism.

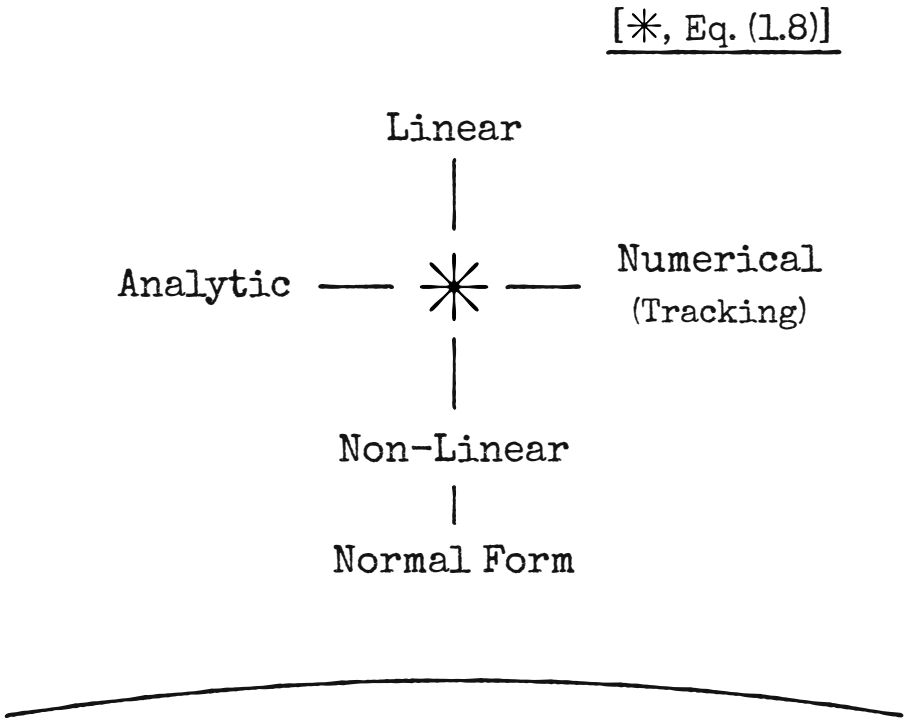

Figure 1.8: The Thesis. In the following chapters, we hope to show that the quasiperiodic expansion of eq. (1.8) can serve as the cornerstone of a formalism unifying both linear and non-linear motion. From there, Normal Form Analysis becomes more intuitive, as it naturally relies on such series. Furthermore, eq. (1.8) will be shown to bridge analytic calculations and numerical tools, enabling us to describe and interpret the complex dynamics of tracking experiments using the very same formalism as in theoretical analysis. With this approach, we hope to recover the insight provided the epicycles theory of the ancient Greeks — an idea that eventually led to the KAM theorem, centuries later.

CHAPTER 2

Topological Foundations

Energy Manifolds and Quasiperiodic Motion

The study of single-particle dynamics in circular accelerators relies on the observation that most trajectories remain regular and confined, despite the underlying non-linearities of the system and the presence of chaotic layers. These regular trajectories are embedded on invariant tori, and their long-term behaviour remains stable. As such, it becomes essential to develop a robust understanding of the dynamics and the topology of these tori within a general Hamiltonian framework.

In this chapter, the evolution of loops and tori under Hamiltonian flow is examined and is connected to the fundamental concept of symplecticity. Building on a Fourier description of these geometric objects, we show that a symplectic area can be consistently defined — even in 6-dimensional phase space — and associated to well-defined integrals of motion. The embedding of single-particle trajectories on these invariant tori is then demonstrated explicitly for periodic systems. Finally, a numerical method — the Numerical Analysis of the Fundamental Frequencies (NAFF) — is introduced and is used to construct these tori from tracking data. This allows to retrieve the corresponding integrals of motion and obtain an insightful description of the motion; both for linear and non-linear cases.

2.1 Hamiltonian Flow

The transport problem of single-particle dynamics is concerned with the description of the motion — positions and momenta — of particles travelling through a beam line. For a particle with n degrees of freedom, a $2n$-dimensional *phase space* can be used to uniquely specify its state at a given longitudinal location. Recall that the usual time variable t of Hamiltonian mechanics was traded for the longitudinal location s in the formulation of eq. (1.6). In the following chapters, 3 degrees of freedom will be implicitly assumed for the sake of generality, yielding a 6D phase space, $\vec{x} = (x, p_x, y, p_y, \zeta, p_\zeta)$.

2.1.1 Complex coordinates

Consider the full phase space, formed by the three pairs of canonically conjugate variables: (x, p_x), (y, p_y), and (ζ, p_ζ). According to Hamilton's equations, a given Hamiltonian $H(\vec{x}; s)$ leads to a set of six coupled differential equations:

$$H(\vec{x}; s) \quad \mapsto \quad \frac{dx}{ds}, \ \frac{dp_x}{ds}, \ \frac{dy}{ds}, \ \frac{dp_y}{ds}, \ \frac{d\zeta}{ds}, \ \frac{dp_\zeta}{ds} \ , \tag{2.1}$$

which describe the Hamiltonian *flow* of the system. Indeed, integrating the set of equations (2.1) between two longitudinal locations, s_1 and s_2, allows us to transport particles along the longitudinal axis, as shown in Fig. 2.1. Naturally, Hamiltonian flow gives rise to the concept of maps [6], which describe the transformation of phase space step-by-step, integrating every point forward in s.

Let us denote the phase space coordinates $\vec{x}$ of a given particle as a set of complex coordinates, $\boldsymbol{\psi} = (\psi_x, \psi_y, \psi_\zeta)^\intercal$, whose three projections — one in each conjugate plane — read:

$$\boldsymbol{\psi} \ : \ \begin{cases} \psi_x \equiv x/\sqrt{\beta_{x_0}} - ip_x\sqrt{\beta_{x_0}} \\ \psi_y \equiv y/\sqrt{\beta_{y_0}} - ip_y\sqrt{\beta_{y_0}} \\ \psi_\zeta \equiv \zeta/\sqrt{\beta_{\zeta_0}} - ip_\zeta\sqrt{\beta_{\zeta_0}} \end{cases} \ , \tag{2.2}$$

after being rescaled by some arbitrary lengths, β_{j_0} ($j \in \{x, y, \zeta\}$), such that all projections of $\boldsymbol{\psi}$ have homogeneous units of $\sqrt{\text{m}}$. To lift this arbitrariness, β_{j_0} can be chosen to be 1 m — as done in this thesis — or chosen to match the Courant-Snyder β-function (periodic or not) at the entrance of the beam line in each plane, as discussed in Chapter 4. The interest of eq. (2.2) lies in the ability to describe any pair of conjugate variables in the complex plane directly, as well as being able to recover the individual coordinates at any points following:

$$x = \frac{1}{2}(\psi_x + \psi_x^*)\sqrt{\beta_{x_0}} \ , \tag{2.3}$$

$$p_x = \frac{i}{2}(\psi_x - \psi_x^*)/\sqrt{\beta_{x_0}} \ , \tag{2.4}$$

and idem for the other projections. Note that the vector $\boldsymbol{\psi}$ is represented in bold font, instead of the usual vectorial arrow, to emphasize the fact that it describes a specific object (a particle).

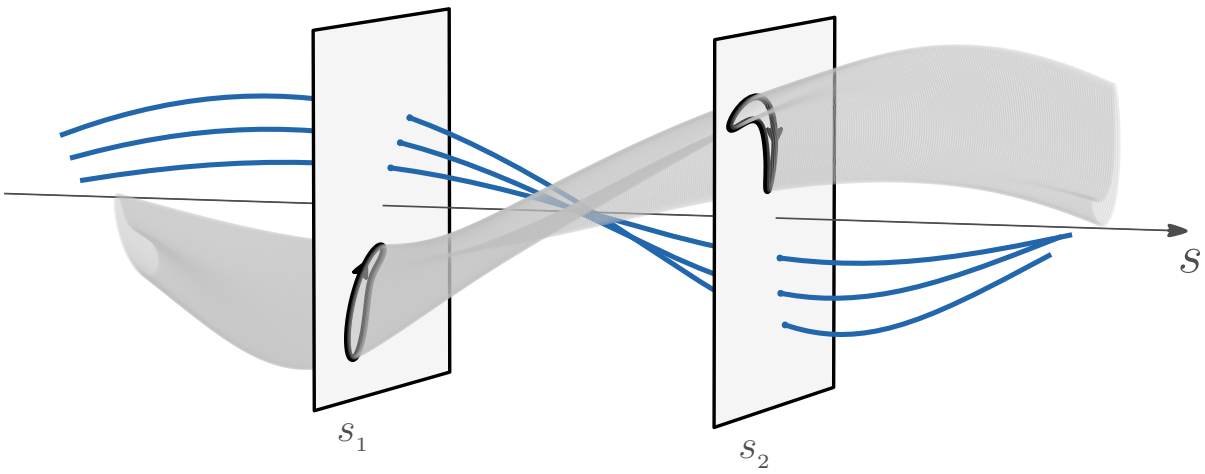

Figure 2.1: Hamiltonian flow of a simple beam line. The horizontal phase space (x, p_x) is recorded at two longitudinal locations, s_1 and s_2. Three particles (in blue), $\boldsymbol{\psi}_1$, $\boldsymbol{\psi}_2$ and $\boldsymbol{\psi}_3$, are transported along the longitudinal axis according to Hamilton's equations. A loop (in black), $\boldsymbol{\mathcal{L}}(\ell) = \boldsymbol{\Psi}(\Theta_x)$, is also transported according to Hamilton's equations.

2.1.2 Symplectic Maps

Transformations from a Hamiltonian flow have the particularity of being *symplectic* [6]: they preserve the area of any *loop* — any closed curve — drawn in phase space. Clearly, this feature cannot be appreciated by studying single particles in the form of $\boldsymbol{\psi}$ from eq. (2.2). Hence, let us consider instead a periodic function of some angles, $\vec{\Theta} = (\Theta_x, \Theta_y, \Theta_\zeta)$, which describes a collection of points, $\vec{X}(\vec{\Theta}) = (X, P_x, Y, P_y, Z, P_\zeta)(\vec{\Theta})$ in the 6-dimensional phase space. Using a similar complex notation, we write:

$$\boldsymbol{\Psi}(\vec{\Theta}) \;:\; \begin{cases} \Psi_x(\vec{\Theta}) \equiv X/\sqrt{\beta_{x_0}} - iP_x\sqrt{\beta_{x_0}} \\ \Psi_y(\vec{\Theta}) \equiv Y/\sqrt{\beta_{y_0}} - iP_y\sqrt{\beta_{y_0}} \\ \Psi_\zeta(\vec{\Theta}) \equiv Z/\sqrt{\beta_{\zeta_0}} - iP_\zeta\sqrt{\beta_{\zeta_0}} \end{cases} , \tag{2.5}$$

where capital letters are used to distinguish the coordinates of this topological (6D) object from the single-particle coordinates $(x, p_x$, etc.) presented earlier. Once again, the individual coordinates can be recovered using:

$$X(\vec{\Theta}) = \frac{1}{2}(\Psi_x + \Psi_x^*)\sqrt{\beta_{x_0}} \,, \tag{2.6}$$

$$P_x(\vec{\Theta}) = \frac{i}{2}(\Psi_x - \Psi_x^*)/\sqrt{\beta_{x_0}} \,, \tag{2.7}$$

and idem for the other projections. With this functional form, $\boldsymbol{\Psi}(\vec{\Theta})$ represents a *torus* (more details in the next section) on which a loop, $\boldsymbol{\mathcal{L}}(\ell)$, can be embedded by letting the angles evolve as a parametric function of a single parameter, *e.g.* $\vec{\Theta}(\ell) = (\Theta_x(\ell), \text{cst.}, \text{cst.})$ with $\Theta_x(\ell) = 2\pi\ell$. An arbitrary loop can be obtained with a general parametrization such as $\vec{\Theta}(\ell) = (\Theta_x(\ell), \Theta_y(\ell), \Theta_\zeta(\ell))$ with $0 \leq \ell \leq 1$. For a purely 2D problem, any torus is de facto a loop and vice versa. Although $\boldsymbol{\psi}$ and $\boldsymbol{\Psi}(\vec{\Theta})$ are used to describe different objects — a particle in one case and a torus in the other — both can be transformed following the Hamiltonian

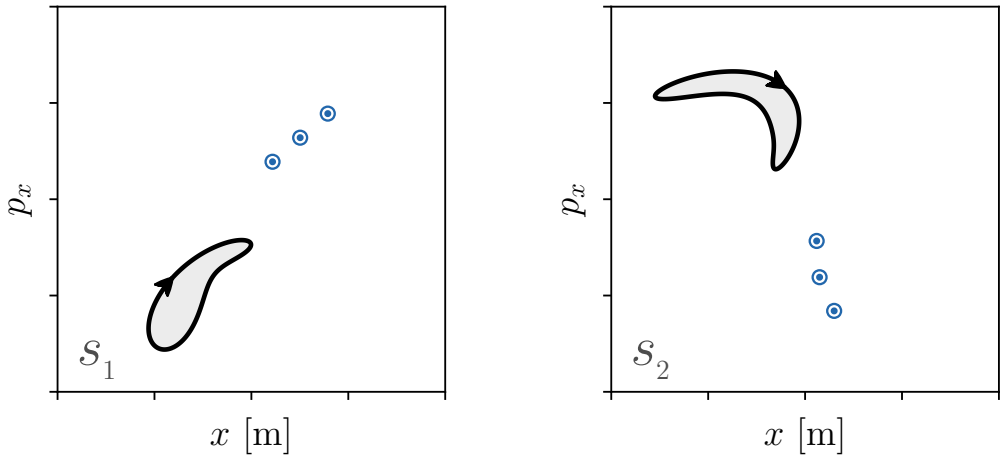

(a) (b)

Figure 2.2: Horizontal phase space (x, p_x) from Fig. 2.1 for the two longitudinal locations, s_1 and s_2. The three particles, $\boldsymbol{\psi}_1$, $\boldsymbol{\psi}_2$ and $\boldsymbol{\psi}_3$, are mapped to new coordinates in the transformation $s_1 \to s_2$. As for the loop, $\boldsymbol{\mathcal{L}}(\ell) = \boldsymbol{\Psi}(\Theta_x)$, it is both displaced and deformed, but the enclosed area (in light grey) is conserved, by virtue of symplecticity.

flow of the system. Every point on $\boldsymbol{\Psi}$ constitutes an initial condition (at a fixed s location) for Hamilton's equations, and one can transport the torus by integrating each point forward. In Fig. 2.1, a simple loop $\boldsymbol{\mathcal{L}}(\ell) = \boldsymbol{\Psi}(\Theta_x)$ is transformed following the Hamiltonian flow of the system alongside some particles, $\boldsymbol{\psi}_1$, $\boldsymbol{\psi}_2$ and $\boldsymbol{\psi}_3$. For this illustration, only the x-projection, $\Psi_x(\Theta_x)$, is considered. Since the transformation is symplectic, one can formally show [6] that the "area" enclosed by the loop — closely linked to the *action* of the loop — is preserved under the Hamiltonian flow. To further investigate this claim, the horizontal phase space at the two longitudinal locations, s_1 and s_2, is reproduced in Fig. 2.2. The three disconnected particles are seen to be mapped to new coordinates in the transformation $s_1 \to s_2$. As for the loop, it is seen to be both displaced and deformed, but the enclosed area (in light grey) is conserved, by virtue of symplecticity. Alternative formulations of the symplectic condition shall be given in Chapter 3.

2.1.3 Fourier Series for Loops and Tori

If Θ_x, Θ_y and Θ_ζ are left to separately vary from 0 to 2π, $\boldsymbol{\Psi}(\vec{\Theta})$ becomes a parametric description of a set of periodic coordinates — a set of $\vec{X}$ in phase space — which all belong to a 3-torus. Broadly speaking, an n-torus is a periodic structure constructed as the product of n independent periodicities, such as $\vec{\Theta} = (\Theta_x, \Theta_y, \Theta_\zeta)$ [29]. If only one angle is left to vary, *e.g.* if $\vec{\Theta}(\ell) = (\Theta_x(\ell), \text{cst.}, \text{cst.})$ with $\Theta_x(\ell) = 2\pi\ell$, then the collection of points forms a loop, embedded on the torus, and evolving in the 6-dimensional phase space. The same can be said for any constraint — or *resonance* condition — which limits the number of free parameters to 1 such that $\vec{\Theta} = \vec{\Theta}(\ell)$. Again, a 1-torus is by definition a loop, as mentioned earlier.

As it turns out, this object is precisely a 6-dimensional generalization of the epicycles. Using a set of three coupled Fourier series, the projections of a given torus $\mathbf{\Psi}$, in each plane, can be written as:

$$\mathbf{\Psi}(\vec{\Theta}) \;:\; \begin{cases} \Psi_x(\vec{\Theta}) = \sum_{\vec{n}} A_{\vec{n}}\; e^{i(\vec{n}\cdot\vec{\Theta})} \\ \Psi_y(\vec{\Theta}) = \sum_{\vec{n}} B_{\vec{n}}\; e^{i(\vec{n}\cdot\vec{\Theta})} \\ \Psi_\zeta(\vec{\Theta}) = \sum_{\vec{n}} C_{\vec{n}}\; e^{i(\vec{n}\cdot\vec{\Theta})} \end{cases}, \qquad \text{with } \mathbf{\Psi}(\vec{\Theta}) \;:\; \mathbb{R}^3 \mapsto \mathbb{C}^3 \tag{2.8}$$

where $\vec{n} \in \mathbb{Z}^3$ is any integer vector and $\vec{n}\cdot\vec{\Theta} = (n_x, n_y, n_\zeta)\cdot(\Theta_x, \Theta_y, \Theta_\zeta)$ are linear combinations of the three angles by which *coupling* effects arise. The spectral amplitudes, $A_{\vec{n}}$, $B_{\vec{n}}$ and $C_{\vec{n}}$ are complex numbers corresponding to the projection of Ψ_j on a given *phasor* of the basis, $|\,\vec{n}\,\rangle = e^{i(\vec{n}\cdot\vec{\Theta})}$, which we can write as the inner product (in Dirac notation):

$$A_{\vec{n}} = \langle\,\vec{n}\,|\,\Psi_x\,\rangle = \frac{1}{(2\pi)^3}\int_0^{2\pi}\int_0^{2\pi}\int_0^{2\pi} \Psi_x(\vec{\Theta})\; e^{-i(\vec{n}\cdot\vec{\Theta})}\; d\Theta_x\, d\Theta_y\, d\Theta_\zeta\;, \tag{2.9}$$

and idem for $B_{\vec{n}}$ and $C_{\vec{n}}$. Before delving into the general 6D case, it is insightful to look at some recognizable expansions for the 2D case. When only $\Psi_x(\Theta_x)$ is considered, one should remember the distinction between the following expansions:

$$\begin{aligned} &\text{(Circle)} && \Psi_x = A_1 e^{i\Theta_x}\;, \\ &\text{(Ellipse)} && \Psi_x = A_1 e^{i\Theta_x} + A_{\text{-}1} e^{-i\Theta_x}\;, \\ &\text{(General)} && \Psi_x = \ldots + A_{\text{-}1} e^{-i\Theta_x} + A_0 + A_1 e^{i\Theta_x} + A_2 e^{i2\Theta_x} + \ldots\;, \end{aligned} \tag{2.10}$$

i.e., expansions with one or two phasors describe, respectively, circles and ellipses; and more phasors can be added to describe a more general loop. An example from each case is shown in Fig. 2.3 for reference. In particular, the constant term, A_0, gives the position of the centroid of the loop — and more generally $\{A_0, B_0, C_0\}$ point to the centroid of the torus in 6D.

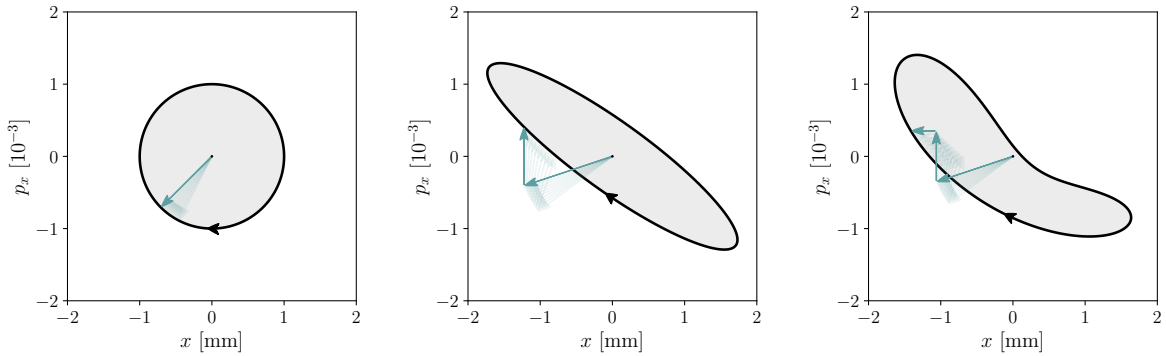

(a) Circle (b) Ellipse (c) General

Figure 2.3: Recognizable cases for 2D phasor expansions. (a) A circle, made of one phasor: $\{A_1\} = \{1\}\,\sqrt{\mu\text{m}}$. (b) An ellipse, made of two phasors: $\{A_1, A_{\text{-}1}\} = \frac{\sqrt{3}}{3}\{(2+i), (1+i)\}\,\sqrt{\mu\text{m}}$. (c) A general loop, here made of three phasors: $\{A_1, A_{\text{-}1}, A_2\} = \frac{1}{2}\{(2+i), (1+i), (i/\sqrt{2})\}\,\sqrt{\mu\text{m}}$. In all three cases, the area enclosed by the loop is $\pi\,\mu\text{m}$.

To appreciate the distinction between loops and tori, one must go beyond the 2D case (in 2D, loops and tori are equivalent). Considering the 6-dimensional phase space, we can parametrize the angles $\vec{\Theta}$ of a given torus to describe an embedded loop, $\mathcal{L}(\ell)$, which yields:

$$\boldsymbol{\mathcal{L}}(\ell) \;:\; \begin{cases} \mathcal{L}_x(\ell) = \Psi_x(\vec{\Theta}(\ell)) \\ \mathcal{L}_y(\ell) = \Psi_y(\vec{\Theta}(\ell)) \\ \mathcal{L}_\zeta(\ell) = \Psi_\zeta(\vec{\Theta}(\ell)) \end{cases}, \quad \text{with } 0 \leq \ell \leq 1 \;, \tag{2.11}$$

where the different projections of $\boldsymbol{\mathcal{L}}(\ell)$ follow the same Fourier series as the projections of $\boldsymbol{\Psi}$, on which it is embedded. By construction, there exist three — and only three — topologically independent closed curves on $\boldsymbol{\Psi}$ that cannot be continuously deformed into one another [29]. Since Θ_x, Θ_y and Θ_ζ are the fundamental periodicities of the structure — as expressed in eq. (2.8) — we can identify the fundamental families of loops to be those corresponding to full cycles over Θ_x, Θ_y or Θ_ζ. To highlight the nature of a given loop, we shall make a distinction between the three families using the following notation:

$$\begin{aligned} \boldsymbol{\Psi}(\Theta_x^{\circlearrowleft}, \Theta_y, \Theta_\zeta) \quad &\mapsto \quad \boldsymbol{\mathcal{L}}(\ell) = \boldsymbol{\Psi}(2\pi\ell, \Theta_y, \Theta_\zeta) \\ \boldsymbol{\Psi}(\Theta_x, \Theta_y^{\circlearrowleft}, \Theta_\zeta) \quad &\mapsto \quad \boldsymbol{\mathcal{L}}(\ell) = \boldsymbol{\Psi}(\Theta_x, 2\pi\ell, \Theta_\zeta) \;, \quad \text{with } 0 \leq \ell \leq 1 \;, \\ \boldsymbol{\Psi}(\Theta_x, \Theta_y, \Theta_\zeta^{\circlearrowleft}) \quad &\mapsto \quad \boldsymbol{\mathcal{L}}(\ell) = \boldsymbol{\Psi}(\Theta_x, \Theta_y, 2\pi\ell) \end{aligned} \tag{2.12}$$

where $\boldsymbol{\Psi}(\Theta_x^{\circlearrowleft}, \Theta_y, \Theta_\zeta)$ denotes a full cycle over Θ_x while all other angles are kept constant, and so on. Any other generic loop on the torus can be obtained by combining these fundamental cycles via generic parametrization of the three angles, $\Theta_x(\ell)$, $\Theta_y(\ell)$ and $\Theta_\zeta(\ell)$.

As shown in the upcoming sections, studying the basic cycles of 4D and 6D tori can provide insightful observations on the phase space dynamics. In particular, separating the fundamental families of loops can be used to visualize the hyperdimensional structures by reducing the dimensionality of the problem. An example of this approach is shown in Fig. 2.4 for a simple 4D torus. In Fig. 2.4(a), various loop projections $\Psi_x(\Theta_x^{\circlearrowleft}, \Theta_y)$ are taken by letting Θ_y vary, sweeping out a surface which reveals the toroidal structure in the (x, p_x) phase space. The procedure is then repeated with the Ψ_y projection to reveal the structure of $\Theta_x^{\circlearrowleft}$ loops in the (y, p_y) phase space, completing the description of the first family. In Fig. 2.4(b), the second family of loops is studied in the same way, giving us a representation of $\Theta_y^{\circlearrowleft}$ loops in both planes, $\Psi_x(\Theta_x, \Theta_y^{\circlearrowleft})$ and $\Psi_y(\Theta_x, \Theta_y^{\circlearrowleft})$.

Similarly, one can also explore all the possible values taken by $\Psi_x(\vec{\Theta})$ and $\Psi_y(\vec{\Theta})$ in their respective phase space, (x, p_x) and (y, p_y), as shown in Fig. 2.5. By flattening the torus in such a way, one essentially obtains the "shadow" of both projections, covering a finite region of the phase space. From there, a given loop can be studied by adding its projection in both planes, *e.g.* $\Psi_x(\Theta_x^{\circlearrowleft}, \Theta_y = \text{cst.})$ and $\Psi_y(\Theta_x^{\circlearrowleft}, \Theta_y = \text{cst.})$ for a given $\Theta_x^{\circlearrowleft}$ loop. Naturally, the projections from any loop must lie within the region covered by the flattened torus. By letting the other angle vary (Θ_y in this case), the loop projections are seen to move within the shadow, eventually painting the entirety of the flattened torus when all combinations of angles are explored. This second technique, more compact, complements the results from Fig. 2.4.

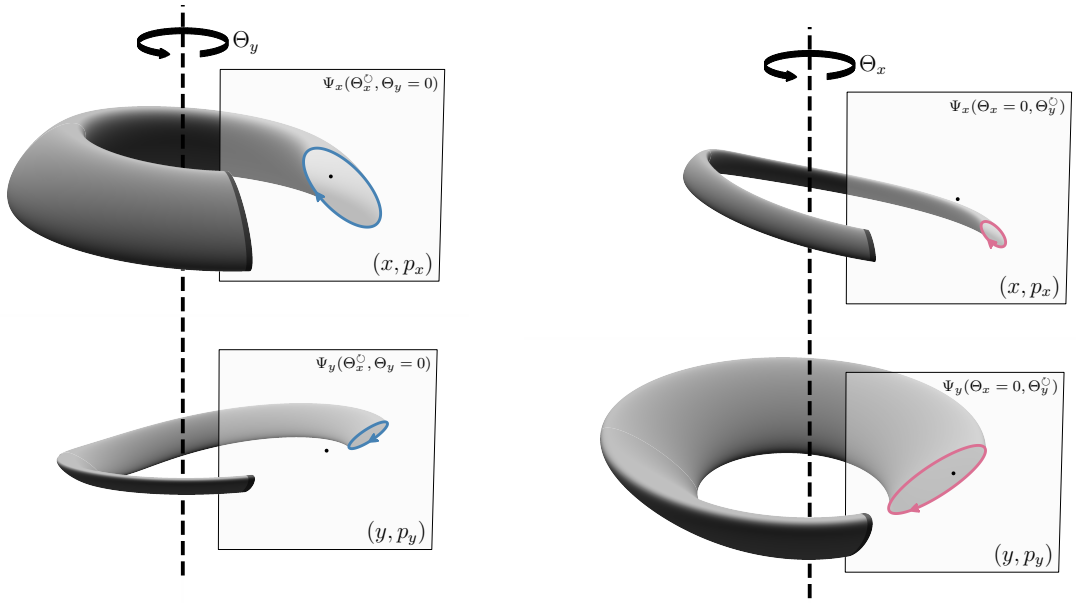

(a) (b)

Figure 2.4: Visualization of the basic cycles of a 4D torus, $\mathbf{\Psi}(\Theta_x^{\circlearrowleft}, \Theta_y)$ and $\mathbf{\Psi}(\Theta_x, \Theta_y^{\circlearrowleft})$ at a fixed s location. (a) Projections of all $\Theta_x^{\circlearrowleft}$ loops in the (x, p_x) phase space (top) and (y, p_y) phase space (bottom). (b) Projections of all $\Theta_y^{\circlearrowleft}$ loops in the (x, p_x) phase space (top) and (y, p_y) phase space (bottom). All loops are travelled following the directional arrows.

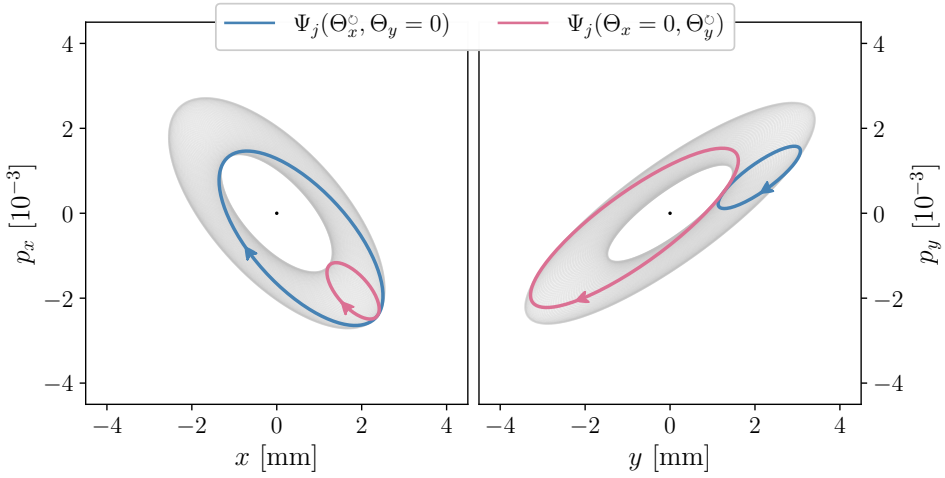

Figure 2.5: Shadow of the 4D $\mathbf{\Psi}$ torus (grey) in both conjugate planes. The projections of two loops, obtained from the two basic cycles $\mathbf{\Psi}(\Theta_x^{\circlearrowleft}, \Theta_y = 0)$ and $\mathbf{\Psi}(\Theta_x = 0, \Theta_y^{\circlearrowleft})$, are also shown. The phasor expansion of the torus contains four phasors in each plane, as given below.

	$\vec{n}$:	$(1,0)$	$(-1,0)$	$(0,1)$	$(0,-1)$
Ψ_x : $A_{\vec{n}}$	$[\sqrt{\mu m}]$	$1.368+1.266i$	$0.429+0.561i$	$0.439+0.410i$	$0.132+0.179i$
Ψ_y : $B_{\vec{n}}$	$[\sqrt{\mu m}]$	$-0.744-0.071i$	$-0.095+0.415i$	$1.888+0.206i$	$0.213-1.050i$

2.1.4 Poincaré Integral Invariants

Let us go back to the area-preserving property of symplectic transformations by considering a closed loop $\boldsymbol{\mathcal{L}}(\ell)$ embedded in the 6-dimensional phase space. The *symplectic area* $\mathcal{A}(\boldsymbol{\mathcal{L}})$ of the loop is in fact the sum of the 3 *phase space areas* of the projections of $\boldsymbol{\mathcal{L}}(\ell)$ on the 3 conjugate planes [6], such that:

$$\mathcal{A}(\boldsymbol{\mathcal{L}}) \equiv \oint_{\mathcal{L}} \Big(P_x \, dX + P_y \, dY + P_\zeta \, dZ \Big) \ , \tag{2.13}$$

where $\vec{X}$ are the coordinates of the loop. Historically, eq. (2.13) is referred to as the Poincaré Integral Invariant, and is precisely the quantity being conserved along the Hamiltonian flow of a time-independent system. This "area" relates to the action of the loop via $I = \mathcal{A}/2\pi$.

In previous sections, we have been considering tori made of 3 independent periodicities, where 3 topologically independent families of loops can be found. On a given torus, $\boldsymbol{\Psi}(\vec{\Theta})$, we can therefore define 3 independent symplectic areas, obtained by integrating over the 3 basic cycles following:

$$\begin{aligned}
\mathcal{A}_x &= \oint_{\Theta_x} \Big(P_x \, dX + P_y \, dY + P_\zeta \, dZ \Big) = \mathcal{A}_{xx} + \mathcal{A}_{xy} + \mathcal{A}_{x\zeta} \\
\mathcal{A}_y &= \oint_{\Theta_y} \Big(P_x \, dX + P_y \, dY + P_\zeta \, dZ \Big) = \mathcal{A}_{yx} + \mathcal{A}_{yy} + \mathcal{A}_{y\zeta} \ , \\
\mathcal{A}_\zeta &= \oint_{\Theta_\zeta} \Big(P_x \, dX + P_y \, dY + P_\zeta \, dZ \Big) = \mathcal{A}_{\zeta x} + \mathcal{A}_{\zeta y} + \mathcal{A}_{\zeta\zeta}
\end{aligned} \tag{2.14}$$

where $\vec{X}$ are coordinates on the torus. Each symplectic area is obtained as the sum of the partial areas in each plane, $\mathcal{A}_{jx} = \oint_{\Theta_j} P_x \, dX$, $\mathcal{A}_{jy} = \oint_{\Theta_j} P_y \, dY$ and $\mathcal{A}_{j\zeta} = \oint_{\Theta_j} P_\zeta \, dZ$, as shown in Fig. 2.6 for a 6D torus. For any given projection, *e.g.* $\mathcal{A}_{xx}$, the area is not expected to be conserved by itself. Instead, the conserved quantity — the symplectic area of the loop — corresponds to the sum of all projections on the conjugate planes. In Fig. 2.6(a,b,c), the three independent symplectic areas obtained from $\Theta_x^{\circlearrowleft}$, $\Theta_y^{\circlearrowleft}$ and $\Theta_\zeta^{\circlearrowleft}$ are shown with unique colors in all three conjugate planes. Areas travelled clockwise are positive — as hinted at by the looping symbol, $\Theta^{\circlearrowleft}$ — and negative otherwise.

Starting from the Fourier expansion of the torus, eq. (2.5), the Poincaré Integral Invariants can be computed and expressed in terms of the complex coefficients of the expansion, which are assumed to be known. Following a short derivation (see Demonstration 2.1 on page 24), one can show that the first partial area is given by:

$$\mathcal{A}_{jx}(\vec{\Theta}) = \pi \sum_{\vec{n}} n_j |\, \langle\, \vec{n} \,|\, \Psi_x \,\rangle\, |^2 + \Delta_{jx}(\vec{\Theta}) = \pi \sum_{\vec{n}} n_j |A_{\vec{n}}|^2 + \Delta_{jx}(\vec{\Theta}) \tag{2.15}$$

with

$$\Delta_{jx}(\vec{\Theta}) = \pi \sum_{\vec{n}} \sum_{\vec{m} \neq \vec{n}} \delta_{n_j, m_j} \Big(n_j |A_{\vec{n}}||A_{\vec{m}}| \cos\Big(\varphi_{\vec{n},j}(\vec{\Theta}) - \varphi_{\vec{m},j}(\vec{\Theta}) \Big) \Big) \tag{2.16}$$

where $\delta_{n_j,m_j} = 1$ if $n_j = m_j$ (0 otherwise) and where, *e.g.*, $\varphi_{\vec{n},x}(\vec{\Theta}) = n_y \Theta_y + n_\zeta \Theta_\zeta + \arg\left[A_{\vec{n}}\right]$ is a phase parameter keeping track of the non-integrated angles as well as the phase of the complex coefficients, $\arg\left(A_{\vec{n}}\right)$. In the different projection planes, the different $\mathcal{A}_{jx}$ and $\Delta_{jx}(\vec{\Theta})$ functions are obtained from eq. (2.15) and eq. (2.16) by permuting the coefficients of the Fourier expansion, *i.e.*, where $\mathcal{A}_{xx} \to \mathcal{A}_{xy} \to \mathcal{A}_{x\zeta}$ are obtained by replacing $A_{\vec{n}} \to B_{\vec{n}} \to C_{\vec{n}}$ and so on.

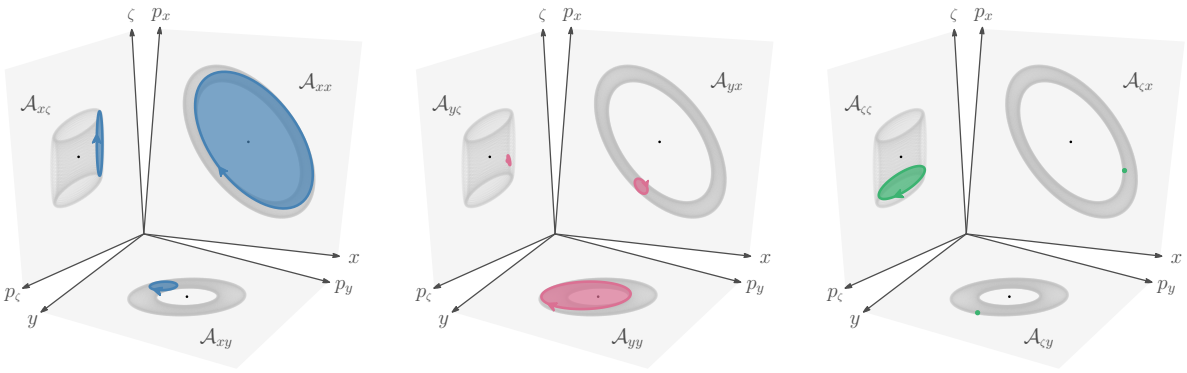

(a) (b) (c)

Figure 2.6: The 3 Poincaré Integral Invariants for a 6D torus. (a) $\mathcal{A}_x$, obtained from the sum of the three partial areas in blue. (b) $\mathcal{A}_y$, obtained from the sum of the three partial areas in pink. (c) $\mathcal{A}_\zeta$, obtained from the sum of the three partial areas in green. In (a,b,c), the (ζ, p_ζ) plane was scaled up for the benefit of the visual representation. Each of the projected areas is positive (positively oriented) since travelled clockwise.

	$\vec{n}$:	$(1,0,0)$	$(-1,0,0)$	$(0,1,0)$	$(0,-1,0)$	$(0,0,1)$	$(0,0,-1)$
Ψ_x : $A_{\vec{n}}$	$[\sqrt{\mu m}]$	$3.461+0.024i$	$3.342+0.024i$	$-0.323-0.204i$	$-0.314+0.193i$	$0.000+0.000i$	$0.000-0.000i$
Ψ_y : $B_{\vec{n}}$	$[\sqrt{\mu m}]$	$0.557-0.319i$	$0.534+0.313i$	$2.002+0.010i$	$1.928+0.010i$	$0.000-0.000i$	$0.000+0.000i$
Ψ_ζ : $C_{\vec{n}}$	$[\sqrt{\mu m}]$	$-0.093+0.070i$	$-0.093-0.070i$	$-0.000-0.020i$	$-0.000+0.020i$	$0.038-0.000i$	$0.038-0.000i$

Hence, the 3 independent Poincaré Integral Invariants of eq. (2.14) can be written as:

$$\begin{aligned}
\mathcal{A}_x(\vec{\Theta}) &= \pi \sum_{\vec{n}} n_x \left(|A_{\vec{n}}|^2 + |B_{\vec{n}}|^2 + |C_{\vec{n}}|^2 \right) + \Delta_x(\vec{\Theta}) \\
\mathcal{A}_y(\vec{\Theta}) &= \pi \sum_{\vec{n}} n_y \left(|A_{\vec{n}}|^2 + |B_{\vec{n}}|^2 + |C_{\vec{n}}|^2 \right) + \Delta_y(\vec{\Theta}) \\
\mathcal{A}_\zeta(\vec{\Theta}) &= \pi \sum_{\vec{n}} n_\zeta \left(|A_{\vec{n}}|^2 + |B_{\vec{n}}|^2 + |C_{\vec{n}}|^2 \right) + \Delta_\zeta(\vec{\Theta})
\end{aligned} , \tag{2.17}$$

where the remainder, $\Delta_j(\vec{\Theta})$, carries all the angular dependence following:

$$\Delta_j(\vec{\Theta}) = \Delta_{jx}(\vec{\Theta}) + \Delta_{jy}(\vec{\Theta}) + \Delta_{j\zeta}(\vec{\Theta}) \ , \tag{2.18}$$

in each plane, $j \in \{x, y, \zeta\}$. In the example of Fig. 2.6, the remainder of $\mathbf{\Psi}$ is zero for all angles since no spectral line contributes to the various Δ_j (since $\delta_{n_j,m_j} = 0$ for $\vec{n} \neq \vec{m}$ in eq. (2.16)). This is to say that all loops from a given family share the same symplectic area with no dependence on the non-integrated angles. If one were to add additional spectral lines, such as $A_{(1,1,0)} \neq 0$ and $B_{(1,1,0)} \neq 0$, then all of Δ_{xx}, Δ_{xy}, Δ_{yx} and Δ_{yy} would become non-zero, introducing an angular dependence on the projected areas. This result does not jeopardize symplecticity: any loop, parametrized by some $\vec{\Theta}(\ell)$, can be transported through the Hamiltonian flow of the system and its area remains invariant. Instead, the claim of eq. (2.17) is that various loops from a given family — *e.g.* from the $\Theta_x^{\circlearrowleft}$ cycle — start with a different symplectic area depending on Θ_y and Θ_ζ. This observation is a key element for the integrability condition, as discussed in the next section.

Demonstration 2.1: Poincaré Integral Invariant.

We wish to evaluate the partial area, $\mathcal{A}_{xx}$, given by:

$$\mathcal{A}_{xx} = \oint_{\Theta_x} P_x dX = \int_0^{2\pi} \left(P_x \frac{\partial X}{\partial \Theta_x} \right) d\Theta_x \ . \tag{2.19}$$

Starting from the Fourier series of eq. (2.5), we can write:

$$\Psi_x(\vec{\Theta}) = \sum_{\vec{n}} A_{\vec{n}} \ e^{i(n_x\Theta_x + n_y\Theta_y + n_\zeta\Theta_\zeta)} \quad \Rightarrow \quad \begin{cases} X = \sum\limits_{\vec{n}} |A_{\vec{n}}| \cos\big(n_x\Theta_x + \varphi_{\vec{n},x}\big) \\ P_x = -\sum\limits_{\vec{n}} |A_{\vec{n}}| \sin\big(n_x\Theta_x + \varphi_{\vec{n},x}\big) \end{cases} , \tag{2.20}$$

where $X = \mathrm{Re}\{\Psi_x\}\sqrt{\beta_{x_0}}$, $P_x = -\,\mathrm{Im}\{\Psi_x\}/\sqrt{\beta_{x_0}}$ and $\varphi_{\vec{n},x}(\vec{\Theta}) = n_y\Theta_y + n_\zeta\Theta_\zeta + \arg\left(A_{\vec{n}}\right)$ is a phase parameter keeping track of the non-integrated angles (here Θ_y and Θ_ζ) as well as the phase of the complex coefficients, $\arg\left(A_{\vec{n}}\right)$. The integrand of eq. (2.19) then reads:

$$\left(P_x \frac{\partial X}{\partial \Theta_x} \right) = \sum_{\vec{n}} \sum_{\vec{m}} n_x |A_{\vec{n}}||A_{\vec{m}}| \sin\big(n_x\Theta_x + \varphi_{\vec{n},x}\big) \sin\big(m_x\Theta_x + \varphi_{\vec{m},x}\big) \tag{2.21}$$

To proceed with the integral, the following orthogonal identity can be used:

$$\int_0^{2\pi} \sin\big(n_x\Theta_x + \varphi_{\vec{n},x}\big) \sin\big(m_x\Theta_x + \varphi_{\vec{m},x}\big) d\Theta_x = \delta_{n_x,m_x} \Big(\pi \cos\big(\varphi_{\vec{n},x} - \varphi_{\vec{m},x}\big) \Big) \tag{2.22}$$

where $\delta_{n_x,m_x} = 1$ if $n_x = m_x$ and 0 otherwise. After integration, we therefore end up with:

$$\mathcal{A}_{xx} = \pi \sum_{\vec{n}} \sum_{\vec{m}} \delta_{n_x,m_x} \Big(n_x |A_{\vec{n}}||A_{\vec{m}}| \cos\big(\varphi_{\vec{n},x} - \varphi_{\vec{m},x}\big) \Big) \tag{2.23}$$

which is the result we were looking for. One can see that eq. (2.23) is tied to the phase parameter φ, which depends on the non-integrated angles (Θ_y and Θ_ζ in this case). Hence, it is relevant to separate the terms that are angle-independent from the others (*i.e.* when $\vec{n} = \vec{m}$, $\varphi_{\vec{n},x} - \varphi_{\vec{m},x} = 0$) to explicitly expose the dependence on $\vec{\Theta}$, yielding:

$$\mathcal{A}_{xx}(\vec{\Theta}) = \pi \sum_{\vec{n}} n_x |A_{\vec{n}}|^2 + \Delta_{xx}(\vec{\Theta}) \tag{2.24}$$

where the angle-dependent part is given by:

$$\Delta_{xx}(\vec{\Theta}) = \pi \sum_{\vec{n}} \sum_{\vec{m} \neq \vec{n}} \delta_{n_x,m_x} \Big(n_x |A_{\vec{n}}||A_{\vec{m}}| \cos\Big(\varphi_{\vec{n},x}(\vec{\Theta}) - \varphi_{\vec{m},x}(\vec{\Theta})\Big) \Big) \tag{2.25}$$

which is the same as eq. (2.23) for $\vec{m} \neq \vec{n}$. In the different planes, the different Δ-functions are obtained from eq. (2.25) by permuting the coefficients of the Fourier expansion, *i.e.*, where $\Delta_{xx} \to \Delta_{xy} \to \Delta_{x\zeta}$ are obtained by replacing $A_{\vec{n}} \to B_{\vec{n}} \to C_{\vec{n}}$.

2.1.5 Integrals of Motion in Periodic Systems

While the Poincaré Integral Invariants highlight the preservation of the symplectic area for any loop transported along the Hamiltonian flow [6], this geometric property does not, in general, imply the existence of dynamical invariants. In periodic systems — such as storage rings — stable solutions must lie on tori which are themselves invariant under the one-turn map: the mapping of any point from the torus must also belong to the torus itself, one full period later. For such systems, the Hamiltonian can be written as a function of the actions alone — as in eq. (1.7) — and the dynamics can be expressed in terms of the action-angle variables.

This canonical structure provides the foundation for Normal Form theory [15], where a sequence of symplectic transformations brings the system into a simplified, integrable form. By contrast, in open-ended or non-periodic systems, tori do not need to map onto themselves. In such cases, the preservation of the symplectic area is no longer sufficient to define conserved action variables, which illustrates the distinction between the Poincaré Integral Invariants and the integrals of motion. This allows us to introduce the notion of *integrability* with the following proposition.

Proposition 2.1: Integrable tori.

A torus, $\mathbf{\Psi}(\vec{\Theta})$, is said to be *integrable* if there exists a sequence of symplectic transformations that can be used to move continuously on the torus, effectively changing the value of Θ_x, Θ_y and Θ_ζ at will. For an integrable torus, the remainders $\Delta_j(\vec{\Theta})$ of all the Poincaré Integral Invariants necessarily cancel out across all angles, that is:

$$\Delta_j(\vec{\Theta}) = \Delta_{jx}(\vec{\Theta}) + \Delta_{jy}(\vec{\Theta}) + \Delta_{j\zeta}(\vec{\Theta}) = 0 \quad \forall \quad \vec{\Theta} \in \mathbb{R}^3,\ j \in \{x, y, \zeta\}\ , \tag{2.26}$$

which is to say that all loops from a given family share the same symplectic area with no angular-dependence.

In that case, three independent actions I_x, I_y and I_ζ can be defined.

By virtue of Proposition 2.1 the Poincaré Integral Invariants can be used to define 3 independent integrals of motion, or actions, following:

$$I_j \equiv \frac{1}{2\pi}\mathcal{A}_j = \frac{1}{2\pi}\oint_{\Theta_j}\left(P_x dX + P_y dY + P_\zeta dZ\right)\ , \tag{2.27}$$

which, for an integrable torus, leads to:

$$\begin{aligned} I_x &= I_{xx} + I_{xy} + I_{x\zeta} = \frac{1}{2}\sum_{\vec{n}} n_x \left(|A_{\vec{n}}|^2 + |B_{\vec{n}}|^2 + |C_{\vec{n}}|^2\right) \\ I_y &= I_{yx} + I_{yy} + I_{y\zeta} = \frac{1}{2}\sum_{\vec{n}} n_y \left(|A_{\vec{n}}|^2 + |B_{\vec{n}}|^2 + |C_{\vec{n}}|^2\right)\ . \\ I_\zeta &= I_{\zeta x} + I_{\zeta y} + I_{\zeta\zeta} = \frac{1}{2}\sum_{\vec{n}} n_\zeta \left(|A_{\vec{n}}|^2 + |B_{\vec{n}}|^2 + |C_{\vec{n}}|^2\right) \end{aligned} \tag{2.28}$$

Although the partial actions $I_{jk}(\vec{\Theta})$ are individually not invariant, their sum in each plane is and they each correspond to a dynamical invariant. This special condition is *sine qua non* with the existence of a Normal Form, as discussed in the next section.

Let us illustrate the angular-dependence further by considering a torus for which the Δ_{jk} functions are not individually zero. To do so, the torus of Fig. 2.4 (here labelled as $\mathbf{\Psi}_0(\vec{\Theta})$) is transformed via a non-linear symplectic transformation such that $\mathbf{\Psi} = \mathcal{M}\,\mathbf{\Psi}_0$ for which $\Psi_x = \Psi_{0,x} + i\frac{3}{40}\left(X_0^2 - Y_0^2\right)$ and $\Psi_y = \Psi_{0,y} - i\frac{3}{20}\left(X_0 Y_0\right)$. The details of such a transformation shall be given in Chapter 3. The resulting torus contains 12 phasors, many of which respect the $\{\delta_{n_j,m_j} = 1 \text{ for } \vec{n} \neq \vec{m}\}$ condition required to make Δ_{xx}, Δ_{xy}, Δ_{yx} and Δ_{yy} non-zero, as shown in Fig. 2.7. When moving on the torus — *i.e.* when changing Θ_x or Θ_y — the Δ-functions are seen to individually vary, but their sums, Δ_x (Fig. 2.7(a)) and Δ_y (Fig. 2.7(b)) cancel out across all angles.

Naturally, the variation of the projected area can be visualized on the torus itself, as shown in Fig. 2.8. When moving on the torus, the individual projected area such as $\mathcal{A}_{xx}$ and $\mathcal{A}_{xy}$, shown in Fig. 2.8(a), are seen to vary between $\Theta_y = 0$ and $\Theta_y = \pi$, but their sum is invariant. The corresponding flattened projections are shown in Fig. 2.9 for completeness.

From Fig. 2.8 and Fig. 2.9, one can see how the integrability condition — formalized in Proposition 2.1 — is necessary, but not sufficient, for the definition of the action-angle variables. If there exists a series of symplectic transformations to continuously move on the torus, then the symplectic area must be invariant across all angles. That being said, one can also imagine a non-integrable torus for which all Δ-functions vanish with their sum, but were no symplectic transformation exists to continuously move on the torus. As such, the integrability condition provides a strong criteria which needs to be satisfied for a torus to be the periodic solution of a periodic Hamiltonian system.

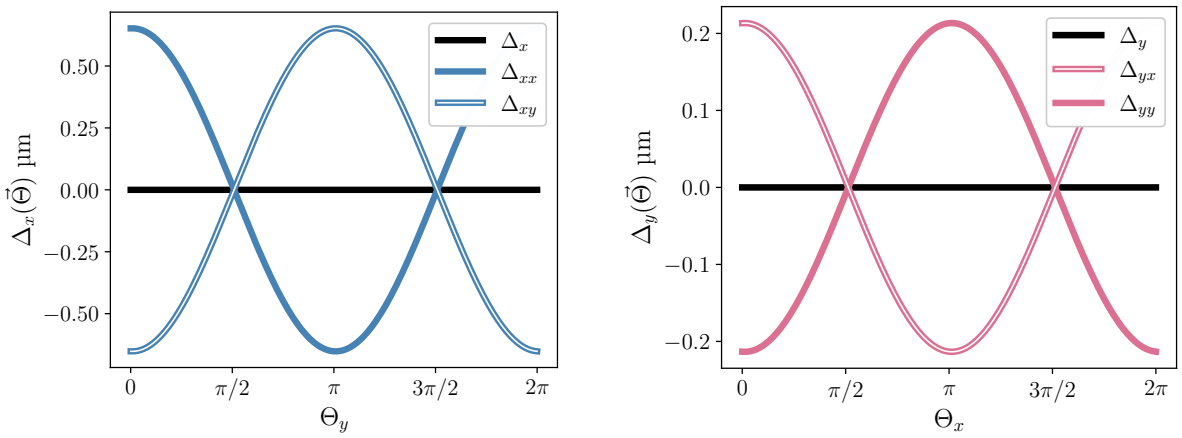

(a) (b)

Figure 2.7: Evolution of the various Δ-functions for an integrable torus. (a) Variation of the symplectic area of $\Theta_x^{\circlearrowleft}$ loops for various values of Θ_y. (b) Variation of the symplectic area of $\Theta_y^{\circlearrowleft}$ loops for various values of Θ_x. In both cases, the total remainders, Δ_x and Δ_y, cancel out across all angles. The basic cycles are illustrated in Fig. 2.8.

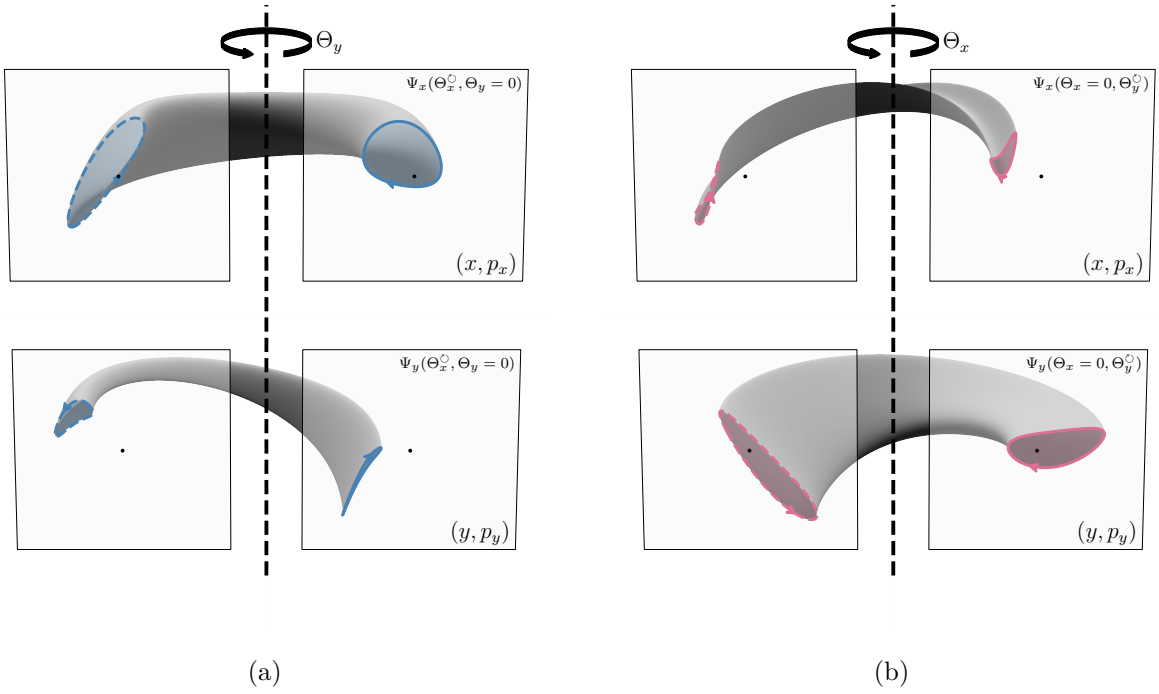

(a) (b)

Figure 2.8: Basic cycles for an integrable 4D torus with angle-dependent symplectic areas. (a) Projections of $\Theta_x^\circlearrowleft$ with $\Theta_y \in [0, \pi]$. (b) Projections of $\Theta_y^\circlearrowleft$ with $\Theta_x \in [0, \pi]$. In both cases, the projected areas vary along the torus but their sum (top and bottom, with common colors) is invariant. The torus considered was obtained from the torus of Fig. 2.4, $\mathbf{\Psi}_0$, after modification by a symplectic transformation: $\Psi_x = \Psi_{0,x} + i\frac{3}{40}\left(X_0^2 - Y_0^2\right)$ and $\Psi_y = \Psi_{0,y} - i\frac{3}{20}\left(X_0 Y_0\right)$.

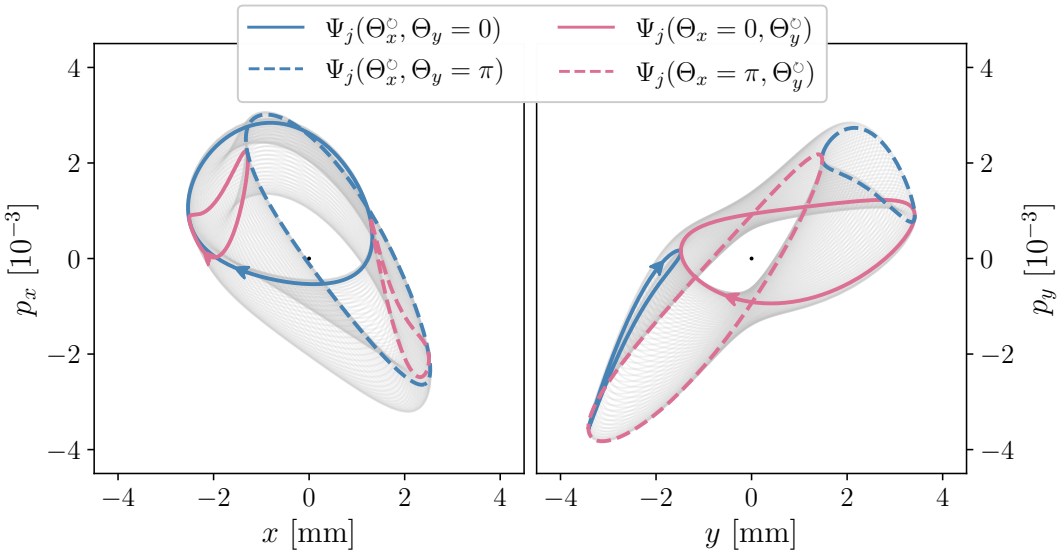

Figure 2.9: Shadow of the integrable 4D torus from Fig. 2.8 in both conjugate planes. The projected areas individually vary along the torus, but their sum (with corresponding colors and line styles) is invariant, as shown in Fig. 2.7

2.1.6 Normal Form

The integrability condition of Proposition 2.1 guarantees the existence of three independent actions, conserved under the Hamiltonian flow. This leads to a set of action–angle variables $(x, p_x) \mapsto (I_x, \Theta_x)$ (idem for y and ζ), for which the Hamiltonian depends only on the actions, $H = H(I_x, I_y, I_\zeta)$. In these coordinates, the actions remain constant, the angles advance linearly through the system, and the invariant torus takes on a circular shape in each conjugate plane. Although the explicit canonical transformation to action–angle variables is generally unknown, the integrals of motion directly provide the expected result using eq. (2.28). For the sake of clarity, it is useful to distinguish three important phase-space representations: $\vec{x}$ (physical), $\vec{\tilde{x}}$ (Courant–Snyder), and $\vec{\widehat{x}}$ (Normal Form). One can transform from physical to Courant–Snyder phase space — where ellipses become circles — via the real symplectic W-matrix [18]:

$$\tilde{\mathbf{\Psi}} = \mathcal{W}^{-1}\,\mathbf{\Psi} \quad \text{with} \quad \tilde{X} = W^{-1} X \ , \tag{2.29}$$

where $\mathcal{W}^{-1}\,\mathbf{\Psi}$ is a linear transformation of $\mathbf{\Psi}$ associated to the W-matrix. This transformation completely circularizes the motion in each degree of freedom for purely linear dynamics (see Chapter 4). When eq. (2.29) is applied to a general non-linear torus, the normalization is only partial: residual distortions and coupling effects remain, as shown in Fig. 2.10(b). To remove these, one must extend the idea of linear normalization to a general (non-linear) symplectic transformation $\mathcal{N}^{-1}\,\mathbf{\Psi}$, which ultimately brings the motion into its *normal form* — a fully decoupled, circular representation of the action-angle variables. By definition:

$$\widehat{\mathbf{\Psi}}(\vec{\Theta}) \ : \ \begin{cases} \widehat{\Psi}_x(\Theta_x) \equiv \sqrt{2I_x}\, e^{i\Theta_x} \\ \widehat{\Psi}_y(\Theta_y) \equiv \sqrt{2I_y}\, e^{i\Theta_y} \\ \widehat{\Psi}_\zeta(\Theta_\zeta) \equiv \sqrt{2I_\zeta}\, e^{i\Theta_\zeta} \end{cases} , \quad \text{with} \quad \widehat{\mathbf{\Psi}} = \mathcal{N}^{-1}\,\mathbf{\Psi} \ , \tag{2.30}$$

where $\mathcal{N}$ is in general unknown, but is guaranteed to exist for integrable cases [15]. This transformation plays the same role as the W-matrix plays for the linear case: it maps the distorted and coupled tori into fully circular, decoupled tori, as shown in Fig. 2.10(c).

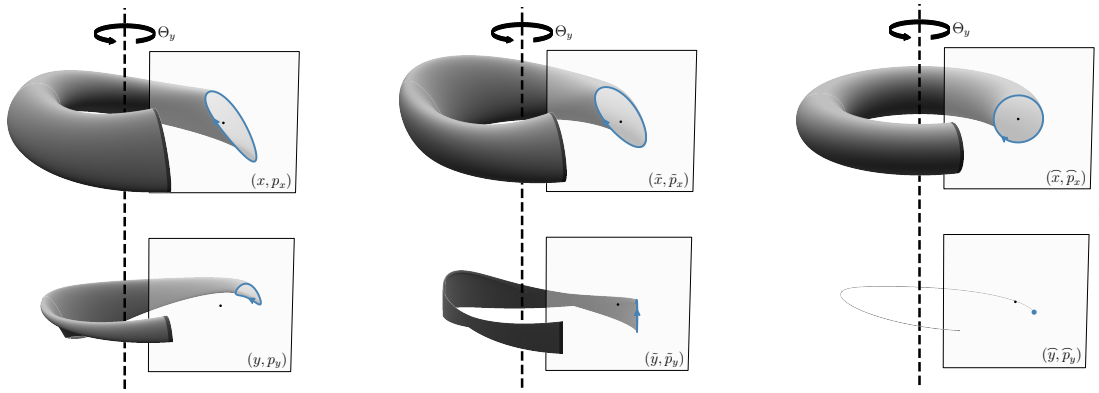

(a) $\mathbf{\Psi}(\Theta_x^{\circlearrowleft}, \Theta_y)$ (b) $\tilde{\mathbf{\Psi}}(\Theta_x^{\circlearrowleft}, \Theta_y)$ (c) $\widehat{\mathbf{\Psi}}(\Theta_x^{\circlearrowleft}, \Theta_y)$

Figure 2.10: Sequence of symplectic transformations to put a simple 4D torus into its normal form. (a) $\mathbf{\Psi}$, taken from Fig. 2.8. (b) $\tilde{\mathbf{\Psi}}$, following the application of the W-matrix. (c) $\widehat{\mathbf{\Psi}}$, the normal form of the torus. The symplectic area is unchanged in (a,b,c).

2.2 Periodicity and Energy Manifold

Let us now return to the original problem of beam transport. In previous sections, the effort was put on the topological description of loops and tori, with little attention devoted to the description of single-particle dynamics. In the following sections, the profound connection between $\boldsymbol{\psi}$ and $\boldsymbol{\Psi}$ — particles and tori — shall be made explicit. Moreover, important numerical methods will be presented for the construction of invariant tori when periodic boundary conditions are imposed.

2.2.1 Regular Motion & Quasiperiodic Expansion

In periodic conservative systems — such as the LHC, assuming a static lattice configuration — the energy is preserved and particle trajectories are constrained to evolve on constant-energy surfaces. In phase space, those surfaces are referred to as *energy manifolds*. It can be shown [29] that for a given integrable trajectory, the energy manifold is an n-torus embedded in a $2n$-dimensional phase space. The KAM theorem, presented earlier (see page 11), guarantees the existence of such tori on restricted regions of the system. It appears therefore natural to put those invariant tori — those energy manifolds — at the core of our description of beam dynamics.

Proposition 2.2: Embedded particles.

In periodic conservative systems, regular trajectories (*i.e.* non-chaotic trajectories) are embedded on well-defined invariant tori which are preserved under the one-turn map of the system. In such cases, the trajectories are quasiperiodic and can be obtained from a stroboscopic sampling of their corresponding invariant torus, *i.e.*:

$$\boldsymbol{\psi}(N) = \boldsymbol{\Psi}(2\pi\vec{Q}N) \tag{2.31}$$

where $\vec{Q} = (Q_x, Q_y, Q_\zeta)$ are the fundamental frequencies of the trajectory and N is the turn number. Outside of resonant conditions, a given particle eventually covers the entire surface of its invariant torus as $\Theta_j = 2\pi Q_j N$, $j \in \{x, y, \zeta\}$, varies with arbitrarily large N values, exploring $\Theta_j \in [0, 2\pi] \pmod{2\pi}$ densely.

Furthermore, the corresponding torus is necessarily integrable, with actions I_x, I_y and I_ζ.

Out of the periodic structure of an energy manifold, $\boldsymbol{\Psi}(\vec{\Theta})$, emerges the quasiperiodic motion of a single particle, $\boldsymbol{\psi}(N)$, turn after turn. As a result, we return to the prize equation (1.8), proposed by King Oscar II, and write:

$$\boldsymbol{\psi}(N) \;:\; \begin{cases} \psi_x(N) = \sum_{\vec{n}} A_{\vec{n}}\; e^{i(2\pi(\vec{n}\cdot\vec{Q})N)} \\ \psi_y(N) = \sum_{\vec{n}} B_{\vec{n}}\; e^{i(2\pi(\vec{n}\cdot\vec{Q})N)} \\ \psi_\zeta(N) = \sum_{\vec{n}} C_{\vec{n}}\; e^{i(2\pi(\vec{n}\cdot\vec{Q})N)} \end{cases}, \tag{2.32}$$

which is again a generalization of the epicycles. In the above expansion, the spectral amplitudes, $A_{\vec{n}}$, $B_{\vec{n}}$ and $C_{\vec{n}}$ are identical to the ones of the invariant torus of the particle. The frequencies in the Fourier expansion, $\vec{n}\cdot\vec{Q}$, correspond to integer linear combinations (or *harmonics*) of the fundamental frequencies $\vec{Q}$. This structure reflects the diophantine condition required by the

KAM theorem. The form of eq. (2.32) is general, and applies equally to linear and non-linear systems, as shown in Fig. 2.11. To give a practical example, one can show (see Chapter 4) that the Fourier expansion for 2D linear motion can be written as:

$$\psi_x(N) = \sqrt{2I_x}\left(\lambda_x^+ e^{i(2\pi Q_x N)} + \lambda_x^- e^{-i(2\pi Q_x N)}\right) \quad \text{with} \quad \lambda_x^\pm = \frac{\beta_x/\beta_{x_0} + i\alpha_x \pm 1}{2\sqrt{\beta_x/\beta_{x_0}}} \tag{2.33}$$

where α_x and β_x are the well-known Courant-Snyder parameters [4]. Remembering that $\psi_x \equiv x/\sqrt{\beta_{x_0}} - ip_x\sqrt{\beta_{x_0}}$, the above formulation turns out to be fully equivalent to the usual formulation of the motion for single-particle linear dynamics:

$$\begin{aligned} x &= \sqrt{2I_x\beta_x}\cos(2\pi Q_x N)\ , \\ p_x &= -\frac{\sqrt{2I_x}}{\sqrt{\beta_x}}\big(\sin(2\pi Q_x N) + \alpha_x\cos(2\pi Q_x N)\big)\ , \end{aligned} \tag{2.34}$$

as illustrated in Fig. 2.11(a). However, as highlighted by A. Chao [30], the Courant-Snyder picture is not without weakness and fails to describe non-linear dynamics in a natural way. For non-linear systems, one should instead expect the particle trajectories to follow a more complex shape, described by a more general quasiperiodic expansion (of which ellipses are only a particular case). These shortcomings are implicitly addressed with the general formulation given in eq. (2.32), as shown in Fig. 2.11(b).

Proposition 2.2 introduces — for the first time — the fundamental frequencies $\vec{Q} = (Q_x, Q_y, Q_\zeta)$ within $\boldsymbol{\psi}(N)$, which appear as a property of the single-particle dynamics. In fact, $\vec{Q}$ is also a key property of the energy manifold of the particle; and more profoundly, an emerging feature of the system, arising due to the periodic boundary conditions imposed on the problem.

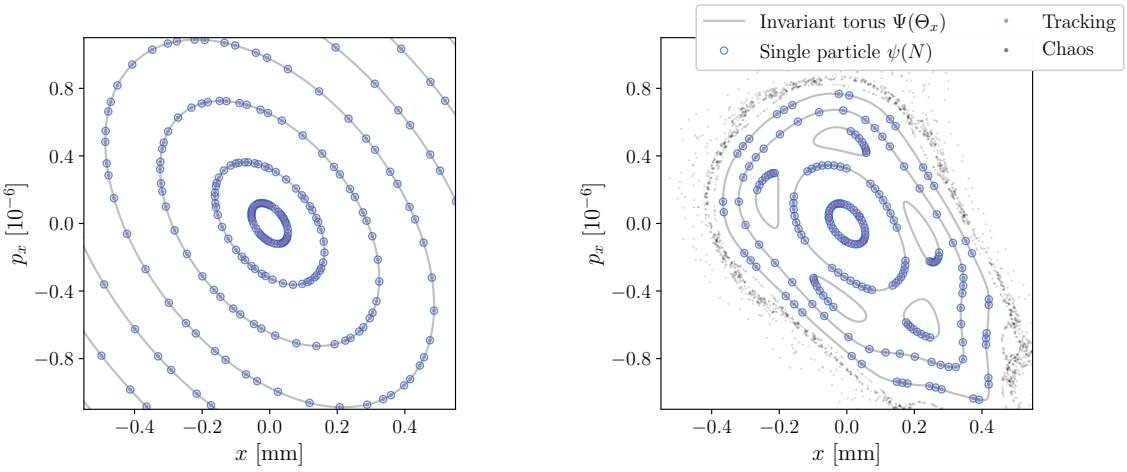

(a) Linear lattice

(b) Non-Linear lattice

Figure 2.11: Comparison of the quasiperiodic motion of single particles, $\boldsymbol{\psi}(N)$, with their respective invariant tori, $\boldsymbol{\Psi}(\Theta_x)$ for two simple 2D systems. (a) A linear lattice. (b) A non-linear lattice (Hénon map). In both cases, the single particle dynamics is obtained as a stroboscopic sampling of the invariant tori. The turn-by-turn tracking, obtained from the iteration of the map, is also shown for comparison.

Let us contextualize the previous claims. For open-ended Hamiltonian flow, a "solution" refers to the integrated trajectory of a given set of initial conditions. When *periodicity* is imposed; either as a mathematical constraint, or due to the physical periodicity of the accelerator lattice — *e.g.* in a FODO cell, or a closed storage ring — one must restrict the search to solutions which are also periodic. The system, constrained in such a way, admits *eigensolutions* which necessarily follow the periodicity of the lattice. A given particle, $\boldsymbol{\psi}$, is constrained to move on some periodic energy manifold $\boldsymbol{\Psi}(\vec{\Theta})$ which is fixed by the system. In that case, $\boldsymbol{\Psi}(\vec{\Theta})$ must be an eigensolution of the one-turn map, $\mathcal{M}$; a condition we write as:

$$\mathcal{M}\,\boldsymbol{\Psi}(\vec{\Theta}) = \Psi(\vec{\Theta} + 2\pi\vec{Q})\ , \tag{2.35}$$

such that any point on $\boldsymbol{\Psi}$ maps to $\boldsymbol{\Psi}$ itself after one turn, albeit with its angles $\vec{\Theta}$ shifted by some quantity, $2\pi\vec{Q} = (2\pi Q_x, 2\pi Q_y, 2\pi Q_\zeta)$. Hence, $\vec{Q}$ appears as an emerging property of the system, tied to a given energy manifold $\boldsymbol{\Psi}$, and imposed by the periodicity of the Hamiltonian flow. In fact, writing eq. (2.35) in the Normal Form phase space yields (by construction):

$$\widehat{\mathcal{M}}\,\widehat{\boldsymbol{\Psi}}(\vec{\Theta})\ :\ \begin{cases} \widehat{\mathcal{M}}\widehat{\Psi}_x(\vec{\Theta}) = e^{i(2\pi Q_x)}\widehat{\Psi}_x(\vec{\Theta}) \\ \widehat{\mathcal{M}}\widehat{\Psi}_y(\vec{\Theta}) = e^{i(2\pi Q_y)}\widehat{\Psi}_y(\vec{\Theta}) \\ \widehat{\mathcal{M}}\widehat{\Psi}_\zeta(\vec{\Theta}) = e^{i(2\pi Q_\zeta)}\widehat{\Psi}_\zeta(\vec{\Theta}) \end{cases}\ , \tag{2.36}$$

which shows that $\vec{Q} = (Q_x, Q_y, Q_\zeta)$ are the true eigenvalues of the problem in that space, where the transformation corresponds to pure rotations of all the angles, $\vec{\Theta}$. An example of the periodic Hamiltonian flow of the Hénon map is shown in Fig. 2.12. Clearly, the two tori shown are invariant under the one-turn map of the system, as described by eq. (2.35).

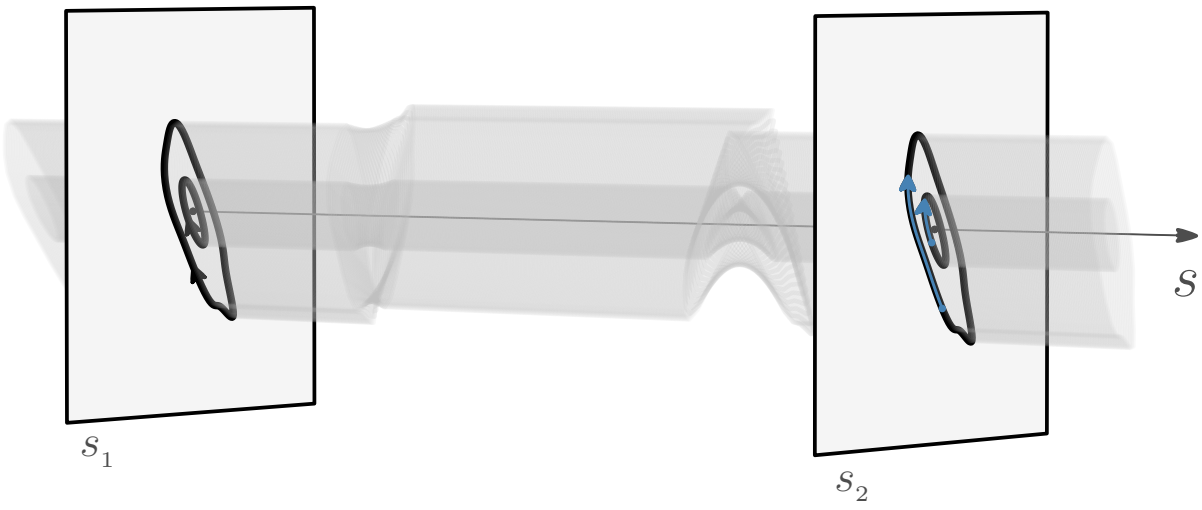

Figure 2.12: Hamiltonian flow of a 2D non-linear periodic lattice (Hénon map), made of drifts, quadrupoles and a single sextupole. The periodicity of the lattice (between s_1 and s_2) imposes additional constraints and only periodic eigensolutions are admitted. The topology of the resulting energy manifolds depends on the amplitude, as shown with two tori, $\boldsymbol{\Psi}_1$ and $\boldsymbol{\Psi}_2$. After one period, the tori are unchanged, albeit dephased by some quantity $2\pi Q_x$, shown with the blue arrows.

In general, the topology of the eigensolutions depends on the distance from the origin, as shown in Fig. 2.13(a). Sufficiently close to an integrable region of the system, one can expect — as a corollary to the KAM theorem — a large set of invariant tori for which the frequency vector depends smoothly on the action variables, $\vec{Q}(I_x, I_y, I_\zeta)$, such that small variations in the actions lead to small, smooth changes in the frequencies [11]. In this sense, the solutions are not isolated instances in phase space, but rather part of a continuous manifold of regular motion. Far away from resonances, the frequency map $\vec{I} \mapsto \vec{Q}(\vec{I})$ is non-degenerate and is as smooth as the underlying Hamiltonian — often smooth and analytic. In other words, the derivatives:

$$\frac{\partial \vec{Q}}{\partial I_j}, \quad \frac{\partial A_{\vec{n}}}{\partial I_j}, \quad \frac{\partial B_{\vec{n}}}{\partial I_j}, \quad \frac{\partial C_{\vec{n}}}{\partial I_j}, \quad \text{for } j \in \{x, y, \zeta\}, \tag{2.37}$$

are continuous and vary smoothly across the family of neighbouring KAM tori, as shown in Fig. 2.13(b). This Jacobi-like relationship between nearby solutions leads to phenomena such as amplitude-dependent detuning, a well-studied problem of beam dynamics [4]. If the detuning is such that the fundamental frequencies are forced to cross a *resonance* condition, written as:

$$\vec{n} \cdot \vec{Q} = n_x Q_x + n_y Q_y + n_\zeta Q_\zeta = q, \quad \text{with } q \in \mathbb{Z}, \tag{2.38}$$

then the aforementioned smoothness can be broken. The precise set of "active" resonances — the set of relevant $\{\vec{n}, q\}$ — is not trivial to describe and depends, in general, on the Hamiltonian. Starting from the origin, the fundamental frequency shall therefore be found in continuity with the *tunes* — or betatron frequency — of the system, at least up to the first resonance gap. In Fig. 2.13, one can see that the properties of the eigensolutions are initially smoothly varying as a function of the action. However, this continuity is eventually broken when $Q_x \to 1/5$ and does not extend smoothly across the resonant gap — delimited by the *separatrix*.

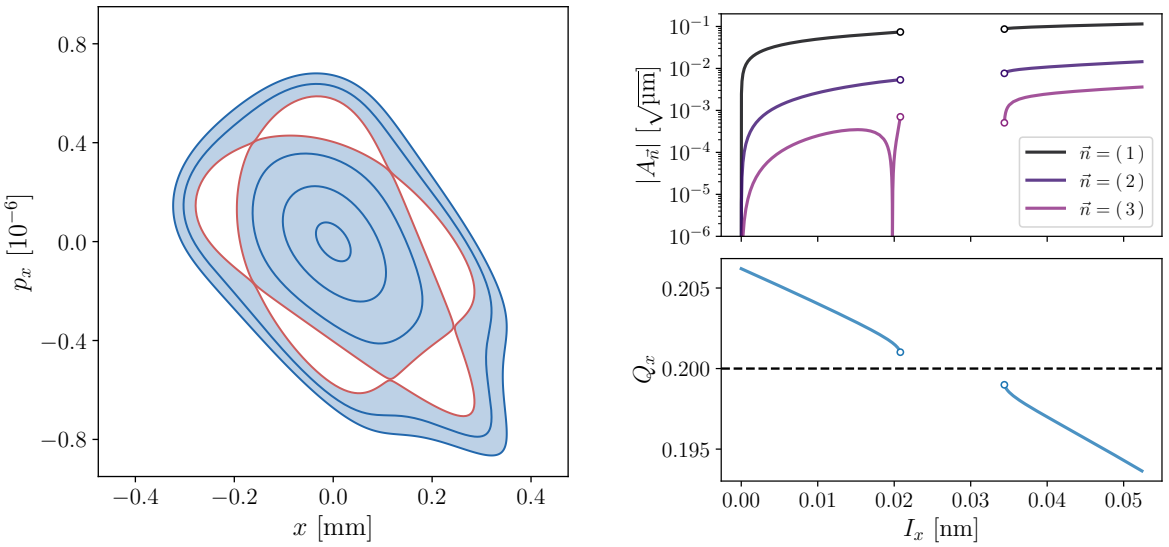

(a) (b)

Figure 2.13: Regularity of the 2D Hénon map around a fifth order resonance. (a) KAM family around the origin, broken by the separatrix and the resonance gap. (b) Fourier coefficients (*e.g.* A_1, A_2, A_3) and fundamental frequency Q_x as a function of the action.

2.2.2 Numerical Analysis of the Fundamental Frequencies (NAFF)

The regularity of the frequency map, highlighted in eq. (2.37), is at the center of the Frequency Map Analysis (FMA). This technique, introduced and extensively developed by J. Laskar, has found widespread application across numerous domains of physics [7, 11, 13, 28]. The impact of Laskar's contributions on the present thesis is substantial: many of the conceptual propositions — particularly the visualization and interpretation of invariant tori — have been made possible through his numerical approach, known as the Numerical Analysis of the Fundamental Frequencies (NAFF) and implemented in the NAFFLIB project [2]. To paraphrase Laskar [11]: "This numerical method relies on the observation that when a quasiperiodic function $f(t)$ is given numerically, it is possible to recover a quasiperiodic approximation of $f(t)$ in a very precise way over a finite time span $[-T, T]$, several orders of magnitude more precisely than what simple Fourier series will provide. Indeed, when computing the Fourier series of $f(t)$ over the finite interval $[-T, T]$, one assumes that $f(t)$ is periodic of period $2T$, which is not true. In the following algorithm, we make a different hypothesis, which is dictated by the knowledge of the regular dynamics of our system, and we search for quasiperiodic approximations."

In our case, the function under study is the complex coordinate $\psi_x(N) = x(N)/\sqrt{\beta_{x_0}} - ip_x(N)\sqrt{\beta_{x_0}}$, which is known over a finite time span $N \in [0, T]$. This description of the motion is typically obtained via tracking, in which case the trajectory $\psi(N)$ is the "true" observable — *i.e.* it is not an approximation — but is ultimately truncated at $N = T$ turns. For this signal, the spectral amplitude $\mathrm{A}(\nu)$ can be computed as a function of the frequency ν following:

$$\mathcal{F}(\psi_x(N)) \quad \mapsto \quad \mathrm{A}(\nu) = \frac{1}{T}\sum_{N=0}^{T-1} \psi_x(N) \cdot e^{-i(2\pi\nu \cdot N)} \cdot \chi_p(N) \ , \tag{2.39}$$

where $\chi_p(N)$ is a weight function, taken to be the Hann window (of order p) centered on the dataset (*i.e.* at $N \to T/2$) and given by:

$$\chi_p(N) = \frac{2^p (p!)^2}{(2p)!}\Big(1 - \cos(2\pi N/T)\Big)^p \ . \tag{2.40}$$

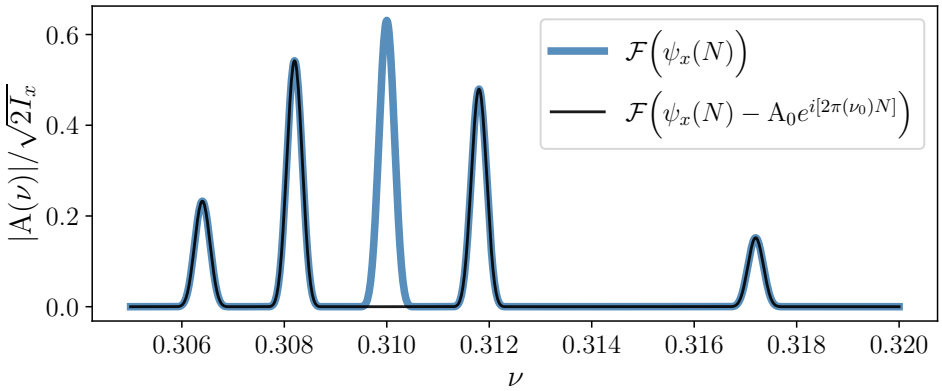

Figure 2.14: Fourier transform of a simple quasiperiodic signal made of five frequencies using a Hann window ($p = 4$) and $T = 10^4$. After finding the dominant frequency component (ν_0, A_0), its contribution is subtracted from the original signal and the procedure is repeated to find (ν_1, A_1), and so on.

The difference between eq.(2.39) and a conventional Discrete Fourier Transform (DFT) is that the DFT looks for discrete values of frequencies following $\nu = m/T$ (with $m \in \mathbb{Z}$) which is not the case here. Letting ν be continuous is equivalent to zero-padding, a technique commonly used in signal processing to improve the resolution of DFT algorithms.

The key element in Laskar's approach, however, is to iteratively identify the dominant frequency components of the signal (ν_0, ν_1, ν_2, etc. ; together with A_0, A_1, A_2, etc.) in order to reconstruct the quasiperiodic expansion of $\psi_x(N)$ in the form of a truncated approximation:

$$\psi_x^{(N_h)}(N) = \sum_{k=0}^{N_h} \mathrm{A}_k \; e^{i[2\pi(\nu_k)N]} \; , \tag{2.41}$$

made of N_h harmonics, ordered with decreasing amplitudes. The main frequency ν_0 is found by locating the maximum of eq. (2.39) — using for example a Newton–Raphson method — before being subtracted from the original signal. The procedure is then repeated to obtain the second dominant frequency, ν_1, and so on. This iterative procedure is shown in Fig. 2.14 for a simple synthetic signal. If $\psi_x(N)$ corresponds to a stable trajectory embedded on a KAM tori, then one can show [11] that the sum $\sum_k \mathrm{A}_k$ is guaranteed to converge and we can generally further assume that $\mathrm{A}_k \to 0$ as $k \to \infty$ such that the approximation improves as N_h is increased. More importantly, Laskar showed that this iterative method ensures — for a KAM solution — that the accuracy of the frequency determination scales with $1/T^2$ without the Hann window ($p = 0$), while for an ordinary FFT method, this accuracy scales with $1/T$. By using the Hann window, the convergence instead scales with $1/T^{2p+2}$. In this thesis, we generally consider $p = 4$, which is not practical for noisy signal (*e.g.* from experimental data) but improves the accuracy of the frequency determination for clean signal. In Fig. 2.15, the convergence of the NAFF algorithm is presented for a non-linear coupled 4D Hénon map. Even for this realistic, non trivial case, one can see that it is possible to retrieve the first 100 harmonics up to machine precision.

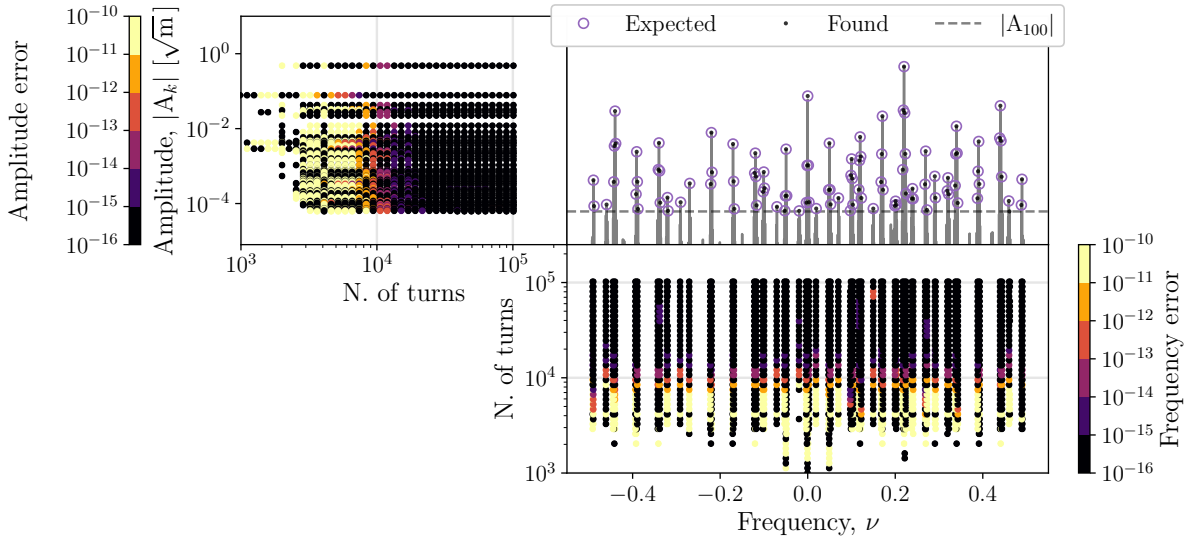

Figure 2.15: Convergence of the NAFF algorithm using a Hann window ($p = 4$) for a non-linear signal taken from the coupled 4D Hénon map. The first $N_h = 100$ harmonics are extracted from the $\psi_x(N)$ signal. In most cases, the frequencies ν_k and their spectral amplitude A_k are found up to numerical precision when $T \geq 10^4$ turns.

Equivalence Principle

For 6D motion, the procedure is applied separately in the three conjugate planes, which allows for a natural treatment of coupled dynamics. Indeed, when $\psi_x(N)$, $\psi_y(N)$ and $\psi_\zeta(N)$ are considered, coupling effects are intrinsically taken into account, turn-by-turn, and various linear combinations of the three fundamental frequencies $\vec{n}\cdot\vec{Q}$ can be found in all three signals. As a result, we obtain a numerical approximation of the full 6D motion $\boldsymbol{\psi}(N)$ (from eq. (2.32)):

$$\boldsymbol{\psi}(N) \;:\; \begin{cases} \psi_x(N) \approx \psi_x^{(N_h)}(N) \\ \psi_y(N) \approx \psi_y^{(N_h)}(N) \\ \psi_\zeta(N) \approx \psi_\zeta^{(N_h)}(N) \end{cases} \quad \text{with} \quad \begin{cases} (\nu_{x,k}, \mathrm{A}_k) \mapsto A_{\vec{n}} \\ (\nu_{y,k}, \mathrm{B}_k) \mapsto B_{\vec{n}} \\ (\nu_{\zeta,k}, \mathrm{C}_k) \mapsto A_{\vec{n}} \end{cases} , \tag{2.42}$$

and

$$\nu_k \mapsto \vec{n}_k \cdot \vec{Q} + n_{0k} \tag{2.43}$$

where $n_{0k} \in \mathbb{Z}$ is an aliasing number used to restrict the frequencies in the domain $\nu_k \in [-0.5, 0.5]$. Establishing the correspondence between the frequencies ν_k and the linear combinations of the three *fundamental* frequencies, $\vec{n}\cdot\vec{Q}$, as done in eq. (2.43), is a subtle matter which ultimately requires the knowledge of $\vec{Q}$. In practice, we often assume that the dominant frequency in each signal $(\nu_{x,0}, \nu_{y,0}, \nu_{\zeta,0})$ corresponds to the fundamental frequency in each plane (Q_x, Q_y, Q_ζ). But when strong coupling effects are present, this assumption is no longer valid and sidebands — *e.g.* synchrotron sidebands, $\vec{n} = (1, 0, \pm 1)$ — can end up having a higher spectral amplitude than that of the fundamental frequency, $A_{(1,0,0)}$. The reader is referred to Chapter 4 for additional details.

The labelling, or mislabelling, of the spectral lines in $\nu_k \mapsto \vec{n}_k \cdot \vec{Q} + n_{0k}$ can lead to various issues which makes FMAs difficult to carry out for strongly coupled systems and seemingly break the continuity expected from eq. (2.37). In fact, one can show [31] that there are infinitely many possible labelling choices — an equivalence principle — for the single-particle motion which preserve the Fourier series of eq. (2.42). The two formulations:

$$\left\{ (\vec{n}, \vec{Q}) \mapsto \vec{I} \right\} \quad \Leftrightarrow \quad \left\{ ((P^\intercal)^{-1}\vec{n}, P\vec{Q}) \mapsto (P^\intercal)^{-1}\vec{I} \right\} \tag{2.44}$$

are equivalent when P is taken to be a unimodular (*i.e.* $\det P = \pm 1$) integer matrix. Permutations respect this condition. For example, if one identifies the sideband $Q_x + Q_\zeta$ to be the horizontal fundamental frequency, $Q_x \leftarrow Q_x + Q_\zeta$, the unimodular matrix

$$P = \begin{pmatrix} 1 & 0 & 1 \\ 0 & 1 & 0 \\ 0 & 0 & 1 \end{pmatrix}, \qquad (P^\intercal)^{-1} = \begin{pmatrix} 1 & 0 & 0 \\ 0 & 1 & 0 \\ -1 & 0 & 1 \end{pmatrix}$$

shows that indexing the frequencies according to $(n_x, n_y, -n_x + n_\zeta)_k$, *e.g.* the line $(1, 0, 0)$ becoming $(1, 0, -1)$ and $(1, 0, 1)$ becoming $(1, 0, 0)$ and so on, yields an equivalent description of the motion through eq. (2.42). That being said, the three actions are also modified to become $(I_x, I_y, -I_x + I_\zeta)$, which are three new constants of the motion, different (and discontinuous) from the ones that would be expected around the origin. In the same way that the frequencies $\nu_k = \vec{n}_k \cdot \vec{Q}$ are preserved under the unimodular transformation P, one can show that the dot

product:

$$\vec{I}' \cdot \vec{Q}' = \left[(P^{\intercal})^{-1}\vec{I}\right] \cdot \left[P\vec{Q}\right] = \vec{I} \cdot \vec{Q} \tag{2.45}$$

is preserved, independently of the unimodular matrix P. Hence, although the mislabelling process can lead to erroneous evaluations of the individual actions, one can always use eq. (2.45) to identify if the problem stems from this issue, or from the numerical evaluation itself. To lift the equivalence condition of eq. (2.44), and uniquely label the spectral lines of the single-particle motion, it appears that the only robust method is to invoke the continuity argument. One can always start from the origin (where coupling should be negligible) and slowly move to the desired observation point while choosing the fundamental frequencies to be in continuity with the ones at the origin, assuming that no resonances are crossed (see Fig. 2.13). In most reasonable cases however, taking the dominant frequency is each plane is generally satisfactory, and will be the method adopted in this thesis.

Reconstruction of the Energy Manifold

The interest behind the numerical decomposition of the motion into its fundamental frequencies — via NAFF — extends well beyond conventional spectral analysis. Starting from tracking data — that is from the raw iterations of an arbitrary map — it becomes possible to extract an approximate quasiperiodic expansion of the motion $\boldsymbol{\psi}^{(N_h)}(N)$ in the form of the prize equation, eq. (1.8). Moreover, according to Proposition 2.2, it also becomes possible to reconstruct the underlying energy manifold on which the trajectory resides. By establishing the correspondence $\nu_k \mapsto \vec{n}_k \cdot \vec{Q} + n_{0k}$ and letting $\vec{\Theta} = 2\pi\vec{Q}N$, we indeed obtain $\boldsymbol{\Psi}^{(N_h)}(\vec{\Theta}) \approx \boldsymbol{\Psi}(\vec{\Theta})$, a torus which approximates the true energy manifold of the particle. From there, the tools developed in this chapter become available to us and the corresponding integrals of motions can be extracted directly from the complex coefficients of the expansion. Two conditions are required for these claims to hold: the particle should belong to a KAM torus and its fundamental frequencies should lie outside of any low-order resonance, ensuring the trajectory densely explores the torus.

This raises a natural question: in the general case, can we find a closed form expression for the Fourier expansion of the energy manifold? As it turns out, this question can be readily answered using concepts of Lie Algebra, which will be developed in Chapter 3. For linear systems, finding the complete expansion is indeed possible. However, for non-linear systems, it will be shown that an infinite amount of harmonics ($N_h \to \infty$) are required for the complete description of the motion. Although the expansion is guaranteed to converge — from the KAM theorem — we are left, in practice, with two choices: to either consider an approximate solution to the problem (the Normal Form approach [15]) or extract a numerical solution using the NAFF algorithm, as discussed here.

In Fig. 2.16, the energy manifold of a particle from the coupled 4D Hénon map is shown using a numerical expansion with $N_h = 100$ harmonics. In Fig. 2.17, the shadow of the torus is shown together with turn-by-turn tracking data from the iterations of the map. One can see that the single-particle motion is confined to stay within the shadow of the torus, leading to an apparent *smearing* of the motion, which should not be surprising following the discussions from this chapter. To confirm that the motion is well-described by the numerical approximation provided, the expansion $\boldsymbol{\psi}^{(100)}(N) = \boldsymbol{\Psi}^{(100)}(2\pi\vec{Q}N)$ is also shown on top of the tracking data.

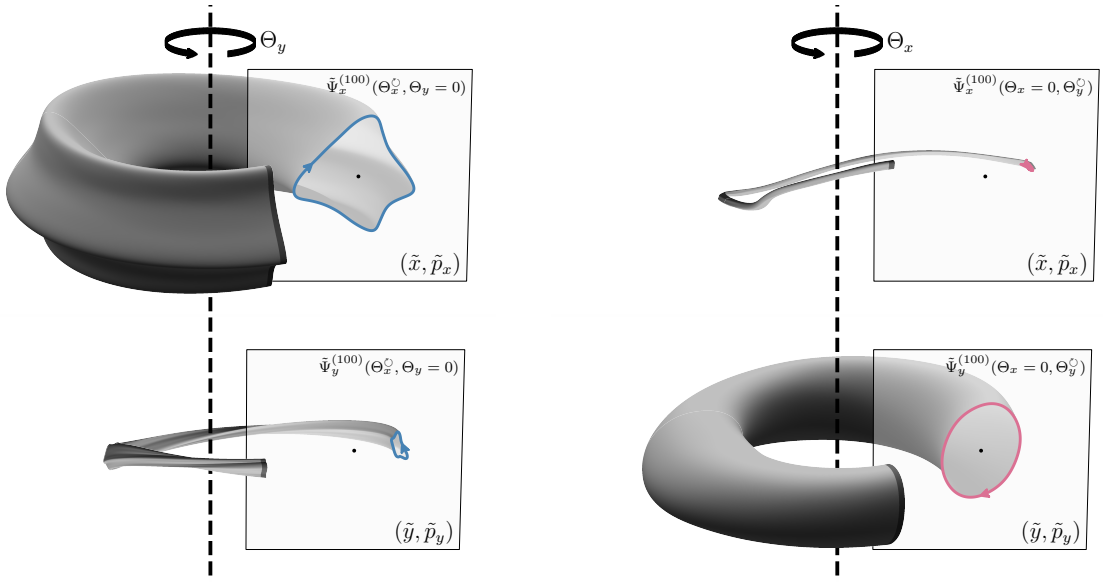

(a) (b)

Figure 2.16: Visualization of the basic cycles of an energy manifold from the 4D Hénon map. (a) Projections of all $\Theta_x^{\circlearrowleft}$ loops in the $(\tilde{x}, \tilde{p}_x)$ phase space (top) and $(\tilde{y}, \tilde{p}_y)$ phase space (bottom). (b) Projections of all $\Theta_y^{\circlearrowleft}$ loops in the $(\tilde{x}, \tilde{p}_x)$ phase space (top) and $(\tilde{y}, \tilde{p}_y)$ phase space (bottom). The $\Theta_x^{\circlearrowleft}$ loop in the $(\tilde{y}, \tilde{p}_y)$ phase space is travelled counter-clockwise and is therefore negative.

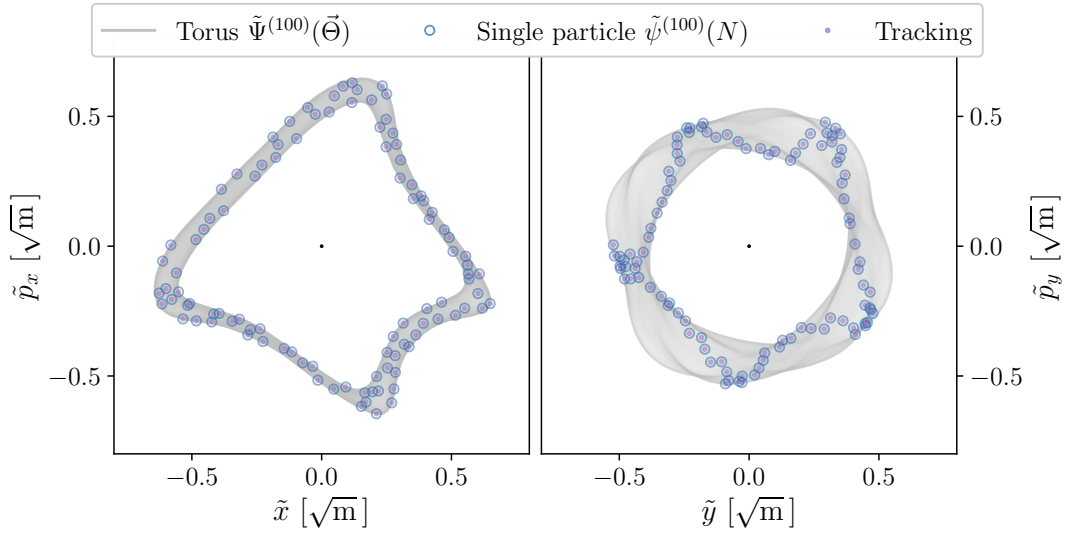

Figure 2.17: Shadow of the torus in both conjugate planes. The single-particle tracking is shown to be confined within the shadow of the torus for all turns. Naturally, the stroboscopic sampling of $\tilde{\Psi}^{(100)}(\vec{\Theta})$ following $\tilde{\psi}^{(100)}(N) = \tilde{\Psi}^{(100)}(2\pi\vec{Q}N)$ is in agreement with the tracking data.

CHAPTER 3

Lie Algebra

Preserving the symplectic structure of phase space is a defining feature of Hamiltonian dynamics and a prerequisite for accurate long-term beam transport. In this respect, Lie algebra offers a natural framework to generate symplectic maps and construct a set of fundamental operators underlying the Hamiltonian flow of realistic beam lines. Within this formalism, particles, loops, and tori can all be transported in a unified way, extending the concepts introduced in Chapter 2.

Building on the work of É. Forest, A. J. Dragt, and others, this chapter develops an element-by-element approach in which physical magnets are replaced by a set of fundamental symplectic operators with exact transfer maps. These operators coincide with the elements implemented in modern tracking codes such as XSUITE, ensuring direct consistency between analytic and numerical treatments. After introducing an algebra for multivariate Fourier series, we show how both single-particle coordinates $\boldsymbol{\psi}$ and tori $\boldsymbol{\Psi}$ can be transformed under the same rules, making it possible to describe spectral content — and the evolution of the energy manifold — directly. This framework yields a self-consistent grammar for beam transport and clarifies the origin of common tracking phenomena, such as the appearance of synchrotron sidebands in six dimensions. Throughout the chapter, emphasis is placed on distinguishing the physical lattice from its model, and on interpreting the latter faithfully, within its well-defined mathematical context.

3.1 Symplectic Integrators

As discussed in Chapter 2, Hamiltonian flow is, by nature, always symplectic. However, for many systems, the equations of motion do not admit closed-form solutions and the motion needs to be integrated step-by-step. If the *integrator* — the method of integration, *e.g.* a simple Runge-Kutta approach — is inappropriately chosen, then the symplectic nature of the solution can be lost. As A. Wolski puts it [4, Chap. 9], this can have dramatic impact on the beam dynamics when tracking particles over many turns in a storage ring: the use of non-symplectic transfer maps can lead to artificial growth or damping in the particle oscillations, resulting in inaccurate information on the stability of the motion. One can therefore understand the interest that was put, over the years, towards the development of symplectic particle tracking codes, driven by the need to accurately investigate the complex dynamics of non-linear systems beyond the reach of analytic calculations. The history of symplectic integrators was extensively reviewed by É. Forest [9] and is outside the scope of this thesis. That being said, several heuristics can be adopted and it is important to clarify the approach taken here.

Since the work of Courant and Snyder in 1958 [4, 32], the linear picture has become the standard description of accelerator physics for many applications. In fact, this theory has been a cornerstone in the design, description, and operation of particle accelerators leading to important breakthroughs in the field. The success of this approach is partly due to the fact that its main assumptions — that of linear and uncoupled dynamics — have proven to be excellent approximations to describe realistic stable machines. However, as modern colliders have become larger and more complex, the need to understand intricate non-linear effects has grown and the limitations of the linear picture have become more apparent.

In this respect, an important goal of this thesis is to unify the "grammar" of the field in a formalism which can naturally describe linear, non-linear, analytic and numerical experiments alike using a self-consistent framework (Fig. 1.8). It appears to the author that typical approaches fall prey to several layers of equivocation — that is: ambiguity in the meaning of terms. In Cognitive Science, it is well-documented [33, 34] that such ambiguities can lead to far-reaching confusion and, if left unattended, reduce the speed of progress in a given field. Studies in beam dynamics regularly start from a physical machine (a real magnetic lattice) which is described numerically using a set *operators* in tracking codes. It should be clear — from the start — that those two systems are fundamentally different from one another; and should therefore be treated as such. As É. Forest said: "This is an extreme view of integration found in accelerator physics: we create models that become reality in the highest sense of the word. Therefore, modelization is what we are doing rather than *bona fide* integration" [É. Forest, 9].

Hoping to perfectly replicate the real machine in the numerical experiment constitutes a first layer of equivocation. Then, in the interpretation of the numerical experiment — the tracking results — one commonly uses incompatible analytic heuristics, which came from an approximate description of the Hamiltonian, leading to yet a second layer of equivocation. We then make claims that are "accurate to some order" (order in the amplitude of the coordinates, or order in the magnet strengths, one does not know) which adds another layer of equivocation.

To avoid these shortcomings, we propose to build a set of fundamental symplectic operators with *exact* transformations — in fact, the same as the ones used for tracking — and study their impact on the beam dynamics. In doing so, we abandon the complete correspondence with the

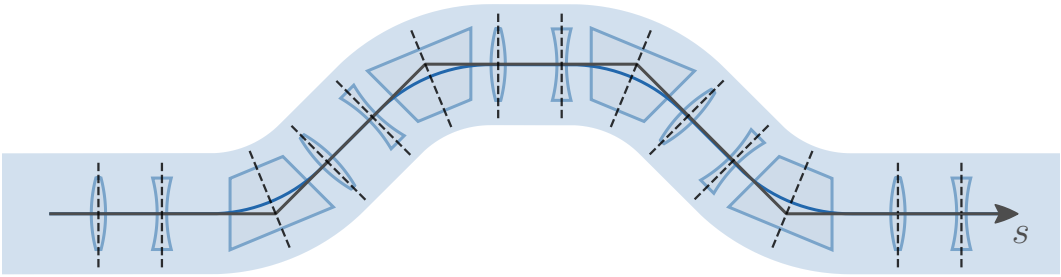

Figure 3.1: Schematic of a simple beam line. The complete description of the physical lattice (in blue) is abandoned to study a simpler model (in black) which can be described exactly. Physical magnets are replaced with a succession of thin kicks separated by drift sections (according to standard splitting methods; described in Sec. 3.3.1). The correspondence can be arbitrarily improved by subdividing the elements in more slices.

physical machine (the first layer of equivocation) to study the numerical machine, as shown in Fig 3.1. Since the solutions are exact with respect to this simplified model, the analytic tools developed in the process can be used to interpret the tracking in a self-consistent way (avoiding the last layers of equivocation). In other words, the complete Hamiltonian $H_\star$ of eq. (1.6):

$$H_\star = p_\zeta - (1+hx)\left[\sqrt{(1+2p_\zeta+\beta_{r_0}^2 p_\zeta^2)-(p_x-a_x)^2-(p_y-a_y)^2}-a_s\right] \ , \tag{3.1}$$

is left aside — definitively — and replaced by a succession of *elements*, for which the local Hamiltonian $H_{s\to s+\Delta s}$ is only defined over the length Δs of each element. These local Hamiltonians shall always take the form:

$$H_{s\to s+\Delta s} \equiv \underbrace{p_\zeta - \delta_\mathrm{p} + \frac{p_x^2+p_y^2}{2(1+\delta_\mathrm{p})}}_{\text{Drift}} \underbrace{- hx(1+\delta_\mathrm{p})}_{\text{Dispersive}} \underbrace{+(1+hx)a_s}_{\text{Magnetic}} \ . \tag{3.2}$$

with $(1+\delta_\mathrm{p}) = \sqrt{1+2p_\zeta+\beta_{r_0}^2 p_\zeta^2}$. Eq. (3.2) is obtained from eq. (3.1) by settings the fields to be purely transverse ($a_x = a_y = 0$) and expanding the square root to second order in the dynamical variables. The three terms (drift, dispersive and magnetic) can be used to describe the various elements needed. Eq. (3.2) being a piecewise description, some implications of Maxwell's equations might be impossible to describe with this simple form. In such cases, additional *ad hoc* elements can be considered and added to the sequence of elements. In the context of this thesis however, eq. (3.2) shall be sufficient to build realistic beam line *models* (as illustrated in Fig 3.1). With this element-based approach, the final *effective* Hamiltonian of the beam line as a whole forever remains unknown — in closed-form, as will be shown from the Baker–Campbell–Hausdorff (BCH) formula. That being said, the global map of the system can still be described by composing the sequence of elements. In essence, this approach is similar to É. Forest's vision: "A Hamiltonian-free description of single particle dynamics for hopelessly complex periodic systems" [16] and builds on the Fourier expansions, as well as the numerical tools such as NAFF, presented in the previous chapter.

3.2 Lie Transformations

Let us consider the physical phase space $\vec{x} = (x, p_x, y, p_y, \zeta, p_\zeta) = (\{q_j, p_j\})$ with $j \in \{x, y, \zeta\}$ describing the position and momentum of a particle in a beam line. The Poisson Bracket $[g, f]$ of any two functions of the phase space, $g(\vec{x})$ and $f(\vec{x})$, is a differential operation defined as:

$$[g, f] \equiv \sum_j \left(\frac{\partial g}{\partial q_j} \frac{\partial f}{\partial p_j} - \frac{\partial g}{\partial p_j} \frac{\partial f}{\partial q_j} \right) , \tag{3.3}$$

which can be rewritten — for convenience — as the *Lie operator* $(: g :)$ acting on $f(\vec{x})$ following:

$$(: g :) f \equiv [g, f] . \tag{3.4}$$

Suppose we wish to evaluate $f(\vec{x})$ along the beam line, *i.e.*, we want to integrate $f(\vec{x})$ in the Hamiltonian flow of the system. Assuming that $f(\vec{x})$ has no explicit dependence on s, the variation in the beam line follows:

$$\frac{df}{ds} = \sum_j \frac{dq_j}{ds} \frac{\partial f}{\partial q_j} + \frac{dp_j}{ds} \frac{\partial f}{\partial p_j} , \tag{3.5}$$

which, using eq. (1.2) and eq. (1.3), yields:

$$\frac{df}{ds} = \sum_j \frac{\partial H}{\partial p_j} \frac{\partial f}{\partial q_j} - \frac{\partial H}{\partial q_j} \frac{\partial f}{\partial p_j} = -[H, f] \quad \text{or} \quad \frac{df}{ds} = (: -H :) f , \tag{3.6}$$

and the solution, integrated between s_1 and s_2, is:

$$\Big[f(\vec{x}) \Big]_{s_2} = e^{(:-G:)} \Big[f(\vec{x}) \Big]_{s_1} , \quad \text{with} \quad G \equiv \int_{s_1}^{s_2} H \, ds , \tag{3.7}$$

where the operator $e^{(:-G:)}$ is the *Lie transformation* of $f(\vec{x})$ with generating function G (units of m) [4, 35, 36]. For this thesis, the Hamiltonian is either constant over some finite length (thick) or punctual (a Dirac-like, thin kick) in which case we can make the following proposition.

Proposition 3.1

For thick ($s \mapsto s + \Delta s$) or thin ($s \mapsto s + ds$ with $ds \to 0$) elements with constant Hamiltonian H, the Lie transformations:

$$\Big[f(\vec{x}) \Big]_{s+\Delta s} = \underbrace{e^{(:-H \Delta s:)}}_{\text{Thick}} \Big[f(\vec{x}) \Big]_s \quad \text{or} \quad \Big[f(\vec{x}) \Big]_{s+ds} = \underbrace{e^{(:-H \, ds:)}}_{\text{Thin}} \Big[f(\vec{x}) \Big]_s , \tag{3.8}$$

integrate Hamilton's equations over the element and therefore maps the function $f(\vec{x})$ through the Hamiltonian flow. The result is always symplectic, by construction. As pointed out by A. J. Dragt [36]: " integrating Hamilton's equations of motion produces symplectic maps, and every symplectic map arises from integrating Hamilton's equations ".

In particular, if $f(\vec{x})$ is taken to be each of the dynamical variables in turn, $\mathcal{M} \, \vec{x} = e^{(:-H \Delta s:)} \, \vec{x}$ provides the full transfer map $\mathcal{M}$ for the element.

As such, Lie transformations appear as an important — and natural — tool to solve the transport problem of beam dynamics. The evolution of any function $f(\vec{x})$ in the Hamiltonian flow of the system can be obtained by taking the Lie transformation of $f(\vec{x})$ with the Hamiltonian as the generating function. Furthermore, Lie transformations are always symplectic and allow us to avoid the challenges discussed earlier. Going back to the definition of Lie operators, eq. (3.4), one can see that successive applications yield:

$$\begin{aligned} (\!: g :\!)^0 f &\equiv f \ , \\ (\!: g :\!)^1 f &= [g, f] \ , \\ (\!: g :\!)^2 f &= [g, [g, f]] \ , \end{aligned} \tag{3.9}$$

where $(\!: g :\!)^0$ is, by definition, the identity operator. The effect of a Lie transformation, $e^{(\!: g :\!)}$, can therefore be expressed as a power expansion in the operator following:

$$e^{(\!: g :\!)} \ f = \sum_{k=0}^{\infty} \frac{(\!: g :\!)^k}{k!} \ f = f + [g, f] + \frac{1}{2}[g, [g, f]] + \dots \tag{3.10}$$

It is noteworthy that the result is the same if the Lie transformation is applied directly to the argument of $f(\vec{x})$, *i.e.* $e^{(\!: g :\!)} f(\vec{x}) = f\left(e^{(\!: g :\!)} \vec{x}\right)$ and hence:

$$e^{(\!: g_1 :\!)} e^{(\!: g_2 :\!)} \ \vec{x} = e^{(\!: g_2 :\!)} \left(e^{(\!: g_1 :\!)} \vec{x}\right) = \left(e^{(\!: g_2 :\!)} \circ e^{(\!: g_1 :\!)}\right) \vec{x} \ . \tag{3.11}$$

In practice, beam lines are made up of several elements (drifts, dipoles, quadrupoles, sextupoles, etc.) traversed sequentially. Following eq. (3.11), sequential transformations are written as compositions. If $H_1, \ H_2, \ \dots, \ H_n$ correspond to the Hamiltonians of the elements of a beam line with lengths $\Delta s_1, \ \Delta s_2, \ \dots, \ \Delta s_n$, then:

$$\mathcal{M} \, \vec{x}_{s_0} = \left(e^{(\!: -H_n \Delta s_n :\!)} \circ \dots \circ e^{(\!: -H_2 \Delta s_2 :\!)} \circ e^{(\!: -H_1 \Delta s_1 :\!)}\right) \ \vec{x}_{s_0} = \vec{x}_{s_n} \ , \tag{3.12}$$

yields the full transformation through the Hamiltonian flow of the system. At this stage, one might be tempted to study the global map $\mathcal{M}$ directly, which is discouraged in this thesis and runs counter to the methodology presented. Again, as S. Wolfram puts it: "we have to go through the same irreducible computational steps as the system itself" [26]. Formally, the composition of Lie transformations follows the Baker–Campbell–Hausdorff (BCH) [35] formula, which gives the effective generating function from a sequence of transformations, g_1 and g_2:

$$e^{(\!: g_1 :\!)} e^{(\!: g_2 :\!)} = e^{(\!: h :\!)} \quad \text{with} \quad h = g_1 + g_2 + \frac{1}{2}[g_1, g_2] + \frac{1}{12}[g_1, [g_1, g_2]] + \frac{1}{12}[g_2, [g_2, g_1]] + \dots \tag{3.13}$$

which is an *infinite* series of nested commutators of g_1 and g_2. In general, there is no finite closed-form expression for h (except for some special cases). In other words, the effective Hamiltonian of a sequence of elements, *e.g.* H_1 and H_2, can only be known (in closed-form) if the elements commute, $[H_1, H_2] = 0$. As such, we shall restrict ourselves to the study of individual elements with exact (closed-form) transformations, which we apply sequentially — and explicitly forgo the search for an effective Hamiltonian. In this sense, Forest's "Hamiltonian-free description of single particle dynamics for hopelessly complex periodic systems" [16] is not a departure from Hamiltonian mechanics; rather, it recognizes the fundamental limitation posed by eq. (3.13) and advocates for an element-by-element approach, as we do.

3.2.1 Application on Complex Coordinates, Loops and Tori

In Chapter 2, we introduced $\boldsymbol{\psi}$ and $\boldsymbol{\Psi}$ as *functions* of the phase space variables in the form of $\psi_j = q_j/\sqrt{\beta_{j0}} - ip_j\sqrt{\beta_{j0}}$ for $j \in \{x, y, \zeta\}$. The transformations of eq. (3.8) can therefore be used to obtain the evolution of $\boldsymbol{\psi}$ or $\boldsymbol{\Psi}$ through the Hamiltonian flow following:

$$e^{(:-H\Delta s:)}\ \boldsymbol{\psi}_1 = \boldsymbol{\psi}_2\ :\ \begin{cases} e^{(:-H\Delta s:)}\ \psi_{1,x} = \psi_{2,x} \\ e^{(:-H\Delta s:)}\ \psi_{1,y} = \psi_{2,y} \\ e^{(:-H\Delta s:)}\ \psi_{1,\zeta} = \psi_{2,\zeta} \end{cases}, \tag{3.14}$$

and

$$e^{(:-H\Delta s:)}\ \boldsymbol{\Psi}_1(\vec{\Theta}) = \boldsymbol{\Psi}_2(\vec{\Theta})\ :\ \begin{cases} e^{(:-H\Delta s:)}\ \Psi_{1,x}(\vec{\Theta}) = \Psi_{2,x}(\vec{\Theta}) \\ e^{(:-H\Delta s:)}\ \Psi_{1,y}(\vec{\Theta}) = \Psi_{2,y}(\vec{\Theta}) \\ e^{(:-H\Delta s:)}\ \Psi_{1,\zeta}(\vec{\Theta}) = \Psi_{2,\zeta}(\vec{\Theta}) \end{cases}, \tag{3.15}$$

which only differ semantically with the capitalization of $\boldsymbol{\psi} \to \boldsymbol{\Psi}$ to remind ourselves that $\boldsymbol{\Psi}(\vec{\Theta})$ is further parametrized by the angles $\vec{\Theta}$. That being said, the effect of a Lie transformation $e^{(:-H\Delta s:)}$ on either $\boldsymbol{\psi}$ or $\boldsymbol{\Psi}$ is identical since the two are equivalent functions of the phase space variables. Based on eq. (3.10), Lie transformations are obtained from a power series of Poisson brackets. It is therefore relevant to list a few identities from which further results can be derived, as done in Demonstration 3.1.

Demonstration 3.1: Useful Poisson bracket identities.

Starting from eq. (3.3) and remembering that $\Psi_x \equiv X/\sqrt{\beta_{x0}} - iP_x\sqrt{\beta_{x0}}$, the following identities can be obtained. Equivalent identities can be similarly obtained for y and ζ.

Coordinates		**Complex Coordinates**	
$[x, p_x] = 1$	(3.16)	$[\Psi_x, \Psi_x^*] = 2i$	(3.17)
$[x, x] = [p_x, p_x] = 0$	(3.18)	$[\Psi_x, \Psi_x] = 0$	(3.19)
$[f(y, p_y, \zeta, p_\zeta), g(x, p_x)] = 0$	(3.20)	$[f(y, p_y, \zeta, p_\zeta), \Psi_x] = 0$	(3.21)
$[x^a p_x^b, x] = -b \cdot x^a p_x^{b-1}$	(3.22)	$[x^a, \Psi_x] = -ia \cdot \sqrt{\beta_{x0}} X^{a-1}$	(3.23)
$[x^a p_x^b, p_x] = a \cdot x^{a-1} p_x^b$	(3.24)	$[p_x^b, \Psi_x] = -b \cdot \frac{1}{\sqrt{\beta_{x0}}} P_x^{b-1}$	(3.25)

The **symplectic condition** states that a transformation is symplectic (*i.e.* canonical) if it preserves the fundamental Poisson brackets. In real coordinates this means that $[q_j, p_k] = \delta_{jk}$ for $j, k \in \{x, y, \zeta\}$. In the complex basis, the equivalent relations are:

$$[\Psi_j, \Psi_k] = 0, \qquad [\Psi_j, \Psi_k^*] = 2i\,\delta_{jk}\ . \tag{3.26}$$

A transformation $\mathcal{M}$ is therefore symplectic if and only if:

$$[\mathcal{M}\Psi_j,\ (\mathcal{M}\Psi_k)^*] = \mathcal{M}[\Psi_j, \Psi_k^*] = 2i\,\delta_{jk}\ , \tag{3.27}$$

for all degrees of freedom $j, k \in \{x, y, \zeta\}$.

A few examples

1. $H\Delta s = ax + bp_x$

Consider that we wish to apply the transformation from a Hamiltonian of the form $H\Delta s = ax + bp_x$, with corresponding transformation $e^{(\!:-(ax+bp_x):\!)}$. Starting in the horizontal plane, we need to evaluate the Poisson bracket $[-(ax + bp_x), \Psi_x]$, which can be done in three ways: either by evaluating the derivatives of eq. (3.3) directly; or by substituting $\Psi_x = X/\sqrt{\beta_{x_0}} - iP_x\sqrt{\beta_{x_0}}$ in the Poisson bracket and consider the left column of Demonstration 3.1; or by directly using the right column of Demonstration 3.1 to get the result. In any case, the first few applications of the Lie operator yield:

$$\begin{aligned}
(\!: -(ax + bp_x) :\!)^0 \Psi_x &= \Psi_x \ , \\
(\!: -(ax + bp_x) :\!)^1 \Psi_x &= [-(ax + bp_x), \Psi_x] = b/\sqrt{\beta_{x_0}} + ia\sqrt{\beta_{x_0}}, \\
(\!: -(ax + bp_x) :\!)^2 \Psi_x &= [-(ax + bp_x), [-(ax + bp_x), \Psi_x]] = 0 \ ,
\end{aligned} \tag{3.28}$$

which allows us to infer that all further application will also vanish, such that we get:

$$e^{(\!:-(ax+bp_x):\!)} \Psi_x(\vec{\Theta}) = \sum_{k=0}^{\infty} \frac{(\!: -(ax + bp_x) :\!)^k}{k!} \ \Psi_x(\vec{\Theta}) = \Psi_x(\vec{\Theta}) + \left(b/\sqrt{\beta_{x_0}} + ia\sqrt{\beta_{x_0}}\right) . \tag{3.29}$$

For the other conjugate planes, eq. (3.21) informs us that all Poisson brackets vanish since $[-(ax + bp_x), \Psi_y] = [-(ax + bp_x), \Psi_\zeta] = 0$. Indeed a transformation which only depends on (x, p_x), has no effect on the other conjugate planes. We can therefore write:

$$e^{(\!:-(ax+bp_x):\!)} \Psi_y(\vec{\Theta}) = \sum_{k=0}^{\infty} \frac{(\!: -(ax + bp_x) :\!)^k}{k!} \ \Psi_y(\vec{\Theta}) = \Psi_y(\vec{\Theta}) \ , \tag{3.30}$$

and idem for ζ. Overall, the transformation yields:

$$e^{(\!:-(ax+bp_x):\!)} \ \boldsymbol{\Psi}(\vec{\Theta}) \ : \ \begin{cases} \Psi_x + \left(b/\sqrt{\beta_{x_0}} + ia\sqrt{\beta_{x_0}}\right) \\ \Psi_y \\ \Psi_\zeta \end{cases} , \tag{3.31}$$

which corresponds to a translation in the (x, p_x) phase space with $X \mapsto X + b$ and $P_x \mapsto P_x - a$.

2. $H\Delta s = axp_x$

Let us now consider a transformation with a Hamiltonian of the form $H\Delta s = axp_x$. Again, the first few applications of the Lie operator lead to:

$$\begin{aligned}
(\!: -axp_x :\!)^0 \ \Psi_x &= \Psi_x \ , \\
(\!: -axp_x :\!)^1 \ \Psi_x &= [-axp_x, \Psi_x] = a\Psi_x^*, \\
(\!: -axp_x :\!)^2 \ \Psi_x &= [-axp_x, [-axp_x, \Psi_x]] = a^2\Psi_x \\
(\!: -axp_x :\!)^3 \ \Psi_x &= [-axp_x, [-axp_x, [-axp_x, \Psi_x]]] = a^3\Psi_x^* \ ,
\end{aligned} \tag{3.32}$$

which allows us to infer that:

$$e^{(\!:-axp_x:\!)}\Psi_x(\vec{\Theta}) = \left(1+\frac{a^2}{2!}+\frac{a^4}{4!}+\dots\right)\Psi_x + \left(1+\frac{a^3}{3!}+\frac{a^5}{5!}+\dots\right)\Psi_x^* \\ = \cosh(a)\Psi_x + \sinh(a)\Psi_x^* \tag{3.33}$$

Just like the previous example, the transformation has no effect in the other conjugate planes, such that we get:

$$e^{(\!:-axp_x:\!)}\,\boldsymbol{\Psi}(\vec{\Theta}) \;:\; \begin{cases} \cosh(a)\Psi_x + \sinh(a)\Psi_x^* \\ \Psi_y \\ \Psi_\zeta \end{cases}, \tag{3.34}$$

which corresponds to a symplectic rescaling of the phase space (a telescope). Indeed, substituting $X/\sqrt{\beta_{x_0}} - iP_x\sqrt{\beta_{x_0}}$ in place of Ψ_x shows that the transformation scales $X \mapsto e^a X$ and $P_x \mapsto e^{-a}P_x$ such that the area is preserved.

3. $H\Delta s = \mu_x\pi\left((x/\sqrt{\beta_{x_0}})^2 + (p_x\sqrt{\beta_{x_0}})^2\right)$

Finally, let us consider a Hamiltonian of the form $H\Delta s = \mu_x\pi\left((x/\sqrt{\beta_{x_0}})^2 + (p_x\sqrt{\beta_{x_0}})^2\right)$ which is typical in the Courant-Snyder analysis of linear systems. In fact, if β_{x_0} is chosen to be the Courant-Snyder parameter β_x, then this Hamiltonian is close to being normalized. In any case, the first few applications of the Lie operator yield:

$$\begin{aligned} (\!: -H\Delta s :\!)^0\,\Psi_x &= \Psi_x \;, \\ (\!: -H\Delta s :\!)^1\,\Psi_x &= [-H\Delta s, \Psi_x] = i2\pi\mu_x\,\Psi_x \;, \\ (\!: -H\Delta s :\!)^2\,\Psi_x &= [-H\Delta s, [-H\Delta s, \Psi_x]] = (i2\pi\mu_x)^2\,\Psi_x \;, \end{aligned} \tag{3.35}$$

which allows us to infer that:

$$e^{(\!:-H\Delta s:\!)}\,\Psi_x(\vec{\Theta}) = \sum_{k=0}^{\infty}\frac{(i2\pi\mu_x)^k}{k!}\,\Psi_x(\vec{\Theta}) = e^{i(2\pi\mu_x)}\,\Psi_x(\vec{\Theta}) \;. \tag{3.36}$$

Again, with no effect in the other conjugate planes, the final transformation reads:

$$e^{\left(\!:-\mu_x\pi((x/\sqrt{\beta_{x_0}})^2+(p_x\sqrt{\beta_{x_0}})^2):\!\right)}\,\boldsymbol{\Psi}(\vec{\Theta}) \;:\; \begin{cases} e^{i(2\pi\mu_x)}\,\Psi_x(\vec{\Theta}) \\ \Psi_y(\vec{\Theta}) \\ \Psi_\zeta(\vec{\Theta}) \end{cases}, \tag{3.37}$$

which corresponds to a rotation of the complex coordinates in the horizontal plane. If $\beta_{x_0} = 1$, then the transformation is also a geometric rotation of the horizontal phase space.

The three examples presented should help the reader in getting familiar with Lie operators and the construction of Lie transformations. Based on the above results, it appears necessary to list the algebraic rules involved in the manipulation of Fourier series such as $\boldsymbol{\Psi}(\vec{\Theta})$ while preserving the functional form of these series. In general, Lie transformations return a function of Ψ_x, Ψ_y, Ψ_ζ which represents a new Fourier series. The algebraic rules required to describe the transformations are presented in Demonstration 3.2 and will be needed for the rest of the thesis. This "algebra" was implemented in python (see PYTORI [3]) to facilitate the analysis.

Demonstration 3.2: Algebra of Multivariate Expansions.

Consider two generic multivariate expansions of the form:

$$\Psi_1(\vec{\Theta}) = \sum_{\vec{n}} A_{\vec{n}}\, e^{i(\vec{n}\cdot\vec{\Theta})} \quad \text{and} \quad \Psi_2(\vec{\Theta}) = \sum_{\vec{n}} B_{\vec{n}}\, e^{i(\vec{n}\cdot\vec{\Theta})} \tag{3.38}$$

with $A_{\vec{n}} = \langle \vec{n} | \Psi_1 \rangle$ and $B_{\vec{n}} = \langle \vec{n} | \Psi_2 \rangle$. One can show that a function of Ψ_1 and Ψ_2 is also a multivariate expansion where the new coefficients are given in terms of $A_{\vec{n}}$ and $B_{\vec{n}}$. The key algebraic rules are as follow.

Addition: The sum of two expansions is given by the sum of the coefficients:

$$\langle \vec{n} | \Psi_1 + \Psi_2 \rangle = A_{\vec{n}} + B_{\vec{n}} \tag{3.39}$$

Multiplication: The product of two expansions is given by the convolution of their coefficients:

$$\langle \vec{n} | \Psi_1 \Psi_2 \rangle = \sum_{\vec{m}} A_{\vec{m}} B_{\vec{n}-\vec{m}} \tag{3.40}$$

Powers: Raising an expansion to an integer power p is computed recursively using repeated convolutions from the multiplication rule, eq. (3.40).

Scalar Multiplication: For a complex scalar c, the expansion becomes:

$$\langle \vec{n} | c\Psi_1 \rangle = cA_{\vec{n}} \tag{3.41}$$

Complex conjugation: The complex conjugate of a multivariate expansion yields:

$$\langle \vec{n} | \Psi_1^* \rangle = A^*_{-\vec{n}} \tag{3.42}$$

Those simple rules can be implemented in programming tools and allow to obtain, from a function of multivariate expansions, the resulting multivariate expansion. A practical example relates to the coordinates (X, P_x) of a torus projection, $\Psi_x(\vec{\Theta})$, which can be obtained as multivariate expansions following:

$$X(\vec{\Theta}) = \frac{1}{2}(\Psi_x + \Psi_x^*)\sqrt{\beta_{x_0}} \;=\; \frac{\sqrt{\beta_{x_0}}}{2} \sum_{\vec{n}} \left(A_{\vec{n}} + A^*_{-\vec{n}}\right)\, e^{i(\vec{n}\cdot\vec{\Theta})}\ , \tag{3.43}$$

$$P_x(\vec{\Theta}) = \frac{i}{2}(\Psi_x - \Psi_x^*)/\sqrt{\beta_{x_0}} = \frac{i}{2\sqrt{\beta_{x_0}}} \sum_{\vec{n}} \left(A_{\vec{n}} - A^*_{-\vec{n}}\right)\, e^{i(\vec{n}\cdot\vec{\Theta})}\ , \tag{3.44}$$

3.2.2 Transformation of common elements

Following the introduction of Lie transformations, let us study the set of fundamental operators (the elements) required to build realistic beam line *models*, as highlighted in Fig. 3.1. It should be emphasized that the transformations given below are exact — with regard to their corresponding local Hamiltonian — and identical to the ones used in XSUITE [18]. As previously mentioned, all Hamiltonians take the form of eq. (3.2).

Thin Quadrupole

The first — and simplest — element to consider is the thin quadrupole, which can act as a focusing or defocusing device similar to optical lenses (see Chapter 1). Assuming the magnet is centered on a straight coordinate system, the corresponding local hamiltonian H_q is:

$$H_q \equiv \frac{1}{2}k_1^+(x^2 - y^2) + \frac{1}{2}k_1^\times(-2xy) \ , \tag{3.45}$$

where

$$k_n^+ + ik_n^\times = \frac{q_e}{\mathrm{p}_0}\left(\frac{\partial^n B_y}{\partial x^n} + i\frac{\partial^n B_x}{\partial x^n}\right) \tag{3.46}$$

are the normal k_n^+ and skew $k_n^\times$ multipolar strength of order n. As done previously, the identities of Demonstration 3.1 can be used to compute the corresponding Lie transformation. For a thin quadrupole, this leads to:

$$e^{(\!:-H_q\,ds:\!)}\,\boldsymbol{\Psi}(\vec{\Theta}) \ : \ \begin{cases} \Psi_x + i\sqrt{\beta_{x_0}}\,(K_1^+X - K_1^\times Y) \\ \Psi_y - i\sqrt{\beta_{y_0}}\,(K_1^+Y + K_1^\times X) \\ \Psi_\zeta \end{cases} , \tag{3.47}$$

where $K_n^+ + iK_n^\times = \int_{\Delta s}(k_n^+ + ik_n^\times)\,ds$ are the integrated multipolar strengths of the thin element in the limit $\Delta s \to 0$. The reader familiar with common transfer maps will notice that eq. (3.47) is nothing more than the usual transfer map for thin quadrupoles with the simple change $(x, p_x) \to (X, P_x)$ and $(y, p_y) \to (Y, P_y)$. In general, the transport of loops and tori can be obtained from the usual transfer maps by replacing the dynamical variables with their corresponding Fourier series. From there, the computation is carried out by using the algebraic rules of Demonstration 3.2. In some cases, other mathematical operations are needed (*e.g.* the quotient of two Fourier series) and additional manipulations need to be done. This is notably the case of the thin dipole element and the drift element, which will be discussed later.

Thin magnetic elements have the particularity of being additive, in the sense that their Hamiltonians commute. Far from being the norm, this exception implies that:

$$e^{(\!:-H_q\,ds:\!)} = e^{(\!:-H_q^+\,ds:\!)}e^{(\!:-H_q^\times\,ds:\!)} \quad \text{with} \quad H_q^+ \equiv \frac{1}{2}k_1^+(x^2 - y^2) \ ; \ H_q^\times \equiv \frac{1}{2}k_1^\times(-2xy) \ , \tag{3.48}$$

according to the BCH formula (eq. (3.13)), since $[H_q^+, H_q^\times] = 0$. As such, we can study *normal* quadrupoles and *skew* quadrupoles separately depending on the orientation of the magnets; or combine the two for the general case. From eq. (3.47), one can see that a normal quadrupole (letting $k_1^+ > 0$ and $k_1^\times = 0$) is indeed focusing in the horizontal plane ($P_x \mapsto P_x - \sqrt{\beta_{x_0}}K_1^+X$) and defocusing in the vertical plane ($P_y \mapsto P_y + \sqrt{\beta_{x_0}}K_1^+Y$) as expected.

Thin Multipole

Consider now the case of a general magnetic field expressed as a multipole expansion following:

$$B_y + iB_x = B_{\text{ref}} \sum_{n=0}^{\infty} (b_n + ia_n) \left(\frac{x+iy}{R_{\text{ref}}} \right)^n = \frac{\text{p}_0}{q_e} \sum_{n=0}^{\infty} \frac{1}{n!} (k_n^+ + ik_n^\times)(x+iy)^n \tag{3.49}$$

where a_n and b_n are generic multipolar coefficients [4] corresponding to some reference field B_{ref} and reference radius R_{ref}. For our purpose, the expansion is rewritten in terms of the normalized multipolar strength k_n^+ and $k_n^\times$, as shown in the right-hand side of the equation. Following XSUITE's convention [18], $n = 0$ corresponds to a dipole field, $n = 1$ to a quadrupole field, $n = 2$ to a sextupole field, and so on. In a straight coordinate system, the local Hamiltonian for a general multipole H_M is:

$$H_M \equiv \text{Re}\left[\sum_{n=0}^{\infty} \tfrac{1}{(n+1)!} (k_n^+ + ik_n^\times)(x+iy)^{n+1} \right] . \tag{3.50}$$

The effect of H_M can be found at any order by separating the different contributions and making use of the monomial transformation:

$$e^{(:-ax^n y^m:)}\, \boldsymbol{\Psi}(\vec{\Theta}) \;:\; \begin{cases} \Psi_x + i\sqrt{\beta_{x_0}} \left(anX^{n-1}Y^m \right) \\ \Psi_y + i\sqrt{\beta_{y_0}} \left(amX^nY^{m-1} \right) \\ \Psi_\zeta \end{cases} . \tag{3.51}$$

After collecting the proper terms (order-by-order) in the expansion of eq. (3.50), the final transformation for a general multipole can be written as the product of monomials:

$$e^{(:-H_M\, ds:)} = \prod_{n,m} e^{(:-a_{n,m} x^n y^m:)} , \tag{3.52}$$

since terms such as $x^n y^m$ and $x^k y^\ell$ always commute, $[x^n y^m, x^k y^\ell] = 0$. In the above, $a_{n,m}$ are functions of the integrated magnet strength following the multipole expansion of eq. (3.50). Additionally, the global transformation can also be written in a concise way following:

$$e^{(:-H_M\, ds:)}\, \boldsymbol{\Psi}(\vec{\Theta}) \;:\; \begin{cases} \Psi_x + i\sqrt{\beta_{x_0}} \text{Re}\{\mathcal{K}\}(X,Y) \\ \Psi_y - i\sqrt{\beta_{y_0}} \text{Im}\{\mathcal{K}\}(X,Y) \\ \Psi_\zeta \end{cases} , \quad \text{with} \quad \mathcal{K}(x,y) = \sum_{n=0} \tfrac{1}{n!} (K_n^+ + iK_n^\times)(x+iy)^n \tag{3.53}$$

where the real and imaginary parts ($\text{Re}\{\mathcal{K}\}$, $\text{Im}\{\mathcal{K}\}$) need to be taken on $\mathcal{K}(x,y)$ before letting $x \to X$ and $y \to Y$ in order to preserve the Fourier structure of the variables. For a numerical implementations of eq. (3.53), this can be achieved through a Horner-like iterative scheme, as done in XSUITE [18].

Thin Bending Dipole

Dipole magnets are elements that generate a uniform magnetic field and can serve two main purposes. They may act as *bending* magnets, providing the transverse deflection necessary to guide the beam along a curved trajectory; or as *orbit correctors*, delivering a localized transverse kick (orbit bump) to the beam. The distinction depends on the local curvature of the reference trajectory, h. Importantly, h is not determined by the equations of motion, but is instead fixed, *a priori*, through the choice of coordinate system. Using the normalized field strength $k_0^+ = \frac{q_e}{\mathrm{p}_0} B_0$, the local Hamiltonian H_b for a thin dipole is:

$$H_b \equiv -hx(1+\delta_\mathrm{p}) + k_0^+ \left(x + \frac{hx^2}{2} \right) \ , \tag{3.54}$$

with $(1+\delta_\mathrm{p}) = \sqrt{1 + 2p_\zeta + \beta_{r_0}^2 p_\zeta^2}$ and where the linear terms are responsible for the beam deflection. If $h = k_0^+$, the linear terms cancel out and the deflection vanishes for on-momentum particles ($\delta_\mathrm{p} = 0$). In that case, a particle with the reference momentum and initially on the reference trajectory remains on the reference trajectory at the exit of the dipole. This is the bending function mentioned above. If, instead, $h = 0$, the beam is deflected away from the reference trajectory and the dipole acts as an orbit corrector. Using the differential form of the Poisson bracket (eq. (3.3)) to handle the square root in $\delta_\mathrm{p}(p_\zeta)$, the Lie transformation for a particle $\boldsymbol{\psi}$ is:

$$e^{(\!:\!-H_b\, ds\!:\!)}\, \boldsymbol{\psi} \ : \ \begin{cases} \psi_x + i\sqrt{\beta_{x_0}} \Big(k_0^+ (1+hx) - h(1+\delta_\mathrm{p}) \Big) \\ \psi_y \\ \psi_\zeta - \dfrac{1}{\sqrt{\beta_{\zeta_0}}} \left(\dfrac{1+\beta_{r_0}^2 p_\zeta}{1+\delta_\mathrm{p}} \right) hx \end{cases} \ , \tag{3.55}$$

where the horizontal kick indeed vanishes if $h = k_0$, $\delta_\mathrm{p} = 0$ and $x = 0$. In this form, eq. (3.55) cannot be used to describe the transport of loops and tori, since quotient of Fourier series are in general ill-defined — and absent from the list of algebraic rules of Demonstration 3.2. To work around this limitation, we write the *chromatic term* $1/(1+\delta_\mathrm{p}) \mapsto \mathcal{C}_\zeta$ as another multivariate expansion:

$$\mathcal{C}_\zeta \equiv (1 + 2P_\zeta + \beta_{r_0}^2 P_\zeta^2)^{-1/2} = 1 + \sum_{k=1}^{\infty} (-1)^k \left[\mathcal{G}_k^{(1/2)} \left(\tfrac{1}{\beta_{r_0}} \right) \right] (\beta_{r_0} P_\zeta)^k \ , \tag{3.56}$$

which follows the same algebraic rules. Here, $\mathcal{C}_\zeta$ is expressed as a Taylor expansion in P_ζ that converges when $|\beta_{r_0} P_\zeta| < 1$ — which is always the case. In eq. (3.56), the $\mathcal{G}_k^{(\alpha)}$ are the Gegenbauer polynomials of order k and parameter α (a generalisation of the Legendre polynomials) and β_{r_0} is the relativistic velocity parameter. We further define the inverse of the chromatic term, $\mathcal{C}_\zeta^{-1}$, as:

$$\mathcal{C}_\zeta^{-1} \equiv (1 + 2P_\zeta + \beta_{r_0}^2 P_\zeta^2)^{1/2} = 1 + \sum_{k=1}^{\infty} (-1)^k \left[\mathcal{G}_k^{(-1/2)} \left(\tfrac{1}{\beta_{r_0}} \right) \right] (\beta_{r_0} P_\zeta)^k \ , \tag{3.57}$$

which also converges for $|\beta_{r_0} P_\zeta| < 1$.

Following these definitions, the thin dipole transformation for loops and tori can be obtained from eq. (3.55) by letting $1/(1+\delta_{\mathrm{p}}) \mapsto \mathcal{C}_\zeta$ to get:

$$e^{(\!:-H_b\, ds:\!)}\, \boldsymbol{\Psi}(\vec{\Theta}) \;:\; \begin{cases} \Psi_x + i\sqrt{\beta_{x_0}}\Big(K_0^+(1+hX) - h\,\mathcal{C}_\zeta^{-1}\Big) \\ \Psi_y \\ \Psi_\zeta - \dfrac{1}{\sqrt{\beta_{\zeta_0}}}\mathcal{C}_\zeta(1+\beta_{r_0}^2 P_\zeta)hX \end{cases}, \tag{3.58}$$

which is non-linear for off-momentum particles ($P_\zeta \neq 0$), but linear otherwise (with $P_\zeta = 0$ and $\mathcal{C}_\zeta = 1$). In general, off-momentum particles are not deflected uniformly and the energy-dependent deviation induced by the magnet leads to dispersion, which is the variation of the closed orbit with energy. To give a sense of the orders of magnitude involved, it is worth remembering that p_ζ is typically in the order of 10^{-4} in the LHC.

Thin RF Cavity

Radiofrequency (RF) cavities are used to accelerate or decelerate particles within a bunch using a time-dependent electromagnetic field. As such, RF cavities are an essential tool to ensure longitudinal (ζ-plane) stability. Here we consider the simplest operational case which keeps particles confined — within a bunch — around the synchronous phase ϕ_{RF}. For a thin RF cavity with frequency f_{RF} and wavenumber $k_{\mathrm{RF}} = 2\pi f_{\mathrm{RF}}/c$, the local Hamiltonian H_{RF} is:

$$H_{\mathrm{RF}} \equiv \frac{V_{\mathrm{N}}}{k_{\mathrm{RF}}}\, \cos\Big(\phi_{\mathrm{RF}} - (k_{\mathrm{RF}}/\beta_{r_0})\,\zeta\Big)\, \delta(s - s_{\mathrm{RF}})\ , \tag{3.59}$$

where $V_{\mathrm{N}} = \frac{q_e V}{\mathrm{p}_0 c}$ is the normalized voltage of the cavity and $\delta(s - s_{\mathrm{RF}})$ is the Dirac delta. Since the true field is s-dependent [4], eq. (3.59) corresponds to the "average" Hamiltonian applied locally at the cavity location s_{RF}. The Lie transformation for a particle ψ reads:

$$e^{(\!:-H_{\mathrm{RF}}\, ds:\!)}\, \boldsymbol{\psi} \;:\; \begin{cases} \psi_x \\ \psi_y \\ \psi_\zeta - i\dfrac{\sqrt{\beta_{\zeta_0}}}{\beta_{r_0}} V_{\mathrm{N}} \sin\Big(\phi_{\mathrm{RF}} - (k_{\mathrm{RF}}/\beta_{r_0})\,\zeta\Big) \end{cases}. \tag{3.60}$$

For loops and tori, the same transformation is obtained via the Maclaurin series expansion of the sine function following:

$$e^{(\!:-H_{\mathrm{RF}}\, ds:\!)}\, \boldsymbol{\Psi}(\vec{\Theta}) \;:\; \begin{cases} \Psi_x \\ \Psi_y \\ \Psi_\zeta - i\dfrac{\sqrt{\beta_{\zeta_0}}}{\beta_{r_0}} V_{\mathrm{N}} \left[\displaystyle\sum_{n=0}^{\infty} \frac{(-1)^n}{n!} \sin\Big(\phi_{\mathrm{RF}} + \frac{n\pi}{2}\Big) \left(\frac{k_{\mathrm{RF}}}{\beta_{r_0}} Z\right)^n\right] \end{cases}, \tag{3.61}$$

which can be computed from our simple algebraic rules. For sufficiently small ζ, this transformation is approximately linear and provides longitudinal focusing, in close analogy to the effect of thin quadrupoles in the transverse plane.

Drift

The last — and most complex — element to study is the drift space, which models the field-free transport between magnets. As discussed in Chapter 1, any longitudinal progress along the beam line (in s) shall be done using drifts. In this framework, it is the only fundamental element which is required to be thick. For that reason, drifts are the source of many complications, including chromatic effects. To clarify: various effects arise when particles travel longitudinally along the beam line, and the burden of this progression is carried out by drifts and drifts only. The local Hamiltonian H_d for a drift is defined as:

$$H_d \equiv p_\zeta - \delta_\mathrm{p} + \frac{p_x^2 + p_y^2}{2(1+\delta_\mathrm{p})} \ , \tag{3.62}$$

with $(1+\delta_\mathrm{p}) = \sqrt{1 + 2p_\zeta + \beta_{r_0}^2 p_\zeta^2}$. Using the differential form of the Poisson bracket (eq. (3.3)), one can show that the corresponding Lie transformation over a length Δs yields:

$$e^{(:-H_d \Delta s:)}\,\boldsymbol{\psi} \ : \ \begin{cases} \psi_x + \dfrac{\Delta s}{\sqrt{\beta_{x_0}}} \dfrac{p_x}{(1+\delta_\mathrm{p})} \\ \psi_y + \dfrac{\Delta s}{\sqrt{\beta_{y_0}}} \dfrac{p_y}{(1+\delta_\mathrm{p})} \\ \psi_\zeta + \dfrac{\Delta s}{\sqrt{\beta_{\zeta_0}}} \left(1 - \dfrac{1+\beta_{r_0}^2 p_\zeta}{(1+\delta_\mathrm{p})} \left(1 + \dfrac{p_x^2+p_y^2}{2(1+\delta_\mathrm{p})^2}\right)\right) \end{cases} , \tag{3.63}$$

for a given particle $\boldsymbol{\psi}$. Once again, we make use of the chromatic term (eq. (3.56)) to write the transformation for loops and tori as:

$$e^{(:-H_d \Delta s:)}\,\boldsymbol{\Psi}(\vec{\Theta}) \ : \ \begin{cases} \Psi_x + \dfrac{\Delta s}{\sqrt{\beta_{x_0}}} P_x \cdot \mathcal{C}_\zeta \\ \Psi_y + \dfrac{\Delta s}{\sqrt{\beta_{y_0}}} P_y \cdot \mathcal{C}_\zeta \\ \Psi_\zeta + \dfrac{\Delta s}{\sqrt{\beta_{\zeta_0}}} \left[1 - \mathcal{C}_\zeta (1+\beta_{r_0}^2 P_\zeta) \left(1 + \dfrac{1}{2}\mathcal{C}_\zeta^2 (P_x^2 + P_y^2)\right)\right] \end{cases} , \tag{3.64}$$

which can be computed using the algebraic rules presented. This important result highlights the complex nature of beam transport in a single equation. Simple drift regions introduce non-linearities (due to $\mathcal{C}_\zeta$, P_x^2 and P_y^2) and couple the longitudinal planes with the transverse one. By restricting ourselves to the study of on-momentum particles, *i.e.* by setting $P_\zeta = 0 \Rightarrow \mathcal{C}_\zeta = 1$, the drift simplifies to:

$$e^{(:-H_d \Delta s:)}\,\boldsymbol{\Psi}(\vec{\Theta}) \ : \ \begin{cases} \Psi_x + \dfrac{\Delta s}{\sqrt{\beta_{x_0}}} P_x \\ \Psi_y + \dfrac{\Delta s}{\sqrt{\beta_{y_0}}} P_y \\ \Psi_\zeta - \dfrac{\Delta s}{\sqrt{\beta_{\zeta_0}}} \left(\dfrac{P_x^2 + P_y^2}{2}\right) \end{cases} , \quad \text{if } P_\zeta = 0 \text{ (on-momentum).} \tag{3.65}$$

which is still non-linear. It should be noted that in most situations (where, *e.g.*, $p_\zeta \sim 10^{-4}$), eq. (3.65) is a good approximation of the transformation. In such a case, the transverse

planes are decoupled from the longitudinal one (the so-called synchrobetatron coupling), which greatly simplifies the problem. That being said, in the general case synchrobetatron coupling is unavoidable in 6D. This is the reason for the emergence of *synchrotron sidebands* in the Fourier spectrum of particles motion, as discussed in the next section.

3.3 Numerical Methods & Models

Let us consider a simple thought experiment to illustrate the insightful perspective that can be gained from the formalism (and the transformations) introduced in this chapter. Imagine a stable particle evolving in a periodic beam line with non-zeros actions $\vec{I} = (I_x, I_y, I_\zeta)$ and fundamental frequencies $\vec{Q} = (Q_x, Q_y, Q_\zeta)$. Let us further assume that, by some feat of beam optics, the energy manifold of the particle at the location s_0 is purely circular, meaning that the corresponding KAM torus $\boldsymbol{\Psi}_0(\vec{\Theta})$ and the turn-by-turn motion $\boldsymbol{\psi}_0(N)$ at that location read:

$$\boldsymbol{\Psi}_0(\vec{\Theta}) \;:\; \begin{cases} \Psi_x = \sqrt{2I_x}\, e^{i\Theta_x} \\ \Psi_y = \sqrt{2I_y}\, e^{i\Theta_y} \\ \Psi_\zeta = \sqrt{2I_\zeta}\, e^{i\Theta_\zeta} \end{cases} \quad \text{and} \quad \boldsymbol{\psi}_0(N) \;:\; \begin{cases} \psi_x = \sqrt{2I_x}\, e^{i[2\pi Q_x]N} \\ \psi_y = \sqrt{2I_y}\, e^{i[2\pi Q_y]N} \\ \psi_\zeta = \sqrt{2I_\zeta}\, e^{i[2\pi Q_\zeta]N} \end{cases} . \tag{3.66}$$

If we wish to study the motion at a further location s_1, separated from s_0 by a drift of length $\Delta s = s_1 - s_0$, one would need to record the tracking at s_1 for every turn to get $\boldsymbol{\psi}_1(N)$. From there, the energy manifold $\boldsymbol{\Psi}_1(\vec{\Theta})$ could be constructed numerically using the methods presented in Chapter 2. That being said, the transformations presented in the present chapter give us an alternative way, which is to directly transform the torus via $\boldsymbol{\Psi}_1 = e^{(:-H_d \Delta s:)}\, \boldsymbol{\Psi}_0$. Taking the horizontal projection as an example, one would expect to find (from eq. (3.64)):

$$\begin{aligned} \Psi_{1,x}(\vec{\Theta}) &= \Psi_{0,x} + \frac{\Delta s}{\sqrt{\beta_{x_0}}}\, P_{0,x} \cdot \mathcal{C}_{0,\zeta} \\ &= \sqrt{2I_x}\, e^{i\Theta_x} + i\frac{\Delta s}{2\beta_{x_0}} \sqrt{2I_x} \left(e^{i\Theta_x} - e^{-i\Theta_x}\right) \times \left[1 + \sum_{k=1}^{\infty} c_k \left(\sqrt{2I_\zeta} \left(e^{i\Theta_\zeta} - e^{-i\Theta_\zeta}\right)\right)^k\right] \end{aligned} \tag{3.67}$$

where $P_x(\vec{\Theta}) = \frac{i}{2}(\Psi_x - \Psi_x^*)/\sqrt{\beta_{x_0}}$ was used and where $c_k = (-1)^k \left[\mathcal{G}_k^{(1/2)}\,(1/\beta_{r_0})\right] \left(i\beta_{r_0}/(2\sqrt{\beta_{\zeta_0}})\right)^k$ are coefficients extracted from eq. (3.56). An example of this transformation is shown in Fig. 3.2. The above result informs us that the energy manifold — and therefore the Fourier spectrum of the particle — should contain contributions from an infinite number of synchrotron sidebands with frequencies $\nu = \pm Q_x \pm kQ_\zeta$ with $k \in \{1, 2, 3, \dots\}$. To put this claim to the test, one can compare the particle's tracking data (from XSUITE) with the stroboscopic sampling of the transformed KAM torus according to Proposition 2.2. The result is shown in Fig. 3.3, where the Fourier spectrum $\mathcal{F}(\psi_x)$ of the tracked particle is compared to the Fourier spectrum $\mathcal{F}(\Psi_x)$ of the torus before and after the transformation of eq. (3.67). The transformation is shown for two truncation numbers ($\mathcal{O}[(P_\zeta)^5]$ and $\mathcal{O}[(P_\zeta)^{20}]$) of the P_ζ series (see Demonstration 3.3 for details on the proper symplectic truncation).

What should be apparent, from Fig. 3.3, is that the transformations presented in this chapter provide a complete account of the evolution of the spectral content through the Hamiltonian flow of a generic system (with $\mathcal{O}[(P_\zeta)^\infty]$). More than the numerical results, we should emphasize the insight provided by this approach. Based on the above example, one should not be surprised

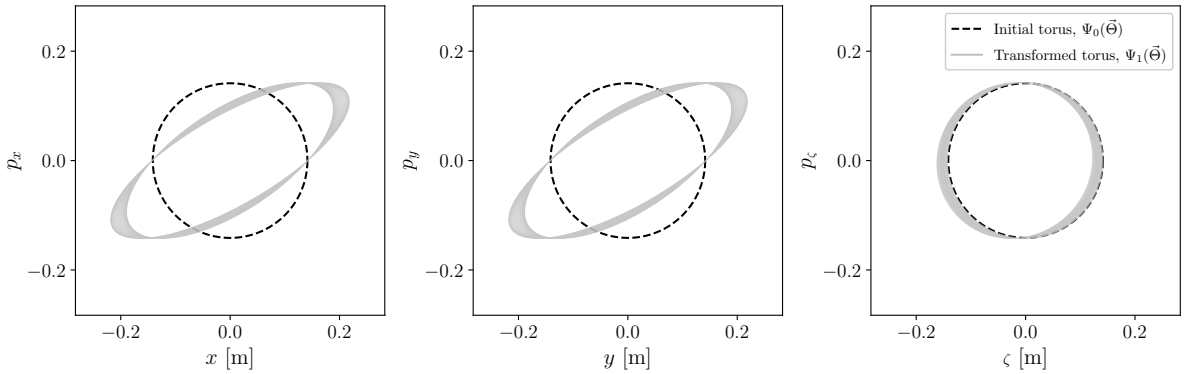

Figure 3.2: Shadow of the transformed torus $\mathbf{\Psi}_1(\vec{\Theta})$ following a simple drift. In the numerical example considered, $\vec{I} = (1, 1, 1) \times 10^{-2}$ m, $\vec{Q} = (0.353, 0.289, 0.002)$ and $\beta_{r_0} = 0.99999$. In realistic machines, $\vec{I}$ is typically in the order of µm or nm such that the transformation is approximately linear and the deformations are less visible.

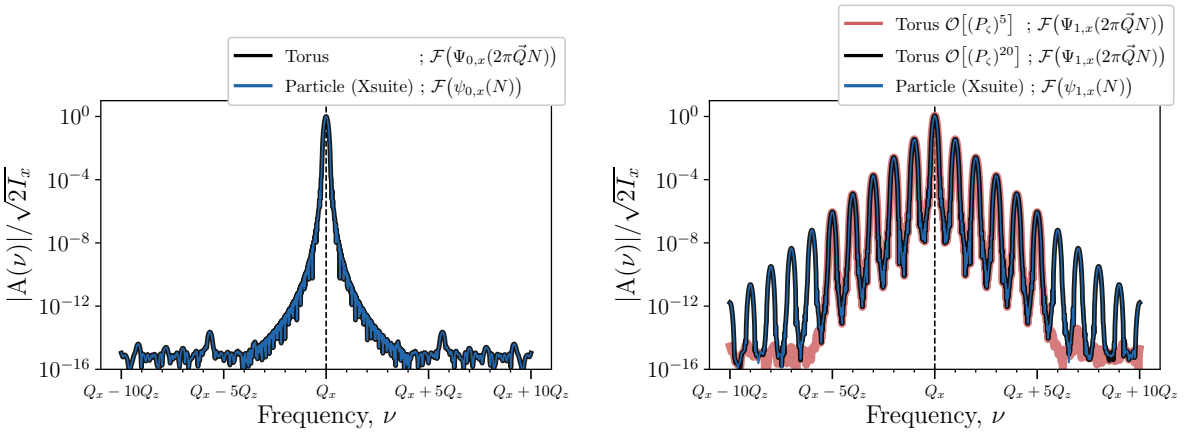

(a) (b)

Figure 3.3: Comparison of the horizontal Fourier spectrum of a tracked particle $\mathcal{F}(\psi_x(N))$ with the Fourier spectrum of the corresponding torus $\mathcal{F}(\Psi_x(2\pi\vec{Q}N))$. (a) Before the drift, at s_0. (b) After the drift, at s_1. With eq. (3.67), the torus is transported from s_0 to s_1 using two truncation numbers ($\mathcal{O}[(P_\zeta)^5]$ and $\mathcal{O}[(P_\zeta)^{20}]$ of the $\mathcal{C}_\zeta$ series in P_ζ) and the result is compared with tracking data. One can see that the number of terms in the expansion controls the number of sidebands observed. Ultimately (for $\mathcal{O}[(P_\zeta)^\infty]$), a complete account of the synchrotron sidebands is obtained.

to see synchrotron sidebands appear when simple tracking experiments are extended from 4D to 6D, since any drift element introduces an infinite number of sidebands. As such, any periodic solution — in 6D — shall also contain an infinite number of spectral lines, as observed in generic tracking experiments. This also explains why the task of finding closed-form expression for the periodic solutions of a periodic system is a complicated one, as discussed in later chapters.

Demonstration 3.3: Symplectic truncation.

The transformations introduced above are exact, closed-form maps of the Hamiltonian flow. For single–particle motion they reduce to simple analytic functions, identical to those used in tracking codes (such as XSUITE). For loops, tori, and more general Fourier-series, applying these maps generates a rich — and typically infinite — spectrum (e.g., through the chromatic factor $\mathcal{C}_\zeta$). In the numerical implementation of such transformations, one is naturally required to truncate the expansion. Following seminal work on the topic [9] the truncation needs to be done on the Hamiltonian itself — before computing the Lie transformation — to ensure that the result is symplectic.

Let us revisit the drift element to highlight this point. Since the nested Poisson bracket in the exponentiation cancel out in this specific case (*i.e.* $(\!: -H\,\Delta s :\!)^2 \mathbf{\Psi} = 0$), the transformation can be written as:

$$e^{(\!:-H_d \Delta s:\!)}\ \mathbf{\Psi}(\vec{\Theta})\ :\ \begin{cases} \Psi_x + \dfrac{\Delta s}{\sqrt{\beta_{x_0}}}\dfrac{\partial H}{\partial p_x} = \Psi_x + \dfrac{\Delta s}{\sqrt{\beta_{x_0}}}\,P_x \cdot \mathcal{C}_\zeta \\ \Psi_y + \dfrac{\Delta s}{\sqrt{\beta_{y_0}}}\dfrac{\partial H}{\partial p_y} = \Psi_y + \dfrac{\Delta s}{\sqrt{\beta_{y_0}}}\,P_y \cdot \mathcal{C}_\zeta \\ \Psi_\zeta + \dfrac{\Delta s}{\sqrt{\beta_{\zeta_0}}}\dfrac{\partial H}{\partial p_\zeta} = \Psi_\zeta + \dfrac{\Delta s}{\sqrt{\beta_{\zeta_0}}}\left[1 - \dfrac{\partial \mathcal{C}_\zeta^{-1}}{\partial P_\zeta} + \dfrac{\partial \mathcal{C}_\zeta}{\partial P_\zeta}\left(\dfrac{P_x^2 + P_y^2}{2}\right)\right] \end{cases}, \tag{3.68}$$

which is identical to eq. (3.64). Indeed, based on eq. (3.56) and eq. (3.57), one can show that the derivatives of the chromatic term $\mathcal{C}_\zeta$ and its inverse $\mathcal{C}_\zeta^{-1}$ yield:

$$\frac{\partial\, \mathcal{C}_\zeta}{\partial P_\zeta} = -(1 + \beta_{r_0}^2 P_\zeta)\, \mathcal{C}_\zeta^3 \quad \text{and} \quad \frac{\partial\, \mathcal{C}_\zeta^{-1}}{\partial P_\zeta} = (1 + \beta_{r_0}^2 P_\zeta)\, \mathcal{C}_\zeta\ , \tag{3.69}$$

which can be used to study the effect of a truncation of $\mathcal{C}_\zeta$ to order N, denoted with $T_N[\mathcal{C}_\zeta]$. Following the truncated power-series algebra (TPSA) approach, truncation can be propagated through derivatives [37, 38]: *i.e.* if $\partial \mathcal{C}_\zeta / \partial P_\zeta = f(\mathcal{C}_\zeta)$, then $\partial(T_N[\mathcal{C}_\zeta])/\partial P_\zeta = T_{N-1}[f(\mathcal{C}_\zeta)]$. In other words, the identities of eq. (3.69) can be used in eq. (3.68) before truncating the result to order $N-1$ to obtain an accurate — and symplectic — transformation of the drift to order N in P_ζ. Although this caveat makes the computation more cumbersome, it is required in numerical codes to ensure the symplecticity of the transformation. For analytic descriptions, the closed-form expressions presented in the previous section should be preferred.

3.3.1 Splitting Methods

Let us revisit Fig. 3.1 and clarify the idea of *correspondence* between a physical element and its model. For a thick magnet, the starting point is the local Hamiltonian of eq. (3.2), written as:

$$H_{TM} = p_\varsigma - \delta_\mathrm{p} + \frac{p_x^2 + p_y^2}{2(1+\delta_\mathrm{p})} + \mathrm{Re}\left[\sum_{n=0}^{\infty} \frac{(k_n^+ + ik_n^\times)}{(n+1)!}(x+iy)^{n+1}\right] \equiv H_d + H_M \ . \tag{3.70}$$

Although the associated map can in principle be written as $e^{(:-H_{TM}\Delta s:)}$, it typically admits no closed-form solution suitable for direct implementation. Our goal is therefore to construct a composition of *exact* (closed-form) symplectic maps from the set of fundamental operators introduced earlier, so that the resulting model achieves an optimal *correspondence* with the physical element [4, 39, 40]. This can be done using the Zassenhaus formula (a counterpart to the BCH formula, eq. (3.13)):

$$e^{(:\epsilon(g_1+g_2):)} = e^{(:\epsilon g_1:)}\, e^{(:\epsilon g_2:)}\, e^{(:-\frac{\epsilon^2}{2}[g_1,g_2]:)}\, e^{(:\frac{\epsilon^3}{6}(2[g_2,[g_1,g_2]]+[g_1,[g_1,g_2]]):)} \cdots \ , \tag{3.71}$$

which shows how nested commutators arise in any factorization of $e^{(:\epsilon(g_1+g_2):)}$, with ϵ as a dimensionless error parameter. One can then look for *symmetric* factorizations that systematically cancel the error terms — and improve the correspondence — order-by-order in ϵ. For separable Hamiltonians $H_{TM} = H_d + H_M$, standard symmetric splittings are:

$$H_{TM} = H_d + H_M = \frac{1}{2}H_d + H_M + \frac{1}{2}H_d \tag{3.72}$$

$$H_{TM} = H_d + H_M = c_1 H_d + c_2 H_M + c_3 H_d + c_4 H_M + c_3 H_d + c_2 H_M + c_1 H_d \tag{3.73}$$

with $c_1 = \frac{1}{12}(4 + 2\sqrt[3]{2} + \sqrt[3]{4})$; $c_2 = 2c_1$; $c_3 = \frac{1}{2} - c_1$; $c_4 = 1 - 4c_1$. Using repeated applications of eq. (3.71) to separate each term, one can show [4] that the resulting maps yield, respectively, 2nd and 4th order integrators (or models) following:

$$e^{(:\epsilon H_{TM}:)} = e^{\left(:\frac{\epsilon}{2}H_d:\right)} e^{(:\epsilon H_M:)} e^{\left(:\frac{\epsilon}{2}H_d:\right)} + \mathcal{O}(\epsilon^3) \tag{3.74}$$

$$e^{(:\epsilon H_{TM}:)} = e^{(:c_1\epsilon H_d:)} e^{(:c_2\epsilon H_M:)} e^{(:c_3\epsilon H_d:)} e^{(:c_4\epsilon H_M:)} e^{(:c_3\epsilon H_d:)} e^{(:c_2\epsilon H_M:)} e^{(:c_1\epsilon H_d:)} + \mathcal{O}(\epsilon^5) \tag{3.75}$$

where the usual generators of the Hamiltonian flow can be obtained by letting $\epsilon \to -\Delta s$. The reader should be aware that the coefficient $c_3 \approx -0.1756$ is negative, such that some steps correspond to negative drifts. This is a known feature of even-order symmetric compositions (beyond 2nd order) where some steps need to be taken backward (while maintaining the actual length of the element, *i.e.* $2c_1 + 2c_3 = 1$). Although not intuitively obvious, this approach does provide a better description of the physical element [4], improving the correspondence with its model.

The important conclusion is that optimizing the accelerator *model* (the composition and number of slices from a given splitting method) can be separated from studying the *fundamental operators* of beam transport. In fact, eq. (3.75) illustrates how the correspondence can in principle be made arbitrarily close — following, *e.g.*, the TEAPOT approach [9] — by increasing the splitting number or by adopting higher-order symmetric factorization. That being said, the resulting map remains a product of the same fundamental operators introduced earlier. Consequently, the analytic tools developed in this chapter, as well as the insight provided by the formalism introduced, can be directly used to interpret the tracking results from the global maps.

Summary: Transformation of common elements.

Drift, eq. (3.64):

$$e^{(:-H_d\,\Delta s:)}\,\boldsymbol{\Psi}(\vec{\Theta}) \;:\; \begin{cases} \Psi_x + \dfrac{\Delta s}{\sqrt{\beta_{x_0}}}\,P_x\cdot\mathcal{C}_\zeta \\ \Psi_y + \dfrac{\Delta s}{\sqrt{\beta_{y_0}}}\,P_y\cdot\mathcal{C}_\zeta \\ \Psi_\zeta + \dfrac{\Delta s}{\sqrt{\beta_{\zeta_0}}}\left[1-\mathcal{C}_\zeta(1+\beta_{r_0}^2P_\zeta)\left(1+\dfrac{1}{2}\mathcal{C}_\zeta^2(P_x^2+P_y^2)\right)\right] \end{cases}$$

with eq. (3.56) and eq. (3.57):

$$\mathcal{C}_\zeta^{\pm1} \equiv (1+2P_\zeta+\beta_{r_0}^2P_\zeta^2)^{\mp1/2} = 1+\sum_{k=1}^{\infty}(-1)^k\left[\mathcal{G}_k^{(\pm1/2)}\left(\tfrac{1}{\beta_{r_0}}\right)\right](\beta_{r_0}P_\zeta)^k$$

Thin dipole, eq. (3.58):

$$e^{(:-H_b\,ds:)}\,\boldsymbol{\Psi}(\vec{\Theta}) \;:\; \begin{cases} \Psi_x + i\sqrt{\beta_{x_0}}\Big(K_0^+(1+hX) - h\,\mathcal{C}_\zeta^{-1}\Big) \\ \Psi_y \\ \Psi_\zeta - \dfrac{1}{\sqrt{\beta_{\zeta_0}}}\mathcal{C}_\zeta(1+\beta_{r_0}^2P_\zeta)hX \end{cases}$$

Thin quadrupole, eq. (3.47):

$$e^{(:-H_q\,ds:)}\,\boldsymbol{\Psi}(\vec{\Theta}) \;:\; \begin{cases} \Psi_x + i\sqrt{\beta_{x_0}}\,(K_1^+X - K_1^\times Y) \\ \Psi_y - i\sqrt{\beta_{y_0}}\,(K_1^+Y + K_1^\times X) \\ \Psi_\zeta \end{cases}$$

Thin multipole, eq. (3.53), using $\mathcal{K}(x,y) = \sum_{n=0}\frac{1}{n!}(K_n^+ + iK_n^\times)(x+iy)^n$:

$$e^{(:-H_M\,ds:)}\,\boldsymbol{\Psi}(\vec{\Theta}) \;:\; \begin{cases} \Psi_x + i\sqrt{\beta_{x_0}}\mathrm{Re}\{\mathcal{K}\}(X,Y) \\ \Psi_y - i\sqrt{\beta_{y_0}}\mathrm{Im}\{\mathcal{K}\}(X,Y) \\ \Psi_\zeta \end{cases}$$

Thin RF cavity, eq. (3.61):

$$e^{(:-H_{\mathrm{RF}}\,ds:)}\,\boldsymbol{\Psi}(\vec{\Theta}) \;:\; \begin{cases} \Psi_x \\ \Psi_y \\ \Psi_\zeta - i\dfrac{\sqrt{\beta_{\zeta_0}}}{\beta_{r_0}}V_{\mathrm{N}}\left[\displaystyle\sum_{n=0}^{\infty}\frac{(-1)^n}{n!}\sin\!\left(\phi_{\mathrm{RF}}+\frac{n\pi}{2}\right)\left(\frac{k_{\mathrm{RF}}}{\beta_{r_0}}Z\right)^n\right] \end{cases}$$

CHAPTER 4

Topological Formulation of Linear Beam Dynamics

The description of coupled motion remains an important conceptual challenge in beam dynamics. While the Courant-Snyder formalism provides an elegant framework for uncoupled systems, its extension to fully coupled 6D dynamics has historically required awkward retrofitting. Building on the Lie algebra tools developed in Chapter 3, this chapter presents a topological approach to linear beam dynamics in which we look for an eigensolution to the transport problem, characterized by a set of optical functions that encode the shape of the tori in each plane, including coupling effects.

Beginning with uncoupled beam lines, we show that any symplectic linear transformation preserves elliptical topologies. This analysis is then extended to transversely coupled systems, and finally to fully coupled 6D motion including the longitudinal plane. For periodic systems, eigensolutions are obtained by solving a simple dephasing condition, from which the fundamental frequencies emerge naturally. A normalization procedure is also introduced to map the physical phase space to the Courant-Snyder phase space, where elliptical eigensolutions become circles. The connection between the optical functions introduced and the traditional Courant-Snyder parameters is made explicit at the end of the chapter.

4.1 The Courant-Snyder Picture

To open this chapter, let us review an illuminating piece of work by A. Chao (one of the most eminent accelerator physicists), titled: "SLIM – A Formalism for Linear Coupled Systems" [10, 30]. Without diminishing the importance of the work of Courant and Snyder [32], Chao presents some of its limitations. Indeed, in the Courant-Snyder tradition we have been doing Accelerator Physics in three steps: find the transport matrices, compute some auxiliary lattice functions ($\alpha_x(s)$, $\beta_x(s)$, $\gamma_x(s)$, etc.) and finally compute the beam's physical properties (beam size, tunes, etc.). In his paper, A. Chao demonstrates that the auxiliary functions themselves do not possess direct physical meanings and are, in fact, "artifacts". Moreover, he argues that the Courant-Snyder picture fails to describe coupled motion in a natural way and often demands some "awkward retrofitting" which ultimately leads to a confused and incomplete picture (in other words: equivocations). Despite recognizing the importance of the Courant-Snyder tradition, A. Chao therefore ventures to build a more general formalism for linear beam dynamics. "Admittedly, one price to pay is that we will lose the elegance of the Courant-Snyder representation, but the other advantages may prove worthwhile" [A. Chao, 30].

Although the approach taken in this thesis is yet a different one, A. Chao's words resonate strongly throughout this chapter. For additional context on the Courant-Snyder tradition, the reader is referred to the textbook by A. Wolski [4, Chap. 3-4]. We shall shortly introduce the *optical* functions $\lambda^{\pm}_{jk}$, which describe the topological signature (the shape) of arbitrary 6D ellipsoids. The reader should keep in mind that those unitless numbers are strongly linked to the usual optical functions $\alpha_x(s)$, $\beta_x(s)$, $\gamma_x(s)$ of the Courant-Snyder theory and share similar conceptual foundations. At the end of the chapter, the bridge between the two formalisms will be given explicitly. After all, the Courant-Snyder parameters are now an integral part of Accelerator Physics; and forever part of the spoken language of accelerator physicists.

4.2 Transverse Motion in Uncoupled Linear Beam Lines

Usual treatments of linear beam dynamics begin by assuming a purely 2D mathematical framework made of 2×2 transfer matrices. In an effort to build towards a complete 6D description of beam dynamics, we shall avoid this simplification and, instead, work directly with the 6D transformations presented in Chapter 3. In order to reach similar grounds however, we make the explicit assumption that only on-momentum particles are considered, such that $p_\zeta = 0$ and $\delta_\mathrm{p} = 0$. Moreover, we restrict ourselves — as a first step — to the study of beam lines made of drifts, dipoles and normal quadrupoles. Under those assumptions, the transformations of Chapter 3 lead to uncoupled motion in the two transverse planes, as shown in Table. 4.1.

Table 4.1: Horizontal Lie transformations for on-momentum ($P_\zeta = 0$) tori.

Element	**Lie transformation (Horizontal plane)**
Drift space	$e^{(\!:\!-H_d\,\Delta s\!:\!)}\,\Psi_x = \Psi_x + \frac{\Delta s}{\sqrt{\beta_{x_0}}}\,P_x$
Thin dipole	$e^{(\!:\!-H_b\,ds\!:\!)}\,\Psi_x = \Psi_x + i\sqrt{\beta_{x_0}}(K_0^+(1+hX) - h)$
Thin (normal) quadrupole	$e^{(\!:\!-H_q^+\,ds\!:\!)}\,\Psi_x = \Psi_x + i\sqrt{\beta_{x_0}}\,K_1^+ X$

Proposition 4.1: Uncoupled linear transformation.

Using the usual identities $X = \frac{1}{2}(\Psi_x + \Psi_x^*)\sqrt{\beta_{x_0}}$ and $P_x = \frac{i}{2}(\Psi_x - \Psi_x^*)/\sqrt{\beta_{x_0}}$, one can see that any combinations of the uncoupled linear transformations of Table 4.1 can be reduced to an uncoupled linear function of Ψ_x, written as:

$$\mathcal{M}\Psi_x = u\,\Psi_x + v\,\Psi_x^* \;, \quad \text{with } \{u, v\} \in \mathbb{C} \;. \tag{4.1}$$

The transformation is symplectic if $|u|^2 - |v|^2 = 1$, as shown in Demonstration 4.1.

To study this generic system in details, let us first look at its effect on a simple ellipse $\Psi_{\mathcal{O}} = A_1 e^{i\Theta_x} + A_{\text{-}1} e^{-i\Theta_x}$ following:

$$\mathcal{M}\,\Psi_{\mathcal{O}} = (uA_1 + vA_{\text{-}1}^*)\,e^{i\Theta_x} + (uA_{\text{-}1} + vA_1^*)\,e^{-i\Theta_x} \;, \tag{4.2}$$

which yields another ellipse with some new coefficients (extracted from $\langle \pm 1 \,|\, \mathcal{M}\,\Psi_{\mathcal{O}} \rangle$). We therefore conclude that a linear transformation like eq. (4.1) transforms an ellipse into a new ellipse; and preserves its topological nature. More generally, a linear transformation preserves the spectral content of the loop — or torus (equivalent here) — on which it is applied: if $A_{\pm n}\, e^{\pm in\Theta_x}$ is present in Ψ_x before the transformation, it will remain in $\mathcal{M}\,\Psi_x$ after the transformation and no new contribution can emerge.

This observation suggests the existence of a special loop, an eigensolution, which maps onto itself after the transformation. To prove this point, we must demonstrate that this eigensolution can be found, readily, from the transformation itself. This will be done shortly, after looking at the simple example of FODO lattices.

Demonstration 4.1: Symplectic condition and matrix form.

Let us consider the general uncoupled linear transformation of eq. (4.1). Based on Demonstration 3.1, the transformation is symplectic if, and only if:

$$[\mathcal{M}\Psi_x,\ (\mathcal{M}\Psi_x)^*] = [u\,\Psi_x + v\Psi_x^*, u^*\,\Psi_x^* + v^*\,\Psi_x] = (|u|^2 - |v|^2)[\Psi_x, \Psi_x^*] = 2i \;, \tag{4.3}$$

which is respected if $|u|^2 - |v|^2 = 1$. In matrix form, the transformation can be applied on the phase space coordinates (x, p_x) following:

$$\begin{pmatrix} x \\ p_x \end{pmatrix}_{s_2} = \begin{pmatrix} \mathrm{Re}(u+v) & \beta_{x_0}\,\mathrm{Im}(u-v) \\ -\,\mathrm{Im}(u+v)/\beta_{x_0} & \mathrm{Re}(u-v) \end{pmatrix} \begin{pmatrix} x \\ p_x \end{pmatrix}_{s_1} \tag{4.4}$$

Conversely, the map parameters $\{u, v\}$ can be obtained from a generic 2×2 matrix following:

$$\begin{pmatrix} a & b \\ c & d \end{pmatrix} \quad \mapsto \quad \begin{aligned} u &= \frac{1}{2}\left[(a+d) + i(b/\beta_{x_0} - c\,\beta_{x_0})\right] \\ v &= \frac{1}{2}\left[(a-d) - i(b/\beta_{x_0} + c\,\beta_{x_0})\right] \end{aligned} \tag{4.5}$$

Example: FODO Lattice

As a seminal example of linear systems, consider a beam line made of equally spaced quadrupoles of alternating focusing ($k_1^+ = +k$) and defocusing ($k_1^+ = -k$) strengths. This arrangement is known as a FODO cell (Focusing, Drift, Defocusing, Drift) and is commonly used in the design of stable beam lines. Importantly, it can be used to construct a periodic FODO lattice where the unit cell is repeated indefinitely. Assuming drifts of length L, illustrated in Fig. 4.1, the transfer map $\mathcal{M}_{\mathcal{O}}$ through a single FODO cell can be expressed as:

$$\mathcal{M}_{\mathcal{O}} = \left(e^{(:-H_d\, L:)} \circ e^{(:+H_q\, ds:)} \circ e^{(:-H_d\, L:)} \circ e^{(:-H_q\, ds:)} \right) \ . \tag{4.6}$$

Applying the transformations from Table 4.1, the final map can be composed, element-by-element, and ultimately written in closed-form following:

$$\begin{aligned} \mathcal{M}_{\mathcal{O}} \Psi_x = \quad & \left(\left[1 - \frac{1}{2} L^2 K^2 \right] + i \frac{L}{2\beta_0} \left[2 + LK + \beta_0^2 K^2 \right] \right) \Psi_x \\ & - \left(\left[LK + \frac{1}{2} L^2 K^2 \right] + i \frac{L}{2\beta_0} \left[2 + LK - \beta_0^2 K^2 \right] \right) \Psi_x^* \ . \end{aligned} \tag{4.7}$$

In general — for "hopelessly complex" periodic systems — it is not possible to find an expression for the complete transformation. This simple exercise is shown here as an example, to familiarize the reader with linear transformations.

As shown in Fig. 4.1, it is well-known that particles in FODO cells are confined to evolve on ellipses. Moving forward in s, these ellipses are sheared and deformed but ultimately go back to their original shape at the end of the FODO cell. This *topological* periodicity follows the periodicity of the lattice, unlike the single-particle trajectory which is never exactly closed — and is in fact quasiperiodic. In action angle variables, the progress along the lattice is given by the phase advance, $\mu_x(s)$, which also describes the progress on the energy manifold itself.

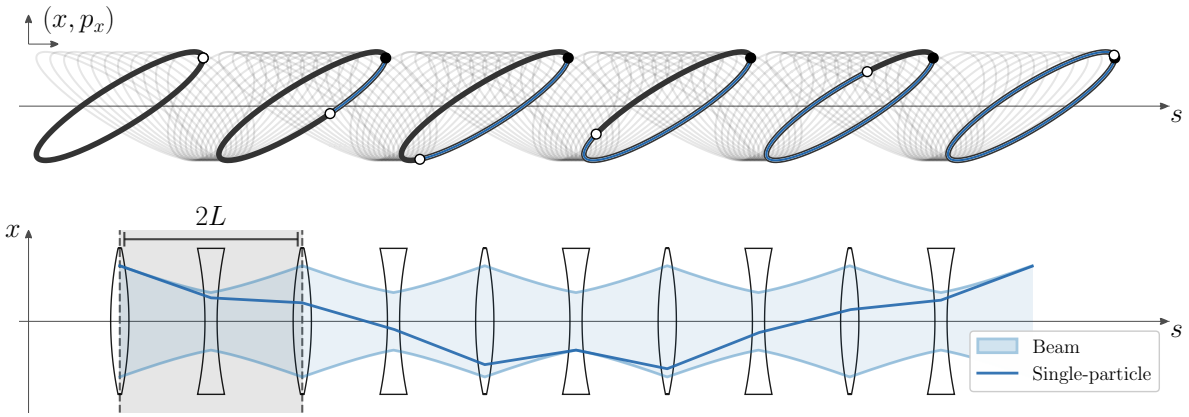

Figure 4.1: Periodic transport of ellipses in an uncoupled FODO lattice. The unit cell is shown at the bottom, together with the beam size and an example of single-particle trajectory. The phase advance, $\mu_x(s)$, increases with s and is responsible for the motion on the ellipse. One can see that the single-particle trajectory is not periodic ($Q_x = \Delta\mu_x = 0.1959$ through the unit cell) whereas the transport of the ellipse is.

4.2.1 Eigensolutions for Uncoupled Linear Periodic Systems

Let us now impose a periodic condition on our system, as discussed in Section 2.2. We would like to find, if it exists, the expression of a closed loop which maps back onto itself after one iteration of $\mathcal{M}$. Such a loop shall respect the dephasing condition (illustrated in Fig. 4.2):

$$\mathcal{M}\ \Psi_x(\Theta_x) = \Psi_x(\Theta_x + 2\pi Q_x) \quad \Leftrightarrow \quad \mathcal{M}\left(\sum_n A_n e^{in\Theta_x}\right) = \sum_n \left(A_n e^{in(2\pi Q_x)}\right) e^{in\Theta_x} \tag{4.8}$$

which enforces the fact that every points belonging to the initial loop, Ψ_x, still belong to the same loop after the transformation, albeit moved by some phase advance (or fundamental frequency) Q_x which is yet to be determined. Here, no assumption is made on the loop, except for the fact that it is uncoupled from the other planes, and the general solution is sought. Applying the transformation of eq. (4.1), one can explicitly write for the left-hand side of eq. (4.8):

$$\mathcal{M}\ \Psi_x(\Theta_x) = \cdots + \Big(uA_{-1}\Big)e^{-i\Theta} + \Big(uA_1\Big)e^{i\Theta} + \cdots + \Big(vA^*_{-1}\Big)e^{i\Theta} + \Big(vA^*_1\Big)e^{-i\Theta} + \dots\ , \tag{4.9}$$

And for the right-hand side:

$$\Psi_x(\Theta_x + 2\pi Q_x) = \cdots + \Big(A_{-1}e^{-i(2\pi Q_x)}\Big)e^{-i\Theta} + \Big(A_1 e^{i(2\pi Q_x)}\Big)e^{i\Theta} + \dots \tag{4.10}$$

In order for the equality to be satisfied, one can group the terms in pairs of $A_{\pm n}$ and write the problem in matrix form following:

$$\begin{pmatrix} A_n \\ A^*_{-n} \end{pmatrix} e^{\pm in(2\pi Q_x)} = \begin{pmatrix} u & v \\ v^* & u^* \end{pmatrix} \begin{pmatrix} A_n \\ A^*_{-n} \end{pmatrix} \tag{4.11}$$

which is a typical eigenvalue problem, with eigenvalues $e^{\pm in(2\pi Q_x)}$, for any given n. However, the characteristic matrix of eq. (4.11) is unique and, importantly, independent of n. Unless the phase advance satisfies a resonance condition (generally avoided, by design, for linear systems), only one n with $e^{\pm in(2\pi Q_x)}$ can be associated to the eigenvalues of the characteristic matrix.

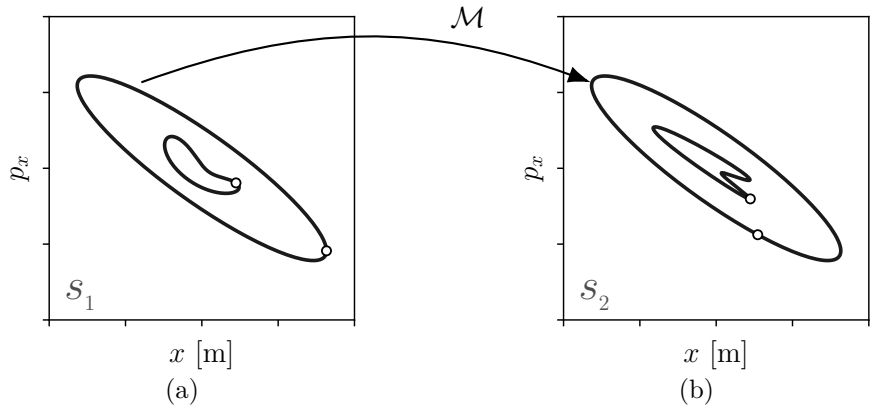

Figure 4.2: Transformation of two closed loop under the linear map $\mathcal{M}$. (a) Before the transformation, at s_1. (b) After the transformation, at s_2. The smaller loop, made of three phasors, is not periodic under the transformation of $\mathcal{M}$. The bigger loop however (the ellipse) is an eigensolution of $\mathcal{M}$ and is periodic under the transformation.

Without loss of generality, we enforce that the fundamental mode $n \pm 1$ shall survive. From there, the eigenvalues of the characteristic matrix give us the fundamental frequency Q_x following:

$$e^{\pm i(2\pi Q_x)} = \mathrm{Re}(u) \pm \sqrt{\mathrm{Re}(u)^2 - 1} \quad \Rightarrow \quad \cos(2\pi Q_x) = \mathrm{Re}(u) \tag{4.12}$$

where the condition $|\,\mathrm{Re}(u)| < 1$ is required to ensure stable bounded motion. Note that this is analog to the usual trace condition of the Courant-Snyder matrix. As a result, none of the other $e^{\pm in(2\pi Q_x)}$ can simultaneously be eigenvalues of the system; and the corresponding eigenvectors must vanish, *i.e.* $A_n = 0 \;\forall\; n \neq \pm 1$. For the fundamental mode $(n \pm 1)$, we are left with:

$$\begin{pmatrix} A_1 \\ A^*_{\text{-}1} \end{pmatrix} = \begin{pmatrix} v/(e^{i(2\pi Q_x)} - u) \\ 1 \end{pmatrix} \,, \tag{4.13}$$

from which we conclude that the loop $\Psi_x(\Theta_x) = A_1\, e^{i\Theta_x} + A_{\text{-}1}\, e^{-i\Theta_x}$, which is an ellipse, is the eigensolution of the transport problem of eq. (4.1). Naturally, the eigenvector (and the eigensolution) can be arbitrarily rescaled. A particularly useful rescaling is one that allows us to factorize the action I_x from the map properties (the *optical* functions, $\lambda_x^{\pm}$) following:

$$\Psi_x(\Theta_x) = \sqrt{2I_x}\left(\lambda_x^+ e^{i\Theta_x} + \lambda_x^- e^{-i\Theta_x}\right) \quad \text{with} \quad \lambda_x^{\pm} = \frac{i\left(u^* + v - e^{\pm i(2\pi Q_x)}\right)}{2\sqrt{\sin(2\pi Q_x)\,\mathrm{Im}(u - v)}} \,, \tag{4.14}$$

where $\lambda_x^{\pm}$ are unitless. Those optical functions solely depend on the machine parameters (similarly to the Courant-Snyder parameters α_x and β_x) and respect the important property $|\lambda_x^+|^2 - |\lambda_x^-|^2 = 1$. Revisiting concepts from Chapter 2, we directly see that this loop (this 1-torus) is integrable with a corresponding Poincaré Integral Invariant:

$$\mathcal{A}_x = \pi\Big(|\,\langle 1\,|\,\Psi_x\,\rangle\,|^2 - |\,\langle -1\,|\,\Psi_x\,\rangle\,|^2\Big) = \pi(2I_x)(|\lambda^+|^2 - |\lambda^-|^2) = 2\pi I_x \,, \tag{4.15}$$

as expected. Furthermore since eq. (4.14) describes the energy manifold of the system, it readily gives the turn-by-turn motion of single-particles $\psi_x(N) = \Psi_x(2\pi Q_x N)$ (through eq. (2.31)) and provides a complete account of the corresponding Fourier spectrum. As shown in Fig. 4.3, contributions with spectral amplitudes $A_{\pm 1} = \sqrt{2I_x}\lambda_x^{\pm}$ are found at the two frequencies $\pm Q_x$.

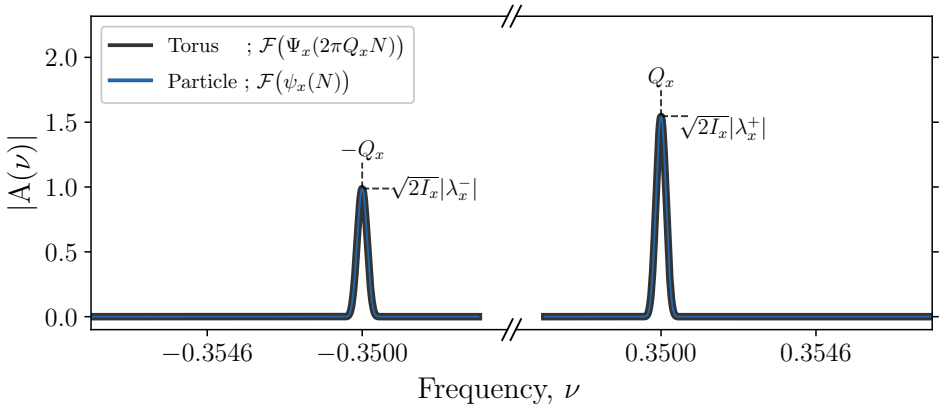

Figure 4.3: Comparison of the Fourier spectrum of particle $\mathcal{F}(\psi_x(N))$ with the corresponding eigensolution torus $\mathcal{F}(\Psi_x(2\pi Q_x N))$ in a linear system with $Q_x = 0.3499$.

4.3 Transverse Motion in Coupled Linear Beam Lines

Let us now consider a slightly different beam line, which includes — as a minimal example — thin quadrupoles with non-zero skew components (see Sec. 3.2.2). Starting from the transformations of p. 57, it is clear that the motion becomes *coupled* between the transverse planes: the transformation of Ψ_x now contains terms proportional to Ψ_y, and vice versa. The relevant transformations for the simplest transversally coupled beam line are summarized in Table 4.2.

Table 4.2: Transverse Lie transformations for on-momentum ($P_\zeta = 0$) tori.

Element	**Lie transformation (Transverse planes)**	
Drift space	$e^{(:-H_d\,\Delta s:)}\,\Psi_x = \Psi_x + \frac{\Delta s}{\sqrt{\beta_{x_0}}}\,P_x$	$e^{(:-H_d\,\Delta s:)}\,\Psi_y = \Psi_y + \frac{\Delta s}{\sqrt{\beta_{y_0}}}\,P_y$
Thin dipole	$e^{(:-H_b\,ds:)}\,\Psi_x = \Psi_x + i\sqrt{\beta_{x_0}}(K_0^+(1+hX) - h)$	$e^{(:-H_b\,ds:)}\,\Psi_y = \Psi_y$
Thin quadrupole	$e^{(:-H_q\,ds:)}\,\Psi_x = \Psi_x + i\sqrt{\beta_{x_0}}\,(K_1^+X - K_1^\times Y)$	$e^{(:-H_q\,ds:)}\,\Psi_y = \Psi_y - i\sqrt{\beta_{y_0}}\,(K_1^+Y + K_1^\times X)$

A pure skew quadrupole (with $k_1^+ = 0$ and $k_1^\times > 0$) is physically equivalent to a normal quadrupole rotated by 45°. Thus, the system under study is — from a practical standpoint — no more complex than the uncoupled case analyzed earlier, and its description should follow naturally. For the general case of a sequence of arbitrarily oriented thin quadrupoles however, the situation cannot be reduced to the uncoupled case by a simple coordinate rotation. Within the Courant–Snyder framework, this case is typically abandoned and alternate formalisms are needed (see, *e.g.*, the approach of Edwards-Teng or Lebedev-Bogacz [41]). Here, we expand on Proposition 4.1 and write the general transformation for transversely coupled linear systems as:

$$\mathcal{M}\,\mathbf{\Psi}(\vec{\Theta}) \;:\; \begin{cases} \mathcal{M}\Psi_x = u_{xx}\Psi_x + u_{xy}\Psi_y + v_{xx}\Psi_x^* + v_{xy}\Psi_y^* \\ \mathcal{M}\Psi_y = u_{yx}\Psi_x + u_{yy}\Psi_y + v_{yx}\Psi_x^* + v_{yy}\Psi_y^* \end{cases}, \tag{4.16}$$

with $\{u_{jk}, v_{jk}\} \in \mathbb{C}$. More compactly, one can equally write:

$$\mathcal{M}\begin{pmatrix}\Psi_x \\ \Psi_y\end{pmatrix} = U\begin{pmatrix}\Psi_x \\ \Psi_y\end{pmatrix} + V\begin{pmatrix}\Psi_x^* \\ \Psi_y^*\end{pmatrix} \quad \text{with} \quad U = \begin{pmatrix}u_{xx} & u_{xy} \\ u_{yx} & u_{yy}\end{pmatrix} \text{ and } V = \begin{pmatrix}v_{xx} & v_{xy} \\ v_{yx} & v_{yy}\end{pmatrix} \tag{4.17}$$

which is a generalization of eq. (4.1). Following Demonstration 3.1, one can show that the symplectic condition in this case can be written as $UU^\dagger - VV^\dagger = \mathrm{I}_{2\times 2}$ and $UV^\intercal - VU^\intercal = 0$ where $U^\dagger = (U^*)^\intercal$. That being said, if the coefficients of eq. (4.16) are obtained from a sequence of symplectic transformations in the form of Table 4.2, the transformation is symplectic by construction. Following the procedure established for the uncoupled case, we would like to find a torus which maps back onto itself after one iteration of $\mathcal{M}$. The dephasing condition, in this case (and in general), reads:

$$\mathcal{M}\,\mathbf{\Psi}(\vec{\Theta}) = \mathbf{\Psi}(\vec{\Theta} + 2\pi\vec{Q}) \tag{4.18}$$

which is required to be respected for all projections, $\Psi_j(\vec{\Theta})$. Remembering that $\Psi_x(\vec{\Theta}) = \sum_{\vec{n}} A_{\vec{n}}\, e^{i(\vec{n}\cdot\vec{\Theta})}$ and $\Psi_y(\vec{\Theta}) = \sum_{\vec{n}} B_{\vec{n}}\, e^{i(\vec{n}\cdot\vec{\Theta})}$ from eq. (2.8), the dephasing condition leads to a similar set of eigenvalue problems to that of eq. (4.11), given by :

$$M\,T_{x,n} = e^{in(2\pi Q_x)}\,T_{x,n} \quad \text{and} \quad M\,T_{y,n} = e^{in(2\pi Q_y)}\,T_{y,n} \tag{4.19}$$

(continued on next page)

$$M = \begin{pmatrix} U & V \\ V^* & U^* \end{pmatrix} = \begin{pmatrix} u_{xx} & u_{xy} & v_{xx} & v_{xy} \\ u_{yx} & u_{yy} & v_{yx} & v_{yy} \\ v^*_{xx} & v^*_{xy} & u^*_{xx} & u^*_{xy} \\ v^*_{yx} & v^*_{yy} & u^*_{yx} & u^*_{yy} \end{pmatrix} \quad T_{x,n} = \begin{pmatrix} A_{(n,0)} \\ B_{(n,0)} \\ A^*_{(-n,0)} \\ B^*_{(-n,0)} \end{pmatrix}, \quad T_{y,n} = \begin{pmatrix} A_{(0,n)} \\ B_{(0,n)} \\ A^*_{(0,-n)} \\ B^*_{(0,-n)} \end{pmatrix}. \tag{4.20}$$

Following similar arguments to those of the previous section, we conclude that outside of resonance conditions, all coefficients $A_{\vec{n}}$ and $B_{\vec{n}}$ must vanish except for the eight coefficients $A_{(\pm1,0)}, A_{(0,\pm1)}, B_{(\pm1,0)}, B_{(0,\pm1)}$. After setting $n = 1$, the eigenvalue problem eq. (4.19) can be solved using standard algorithms to find the eigensolutions of the transport problem. This yields the two fundamental frequencies Q_x and Q_y from the four eigenvalues ($e^{\pm i(2\pi Q_x)}$ and $e^{\pm i(2\pi Q_y)}$) and the corresponding eigenvectors. Once again, the eigenvectors can be rescaled to factorize the actions I_x and I_y from the map properties; described with the optical functions $\lambda^{\pm}_{jk}$ for $j, k \in \{x, y\}$. In the end, the eigensolution of the transport problem eq. (4.16) can be written as:

$$\boldsymbol{\Psi}(\vec{\Theta}) \; : \; \begin{cases} \Psi_x(\vec{\Theta}) = \sqrt{2I_x}(\lambda^+_{xx} e^{i\Theta_x} + \lambda^-_{xx} e^{-i\Theta_x}) + \sqrt{2I_y}(\lambda^+_{xy} e^{i\Theta_y} + \lambda^-_{xy} e^{-i\Theta_y}) \\ \Psi_y(\vec{\Theta}) = \sqrt{2I_x}(\lambda^+_{yx} e^{i\Theta_x} + \lambda^-_{yx} e^{-i\Theta_x}) + \sqrt{2I_y}(\lambda^+_{yy} e^{i\Theta_y} + \lambda^-_{yy} e^{-i\Theta_y}) \end{cases} \tag{4.21}$$

which is a direct generalization of the decoupled case, eq. (4.14). The procedure to extract the numerical values of the optical functions ($\lambda^{\pm}_{jk}$) from the map parameters (U and V) is presented later in Demonstration 4.2 along with the general case. Eq. (4.21) highlights the fact that four spectral lines should be expected in the Fourier spectrum of a transversely

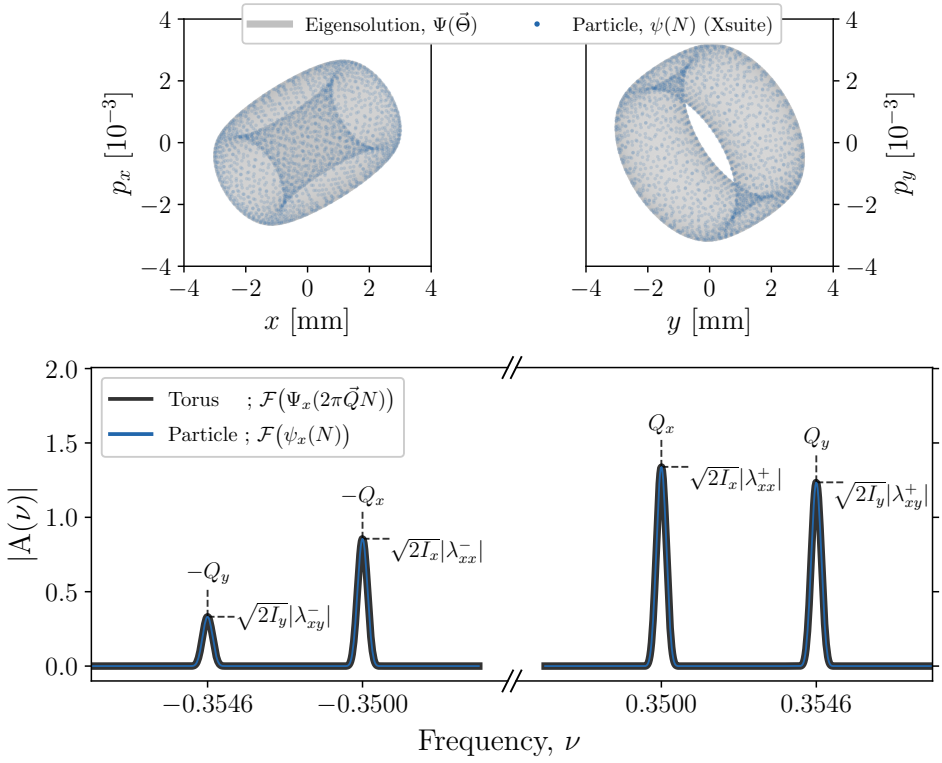

Figure 4.4: Comparison of the single-particle motion $\boldsymbol{\psi}(N)$ with the eigensolution torus $\boldsymbol{\Psi}(\vec{\Theta})$ in a coupled beam line. (Top) In phase space. (Bottom) Horizontal Fourier spectrum. A complete account of the spectral lines is given by eq. (4.21).

coupled linear system, as shown in Fig. 4.4. In this simple example, a skew FODO cell is built by using quadrupoles with $k_1^+ = (\pm k + \Delta k)\cos(2\theta)$ and $k_1^\times = (\pm k + \Delta k)\sin(2\theta)$, which corresponds to normal quadrupoles rotated by an angle θ. The slight offset in strength, Δk, is used to obtain different fundamental frequencies in x and y. This yields a fully coupled system described by eq. (4.21). For Fig. 4.4, $\theta = 30°$ such that the same system could be obtained by using normal quadrupoles ($k_1^\times = 0$) and rotate the entire beam line by 30°. Hence, the system considered in Fig. 4.3 is physically identical to the one considered in Fig. 4.4, up to a rotation of the coordinate system. We can therefore see that changing the coordinate system (here by a rotation) yields different spectrum in which new lines can be created or destroyed.

An important misconception should be addressed on the basis of Fig. 4.4. It is commonly said that the "highest peak" in the Fourier spectrum of a particle corresponds to its fundamental frequency. However, it should be clear from eq. (4.21) and Fig. 4.4 that the highest peak in $\mathcal{F}(\psi_x)$ can correspond to Q_y if the action of the particle, I_y, is sufficiently high. The manifestation of this effect ultimately depends on the initial conditions of the particle under study. By only looking at the highest peaks in the spectra ($\mathcal{F}(\psi_x)$ and $\mathcal{F}(\psi_y)$), one could erroneously conclude that the particle is "on resonance" (or "locked"), with $Q_x = Q_y$, which is clearly not the case.

4.4 Fully Coupled Linear Beam Lines

Proposition 4.2: Coupled linear transformation.

Let us consider a 6D phase phase. Any linear transformation of $\mathbf{\Psi}$ can be written as:

$$\mathcal{M}\,\mathbf{\Psi} = U\,\mathbf{\Psi} + V\,\mathbf{\Psi}^*, \quad \text{with } \{U, V\} \in \mathbb{C}^{3\times 3}\ , \tag{4.22}$$

with $\mathbf{\Psi}(\vec{\Theta}) = (\Psi_x, \Psi_y, \Psi_\zeta)^\intercal$, which is symplectic if $UU^\dagger - VV^\dagger = \mathrm{I}_{3\times 3}$ and $UV^\intercal - VU^\intercal = 0$. By considering the augmented basis $(\mathbf{\Psi}, \mathbf{\Psi}^*)^\intercal$, this equation can equally be written as:

$$\mathcal{M}\begin{pmatrix}\mathbf{\Psi}\\ \mathbf{\Psi}^*\end{pmatrix} = M\begin{pmatrix}\mathbf{\Psi}\\ \mathbf{\Psi}^*\end{pmatrix} \quad \text{with} \quad M = \begin{pmatrix}U & V\\ V^* & U^*\end{pmatrix} \in \mathbb{C}^{6\times 6}\ . \tag{4.23}$$

The periodic solution of the the transport problem in $\mathcal{M}$ is given by the eigensolutions of M. The fundamental frequencies Q_k are found from the eigenvalues, $e^{\pm i(2\pi Q_k)}$, and the optical functions $\lambda_{jk}^\pm$ are found from the eigenvectors, $T_k \propto (\lambda_{xk}^+, \lambda_{yk}^+, \lambda_{\zeta k}^+, (\lambda_{xk}^-)^*, (\lambda_{yk}^-)^*, (\lambda_{\zeta k}^-)^*)^\intercal$ ($j, k \in \{x, y, \zeta\}$), with a suitable normalization. The eigensolution can then be written as:

$$\mathbf{\Psi}: \begin{cases} \Psi_x(\vec{\Theta}) = \sqrt{2I_x}(\lambda_{xx}^+ e^{i\Theta_x} + \lambda_{xx}^- e^{-i\Theta_x}) + \sqrt{2I_y}(\lambda_{xy}^+ e^{i\Theta_y} + \lambda_{xy}^- e^{-i\Theta_y}) + \sqrt{2I_\zeta}(\lambda_{x\zeta}^+ e^{i\Theta_\zeta} + \lambda_{x\zeta}^- e^{-i\Theta_\zeta})\\ \Psi_y(\vec{\Theta}) = \sqrt{2I_x}(\lambda_{yx}^+ e^{i\Theta_x} + \lambda_{yx}^- e^{-i\Theta_x}) + \sqrt{2I_y}(\lambda_{yy}^+ e^{i\Theta_y} + \lambda_{yy}^- e^{-i\Theta_y}) + \sqrt{2I_\zeta}(\lambda_{y\zeta}^+ e^{i\Theta_\zeta} + \lambda_{y\zeta}^- e^{-i\Theta_\zeta})\\ \Psi_\zeta(\vec{\Theta}) = \sqrt{2I_x}(\lambda_{\zeta x}^+ e^{i\Theta_x} + \lambda_{\zeta x}^- e^{-i\Theta_x}) + \sqrt{2I_y}(\lambda_{\zeta y}^+ e^{i\Theta_y} + \lambda_{\zeta y}^- e^{-i\Theta_y}) + \sqrt{2I_\zeta}(\lambda_{\zeta\zeta}^+ e^{i\Theta_\zeta} + \lambda_{\zeta\zeta}^- e^{-i\Theta_\zeta}) \end{cases} \tag{4.24}$$

or in a more compact form:

$$\mathbf{\Psi}(\vec{\Theta}) = \Lambda_+ \begin{pmatrix}\sqrt{2I_x}\,e^{i\Theta_x}\\ \sqrt{2I_y}\,e^{i\Theta_y}\\ \sqrt{2I_\zeta}\,e^{i\Theta_\zeta}\end{pmatrix} + \Lambda_- \begin{pmatrix}\sqrt{2I_x}\,e^{i\Theta_x}\\ \sqrt{2I_y}\,e^{i\Theta_y}\\ \sqrt{2I_\zeta}\,e^{i\Theta_\zeta}\end{pmatrix}^* \quad \text{with} \quad \Lambda_\pm = \begin{pmatrix}\lambda_{xx}^\pm & \lambda_{xy}^\pm & \lambda_{x\zeta}^\pm\\ \lambda_{yx}^\pm & \lambda_{yy}^\pm & \lambda_{y\zeta}^\pm\\ \lambda_{\zeta x}^\pm & \lambda_{\zeta y}^\pm & \lambda_{\zeta\zeta}^\pm\end{pmatrix}\ . \tag{4.25}$$

This solution is unique, up to an arbitrary phase advance $\vec{\Theta} \mapsto \vec{\Theta} + \vec{\mu}$.

Demonstration 4.2: Courant-Snyder gauge.

As discussed in Proposition 4.2, the solution given in eq. (4.25) is unique up to an arbitrary phase advance $\vec{\Theta} \mapsto \vec{\Theta} + \vec{\mu}$, which could equally be placed on the eigenvectors of M following $T_k \mapsto e^{i(2\pi\phi_k)} T_k$, for $k \in \{x, y, \zeta\}$. This choice of phase is a *gauge* which needs to be fixed in order to obtain a unique set of optical functions. Let us define the gauge-invariant quantities:

$$\beta_{jk} \equiv |\lambda^+_{jk} + (\lambda^-_{jk})^*|^2 \ , \tag{4.26}$$

which are the generalized Courant-Snyder β-functions. By convention, we use the Courant-Snyder gauge: for each eigenvector $T_k = (T^+_{xk}, T^+_{yk}, T^+_{\zeta k}, (T^-_{xk})^*, (T^-_{yk})^*, (T^-_{\zeta k})^*)^\intercal$, we fix:

$$\lambda^+_{kk} + (\lambda^-_{kk})^* = e^{i(2\pi\phi_k)} \left(T^+_{kk} + (T^-_{kk})^*\right) = \sqrt{\beta_{kk}} \ \in \mathbb{R}^+ \ , \tag{4.27}$$

to be real and positive. Concretely, this fixes $2\pi\phi_k = -\arg(T^+_{kk} + (T^-_{kk})^*)$ for $k \in \{x, y, \zeta\}$. Then, $\sqrt{\beta_{kk}} \equiv \sqrt{\beta_k}$ can be used to compute the physical beam size according to the usual Courant-Snyder theory. Moreover, the various β_{jk} can be used to choose a robust *labeling rule* for the eigenmodes in the diagonalization of M: we enforce that the mode T_k (associated with the fundamental frequency Q_k) shall be labelled such that $\max(\beta_{jk}) = \beta_{kk}$ in all three planes. This is always possible except for some singular cases (*e.g.* perfectly skewed systems).

Looking at the transformations found on p. 57, it should be noted — and emphasized — that common accelerator elements are intrinsically non-linear in the longitudinal plane. Moreover, when longitudinal stability is required, RF cavities need to be used, which unavoidably introduces an off-momentum contribution. As a result, the assumption ($P_\zeta = 0$) leading to Table 4.1 and Table 4.2 can no longer be used and the system as a whole becomes non-linear in all planes. Hence, the general linear transformation given in Proposition 4.2 is first and foremost a mathematical construct which cannot be *truly* reproduced in a physical system. That being said, it is always possible, even in the non-linear case, to extract the linear part of the map and study it on the basis of eq. (4.22). The information obtained in such a way can then be used as an approximate description of the motion at small amplitudes ($|\vec{\Psi}| \ll 1$); or as a tool used to *normalize* the linear part of the map. By doing so, one moves the problem into the Courant-Snyder phase space, where all linear transformations correspond to simple rotations, and non-linear transformations correspond to more general deformations. The following section describes this normalization procedure, while non-linear transformations are discussed in Chapter 5.

4.5 Normalization and Courant-Snyder Phase Space

So far, our study of linear systems showed us that the eigensolutions of linear transfer maps can be found by imposing the dephasing condition, eq. (4.18), and solve for the spectral coefficients $A_{\vec{n}}$, $B_{\vec{n}}$, $C_{\vec{n}}$ in all planes. This ultimately leads to the construction of a complex matrix M following the formulation presented in Proposition 4.2. The solution, eq. (4.25), is a fixed topological object. Based on Proposition 2.2, this equally gives the single-particle dynamics by considering a stroboscopic variation of the angles, $\vec{\Theta} \mapsto 2\pi\vec{Q}N$, turn after turn. We have also previously shown (in Chapter 2) that the actions $I_j = \frac{1}{2}\sum_{\vec{n}} n_j \left(|\langle \vec{n} | \Psi_x \rangle|^2 + |\langle \vec{n} | \Psi_y \rangle|^2 + |\langle \vec{n} | \Psi_\zeta \rangle|^2\right)$ are invariant along the beam line, by virtue of simplicity.

That being said, it should be clear from Fig. 4.1 that the topology of the torus changes throughout the beam line and is not invariant in itself. By that we mean that the components of $\mathbf{\Psi}$, which dictate the orientation of the ellipse in Fig. 4.1 (and of the 6D ellipsoid in the general case), change as a function of s. Naturally, the single-particle spectra — given by the same components — also change. To formalize this point, let us go back to the simple case of uncoupled dynamics. The claim is that for any position s along the beam line, there is a suitable factorization of the motion (see Demonstration 4.2) in terms of the action I_x, the phase $\mu_x(s)$ and the optical functions $\lambda_x^{\pm}(s)$, such that the ellipse $\Psi_x(\Theta_x, s)$ can be written as:

$$\begin{aligned}\Psi_x(\Theta_x, s) &= A_1(s)\, e^{i\Theta_x} + A_{\text{-}1}(s) e^{-i\Theta_x} \\ &= \sqrt{2I_x}\left(\lambda_x^+(s) e^{i2\pi\mu_x(s)} e^{i\Theta_x} + \lambda_x^-(s) e^{-i2\pi\mu_x(s)} e^{-i\Theta_x}\right) \ . \end{aligned} \tag{4.28}$$

By convention, the initial phase is set to be zero, $\mu_x(0) = 0$, and the phase advance is obtained from $\Delta\mu_x = \mu_x(s) - \mu_x(0) = \pm\frac{1}{2\pi}\arg\left(A_{\pm 1}(s)/(\sqrt{2I_x}\lambda_x^{\pm}(s))\right)$. If only one could normalize the geometry of the ellipse — simplify the topology — for any s along the beam line, then the motion would be reduced to that of a pure rotation given by the phase advance, $\mu_x(s)$. In essence, this is similar to the diagonalization process of a matrix, where we look for a space in which the matrix takes on a simpler form. As discussed in Section 2.1.6, this space shall be called the Courant-Snyder (C.S.) phase space (*i.e.* the linear Normal Form), denoted with the coordinates $\vec{\tilde{x}}$ and their complex counterpart $\tilde{\boldsymbol{\psi}}(N)$ and $\tilde{\mathbf{\Psi}}(\vec{\Theta})$. By construction, $\tilde{\Psi}_x(\Theta_x) = \sqrt{2I_x} e^{i2\pi\mu_x(s)} e^{i\Theta_x}$ for a linear solution, such that eq. (4.28) can be written as:

$$\Psi_x(\Theta_x, s) = \lambda_x^+(s)\tilde{\Psi}_x(\Theta_x, s) + \lambda_x^-(s)\tilde{\Psi}_x^*(\Theta_x, s) \ , \tag{4.29}$$

which is readily a transformation of $\tilde{\Psi}_x \mapsto \Psi_x$. The Courant-Snyder normalization, therefore, corresponds to the inverse of eq. (4.29). Remembering that $|\lambda_x^+(s)|^2 - |\lambda_x^-(s)| = 1$, we get:

$$\begin{aligned}\tilde{\Psi}_x(\Theta_x, s) = \lambda_x^{+*}(s)\ \Psi_x(\Theta_x, s) - \lambda_x^-(s)\ \Psi_x^*(\Theta_x, s) &= \sqrt{2I_x}\left(|\lambda_x^+(s)|^2 - |\lambda_x^-(s)|^2\right) e^{i2\pi\mu_x(s)} e^{i\Theta_x} \\ &= \sqrt{2I_x}\ e^{i2\pi\mu_x(s)} e^{i\Theta_x} \ , \end{aligned} \tag{4.30}$$

which is indeed a pure rotation, as a function of s, on a circle with constant radius $\sqrt{2I_x}$. For the rest of the thesis, the s-argument shall be omitted for simplicity, but one must always keep in mind that all optical functions (and spectral content) vary along the beam line in s.

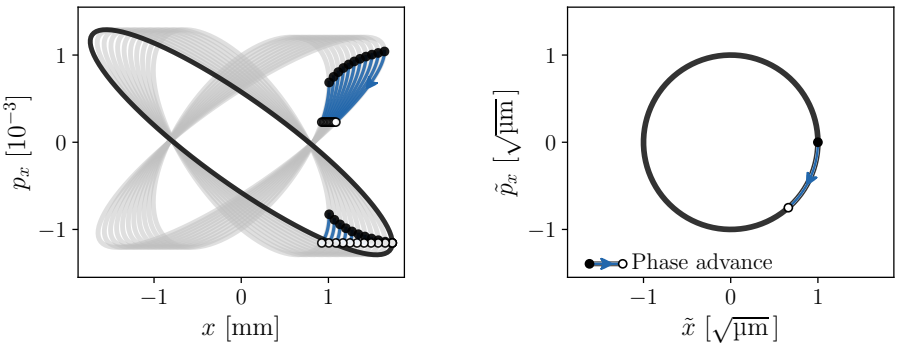

Figure 4.5: Linear transformation (drift → quad. → drift). (Left) In the physical phase space, $\Psi_x(\Theta_x, s)$. (Right) In the Courant-Snyder phase space, $\tilde{\Psi}_x(\Theta_x, s)$. In the C.S. phase space, linear transformations reduce to a pure rotation given by the phase advance, $\mu_x(s)$.

It is important to note that the Courant-Snyder coordinates $\vec{\tilde{x}}$ carry homogenous units of $\sqrt{\mathrm{m}}$, as shown in Fig. 4.5 — which are also the units of both $\mathbf{\Psi}$ and $\tilde{\mathbf{\Psi}}$. Hence, in the Courant-Snyder phase space, the complex coordinates are given in terms of the phase space coordinates following:

$$\tilde{\mathbf{\Psi}}(\vec{\Theta}) \;:\; \begin{cases} \tilde{\Psi}_x(\vec{\Theta}) \equiv \tilde{X} - i\tilde{P}_x \\ \tilde{\Psi}_y(\vec{\Theta}) \equiv \tilde{Y} - i\tilde{P}_y \\ \tilde{\Psi}_\zeta(\vec{\Theta}) \equiv \tilde{Z} - i\tilde{P}_\zeta \end{cases}, \tag{4.31}$$

without the need for the rescaling parameters (β_{j_0} for $j \in \{x, y, \zeta\}$) used in eq. (2.5).

The previous normalization concepts can readily be generalized to a higher number of dimensions. Eq. (4.29) becomes the *construction* transformation $\mathcal{W}$, since it allows to construct the physical phase space torus $\mathbf{\Psi}$ from the normalized torus $\tilde{\mathbf{\Psi}}$. The normalization transformation is then given by its inverse, $\mathcal{W}^{-1}$. Considering $\mathbf{\Psi}(\vec{\Theta}) = (\Psi_x, \Psi_y, \Psi_\zeta)^\intercal$, both transformations can be written as:

$$\begin{array}{ll} \text{(Construction)} & \mathbf{\Psi} = \mathcal{W}\,\tilde{\mathbf{\Psi}} \quad = \Lambda_+\,\tilde{\mathbf{\Psi}} + \Lambda_-\,\tilde{\mathbf{\Psi}}^* \\ \text{(Normalization)} & \tilde{\mathbf{\Psi}} = \mathcal{W}^{-1}\,\mathbf{\Psi} = \Lambda_+^\dagger\,\mathbf{\Psi} - \Lambda_-^\intercal\,\mathbf{\Psi}^* \end{array} \quad \text{with} \quad \Lambda_\pm = \begin{pmatrix} \lambda^\pm_{xx} & \lambda^\pm_{xy} & \lambda^\pm_{x\zeta} \\ \lambda^\pm_{yx} & \lambda^\pm_{yy} & \lambda^\pm_{y\zeta} \\ \lambda^\pm_{\zeta x} & \lambda^\pm_{\zeta y} & \lambda^\pm_{\zeta\zeta} \end{pmatrix}, \tag{4.32}$$

which is symplectic with $\Lambda_+\Lambda_+^\dagger - \Lambda_-\Lambda_-^\dagger = \mathrm{I}_{3\times3}$ and $\Lambda_+\Lambda_-^\intercal - \Lambda_-\Lambda_+^\intercal = 0$. One should note that the construction transformation is simply a compact version of eq. (4.24) (equivalent to eq. (4.25)) when $\tilde{\mathbf{\Psi}}$ is circular in the C.S. phase space — which is the case for linear solutions. The Courant-Snyder phase space is an insightful conceptual tool which can be used to study various effects and play with what A. Chao called "Phase Space Gymnastics" [42] (*i.e.* the design of beam lines used to manipulate the phase space at will). This is described in Proposition 4.3.

Proposition 4.3: Phase Space Gymnastics.

Consider a transformation $\mathcal{M}_{1\to2}$ which maps the location s_1 to the location s_2. If the optical functions $\Lambda_{1,\pm}$ and $\Lambda_{2,\pm}$ are known at the two locations, together with the phase advance $\Delta\vec{\mu} = \vec{\mu}_2 - \vec{\mu}_1$, then the corresponding linear transformation can always be found in the form of eq. (4.22). In the Courant-Snyder phase space, the transformation $\tilde{\mathcal{M}}_{1\to2}$ is given by a pure rotation following:

$$\tilde{\mathcal{M}}_{1\to2}\,\tilde{\mathbf{\Psi}} = \tilde{R}(\Delta\vec{\mu})\,\tilde{\mathbf{\Psi}} \quad \text{with} \quad \tilde{R}(\Delta\vec{\mu}) \equiv \begin{pmatrix} e^{i(2\pi\Delta\mu_x)} & 0 & 0 \\ 0 & e^{i(2\pi\Delta\mu_y)} & 0 \\ 0 & 0 & e^{i(2\pi\Delta\mu_\zeta)} \end{pmatrix} \tag{4.33}$$

As a result, the corresponding physical phase space transformation can be obtained from $\mathcal{M}_{1\to2} = \mathcal{W}_2\,\tilde{R}\,\mathcal{W}_1^{-1}$; *i.e.* by first going in the Courant-Snyder phase space at the starting location s_1, applying the rotation and returning to the physical phase space with the construction $\mathcal{W}_2$ at the final location s_2. In the end, the transformation can be written as:

$$\mathcal{M}_{1\to2}\mathbf{\Psi} = U\mathbf{\Psi} + V\mathbf{\Psi}^* \quad \text{with} \quad \begin{cases} U = \;\; \Lambda_{2,+}\tilde{R}\,\Lambda_{1,+}^\dagger - \Lambda_{2,-}\tilde{R}^*\,\Lambda_{1,-}^\dagger \\ V = -\Lambda_{2,+}\tilde{R}\,\Lambda_{1,-}^\intercal + \Lambda_{2,-}\tilde{R}^*\,\Lambda_{1,+}^\intercal \end{cases}. \tag{4.34}$$

For periodic optical functions, the above still holds with $\Lambda_{1,\pm} = \Lambda_{2,\pm} = \Lambda_\pm$.

Example: Transverse Rotation

Let us consider again Fig. 4.3 and Fig. 4.4, which were said to only differ by a transverse rotation of $\theta = 30°$. One can show that the U-V transformation for a generic transverse rotation yields:

$$U = \begin{pmatrix} \cos(\theta) & \sin(\theta) \\ -\sin(\theta) & \cos(\theta) \end{pmatrix}, \qquad V = 0\ . \qquad \text{(Transverse } \theta\text{-Rotation)}$$

According to eq. (4.34), we should also be able to find a suitable U-V transformation to take us from Fig. 4.4 (the coupled location) to Fig. 4.3 (the uncoupled location). Considering $\Lambda_{1,\pm}$ to be the optics of the coupled case (as measured from the particle spectra) and $\Lambda_{2,\pm}$ to be the optics of the uncoupled case, we find, numerically:

$$U = \quad \Lambda_{2,+}\tilde{R}\,\Lambda_{1,+}^{\dagger} - \Lambda_{2,-}\tilde{R}^{*}\,\Lambda_{1,-}^{\dagger} = \begin{pmatrix} 0.866 & -0.5 \\ 0.5 & 0.866 \end{pmatrix}, \quad V = 0\ , \qquad \text{(Fig. 4.4} \rightarrow \text{Fig. 4.3)}$$

which is indeed a transverse rotation with $\theta = -30°$. In the above equation, we imposed a phase advance of zero (instantaneous transformation), such that $\tilde{R} = \mathrm{I}_{2\times 2}$.

Example: Normalization and Compensation

In the next example, we wish to show that the normalization transformation of eq. (4.32) is not merely an abstract tool, but that it can also be *built* with a sequence of physical elements. This is particularly useful for the problem of compensation, which we frame as follows: "Given a generic transformation, $\mathcal{M}$, can we find a *compensator* $\mathcal{M}_C$, such that the overall transformation $\mathcal{M}_C \circ \mathcal{M}$ becomes transparent for all $\mathbf{\Psi}$, albeit for an arbitrary phase advance?". In other words (and in a similar way to eq. (4.18)) we wish to find an $\mathcal{M}_C$ such that:

$$\mathcal{M}_C \circ \mathcal{M}\,\mathbf{\Psi}(\vec{\Theta}) = \mathbf{\Psi}(\vec{\Theta} + 2\pi\vec{\mu}) \quad \forall\ \mathbf{\Psi}\ . \tag{4.35}$$

To achieve this result, the normalization transformation $\mathcal{W}^{-1}$ can be used. First, we note that $\mathcal{W}^{-1}$ is just a particular case of the linear transformation eq. (4.34). Here, $\Lambda_{1,\pm}$ correspond to the optics at the observation location and $\Lambda_{2,\pm}$ (the target optics) are by construction given by the fundamental matrices $\Lambda_{2,+} = \mathrm{I}_{3\times 3}$ and $\Lambda_{2,-} = 0$. This latter condition is equivalent, in the Courant-Snyder theory, to decoupled optics with $\beta_x = \beta_y = 1$ m and $\alpha_x = \alpha_y = 0$.

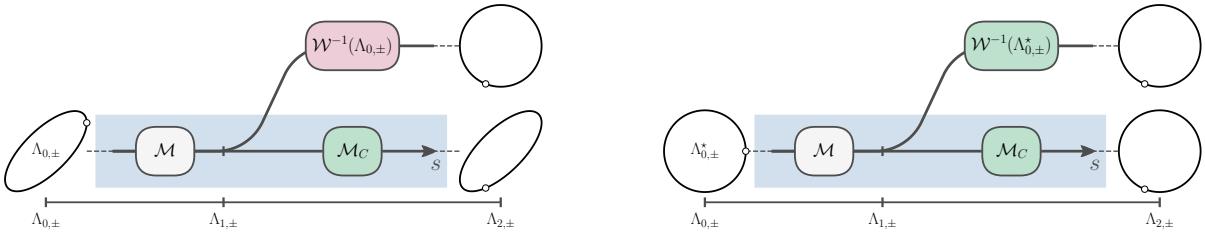

(a) (b)

Figure 4.6: Visual representation of the compensation problem. (a) For any initial $\mathbf{\Psi}$ matched to an optics $\Lambda_{0,\pm}$, the map $\mathcal{M}_C \circ \mathcal{M}$ returns the same $\mathbf{\Psi}$ up to a phase advance. In parallel, the map $\mathcal{W}^{-1}(\Lambda_{0,\pm}) \circ \mathcal{M}$ (which itself depends on $\Lambda_{0,\pm}$) always returns a circle with $(\Lambda_{2,+}, \Lambda_{2,-}) = (\mathrm{I}, 0)$. The two maps are, in general, different. (b) In the specific case where $\mathbf{\Psi}$ is matched to the circular optics $(\Lambda^{\star}_{0,+}, \Lambda^{\star}_{0,-}) = (\mathrm{I}, 0)$, both outputs are identical. We have therefore found the compensator, $\mathcal{M}_C = \mathcal{W}^{-1}(\Lambda^{\star}_{0,\pm})$.

The situation is illustrated in Fig. 4.6. To understand the approach, some nuances need to be added to the concept of *optics*. Based on eq. (4.25), one should see that $\Lambda_\pm$ give, first and foremost, a description of the topological signature of any arbitrary 6D ellipsoid. For periodic beam lines however, the eigensolutions admit a specific topological signature (property of the lattice) which bears the name of *optics*. Indeed, in the design of a beam line, the optician studies some key topological properties (α, β, γ in the Courant-Snyder tradition) and their evolution along the lattice. For periodic systems, those are forced to correspond to the topological signature of the eigensolutions. For open-ended transfer lines however, the *optics* shall be seen as the reference topology chosen by the optician. If an ellipsoid differs from this reference signature $\Lambda_\pm$, it is said to be *mismatched*. If, instead, the ellipsoid corresponds to the reference topological signature, it is said to be *matched*. In open-ended transfer lines, the optician is free to chose any desired optics.

To solve the compensation problem according to Fig. 4.6, one can use the fact that the the normalization map depends on the chosen optics, $\mathcal{W}^{-1}(\Lambda_{0,\pm})$. In the specific case where a circular optics is chosen following $(\Lambda^\star_{0,+}, \Lambda^\star_{0,-}) = (\mathrm{I}, 0)$, then the normalization $\mathcal{W}^{-1}(\Lambda^\star_{0,\pm})$ corresponds precisely to the compensation map which fulfills eq. (4.35). In fact, we can write:

$$\begin{aligned} \forall\ \Lambda_{0,\pm} \mapsto \Lambda_{2,\pm}: \quad & \mathcal{M}_C = \mathcal{W}(\Lambda_{2,\pm}) \circ \mathcal{W}^{-1}(\Lambda_{0,\pm}) && \text{(see Fig. 4.6(a))} \\ \Rightarrow \quad & \mathcal{M}_C = \mathrm{I} \circ \mathcal{W}^{-1}(\Lambda^\star_{0,\pm}) = \mathcal{W}^{-1}(\Lambda^\star_{0,\pm}) && \text{(see Fig. 4.6(b))} \end{aligned}$$

since $\mathcal{W}(\Lambda^\star_{2,\pm}) = \mathrm{I}$. To support these claims, let us consider a numerical experiment with a generic map $\mathcal{M}$ composed of several drifts, normal quadrupoles and skew quadrupoles such that:

$$\mathcal{M}\,\mathbf{\Psi} = U\mathbf{\Psi} + V\mathbf{\Psi}^* \quad \text{with} \quad \begin{matrix} U = \begin{pmatrix} -0.88 + 1.14i & -0.00 - 0.01i \\ 0.00 - 0.01i & -0.88 + 0.55i \end{pmatrix} \\ V = \begin{pmatrix} -0.94 - 0.44i & 0.02 + 0.01i \\ 0.02 + 0.01i & 0.24 + 0.15i \end{pmatrix} \end{matrix}. \tag{4.36}$$

Starting with the circular optics $(\Lambda^\star_{0,+}, \Lambda^\star_{0,-}) = (\mathrm{I}_{2\times2}, 0)$, we find that the normalization transformation required at s_1 follows:

$$\mathcal{W}^{-1}(\Lambda^\star_{0,\pm})\,\mathbf{\Psi} = \Lambda^\dagger_{1,+}\,\mathbf{\Psi} - \Lambda^\intercal_{1,-}\,\mathbf{\Psi}^* \quad \text{with} \quad \begin{matrix} \Lambda^\dagger_{1,+} = \begin{pmatrix} 1.41 + 0.28i & -0.01 - 0.01i \\ -0.01 - 0.01i & 1.04 - 0.00i \end{pmatrix} \\ -\Lambda^\intercal_{1,-} = \begin{pmatrix} -1.00 + 0.28i & 0.03 - 0.01i \\ 0.03 - 0.00i & 0.28 - 0.00i \end{pmatrix} \end{matrix}, \tag{4.37}$$

which we claim is the compensator transformation (in the form $\mathcal{M}_C\,\mathbf{\Psi} = U_C\mathbf{\Psi} + V_C\mathbf{\Psi}^*$). To confirm the result, we can look for another compensation map which we *know* should give the intended result. Namely: the inverse of $\mathcal{M}$ followed by an arbitrary phase advance, $\mathcal{M}_C = \tilde{R} \circ \mathcal{M}^{-1}$. Reversing the line element-by-element in the numerical experiment (followed by the original phase advance $\tilde{R}$) yields:

$$\mathcal{M}_C\,\mathbf{\Psi} = \tilde{R} \circ \mathcal{M}^{-1}\,\mathbf{\Psi} = U_C\,\mathbf{\Psi} + V_C\,\mathbf{\Psi}^* \quad \text{with} \quad \begin{matrix} U_C = \begin{pmatrix} 1.41 + 0.28i & -0.01 - 0.01i \\ -0.01 - 0.01i & 1.04 - 0.00i \end{pmatrix} \\ V_C = \begin{pmatrix} -1.00 + 0.28i & 0.03 - 0.01i \\ 0.03 - 0.00i & 0.28 - 0.00i \end{pmatrix} \end{matrix} \tag{4.38}$$

which is indeed the same map as the one obtained from the normalization transformation in eq. (4.37). Since we know eq. (4.38) works for all $\mathbf{\Psi}$ (it is the inverse of $\mathcal{M}$, after all), we can be certain that eq. (4.37) also works for all $\mathbf{\Psi}$. Note that this simple experiment can be carried out analytically for any generic U-V transformation following the very same steps. The numerical route was however preferred, in this case, to give a tangible demonstration to the reader.

Demonstration 4.3: Bridge to Courant-Snyder and back.

As mentioned in Chapter 2 (eq. (2.29)), the Courant-Snyder normalization of eq. (4.32) can equally be carried out on the real coordinates $\vec{x}$ via the use of the real symplectic W-matrix [18] following:

$$\tilde{\mathbf{\Psi}} = \mathcal{W}^{-1}\,\mathbf{\Psi} \quad \Leftrightarrow \quad \vec{\tilde{X}} = W^{-1}\vec{X}\ , \tag{4.39}$$

This W-matrix is typically considered to be the 6-dimensional generalization of the Courant-Snyder parameters. To make the transformation explicit, the (inverse) *construction* transformation can be written as:

$$\begin{pmatrix} x \\ p_x \\ y \\ p_y \\ \zeta \\ p_\zeta \end{pmatrix} = \begin{pmatrix} W_{11} & W_{12} & & & & \\ W_{21} & W_{22} & & & & \\ & & \ddots & & & \\ & & & W_{55} & W_{56} \\ & & & W_{65} & W_{66} \end{pmatrix} \begin{pmatrix} \tilde{x} \\ \tilde{p}_x \\ \tilde{y} \\ \tilde{p}_y \\ \tilde{\zeta} \\ \tilde{p}_\zeta \end{pmatrix} = \begin{pmatrix} W_{xx} & W_{xy} & W_{x\zeta} \\ W_{yx} & W_{yy} & W_{y\zeta} \\ W_{\zeta x} & W_{\zeta y} & W_{\zeta\zeta} \end{pmatrix} \begin{pmatrix} \tilde{x} \\ \tilde{p}_x \\ \tilde{y} \\ \tilde{p}_y \\ \tilde{\zeta} \\ \tilde{p}_\zeta \end{pmatrix} \tag{4.40}$$

where $W_{jk} \in \mathbb{R}^{2\times 2}$ are 2×2 block matrices of the form $W_{xx} = \begin{pmatrix} W_{11} & W_{12} \\ W_{21} & W_{22} \end{pmatrix}$ and so on for $j,k \in \{x,y,\zeta\}$. The optical functions $\lambda^{\pm}_{jk}$ can be directly obtained from the W-matrix following:

$$\lambda^{\pm}_{xx} = \frac{1}{2}\Big(W_{11} \pm W_{22}\Big) - i\frac{1}{2}\Big(W_{21} \mp W_{12}\Big)\ , \tag{4.41}$$

and so on for all $W_{jk} \mapsto \lambda^{\pm}_{jk}$ (block-by-block). After enforcing the Courant-Snyder gauge (Demonstration 4.2), the generalized Courant-Snyder parameters α_{jk} and β_{jk} can be defined, together with the block determinant d_{jk}, based on the optical functions. Let $a = (\lambda^{+}_{jk})^* + \lambda^{-}_{jk}$ and $b = \lambda^{+}_{jk} - (\lambda^{-}_{jk})^*$, then :

$$\begin{cases} \beta_{jk} \equiv |a|^2 = |\lambda^{+}_{jk} + (\lambda^{-}_{jk})^*|^2 \\ \alpha_{jk} \equiv \mathrm{Im}\{ab\} = \mathrm{Im}\Big\{((\lambda^{+}_{jk})^* + \lambda^{-}_{jk})(\lambda^{+}_{jk} - (\lambda^{-}_{jk})^*)\Big\} \\ d_{jk} \equiv \mathrm{Re}\{ab\} = \mathrm{Re}\Big\{((\lambda^{+}_{jk})^* + \lambda^{-}_{jk})(\lambda^{+}_{jk} - (\lambda^{-}_{jk})^*)\Big\} \end{cases}\ . \tag{4.42}$$

In turn, the optical functions can be obtained from the generalized Courant-Snyder parameters following:

$$\lambda^{\pm}_{jk}(s) = \frac{\beta_{jk} + i\alpha_{jk} \pm d_{jk}}{2\sqrt{\beta_{jk}}} \tag{4.43}$$

where we have assumed that the arbitrary rescaling parameters β_{j_0} defined in Chapter 2 were all fixed to 1 m (in the alternative, one needs to replace $\beta_{jk} \mapsto \beta_{jk}/\beta_{j_0}$). For the *uncoupled* case: off-diagonal terms are zeros, the block determinants are all $d_{jj} = 1$, the generalized Courant-Snyder parameters are the usual $\alpha_{xx} \mapsto \alpha_x$, $\beta_{xx} \mapsto \beta_x$ and so on, and the optical functions reduce to:

$$\lambda^{\pm}_{x} = \frac{\beta_x/\beta_{x_0} + i\alpha_x \pm 1}{2\sqrt{\beta_x/\beta_{x_0}}}\ , \quad \text{and} \quad \lambda^{\pm}_{y} = \frac{\beta_y/\beta_{y_0} + i\alpha_y \pm 1}{2\sqrt{\beta_y/\beta_{y_0}}}\ . \tag{4.44}$$

CHAPTER 5

Topological Formulation of Non-Linear Beam Dynamics

Non-linear effects fundamentally alter the character of single-particle dynamics. While linear systems are scale-invariant (they preserve the same topology across all amplitudes), non-linearities introduce amplitude-dependent deformations, detuning, resonance islands, and chaotic layers. The central question of this chapter is whether the topological framework developed in the previous chapters can be extended to describe and study these non-linear effects, even when closed-form analytic solutions are unavailable.

We begin by showing that the Courant-Snyder phase space greatly simplifies the non-linear picture: all symplectic transformations can be decomposed into rotations and shears. Linear contributions reduce to pure rotations, while non-linearities manifest as amplitude-dependent shears that distort the invariant tori. This geometric observation motivates the definition of a non-linear residual, which quantifies the departure from linear transport. As a practical figure of merit, the non-linear residual is shown to correlate strongly with the dynamic aperture of complex lattices — offering a computationally efficient tool for machine optimization. Applications to beam-beam compensation in the HL-LHC demonstrate how minimizing the non-linear residual translates directly into improved dynamic aperture. Finally, the connection between this topological framework and classical Normal Form analysis is established, providing a unified interpretation of resonance driving terms and their role in shaping the long-term stability of non-linear periodic systems.

5.1 A Non-Linear Framework

In the last chapter, we showed how any linear transformations of $\mathbf{\Psi}$ could be written in terms of a U-V matrix transformation (see Demonstration 4.2). This unsurprising result is in line with usual treatments of linear beam dynamics, where the elements *operators* themselves are described using transfer matrices. In our case, the operators used in the construction of the U-V matrices are not matrices themselves, but rather generic Lie transformations (taken from Chapter 3, p. 57). Here, it should be emphasized that this U-V framework is only a convenient way to group the terms of the linear contribution of $\mathcal{M}$, which in general is a *function* of $\mathbf{\Psi}$. This approach allows for a natural extension of the linear treatment into a non-linear one.

Proposition 5.1: Non-linear transformations.

Let us consider a 6D phase phase. Any symplectic transformation of $\mathbf{\Psi}$ can be written as:

$$\mathcal{M}\,\mathbf{\Psi} = U\,\mathbf{\Psi} + V\,\mathbf{\Psi}^* + f(\mathbf{\Psi}), \quad \text{with } \{U, V\} \in \mathbb{C}^{3\times 3} \text{ and } f(\mathbf{\Psi}) : \mathbb{C}^3 \mapsto \mathbb{C}^3 \ , \tag{5.1}$$

or more explicitly:

$$\mathcal{M}\,\mathbf{\Psi} : \begin{cases} \mathcal{M}\Psi_x = u_{xx}\Psi_x + u_{xy}\Psi_y + u_{x\zeta}\Psi_\zeta + v_{xx}\Psi_x^* + v_{xy}\Psi_y^* + v_{x\zeta}\Psi_\zeta^* + f_x(\Psi_x, \Psi_y, \Psi_\zeta) \\ \mathcal{M}\Psi_y = u_{yx}\Psi_x + u_{yy}\Psi_y + u_{y\zeta}\Psi_\zeta + v_{yx}\Psi_x^* + v_{yy}\Psi_y^* + v_{y\zeta}\Psi_\zeta^* + f_y(\Psi_x, \Psi_y, \Psi_\zeta) \\ \mathcal{M}\Psi_y = u_{\zeta x}\Psi_x + u_{\zeta y}\Psi_y + u_{\zeta\zeta}\Psi_\zeta + v_{\zeta x}\Psi_x^* + v_{\zeta y}\Psi_y^* + v_{\zeta\zeta}\Psi_\zeta^* + f_\zeta(\Psi_x, \Psi_y, \Psi_\zeta) \end{cases} , \tag{5.2}$$

where f_x, f_y, f_ζ are non-linear functions of the three projections $\Psi_x, \Psi_y, \Psi_\zeta$.

In fact, this description of non-linear systems was already implicitly present throughout the results of Chapter 3. Looking back at eq. (3.12), let us recall that a map composed of a sequence of elements $H_1,\ H_2,\ \ldots,\ H_n$ with lengths $\Delta s_1,\ \Delta s_2,\ \ldots,\ \Delta s_n$ can be written as:

$$\mathcal{M}\,\mathbf{\Psi}_0 = \left(e^{(:-H_n \Delta s_n:)} \circ \cdots \circ e^{(:-H_2 \Delta s_2:)} \circ e^{(:-H_1 \Delta s_1:)} \right) \mathbf{\Psi}_0 = \mathbf{\Psi}_n \ . \tag{5.3}$$

After applying the sequence of transformations element-by-element on $\mathbf{\Psi}$, one can indeed always write the overall transformation in the form of a set of non-linear functions of the projections $(\Psi_x, \Psi_y, \Psi_\zeta)$, as shown in eq. (5.2). The linear contribution can conveniently be written in terms of a U-V transformation while the quadratic, cubic and higher order terms are explicitly contained in the non-linear functions f_x, f_y and f_ζ.

These non-linear contributions fundamentally change the character of the motion by introducing a myriad of new effects. Examples were already given in Fig. 1.7 and Fig. 2.11 for a thin sextupole kick (leading to quadratic terms in f_x and f_y); and in Fig. 3.3 for an off-momentum drift (leading to terms of infinite order in f_x, f_y and f_ζ). In the linear picture of Chapter 4, the topology was independent of the actions $\vec{I}$ — the tori preserved their shapes and fundamental frequencies $\vec{Q}$ across all amplitudes. In contrast, non-linear effects break this scale invariance: they deform the invariant tori in an amplitude-dependent way, giving rise to *detuning* with amplitude, *resonance* islands and *chaotic* layers.

From a mathematical standpoint, this means that the eigensolutions of the map $\mathcal{M}$ can no longer be reduced to a simple matricial eigenvalue problem. Although the dephasing condition eq. (4.18) still applies, each set of actions $\vec{I}$ now defines its own torus and its own set of fundamental frequencies $\vec{Q}(\vec{I})$, determined by the higher-order terms in $f(\mathbf{\Psi})$. Because of this important change, we postpone the discussion of non-linear eigensolutions to the end of this chapter. Instead, we begin by developing a series of descriptive tools to capture the consequences of non-linearities in simple transport systems and open-ended beam lines.

5.2 Rotations and Shears

Let us consider a generic beam line with a given set of optical functions $\Lambda_\pm$. Recall, following Chapter 4, that the *optics* is the reference linear topology chosen by the optician. Based on eq. (4.25), any matched (but otherwise general) torus $\mathbf{\Psi}$ can be written as:

$$\mathbf{\Psi}(\vec{\Theta}) \;:\; \begin{cases} \Psi_x = \sum_{\vec{n}} A_{\vec{n}}\; e^{i(\vec{n}\cdot\vec{\Theta})} \\ \Psi_y = \sum_{\vec{n}} B_{\vec{n}}\; e^{i(\vec{n}\cdot\vec{\Theta})} \\ \Psi_\zeta = \sum_{\vec{n}} C_{\vec{n}}\; e^{i(\vec{n}\cdot\vec{\Theta})} \end{cases} \quad , \quad \text{with} \quad \begin{pmatrix} A_{(\pm1,0,0)} & A_{(0,\pm1,0)} & A_{(0,0,\pm1)} \\ B_{(\pm1,0,0)} & B_{(0,\pm1,0)} & B_{(0,0,\pm1)} \\ C_{(\pm1,0,0)} & C_{(0,\pm1,0)} & C_{(0,0,\pm1)} \end{pmatrix} = \Lambda_\pm \begin{pmatrix} \sqrt{I_x}e^{\pm i(2\pi\phi_x)} \\ \sqrt{I_y}e^{\pm i(2\pi\phi_y)} \\ \sqrt{I_\zeta}e^{\pm i(2\pi\phi_\zeta)} \end{pmatrix} \tag{5.4}$$

where, in other words, the first order lines ($|\vec{n}| = 1$) are all proportional to their corresponding optical function. It should be noted that the Courant-Snyder normalization $\mathcal{W}^{-1}$ (eq. (4.32)) is a general transformation which does not presuppose any particular topology for $\mathbf{\Psi}$. We can therefore apply it on any generic torus to go into the Courant-Snyder phase space following:

$$\tilde{\mathbf{\Psi}} = \mathcal{W}^{-1}\,\mathbf{\Psi} = \Lambda_+^\dagger\,\mathbf{\Psi} - \Lambda_-^\intercal\,\mathbf{\Psi}^* \tag{5.5}$$

which gives us a new torus $\tilde{\mathbf{\Psi}}$ with new spectral content, $\langle\,\vec{n}\,|\,\tilde{\Psi}_j\,\rangle$ for $j \in \{x, y, \zeta\}$. By construction, an ellipse that is matched to the optics is transformed into a circle via $\mathcal{W}^{-1}$. Any other torus, however, is only partially "circularized".

By definition (Proposition 4.3), the Courant-Snyder normalization dramatically simplifies the transport through linear systems, which is then reduced to pure rotations. Once again, this is a general result which does not depend on the shape of $\mathbf{\Psi}$, as shown in in Fig. 5.1. If the transport from s_1 to s_2 is made of linear elements, then in the Courant-Snyder phase space (eq. (4.33)):

$$\tilde{\mathcal{M}}_{1\to2}\,\tilde{\mathbf{\Psi}} = \tilde{R}(\Delta\vec{\mu})\,\tilde{\mathbf{\Psi}} \quad \text{with} \quad \tilde{R}(\Delta\vec{\mu}) \equiv \begin{pmatrix} e^{i(2\pi\Delta\mu_x)} & 0 & 0 \\ 0 & e^{i(2\pi\Delta\mu_y)} & 0 \\ 0 & 0 & e^{i(2\pi\Delta\mu_\zeta)} \end{pmatrix} , \tag{5.6}$$

which is a geometric rotation of the phase space. It therefore appears natural to begin our study of non-linear effects from within the Courant-Snyder phase space. There, the basic matched torus is readily given by $\tilde{\mathbf{\Psi}} = (\sqrt{I_x}\;e^{i\Theta_x}, \sqrt{I_y}\;e^{i\Theta_y}, \sqrt{I_\zeta}\;e^{i\Theta_\zeta})^\intercal$ and linear transport takes the form of pure rotations, $\tilde{R}(\Delta\vec{\mu})\,\tilde{\mathbf{\Psi}}$.

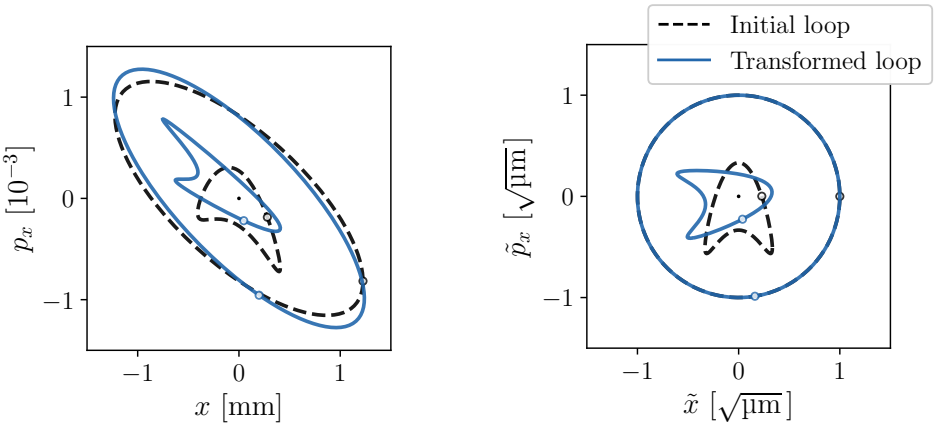

Figure 5.1: Courant-Snyder normalization and linear transport for generic 2D loops. (a) In the physical phase space, linear transformations appear as combined shears (horizontal and vertical). (b) In the Courant-Snyder phase space, linear transformations appear as geometric rotations of the phase space. Additionally, we see that any matched (but otherwise general) loop is partially "circularized" by $\mathcal{W}^{-1}$.

Based on the summary page of Chapter 3 (p. 57), it should be noted that all the transformations considered are *shearing* transformations, either horizontally or vertically:

$$\begin{aligned} &\text{(Horizontal shear)} && \Psi_j \;\mapsto\; \Psi_j + c_1\, f(\mathbf{\Psi}) && \text{with } \{c_1, c_2\} \in \mathbb{R},\ j \in \{x, y, \zeta\}, \\ &\text{(Vertical shear)} && \Psi_j \;\mapsto\; \Psi_j + i\, c_2\, g(\mathbf{\Psi}) && \text{and } f(\mathbf{\Psi}),\ g(\mathbf{\Psi}) \text{; functions of } \mathbf{\Psi}, \end{aligned} \tag{5.7}$$

i.e., contributions are either added to the real part of Ψ_j (position), or to its imaginary part (momentum). In linear systems, there is a sequence of shearing transformations which map an ellipse back onto itself with a given phase advance (*e.g.* in a FODO cell). When going in the Courant-Snyder phase space, this effect is simplified in the form of pure rotations, as shown in Fig. 5.1. Otherwise, the categorization proposed in eq. (5.7) still applies, as summarized below.

Proposition 5.2: Rotations and shears.

In the Courant-Snyder phase space, all single-element transformations $e^{(\cdot - \tilde{H}\cdot)}$ can be placed into one of three categories:

$$\begin{aligned} &\text{(Horizontal shear)} && \tilde{\Psi}_j \;\mapsto\; \tilde{\Psi}_j + c_1\, f(\tilde{\mathbf{\Psi}}) && \\ &\text{(Vertical shear)} && \tilde{\Psi}_j \;\mapsto\; \tilde{\Psi}_j + i\, c_2\, g(\tilde{\mathbf{\Psi}}) && \text{with } \{c_1, c_2\} \in \mathbb{R},\ j \in \{x, y, \zeta\}, \\ &\text{(Rotation)} && \tilde{\Psi}_j \;\mapsto\; \tilde{\Psi}_j\, e^{i(2\pi\Delta\mu_j)} && \text{and } f(\tilde{\mathbf{\Psi}}),\ g(\tilde{\mathbf{\Psi}}) \text{; functions of } \tilde{\mathbf{\Psi}}. \end{aligned} \tag{5.8}$$

For on-momentum tori: drifts, dipoles and quadrupoles form linear transformations in the transverse plane which lead to rotations. For off-momentum tori: drifts lead to (often negligible) horizontal shears. Lastly, non-linear multipoles of arbitrary order lead to vertical shears, commonly called *kicks*.

In the longitudinal plane however, drifts always lead to horizontal shears.

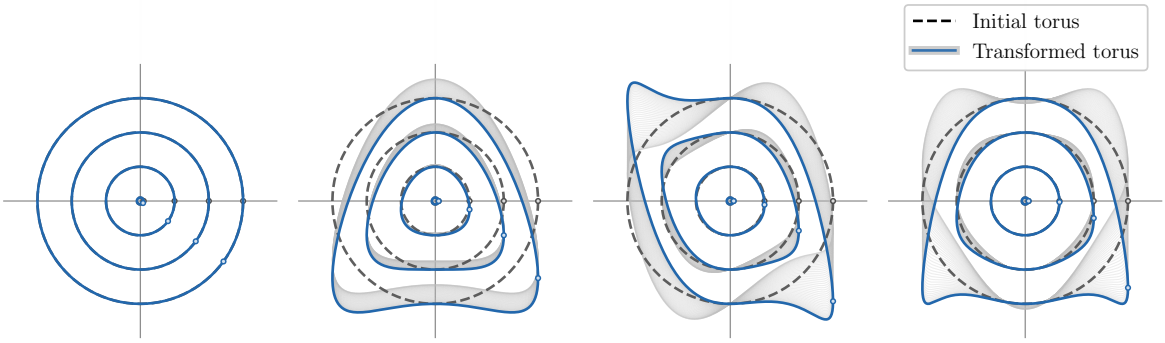

(a) Rotation (b) Sextuple (c) Octupole (d) Decapole

Figure 5.2: Visualization of non-linear transformations in the horizontal $(\tilde{x}, \tilde{p}_x)$ Courant-Snyder phase space. (a) For on-momentum tori, any sequence of drifts, dipoles and quadrupoles lead to pure rotations. (b,c,d) Multipoles of arbitrary order lead to vertical shears, also called kicks. The initial torus considered is purely circular, $\tilde{\mathbf{\Psi}}_0 = (\sqrt{I_x}\, e^{i\Theta_x}, \sqrt{I_y}\, e^{i\Theta_y})^\intercal$. For the transformed torus, both the shadow is shown (in grey) as well as a basic cycle $\tilde{\Psi}_x(\Theta_x^\circlearrowleft, \Theta_y = \pi/2)$, corresponding to $\tilde{Y}_0 = 0$.

The categorization of Proposition 5.2 can be particularly useful for the visualization of non-linear effects. Following similar ideas to those presented in Chapter 4, the *deformation* caused by non-linear effects can be highlighted by studying the deformation of an initially circular torus, $\tilde{\mathbf{\Psi}}_0 = (\sqrt{I_x}\, e^{i\Theta_x}, \sqrt{I_y}\, e^{i\Theta_y})^\intercal$, as shown in Fig. 5.2. As one can see, linear transformations lead to a geometric rotation of the phase space which is, importantly, independent of the distance from the origin (the amplitude). Non-linear transformations however, lead to important distortions which cause an amplitude-dependant change in the angle (*i.e.* $\tilde{\mathbf{\Psi}}_0(\vec{\Theta}) \mapsto \tilde{\mathbf{\Psi}}_1(\vec{\Theta} + 2\pi\vec{\mu}(\vec{I}))$), seen from the $\Theta_x = 0$ dots in Fig. 5.2(b,c,d). Moreover, non-linear coupling arises, leading to the *smearing* of the torus shadow.

That being said, the apparent complexity of Fig. 5.2 remains both "well-behaved" and "in-line" with the intuitive description of non-linear effects. With the latter, we mean that the expected polynomial kick — *i.e.* $\tilde{x}^2$ for a sextupole, $\tilde{x}^3$ for an octupole and so on — can be clearly seen in the deformations of Fig. 5.2(b,c,d), especially for the basic cycle $\tilde{\Psi}_x(\Theta_x^\circlearrowleft, \Theta_y = \pi/2)$ shown in blue. This choice of angle ($\Theta_y = \pi/2$) is equivalent to setting $\tilde{Y}_0 = 0$ on the torus before the transformation. Then, by well-behave we mean that the transformation is analytic and finite throughout the entire phase space $\vec{\tilde{x}}$ — just like $\tilde{x}^2$, $\tilde{x}^3$ and so on — which means that *chaos* is yet to emerge despite the presence of arbitrarily strong non-linearities. In fact, as discussed towards the end of the chapter, this suggests that chaos arises when transformations (just like the ones of Fig. 5.2) are *iterated* many times. More specifically, when looking for the eigensolution of a transport problem, we inevitably question the *infinite*: the solution, if it exists as a convergent series (see Chapter 1), must warrant us stability for an infinite number of iterations of the map since it is, by definition, unchanged after any single iteration.

5.3 Non-Linear Residual

Following Fig. 5.2, one would naturally like to have a metric to quantify the distortion of a given torus and measure its departure from a circular one. This was, indeed, an important research topic during the Superconducting Super Collider (SSC) era and associated to a critical machine parameter in the design phase of the project [43–45]. To quote J. Bengtsson and J. Irwin: "Early in the design process for the SSC, the concepts of tune shift and *smear* were chosen as first order measures of merit of machine designs. Smear was to be a measure of departure from linearity. It has been used extensively by the SSC Central Design Group recently in comparing various systematic multipole error correction schemes." [44]. They then go on to mention that although the intention of the concept is clear, different quantitative definitions have emerged which warranted the contribution from M. Furman and S. Peggs: "A Standard for the *Smear*" [45]. Prior to both of these works, É. Forest used the concept of *smear* to define a *linear aperture*, which quantified the region of phase space where motion remained approximately linear. Most probably, this notion eventually inspired the broader *dynamic aperture* concept; which refers to the long-term stability boundary in the presence of chaos (discussed in following sections).

We now propose a similar concept with a few caveats that imposes us to introduce a new name in defining the *non-linear residual* (NLR), $\mathcal{R}$. Whereas the smear from the SSC era was sometimes presented as a statistical quantity associated to a distribution, $\mathcal{R}$ shall be an analytic property of a torus. Importantly, studying the evolution of the non-linear residual through a lattice (for an initially circular torus) shall inform us on the strength of non-linearities in the machine. That being said, for a standalone torus, $\mathcal{R}$ shall simply measure its distortion. A natural choice for this metric would be to use the average radial excursion over the entire torus, as we do below.

Proposition 5.3: Non-linear residual.

For any torus $\tilde{\mathbf{\Psi}}$ in the Courant-Snyder phase space, one can compute the average Courant-Snyder linear invariant $\langle \vec{J} \rangle = (\langle J_x \rangle, \langle J_y \rangle, \langle J_\zeta \rangle)^\intercal$ from the average radial excursion following:

$$\langle J_x \rangle \equiv \frac{1}{2} \left\langle \tilde{X}^2 + \tilde{P}_x^2 \right\rangle_{\vec{\Theta}}, \quad \langle J_y \rangle \equiv \frac{1}{2} \left\langle \tilde{Y}^2 + \tilde{P}_y^2 \right\rangle_{\vec{\Theta}}, \quad \langle J_\zeta \rangle \equiv \frac{1}{2} \left\langle \tilde{Z}^2 + \tilde{P}_\zeta^2 \right\rangle_{\vec{\Theta}}, \tag{5.9}$$

where the average $\langle \cdot \rangle_{\vec{\Theta}}$ is taken over all angles $\vec{\Theta}$. The non-linear residual $\mathcal{R}$ can then be computed following:

$$\mathcal{R} \equiv \frac{\| \langle \vec{J} \rangle - \vec{I} \|}{\| \vec{I} \|} \qquad \text{with } \mathcal{R} \in \mathbb{R}^+ \tag{5.10}$$

which corresponds to the relative error of the C.-S. linear invariants with regards to the true actions $\vec{I} = (I_x, I_y, I_\zeta)^\intercal$ of the torus. Since $\sqrt{2I_j}$ is the effective radius of the torus in each plane, the non-linear residual measures the error of the average radial excursion.

The non-linear residual is a dimensionless measure of the torus distortion, which vanishes ($\mathcal{R} = 0$) for a circular torus and is strictly positive ($\mathcal{R} > 0$) otherwise.

Following the guidelines of M. Furman and S. Peggs, any metric used for the task at hand shall respect three fundamental properties [45]: it must be invariant under linear maps, it must be orientation invariant and it must finally be scale invariant. We could add to this list that the metric shall also be generalizable to an arbitrary number of dimensions. These requirements

ensure that the metric is independent of the observation point in the lattice, unless additional non-linear deformations are imposed on the torus. The non-linear residual $\mathcal{R}$, as defined in Proposition 5.4, respects all of these requirements. Being measured in the Courant-Snyder phase space, all linear transformations are pure rotations and the first two requirements are equivalent. Since $\mathcal{R}$ is evaluated from the geometric radial excursion, it is naturally orientation invariant.

To demonstrate that $\mathcal{R}$ is also scale invariant, the results of Demonstration 5.1 are needed. From there, one can compare the true action I_x with the C.-S. linear invariant $\langle J_x \rangle$, given by:

$$I_x = \frac{1}{2}\sum_{\vec{n}} n_x \left(\left|\tilde{A}_{\vec{n}}\right|^2 + \left|\tilde{B}_{\vec{n}}\right|^2 + \left|\tilde{C}_{\vec{n}}\right|^2 \right) \quad \text{and} \quad \langle J_x \rangle = \frac{1}{2}\sum_{\vec{n}} |\tilde{A}_{\vec{n}}|^2 \ . \tag{5.11}$$

Indeed, the actions from eq. (2.28) can indifferently be computed in the physical phase space or the Courant-Snyder phase space ($A_{\vec{n}} \leftrightarrows \tilde{A}_{\vec{n}}$) since the normalization transformation is symplectic. Hence, the non-linear residual can be obtained directly as a function of the Fourier coefficients of $\tilde{\mathbf{\Psi}}$ following $\mathcal{R}(\tilde{\mathbf{\Psi}}) = \mathcal{R}(\{\tilde{A}_{\vec{n}}, \tilde{B}_{\vec{n}}, \tilde{C}_{\vec{n}}\})$. By inspection of eq. (5.10), one can see that a uniform rescaling of the torus $\sqrt{\varepsilon}\,\tilde{\mathbf{\Psi}} \mapsto \{\sqrt{\varepsilon}\,\tilde{A}_{\vec{n}}, \sqrt{\varepsilon}\,\tilde{B}_{\vec{n}}, \sqrt{\varepsilon}\,\tilde{C}_{\vec{n}}\}$ leaves $\mathcal{R}$ unchanged, *i.e.*:

$$\mathcal{R}(\tilde{\mathbf{\Psi}}) = \mathcal{R}(\sqrt{\varepsilon}\,\tilde{\mathbf{\Psi}}) \quad \text{for } \sqrt{\varepsilon} \in \mathbb{R} \ , \tag{5.12}$$

where the rescaling parameter $\sqrt{\varepsilon}$ was purposely given the form of an emittance to emphasize the invariance of the non-linear residual with regard to the expected beam size.

Demonstration 5.1: Average radial excursion.

Starting from a general torus projection $\tilde{\Psi}_x = \sum_{\vec{n}} \tilde{A}_{\vec{n}}\, e^{i(\vec{n}\cdot\vec{\Theta})}$, we wish to compute the average radial excursion in that plane, which corresponds to the C.-S. linear invariant $\langle J_x \rangle$. First, we note that by definition, $\tilde{\Psi}_x = \tilde{X} - i\tilde{P}_x$, such that:

$$\langle J_x \rangle \equiv \frac{1}{2}\left\langle \tilde{X}^2 + \tilde{P}_x^2 \right\rangle_{\vec{\Theta}} = \frac{1}{2}\left\langle \tilde{\Psi}_x \tilde{\Psi}_x^* \right\rangle_{\vec{\Theta}} \ . \tag{5.13}$$

Similar to the approach of Demonstration 2.1, the result can be expressed in terms of the coefficients of the Fourier expansion following an explicit calculation of the integral:

$$\begin{aligned} \left\langle \tilde{\Psi}_x {\tilde{\Psi}_x}^* \right\rangle_{\vec{\Theta}} &= \frac{1}{(2\pi)^3} \oint_{\Theta_x} \oint_{\Theta_y} \oint_{\Theta_\zeta} \left[\sum_{\vec{n}} \tilde{A}_{\vec{n}}\, e^{i(\vec{n}\cdot\vec{\Theta})} \times \sum_{\vec{m}} \tilde{A}^*_{\vec{m}}\, e^{-i(\vec{m}\cdot\vec{\Theta})} \right] d\Theta_x d\Theta_y d\Theta_\zeta \\ &= \sum_{\vec{n}} |\tilde{A}_{\vec{n}}|^2 \end{aligned} \tag{5.14}$$

which is obtained by using the orthogonal identity $\int_0^{2\pi} e^{i(n_j\Theta_j)} e^{-i(m_j\Theta_j)}\, d\Theta_j = 2\pi\ \delta_{n_j m_j}$ for $j \in \{x, y, \zeta\}$. Hence, for the three different planes with Fourier coefficients $\tilde{A}_{\vec{n}}$, $\tilde{B}_{\vec{n}}$ and $\tilde{C}_{\vec{n}}$, the three average radial excursions are:

$$\langle J_x \rangle = \frac{1}{2}\sum_{\vec{n}} |\tilde{A}_{\vec{n}}|^2, \quad \langle J_y \rangle = \frac{1}{2}\sum_{\vec{n}} |\tilde{B}_{\vec{n}}|^2, \quad \langle J_\zeta \rangle = \frac{1}{2}\sum_{\vec{n}} |\tilde{C}_{\vec{n}}|^2 \ . \tag{5.15}$$

The parallels with the true actions I_x, I_y and I_ζ (eq. (2.28)) should be striking.

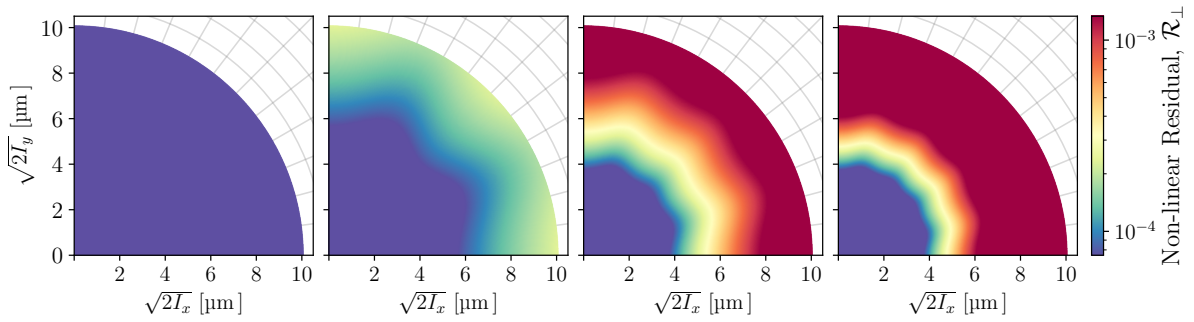

(a) Rotation (b) Sextupole (c) Octupole (d) Decapole

Figure 5.3: Non-linear residual for the multipolar deformations of Fig. 5.2 (magnetic strength reduced by 100). (a) Rotation, where $\mathcal{R}_\perp = 0$. (b,c,d) Multipolar kicks. $\mathcal{R}_\perp(\vec{I})$ is shown as a function of the actions of the initial circular torus, $\tilde{\mathbf{\Psi}}_0 = (\sqrt{I_x}\, e^{i\Theta_x}, \sqrt{I_y}\, e^{i\Theta_y})^\intercal$.

In lattice design, one must find practical solutions that both achieve the desired phase space gymnastics (Proposition 4.3) and maximize the region of stable motion. The goal is to push the chaotic layers further away from the reference particle and thereby improve the dynamic aperture — *i.e.* the set of initial conditions in phase space corresponding to bounded motion. In this regard, there is an important distinction between the transverse planes and the longitudinal plane that must be acknowledged. The multipolar magnets acting in the transverse plane provide kicks that grow in strength with the particle's amplitude ($\propto \tilde{x}^2, \tilde{x}^3$, etc.). In contrast, the longitudinal kick of the RF cavities is a restoring potential provided by a sinusoid. Consequently, the dynamic aperture is dominated by transverse non-linearities while longitudinal motion is typically confined within the RF bucket. This asymmetry justifies the primary focus on transverse non-linear optimization when studying lattice design.

Proposition 5.4: Transverse non-linear residual and dynamic aperture.

For practical lattice design, one can study the transverse non-linear residual $\mathcal{R}_\perp$ following:

$$\mathcal{R}_\perp \equiv \sqrt{\frac{(\langle J_x \rangle - I_x)^2 + (\langle J_y \rangle - I_y)^2}{I_x^2 + I_y^2}}\ , \tag{5.16}$$

which is equivalent to eq. (5.10) after dropping the longitudinal contribution. As will be shown in the following sections, minimizing $\mathcal{R}_\perp$ is found to improve the dynamic aperture.

As a simple example, let us study the transverse deformations from the multipolar kicks of Fig. 5.2. This can be done by measuring the deformation of an initially circular torus, $\tilde{\mathbf{\Psi}}_0 = (\sqrt{I_x}\, e^{i\Theta_x}, \sqrt{I_y}\, e^{i\Theta_y}, 0)^\intercal$ through the different elements, similarly to what was visually represented in the figure. Since $\mathcal{R}_\perp$ is a positive scalar, it becomes possible to study $\mathcal{R}_\perp(\vec{I})$, *i.e.* the dependance of the deformations as a function of the actions of the initial torus $\mathbf{\Psi}_0$. This is shown in Fig. 5.3 for the same multipolar deformations as in Fig. 5.2, albeit reduced (in strength) by a factor 100 to yield a range of $\mathcal{R}_\perp$ which is similar to what can be tolerated in the LHC [46]. It should be noted that the non-linear residual is a relative metric: what can or cannot be tolerated to obtain a satisfactory dynamic aperture needs to be determined *a priori*, depending on the global characteristics of the lattice. Examples for the LHC will be presented in the following sections, after prior discussions on the problem of non-linear compensation.

5.4 Non-Linear Compensation

In Chapter 4, a simple example of *compensation* was given. The conclusion, importantly, showed that compensation, normalization and inversion are all connex concepts. The normalization transformation can be built as a physical system which corresponds to the inverse of the map. This type of compensation neutralizes the effect of the original map completely.

5.4.1 Sextupolar compensation

Here, we would like to broaden these concepts and discuss of compensation as a way to mitigate unwanted effects while preserving wanted effects. The seminal example for this is the addition of sextupoles in typical transfer lines to mitigate chromatic aberrations, as discussed in Chapter 1 (Fig. 1.6). Based on the visual representation of the sextupole kick in Fig. 5.2, one can see that a geometric rotation of the phase space by 180° (corresponding to $\mu_x = \mu_y = 0.5$) would produce the *inverse* kick. This is illustrated in Fig. 5.4. As a result, we can intuitively conclude that any two sextupoles separated by a linear transformation with a global 180° phase advance would produce a compensated pair of sextupoles, as illustrated in Fig. 5.4(c). The transverse $\mathcal{R}_\perp$ could grow importantly between the two sextupoles, but the deformations will eventually be cancelled out at the exit of the second one. A key point however, is that only the transverse deformation is being compensated. In the longitudinal plane, the chromatic correction provided by the sextupoles (and mainly evolving within the drifts) remains. This gives us a clear design criterion to use sextupoles while preserving the dynamic aperture of the machine by limiting the transverse non-linearities.

One should note that the approach is similar to what was presented earlier in Chapter 4. By *choosing* to study the deformation of a an initially circular torus $\tilde{\mathbf{\Psi}}_0 = (\sqrt{I_x}\ e^{i\Theta_x}, \sqrt{I_y}\ e^{i\Theta_y}, 0)^\intercal$ through the system, we find a clear criteria to establish that a proper compensation was achieved. The compensator corresponds, once again, to the inverse of the map combined with a geometric rotation. Since this geometric interpretation takes place in the C.-S. phase space, one would also have to scale the strength of each sextupole by the optics $\Lambda_\pm$ at the sextupoles locations.

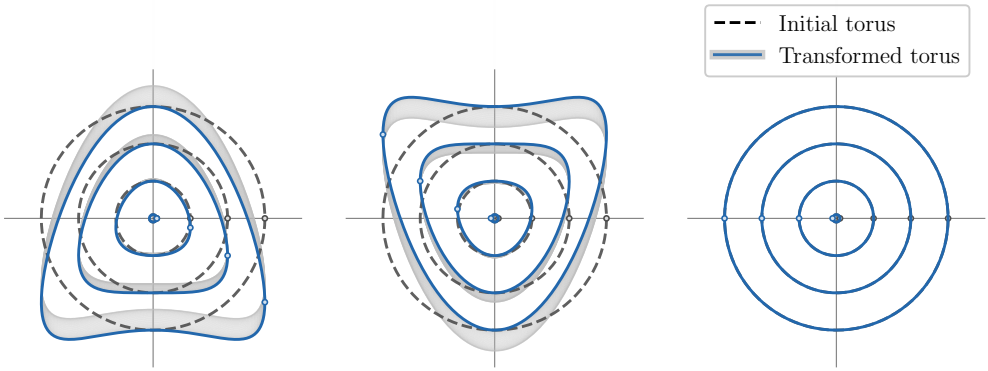

(a) After sextupole (b) After rotation (c) Compensated pair

Figure 5.4: Non-linear compensation of a sextupole pair. (a) Deformation after the first sextupole. (b) Deformation after a global 180° phase advance. (c) Restoration of $\mathcal{R}_\perp = 0$ after the second sextupole. The two sextupoles self-compensate in the transverse plane.

5.4.2 Beam-Beam Compensation

This next example, as it turns out, is where it all started. The research project which led to this dissertation initially had for objective to further our understanding of beam-beam compensation and study operational scenarios for the use of the beam-beam wire compensator (BBWC) device. Let us therefore present the core principles behind the idea of beam-beam compensation.

Alongside electron cloud effects, the main source of non-linearities in the LHC (and the upgraded High-Luminosity LHC (HL-LHC)) is the beam-beam (BB) effect, arising from the electromagnetic interaction between the two counter-rotating beams. In the interaction regions, the two beams share a common beam pipe and perturb one another. Head-On (HO) collisions take place at the interaction points, whereas Long-Range (LR) interactions are distributed on both sides of the IPs. These interactions, akin to multipolar errors, occur several times (≈50) per IR for the nominal bunches and strongly contribute to the excitation of high-order resonances, eventually leading to the reduction of dynamic aperture [47–49]. To mitigate this problem, current-carrying wires have been proposed as a correction device to compensate the BBLR kicks [50, 51]. More details can be found in Papers I – V (in appendix).

Equivalence Principle

In the transverse plane, the beam-beam kick from a gaussian bunch of protons with size σ is purely radial and scales with the radial distance, r, following (see Paper IV and Paper V):

$$\Delta p_r = -e\frac{\mu_0}{2\pi r}\,(IL)_{\text{eq}} \times \left(1 - e^{-r^2/2\sigma^2}\right)\ , \tag{5.17}$$

where $(IL)_{\text{eq}} = -N_b \cdot (ec) \cdot [(1+\beta_r^2)/(2\beta_r)]$ is the equivalent current for a bunch of intensity N_b traveling with a relativistic velocity parameter β_r. One can see that the beam-beam *long-range* kick (BBLR, a regime where $r \gg \sigma$) is equivalent to the kick of an infinite wire powered with the equivalent current $(IL)_{\text{eq}}$. In turn, it can be shown that the magnetic field of an infinite wire is the one of a pure multipole, exciting contributions from all multipolar components (Paper IV):

$$(k_n^+ L + i k_n^\times L) = -n!\left(\frac{q_0}{\mathrm{p}_0}\frac{\mu_0}{2\pi}\right)\frac{(IL)}{(x_w + i y_w)^{n+1}} \tag{5.18}$$

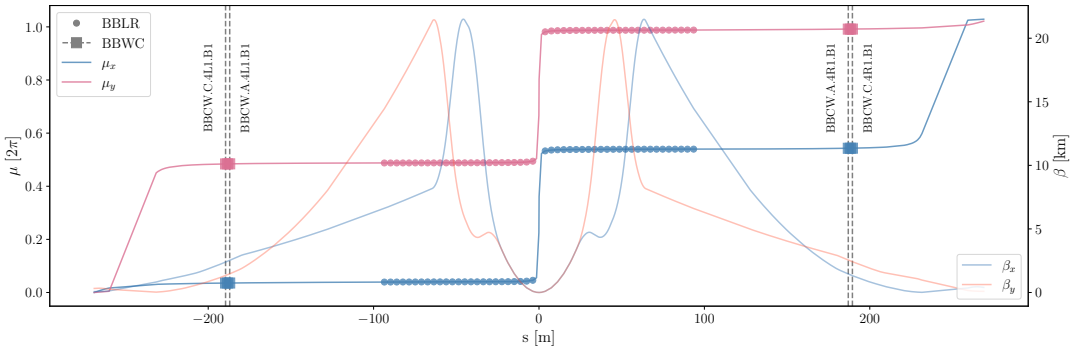

Figure 5.5: HL-LHC optics around IP1 at the end of the luminosity-levelling (see Paper IV). The location of the BBWCs is shown with coloured squares whereas the BBLRs kicks are shown with the coloured dots. Both the BBLRs and the BBWCs are in phase.

As such, the effect on the beam dynamics scales with the C.-S. β-functions (β_x, β_y) at the location of the kick and depends on the beta ratio, $\rho = \beta_y/\beta_x$. In principle, any single BBLR kick can be naturally compensated using a dedicated BBWC installed in phase at the appropriate beta ratio ($\rho_{\mathrm{BBLR}} = \rho_{\mathrm{BBWC}}$) and at the appropriate distance from the beam. That being said, the HL-LHC lattice contains many BBLRs distributed over the IRs (≈50, with varying beta ratios), and only 2 BBWCs located after the separation dipoles on each sides of the IRs, as shown in Fig. 5.5. This specific compensation scheme, introduced and thoroughly studied in earlier work [52], makes use of the antisymmetric optics of the IRs to reduce the number of BBWCs required. Indeed, with the phase advance between the BBLRs being negligible and the antisymmetric optics of HL-LHC (left to right, $\rho_{\mathrm{L}} = 1/\rho_{\mathrm{R}}$), it has been shown that the overall RDTs of the lattice could be optimally compensated using only a pair of wires.

This equivalence principle — reducing 50 BBLRs to 2 BBWCs — is an important feature of the problem. Departing from the idealized compensation scheme presented above, we wish to show that the non-linear residual can be used to study the problem under more general conditions — *i.e.* using the complete LHC lattice. More importantly, we wish to study the compensation of a set realistic beam-beam kicks (from the 6D Hirata method [18]), which we cannot express simply in terms of Lie algebra to get a transformation of $\mathbf{\Psi}$. Hence, the methods developed over the last few chapters need to be replaced by regular particle tracking. That being said, the insight gained through the dissertation remains.

To start, we distribute a set of particles on a circular torus of fixed radius following $\tilde{\boldsymbol{\psi}}_0 = (r_x\, e^{i\phi_x}, r_y\, e^{i\phi_y}, 0)^\intercal$ where ϕ_x and ϕ_y are used to sample the entire torus densely. For N particles, we can choose $(\phi_x, \phi_y) = (2\pi\nu_x N, 2\pi\nu_x N)$ where ν_x and ν_y are arbitrary frequencies which only need not to satisfy any resonant conditions — and so should be taken to be two independent irrational numbers. As a first example, the idealized case of a single isolated BBLR kick is shown in Fig. 5.6(a). The particles are tracked in the physical phase space and then normalized according the the usual C.-S. normalization after the kick. One can see the very same smearing concept as of Fig. 5.2, here made visible with particles and regular tracking.

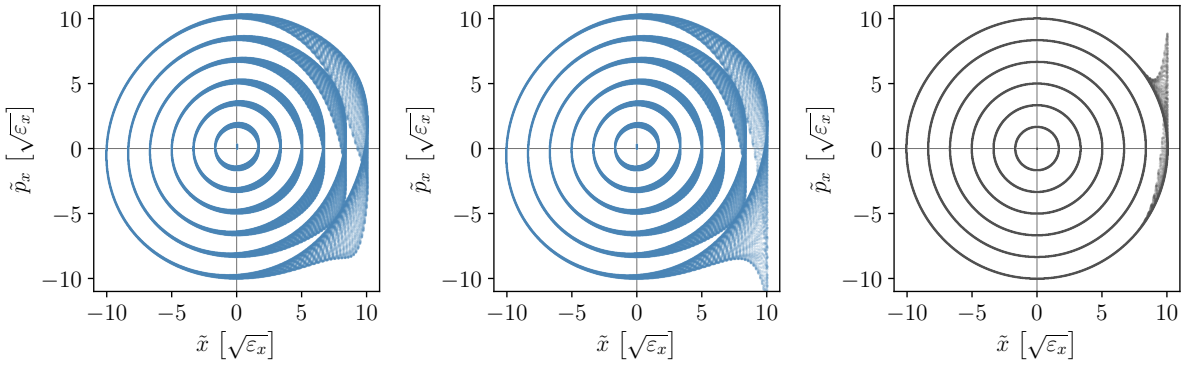

(a) BBLR kick (b) BBWC kick (c) Compensation

Figure 5.6: Torus deformation seen from regular particle tracking. (a) BBLR kick, computed from the 6D Hirata method [18]. (b) BBWC kick computed from an infinite current-carrying wire (see Paper IV). (c) Compensation of a single BBLR kick with the appropriate BBWC. At large amplitudes, the long-range approximation is no longer valid.

Since the physical dimensions of the beam are relevant for this applied case, the C.-S. coordinates are expressed in units of emittance $\sqrt{\varepsilon}$, such that $\tilde{x} = 1\ \sqrt{\varepsilon_x} \ \mapsto \ x = 1\ \sqrt{\beta_x \varepsilon_x} = 1\ \sigma_x$, which relates to the beam size in each plane. In Fig. 5.6(b), the equivalent BBWC kick is shown, computed by infinite current-carrying wire (as in Paper IV). One can see that the deformation is similar to that of the BBLR up to some amplitude. The difference is shown in Fig. 5.6(c) when the two kicks are applied sequentially (in compensation), where we see that a circular torus is retrieved. At large amplitudes, the opposing beam is in close range and the long-range approximation of eq. (5.17) is no longer valid.

As done previously, the non-linear residual $\mathcal{R}_\perp$ can be used to study the quality of the compensation as a function of the initial position of the particles (here with $x_0 - ip_{x_0} = r_x e^{i\phi_x}$). The situation illustrated in Fig. 5.6(c) is studied for various initial conditions in Fig. 5.7(a). One can see that the compensation is excellent over the entire transverse space, up to a horizontal initial amplitude of 8 σ_x for an opposing beam located at around 11 σ_x. It should be noted, however, that this idealized compensation considers a perfectly round beam, which can naturally be compensated with a single wire.

When the opposing beam is not round, as shown in Fig. 5.7(b), the compensation is significantly altered and the long-range approximation breaks down much earlier than in Fig. 5.7(a). An interesting finding — which can easily be tested and validated through the measure of the non-linear residual — is that a pair of wires can be used to retrieve a satisfactory compensation, as shown in Fig. 5.7(c). Indeed, placing a pair of wires with half the current at the focal points of an elliptic beam allows us to compensate the beam-beam kick almost as effectively as in the ideal round case. Mathematically, the two situations overlap when the elliptical beam is changed into a round beam, with the two focal points ultimately located at the center of the circle. This interesting case study is an example of a situation which would be difficult to analyse analytically, but which is made simple by the use of the non-linear residual.

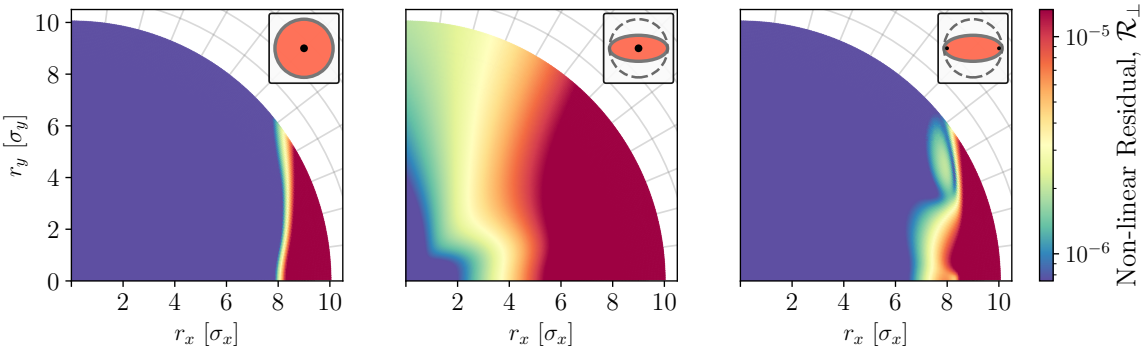

(a) Round beam (b) Non-round beam (c) Elliptic compensation

Figure 5.7: Non-linear residual for compensation of a single beam-beam long-range kick. (a) Round beam. (b) Non-round beam, showing partial compensation. (c) Non-round beam, compensated with two wires (half current) placed at the focal points of the opposing beam. The beam shape considered is shown in each of the insets in the right corners.

5.5 Dynamic Aperture Studies

As mentioned earlier, the practical goal of the approach presented is to inform us and guide us in optimizing the lattice design. It should be said that the methods presented here bear strong parallels with the *linear aperture* of É. Forest [43] which were based on the *smear*. That being said, the author had no knowledge of this text prior to these studies and the findings were found independently (thereby showing a convincing convergence of ideas).

Fig. 5.7 showed an idealized single BBLR compensation. In a more realistic scenario, 50 BBLRs need to be compensated with the help of 2 BBWCs as discussed around Fig. 5.5. Although we typically assume that there is no phase advance between each long-range interactions, this is of course an approximation. More importantly, since the optics continuously vary along the interaction points, each long-range interaction varies in strength and there is no trivial solution on how to operate the BBWC (*i.e.* choosing the distance and the current at which to operate) to optimally compensate the non-linear perturbations. The ultimate figure of merit to inform us on quality of the compensation is the dynamic aperture. That being said, dynamic aperture studies are costly and often require several days of computation — even when parallelized over 10,000 CPUs.

The conceptual results of this chapter suggest that by improving the linearity of the machine ($\mathcal{R}_\perp \to 0$), one should be able to push the chaotic layer away from the reference particle and improve the dynamic aperture. More precisely: to extend the dynamic aperture beyond the 6 σ target of the HL-LHC project, one should ensure that the linearity of the machine is satisfactory up to that point, as shown in Fig. 5.8. Here, a circular torus is tracked through an isolated segment of the HL-LHC lattice — namely through IR1, where the BBLR interactions take place. In Fig. 5.8(a), one can see that without BBWC compensation, the non-linear residual rapidly decreases between the core of the beam ($(r_x, r_y) \to 0$) and the 6 σ boundary shown with the black line. However, when powering the BBWC at a suitable distance and current, the linearity of the core is extended beyond the 6 σ boundary, as shown in Fig. 5.8(b). Here, $\mathcal{R}_\perp$ is computed in a single pass through IR1, instead of the 10^6 turns required by typical dynamic aperture studies.

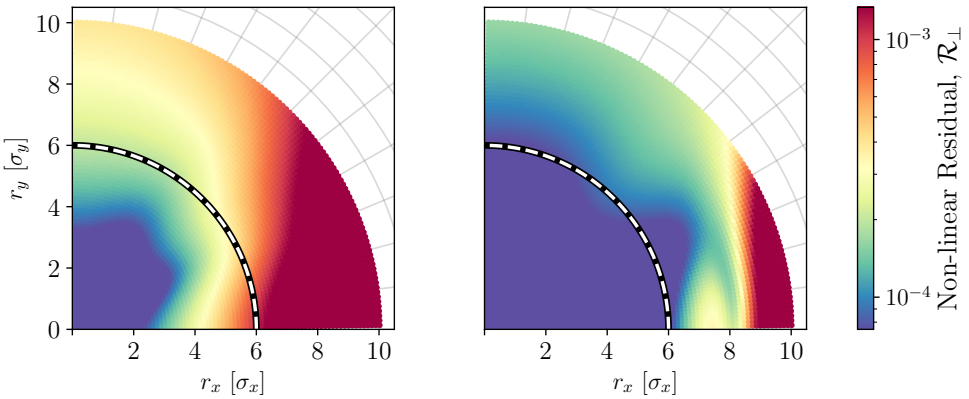

(a) Baseline, BBCW OFF (b) Baseline, BBCW ON

Figure 5.8: Non-linear residual for a realistic beam-beam compensation through IR1 in the HL-LHC lattice. (a) Without compensation, the non-linear residual decreases between the core and the 6 σ target. (b) With compensation, the linearity of the core is extended beyond the 6 σ target. The BBWC are operated at 400 A $\cdot$ m and 15 σ in this case.

Assuming that the dynamic aperture of the machine is mainly limited by the transverse non-linearities in IR1 and IR5 (which are very similarly designed), one would expect that optimizing $\mathcal{R}_\perp$ in those regions could have a significant impact on improving the dynamic aperture of the machine as a whole. More details can be found in Paper IV. To study this, various operational conditions for the BBWC (current and distance) are considered. In each case, the non-linear residual $\mathcal{R}_\perp$ is evaluated in a narrow band around the 6 σ target highlighted in Fig. 5.8. The worst value (maximum $\mathcal{R}_\perp$) is kept as an indicator of the compensation and shown for all distances x_w and currents I_w in Fig. 5.9(a). It should be noted that only IR1 is considered to evaluate the non-linear residual. In a second step, the dynamic aperture is evaluated for the entire machine by tracking particles for the usual 10^6 turns required in typical DA studies (see Paper IV and Paper V). The result is shown in Fig. 5.9(b).

Comparing the two metrics, one can see that there is a strong correlation between minimizing the non-linear residual and maximizing the dynamic aperture. The salient features of Fig. 5.9(b) can indeed be observed in Fig. 5.9(a): the optimal band in the center, a gradual improvement of the DA from the powering of the wires ($I_w = 0$) up to this optimal band, and the worsening of the DA above this band (overpowering of the BBWCs). Naturally, the precise variation of the dynamic aperture is not fully captured by the non-linear residual, since the former is a global effect which also depends on the interaction of the compensation with the rest of the lattice.

Finally, important insight can be gathered on the basis of Fig. 5.9(a), namely the effect of the compensation on the so-called PACMAN bunches, which receive on average half of the beam-beam kicks compared with the nominal bunches. Indeed, the colorbar of Fig. 5.9(a) additionally shows the corresponding BBLR residual strength as a fraction of a total compensation. This metric was obtained by scaling down the BBLR strength between 0 and 100% without compensation and evaluating $\mathcal{R}_\perp$ in each cases. The simple conclusion is that anywhere within the yellow band of Fig. 5.9(a), PACMAN bunches (seeing 50% of BBLRs) are fully compensated whereas nominal bunches are only partially (50%) compensated. Hence, there is a large set of BBWC operational conditions which significantly improve the DA for both nominal and PACMAN bunches.

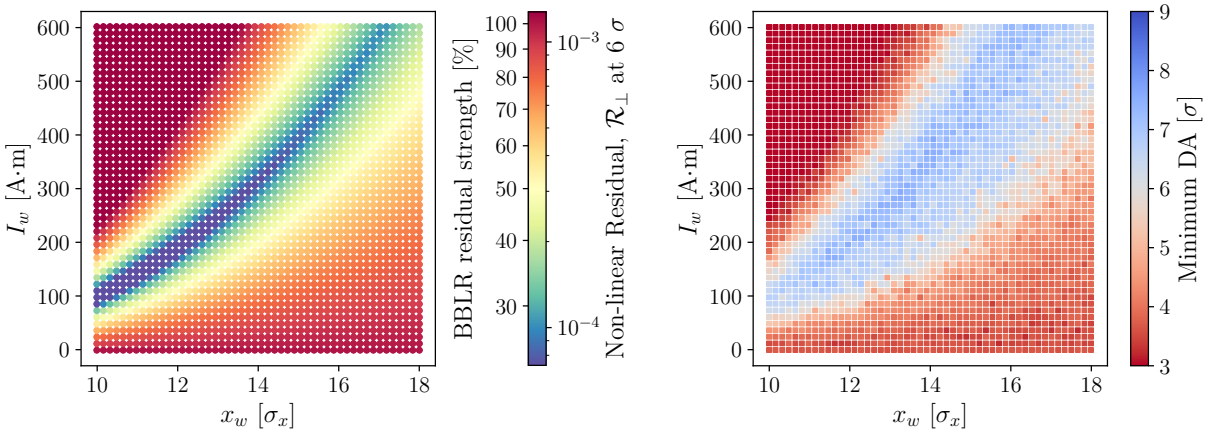

(a) Non-linear residual, IR1 (b) DA, full lattice

Figure 5.9: Comparison of the non-linear residual with the dynamic aperture for the problem of beam-beam compensation. (a) Non-linear residual, evaluated through IR1. (b) Dynamic aperture for the full lattice, obtained by tracking particles for 10^6 turns.

5.6 Eigensolutions for Non-Linear Periodic Systems

In the previous sections, an insightful description of non-linear transformations was provided based on a visual interpretation of torus deformation and the introduction of the non-linear residual $\mathcal{R}$ as a metric to quantify said deformation. In the Courant-Snyder phase space, we showed that all single-element transformations can be placed into one of three categories: horizontal shears, vertical shears and rotations (Proposition 5.2). This topological description ultimately led to the demonstration of a correlation between the non-linear residual and the dynamic aperture, an important metric for lattice design. To close this chapter (and the thesis), we shall return to the general non-linear transformation presented in Proposition 5.1 and look for methods of analysis to further our understanding on non-linear effects — namely, Normal Form Analysis.

Outside of the aforementioned analytic tools, it should be noted that the Fourier description introduced in Chapter 2 always holds for integrable tori. The reader shall therefore remember that numerical approximations of the motion — constructed through the Numerical Analysis of the Fundamental Frequencies (NAFF, Section 2.2.2) — can always be obtained through tracking whenever analytic descriptions fail. Establishing a strong theoretical background for the interpretation of these numerical results is, ultimately, the overarching goal of the thesis.

5.6.1 The Hénon map

Following our study of linear systems in Chapter 4, one would like to know what happens to the motion when stepping outside of the assumptions of linear systems. To study this, we consider once again on-momentum tori (with $P_\zeta = 0$) — to ensure that the transverse planes remain decoupled from the longitudinal one — and we add to the list of elements of Table 4.2 the simplest non-linear multipole magnet. This is the normal thin sextupole, $H_s^+ = \frac{1}{6}k_2^+(x^3 - 3xy^2)$, which transforms Ψ_x and Ψ_y according to:

$$e^{(:-H_s^+\,ds:)}\,\boldsymbol{\Psi} : \begin{cases} e^{(:-H_s^+\,ds:)}\,\Psi_x = \Psi_x + i\frac{1}{2}\sqrt{\beta_{x_0}}\,k_2^+\,\left(X^2 - Y^2\right) \\ e^{(:-H_s^+\,ds:)}\,\Psi_y = \Psi_x - i\sqrt{\beta_{y_0}}\,k_2^+\,(XY) \end{cases} \tag{5.19}$$

Consider the effect of this sextupole, followed by an uncoupled linear map $\mathcal{M}_{1\to 2}$. In the physical phase space, the global transformation is $\mathcal{M} = \mathcal{M}_{1\to 2} \circ e^{(:-H_s^+\,ds:)}$. Since we know that $\tilde{\mathcal{M}}_{1\to 2} = \tilde{R}(\Delta\vec{\mu})$ simplifies to a pure rotation in the C.-S. phase space, it is convenient to study the global map $\tilde{\mathcal{M}}$ directly in that space, where the transformation of the sextupole can be obtained by rewriting the Hamiltonian H_s^+ in terms of the C.-S. coordinates $\tilde{x}$ and $\tilde{y}$. Assuming an uncoupled linear case, this can be done directly with the Courant-Snyder parameter β_x following $x \mapsto \sqrt{\beta_x}\,\tilde{x}$ and $y \mapsto \sqrt{\beta_y}\,\tilde{y}$, which yields $\tilde{H}_s^+ = \frac{1}{6}k_2^+(\beta_x^{3/2}\tilde{x}^3 - 3\sqrt{\beta_x}\beta_y\,\tilde{x}\tilde{y}^2)$. Letting $\eta = \beta_y/\beta_x$, the sextupole transformation in the Courant-Snyder phase space becomes:

$$e^{(:-\tilde{H}_s^+\,ds:)}\,\tilde{\boldsymbol{\Psi}} : \begin{cases} e^{(:-\tilde{H}_s^+\,ds:)}\,\tilde{\Psi}_x = \tilde{\Psi}_x + i\frac{1}{2}\beta_x^{3/2}\,k_2^+\,\left(\tilde{X}^2 - \eta\,\tilde{Y}^2\right) \\ e^{(:-\tilde{H}_s^+\,ds:)}\,\tilde{\Psi}_y = \tilde{\Psi}_x - i\beta_x^{3/2}\,k_2^+\,\eta\,\left(\tilde{X}\tilde{Y}\right) \end{cases} \tag{5.20}$$

Finally, using $\tilde{X} = \frac{1}{2}(\tilde{\Psi}_x + \tilde{\Psi}_x^*)$, the global map of our system can be written as:

$$\tilde{\mathcal{M}}\,\tilde{\mathbf{\Psi}} : \begin{cases} \tilde{\mathcal{M}}\,\tilde{\Psi}_x = e^{i(2\pi\mu_x)}\Big(\tilde{\Psi}_x + h_1\Big((\tilde{\Psi}_x + \tilde{\Psi}_x^*)^2 - \eta\,(\tilde{\Psi}_y + \tilde{\Psi}_y^*)^2\Big)\Big) \\ \tilde{\mathcal{M}}\,\tilde{\Psi}_y = e^{i(2\pi\mu_y)}\Big(\tilde{\Psi}_y - 2h_1\eta\,(\tilde{\Psi}_x + \tilde{\Psi}_x^*)(\tilde{\Psi}_y + \tilde{\Psi}_y^*)\Big) \end{cases}, \tag{5.21}$$

with $h_1 = i\frac{1}{8}\beta_x^{3/2}\,k_2^+$ and again $\eta = \beta_y/\beta_x$. One recognizes that eq. (5.21) is indeed a non-linear transformation of $\tilde{\mathbf{\Psi}}$, as introduced in Proposition 5.1. In the particular case where $h_1 = -i/4$, eq. (5.21) is the 4D Hénon map [15]. Furthermore, if the non-linear coupling parameter η (which controls the contribution of Ψ_y in the Ψ_x transformation and vice versa) vanishes, $\eta = 0$, or if the y-coordinate is zero, $\tilde{\Psi}_{y_0} = 0$, then eq. (5.21) reduces to the well-known Hénon map [24, 25]:

$$\text{(Hénon map)} \qquad \tilde{\mathcal{M}}\,\tilde{\Psi}_x = e^{i(2\pi\mu_x)}\Big(\tilde{\Psi}_x - \frac{i}{4}(\tilde{\Psi}_x + \tilde{\Psi}_x^*)^2\Big)\,. \tag{5.22}$$

As discussed in Chapter 1, this historical map is an important example of a "simple" chaotic system. What we have just showed is that it describes precisely the horizontal motion in a lattice composed of an uncoupled linear section and single thin sextupole kick. The effective hamiltonian for the global transformation is not trivial to describe [15], but the transformation itself, eq. (5.22), and its physical composition (linear section and thin sextupole) are clear.

We should emphasize that the motion described by eq. (5.22) takes place in the Courant-Snyder phase space directly. In earlier chapters (Fig. 1.7 and Fig. 2.11), the Hénon motion was transported in the physical phase space by choosing a particular set of optics. A key aspect of the Hénon map however, is that it only depends on a single map parameter, μ_x, which corresponds to the phase advance of the linear section. The value of h_1 is irrelevant and changing it is equivalent to a simple rescaling of the entire phase space (*i.e.* changing $h_1 \mapsto a h_1$ is equivalent to rescaling the coordinates by $\tilde{\Psi}_x \mapsto a\tilde{\Psi}_x$, and leaves the picture unchanged).

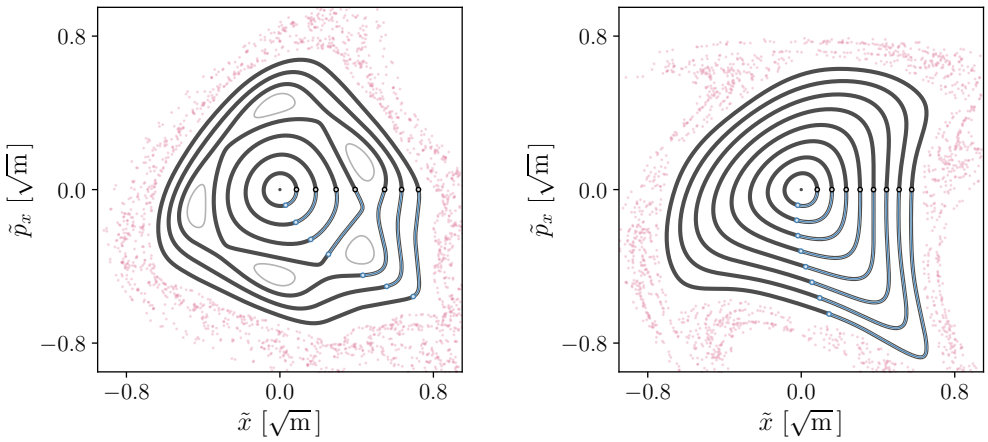

(a) $\mu_x = 0.2071$ (b) $\mu_x = 0.2981$

Figure 5.10: Invariant tori of the 2D Hénon map (grey) outside of the chaotic region (red) for two map parameters. (a) $\mu_x = 0.2071$ and (b) $\mu_x = 0.2981$. The invariant tori were constructed using the NAFF approach (see Chapter 2) after tracking the corresponding particles for 10^4 turns. The phase advance is shown on each torus, after one iteration of the map.

5.6.2 Normal Form Analysis

We now look for analytic methods to obtain the (approximate) eigensolutions of non-linear systems. To do so, the concepts presented throughout the dissertation can be extended to the study of Normal Forms. For a rigorous treatment of Normal Forms (including distinction between resonant and non-resonant cases), the reader is referred to the original work of A. Bazzani, E. Todesco and G Turchetti [15]. What we provide here is an intuitive interpretation of the concepts, in continuity with the linear formalism presented in Chapter 4. Two key ideas make the basis of normal-form analysis, namely: an order-by-order construction of the eigensolutions and a generalisation of the dephasing condition, eq. (4.18).

Order-by-order

To keep track of the order of the expansions, we first introduce the normal-form basis vector $\boldsymbol{\rho} = (\rho_x, \rho_y, \rho_\zeta)^\intercal$, serving as a new generating element for arbitrary multivariate expansions. We define:

$$\boldsymbol{\rho} : \begin{cases} \rho_x \equiv \sqrt{2I_x} e^{i\Theta_x} \\ \rho_y \equiv \sqrt{2I_y} e^{i\Theta_y} \\ \rho_\zeta \equiv \sqrt{2I_\zeta} e^{i\Theta_\zeta} \end{cases} \quad \text{such that} \quad \widehat{\boldsymbol{\Psi}} : \begin{cases} \widehat{\Psi}_x = \rho_x \\ \widehat{\Psi}_y = \rho_y \\ \widehat{\Psi}_\zeta = \rho_\zeta \end{cases} . \tag{5.23}$$

One can see that $2I_x = \rho_x \rho_x^* = |\rho_x|^2$ is a conserved quantity (and idem for other planes). Following this definition, generic tori such as $\boldsymbol{\Psi}$ or $\tilde{\boldsymbol{\Psi}}$ can also be expressed in terms of $\boldsymbol{\rho}$. We therefore extend our original Fourier definition (eq. (2.8)) and write $\tilde{\boldsymbol{\Psi}}$ as:

$$\tilde{\boldsymbol{\Psi}}(\vec{\Theta}) \ : \ \begin{cases} \tilde{\Psi}_x = \sum_{\vec{n}} \tilde{A}_{\vec{n}} \ e^{i(\vec{n}\cdot\vec{\Theta})} = \sum_{jklmpq} \tilde{a}_{jklmpq} \, (\rho_x^j \rho_x^{*k})(\rho_y^l \rho_y^{*m})(\rho_\zeta^p \rho_\zeta^{*q}) \\ \tilde{\Psi}_y = \sum_{\vec{n}} \tilde{B}_{\vec{n}} \ e^{i(\vec{n}\cdot\vec{\Theta})} = \sum_{jklmpq} \tilde{b}_{jklmpq} \, (\rho_x^j \rho_x^{*k})(\rho_y^l \rho_y^{*m})(\rho_\zeta^p \rho_\zeta^{*q}) \\ \tilde{\Psi}_\zeta = \sum_{\vec{n}} \tilde{C}_{\vec{n}} \ e^{i(\vec{n}\cdot\vec{\Theta})} = \sum_{jklmpq} \tilde{c}_{jklmpq} \, (\rho_x^j \rho_x^{*k})(\rho_y^l \rho_y^{*m})(\rho_\zeta^p \rho_\zeta^{*q}) \end{cases} , \tag{5.24}$$

with $\{j, k, l, m, p, q\} \in \mathbb{N}$. Eq. (5.24) highlights that a torus can be viewed either as a sum of rotating vectors (the epicycles), or equivalently as a sum of multi-dimensional volume elements; obtained from the Hadamard product of the normal-form basis vectors. The left-hand side allows for a physical interpretation of the tori; and explicitly relates to the spectral content, as discussed previously. In contrast, the right-hand side provides an algebraic (polynomial) structure which relates directly to the Normal Form. Since the construction $\boldsymbol{\Psi}(\boldsymbol{\rho})$ is essentially a canonical transformation from $\widehat{\boldsymbol{\Psi}} \mapsto \tilde{\boldsymbol{\Psi}}$, the coefficients $\tilde{a}_{jklmpq}$ are not arbitrary and must satisfy the symplectic condition. Based on Demonstration 3.1, these coefficients must be such that $[\tilde{\Psi}_x, \tilde{\Psi}_x^*] = [\tilde{\Psi}_y, \tilde{\Psi}_y^*] = [\tilde{\Psi}_\zeta, \tilde{\Psi}_\zeta^*] = 2i$ when starting from $[\rho_x, \rho_x^*] = [\rho_y, \rho_y^*] = [\rho_\zeta, \rho_\zeta^*] = 2i$.

It should be emphasized that $\tilde{a}_{jklmpq}$ are precisely the resonance driving terms (RDTs) used in the literature [14, 15, 53–55]. Additionally, one can see that $\boldsymbol{\Psi}(\boldsymbol{\rho})$ can be *collapsed* into $\boldsymbol{\Psi}(\vec{\Theta})$ at any point (meaning $\boldsymbol{\Psi}(\boldsymbol{\rho}) \mapsto \boldsymbol{\Psi}(\vec{\Theta})$) by summing the contribution of all RDTs which contribute to a given spectral line:

$$\tilde{A}_{\vec{n}} = \langle \vec{n} | \, \tilde{\Psi}_x \rangle = \sum_{jklmpq} \begin{cases} \tilde{a}_{jklmpq} \, (2I_x)^{\frac{j+k}{2}} (2I_y)^{\frac{l+m}{2}} (2I_\zeta)^{\frac{p+q}{2}} & \text{if } (j,l,p) - (k,m,q) = \vec{n} \\ 0 & \text{otherwise} \end{cases} \tag{5.25}$$

For that reason, spectral components like $\tilde{A}_{\vec{n}}$ are sometimes referred-to as the *combined* RDTs in the literature [14]. We shall shortly use these concepts to construct the Normal Form of the 2D Hénon map "up to 6^{th} order". Here, the order refers to the polynomial degree in the normal-form variables $\boldsymbol{\rho}$. In this framework, ρ_x and ρ_x^* are treated as formally independent complex variables and both contribute to the order. For an expansion of order n (*i.e.* $\rho_x^j \rho_x^{*k} \propto |\rho_x|^n$), all terms of total degree higher than n are neglected, that is $\mathcal{O}(|\rho_x|^{n+1})$, or $\mathcal{O}(I_x^{(n+1)/2})$.

Dephasing condition

Let us go back to the dephasing equation (eq. (4.18)), which was foundational for Chapter 4. Indeed, it allows to establish a clear condition for $\boldsymbol{\Psi}$ to be an eigensolution of $\mathcal{M}$:

$$\mathcal{M}\,\boldsymbol{\Psi}(\vec{\Theta}) = \boldsymbol{\Psi}(\vec{\Theta} + 2\pi\vec{Q})\ . \tag{5.26}$$

As it turns out, this equation is perfectly general. If $\mathcal{M}$ is a non-linear map, one simply needs to make explicit the fact that the fundamental frequencies $\vec{Q}$ are functions of the actions $\vec{Q}(\vec{I})$. However, the insight of eq. (5.26) remains: a torus $\boldsymbol{\Psi}$ is an eigensolution of $\mathcal{M}$ if its transformation corresponds to a simple dephasing of the angle variables $\vec{\Theta} \mapsto \vec{\Theta} + 2\pi\vec{Q}(\vec{I})$.

The normal-form motion is an amplitude dependent rotation: to each set of actions $\vec{I}$ corresponds a set of fundamental frequencies $\vec{Q}$. Once again, $\vec{Q}$ can be written in terms of the normal-form basis vector $\boldsymbol{\rho}$. However, due to additional symmetries on the angle coordinates [15, Chap. 3], the expansion of $\vec{Q}$ can be expressed as powers of $I_x^j I_y^k I_\zeta^l$ directly, which yields:

$$2\pi\vec{Q}: \begin{cases} 2\pi Q_x = \sum\limits_{jkl} \omega_{x,jkl}\ (\rho_x\rho_x^*)^j(\rho_y\rho_y^*)^k(\rho_\zeta\rho_\zeta^*)^l \\ 2\pi Q_y = \sum\limits_{jkl} \omega_{y,jkl}\ (\rho_x\rho_x^*)^j(\rho_y\rho_y^*)^k(\rho_\zeta\rho_\zeta^*)^l \\ 2\pi Q_\zeta = \sum\limits_{jkl} \omega_{\zeta,jkl}\ (\rho_x\rho_x^*)^j(\rho_y\rho_y^*)^k(\rho_\zeta\rho_\zeta^*)^l \end{cases} \tag{5.27}$$

where $\omega_{x,jkl}$ ($\{j,k,l\} \in \mathbb{N}$) are coefficients to be found — in all planes. Recall, indeed, that $\vec{Q}(\vec{I})$ is an emerging property of the map for any given action (see Chapter 2). To see how eq. (5.27) is linked to the dephasing condition, a short demonstration is given below.

Let us consider a 2D case and omit the plane index for simplicity. In Chapter 4, the dephasing equation $\Psi(\Theta) \mapsto \Psi(\Theta + 2\pi Q)$ informed us to look for solutions which could be obtained following $\tilde{A}_n \mapsto \tilde{A}_n e^{in(2\pi Q)}$, *i.e.* by changing the phase of each component uniformly. This is indeed appropriate for linear systems where the phase advance is independent of the action: any solution shall respect this unique condition, and the criteria is a strong one. In non-linear systems however, the phase advance depends on the action following eq. (5.27):

$$2\pi Q(I) = \omega_0 + \omega_1(\rho\rho^*) + \omega_2(\rho\rho^*)^2 + \omega_3(\rho\rho^*)^3 + \mathcal{O}(|\rho|^7)\ . \tag{5.28}$$

In such a case, imposing a uniform dephasing breaks the search for general solutions — only one particular solution with a given action I and corresponding phase advance Q can be found.

Instead, one should look for the effect of the map on the basis vector ρ itself. By definition, the transformation $\widehat{\mathcal{M}}\,\widehat{\Psi}$ is a pure rotation. Using $e^{a+b} = e^a(1 + b + \frac{1}{2}b^2 + \dots)$, we get:

$$\begin{aligned}\widehat{\mathcal{M}}\,\widehat{\Psi} = e^{i(2\pi Q(I))}\,\rho &= e^{i\omega_0}\left(1 + i\omega_1(\rho\rho^*) + \left(i\omega_2 - \tfrac{1}{2}\omega_1^2\right)(\rho\rho^*)^2 + \mathcal{O}(|\rho|^6)\right)\,\rho \\ &= e^{i\omega_0}\left(\rho + i\omega_1(\rho^2\rho^*) + \left(i\omega_2 - \tfrac{1}{2}\omega_1^2\right)(\rho^3\rho^{*2}) + \mathcal{O}(|\rho|^7)\right)\ ,\end{aligned} \tag{5.29}$$

which gives us the transformation of ρ through the map at various orders:

$$\begin{aligned}\text{(First order)} \qquad & e^{i(2\pi Q(I))}\,\rho \quad \mapsto \quad e^{i\omega_0}\,\rho \\ \text{(Second order)} \qquad & e^{i(2\pi Q(I))}\,\rho \quad \mapsto \quad e^{i\omega_0}\,\rho \\ \text{(Third order)} \qquad & e^{i(2\pi Q(I))}\,\rho \quad \mapsto \quad e^{i\omega_0}\,\rho + i\omega_1 e^{i\omega_0}(\rho^2\rho^*)\end{aligned} \tag{5.30}$$

where, again, ω_0 and ω_1 are coefficients to be found. One should note that the transformation to first and second order are identical. The variation of the phase advance with amplitude, therefore, is a third order effect. Based on eq. (5.29), the next correction to the phase advance shall arise as a fifth order effect, and so on. This result is an additional criteria which should be enforced when evaluating the dephasing condition. In fact, an alternative formulation of eq. (5.26) is:

$$\mathcal{M}\,\mathbf{\Psi}(\vec{\Theta}) = \mathbf{\Psi}(\vec{\Theta} + 2\pi\vec{Q}(\vec{I})) \qquad \Leftrightarrow \qquad \mathcal{M}\,\mathbf{\Psi}(\boldsymbol{\rho}) = \mathbf{\Psi}(e^{i(2\pi\vec{Q}(\vec{I}))}\,\boldsymbol{\rho})\ , \tag{5.31}$$

which are both equivalent. On the left-hand side of each equality, we compute the effect of the transformation. On the right-hand side of each equality, we enforce what we expect to find — a dephasing of the angles, or, the rotation of the normal-form basis vector. The interest of the $\boldsymbol{\rho}$-based approach is that it enforces the expected dependance of the phase advance on the amplitude, order-by-order, whereas the $\vec{\Theta}$-based approach is agnostic to this dependance.

The Normal Form procedure, therefore, can be summarized as follows: establish a trial torus $\mathbf{\Psi}$ truncated at the first order; transform it through the map $\mathcal{M}$; truncate the result; and finally, compare it with the expected solution from the dephasing condition (also truncated). Then, solve for the unknown coefficients (a_{jklmpq}, combined with the emerging $\omega_{x,j'k'l'}$) : this yields the first order eigensolution. The procedure is then repeated, order-by-order, to obtain higher order solutions. In fact, the first order solution was already explicitly given in Chapter 4. Truncating the equations of Proposition 5.1 to first order yields a linear problem. In that case, solving for the coefficients leads to the construction of the M matrix from Proposition 4.2: the coefficients $\{a_{jklmpq}, b_{jklmpq}, c_{jklmpq}\}$ (with $|jklmpq| \leq 1$) are then given by the eigenvectors of M and the three emerging coefficients $\omega_{x,000}, \omega_{y,000}, \omega_{\zeta,000}$ correspond to the eigenvalues of M. We can therefore start the Normal Form procedure to second order directly (*i.e.* start in the C.-S. phase space with $\tilde{\mathbf{\Psi}}$) by building on the results of Chapter 4.

We should emphasize, finally, that this procedure is a *propagative* method: we do not study the properties of the map *per se*; rather, we start from a trial solution of order n and look for the coefficients which respect the dephasing condition. Unlike the classical Lie-operator approach, where one seeks a generating function that conjugates the map to its Normal Form, our proposal is to treat the Normal Form as a propagative eigensolution problem, solved order-by-order. Let us now illustrate the above ideas by constructing the Normal Form of the 2D Hénon map, up to 3^{rd} order explicitly, and up to 6^{th} order for the plots.

Application to the Hénon map

Let us construct, order-by-order, approximate eigensolutions for the 2D Hénon map, eq. (5.22):

$$\text{(Hénon map)} \qquad \tilde{\mathcal{M}}\,\tilde{\Psi} = e^{i(2\pi\mu)}\Big(\tilde{\Psi} - \frac{i}{4}(\tilde{\Psi}+\tilde{\Psi}^*)^2\Big) \tag{5.32}$$

where we omit the x-index for simplicity. Based on eq. (5.24)(for $\tilde{\Psi}$) and eq. (5.27)(for $Q(I)$), we expect solutions of the form:

$$\tilde{\Psi} = \sum_{jk} \tilde{a}_{jk}\,(\rho^j \rho^{*k}), \quad \text{and} \quad 2\pi Q(I) = \sum_j \omega_j\,(\rho\rho^*)^j \ . \tag{5.33}$$

To first order, $\tilde{\Psi}^{(1)}$ and $Q^{(1)}$, we get the result from the linear contribution of the map:

$$\tilde{\Psi}^{(1)} = \rho \ , \qquad \text{and} \qquad 2\pi Q^{(1)} = 2\pi\mu \ , \tag{5.34}$$

which fixes the coefficients $\tilde{a}_{00}=0$, $\tilde{a}_{01}=0$, $\tilde{a}_{10}=1$ and $\omega_0 = 2\pi\mu$. To second order, we therefore look for solutions of the form (note eq. (5.30)):

$$\tilde{\Psi}^{(2)} = \tilde{\Psi}^{(1)} + \tilde{a}_{20}\,\rho^2 + \tilde{a}_{11}\,\rho\rho^* + \tilde{a}_{02}\,\rho^{*2}, \qquad \text{and} \qquad 2\pi Q^{(2)} = 2\pi Q^{(1)} \ , \tag{5.35}$$

where new coefficients need to be found. Transporting $\tilde{\Psi}^{(2)}$ on one hand (left-hand side) and rotating the basis vector ρ on the other (right-hand side) allows us to enforce the dephasing condition eq. (5.31) and yields the system of equations:

$$\begin{cases} (\tilde{a}_{20} - \frac{i}{4})\,e^{i\omega_0} = \tilde{a}_{20}\,e^{2i\omega_0} \\ (\tilde{a}_{11} - \frac{i}{2})\,e^{i\omega_0} = \tilde{a}_{11} \\ (\tilde{a}_{02} - \frac{i}{4})\,e^{i\omega_0} = \tilde{a}_{02}\,e^{-2i\omega_0} \end{cases} \quad \Rightarrow \quad (\tilde{a}_{20},\tilde{a}_{11},\tilde{a}_{02}) = \Big(\frac{i/4}{1-e^{i\omega_0}},\ \frac{i/2}{1-e^{-i\omega_0}},\ \frac{i/4}{1-e^{-3i\omega_0}}\Big) \tag{5.36}$$

from which we get all the second order coefficients ($\omega_0 = 2\pi\mu$ was already found at the first order). With $\tilde{\Psi}^{(2)}$ in hand, we look for the third order expansion:

$$\begin{cases} \tilde{\Psi}^{(3)} &= \tilde{\Psi}^{(2)} + \tilde{a}_{30}\,\rho^3 + \tilde{a}_{21}\,\rho^2\rho^{*1} + \tilde{a}_{12}\,\rho^1\rho^{*2} + \tilde{a}_{03}\,\rho^{*3} \\ 2\pi Q^{(3)} &= 2\pi Q^{(2)} + \omega_1(\rho\rho^*) \end{cases} . \tag{5.37}$$

Again, we use the dephasing condition to solve for the coefficients. This time, the effect on ρ is not a simple rotation, but rather $e^{i(2\pi Q(I))}\,\rho \ \mapsto\ e^{i\omega_0}\,\rho + i\omega_1 e^{i\omega_0}(\rho^2\rho^*)$ as per eq. (5.30). This leads to:

$$\begin{cases} \Big(\tilde{a}_{30} - \frac{i(\tilde{a}_{20}+\tilde{a}^*_{02})}{2}\Big)\,e^{i\omega_0} = \tilde{a}_{30}\,e^{3i\omega_0} \\ \Big(\tilde{a}_{21} - \frac{i(\tilde{a}_{20}+\tilde{a}_{11}+\tilde{a}^*_{11}+\tilde{a}^*_{02})}{2}\Big)\,e^{i\omega_0} = (\tilde{a}_{21}+i\omega_1)\,e^{i\omega_0} \quad \Rightarrow \quad \omega_1 = -\frac{i(\tilde{a}_{20}+\tilde{a}_{11}+\tilde{a}^*_{11}+\tilde{a}^*_{02})}{2} \\ \Big(\tilde{a}_{12} - \frac{i(\tilde{a}_{02}+\tilde{a}_{11}+\tilde{a}^*_{11}+\tilde{a}^*_{20})}{2}\Big)\,e^{i\omega_0} = \tilde{a}_{12}\,e^{-i\omega_0} \\ \Big(\tilde{a}_{03} - \frac{i(\tilde{a}_{02}+\tilde{a}^*_{20})}{2}\Big)\,e^{i\omega_0} = \tilde{a}_{03}\,e^{-3i\omega_0} \end{cases} \tag{5.38}$$

The second equation (in $\tilde{a}_{21}$) directly yields the value of the phase advance correction, ω_1, while the others provide the values of $\{\tilde{a}_{30},\tilde{a}_{12},\tilde{a}_{03}\}$ based on the second order coefficients. We are therefore left with a single unknown, $\tilde{a}_{21}$. As discussed below eq. (5.24), the coefficients are not

arbitrary and must satisfy an additional symplectic constraint to ensure that $\tilde{\Psi}(\rho)$ is a canonical construction. Here, while the complete rotation of the basis vector $e^{i(2\pi Q(I))}\,\rho$ from eq. (5.31) represents an exact symplectic transformation, the truncated version $e^{i\omega_0}\,\rho + i\omega_1 e^{i\omega_0}(\rho^2\rho^*)$ does not automatically preserve symplecticity. The remaining degree of freedom in $\tilde{a}_{21}$ is precisely what restores it. At the third order, the symplectic condition for $\tilde{a}_{21}$ reads:

$$\tilde{a}_{21} + \tilde{a}_{21}^* = 2|\tilde{a}_{02}|^2 - 2|\tilde{a}_{20}|^2 \tag{5.39}$$

which fixes the real part of $\tilde{a}_{21}$ and leaves the imaginary part free (gauge choice). Following this step, all the coefficients for the third order Normal Form $\tilde{\Psi}^{(3)}$ are known. As we have shown, the procedure is algorithmic and can be carried out to higher order, albeit with increasing complexity in the expressions of the coefficients, $\tilde{a}_{jk}$ and $\omega_{j'}$. In the end, we obtain (explicitly):

$$\tilde{\Psi}^{(n)}(I,\Theta) = \sum_{j+k\leq n} \tilde{a}_{jk}\,(\rho^j\rho^{*k}) \mapsto \sum_m \tilde{A}_m(\rho)\,e^{im\Theta}, \quad \text{and} \quad 2\pi Q(I) = \sum_{j\leq n} \omega_j\,(\rho\rho^*)^j\ , \tag{5.40}$$

where of course $\rho = \sqrt{2I}\,e^{i\Theta}$. This procedure was carried out up to order 6 using PYTORI [3], and the results are shown in Fig. 5.11 for the two Hénon maps shown previously in Fig. 5.10. The interest of eq. (5.40) is that it provides a functional form (in I and Θ) of the invariant tori of the map, whereas the NAFF-based tori shown earlier in Fig. 5.10 need to be computed separately from single-particle tracking. That being said, the two methods yield solutions of different accuracy (numerical precision for NAFF and n^{th} order expansion for the normal form).

In Fig. 5.11(a), one can see that $\tilde{\Psi}^{(6)}(I,\Theta)$ breaks down beyond the separatrix, as illustrated with the dashed-line tori. In fact, the continuity of the Normal Form does not extend smoothly across the resonant gap (see Fig. 2.13 for details). This observation highlights the fact that eq. (5.24) is essentially a Taylor expansion of the spectral coefficients $\tilde{A}_m(I)$, centered around $\rho_0 = 0$. To obtain a proper Normal Form beyond the separatrix, one would need to look for a new set of $\tilde{a}_{jk}$ coefficients, centered on a ρ_0 lying beyond the resonance gap. In Fig. 5.11(b) however, there are no low-order resonances and the Normal Form is a good approximation of the tori up to the chaotic region.

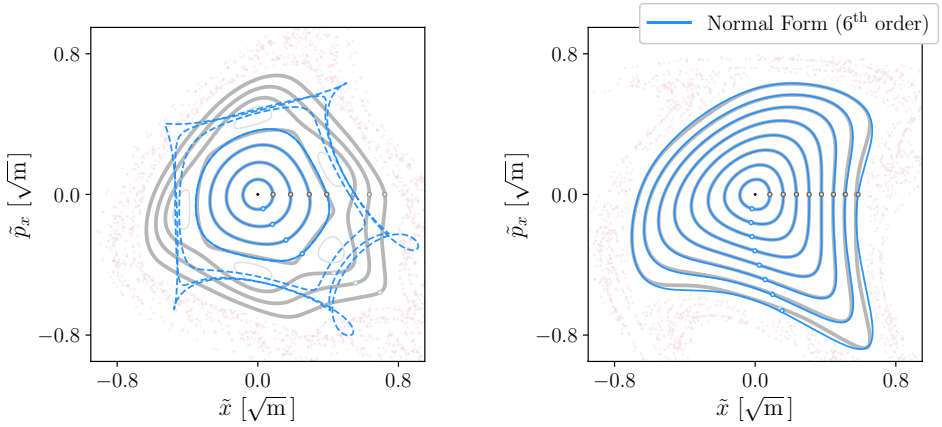

(a) $\mu_x = 0.2071$ (b) $\mu_x = 0.2981$

Figure 5.11: Normal Form (6^{th} order) of the 2D Hénon map taken from Fig. 5.10. (a) $\mu_x = 0.2071$ and (b) $\mu_x = 0.2981$. The functional form $\tilde{\Psi}^{(6)}(I,\Theta)$ provides an approximate description of the eigensolutions, centered around the origin, $\rho_0 = 0$.

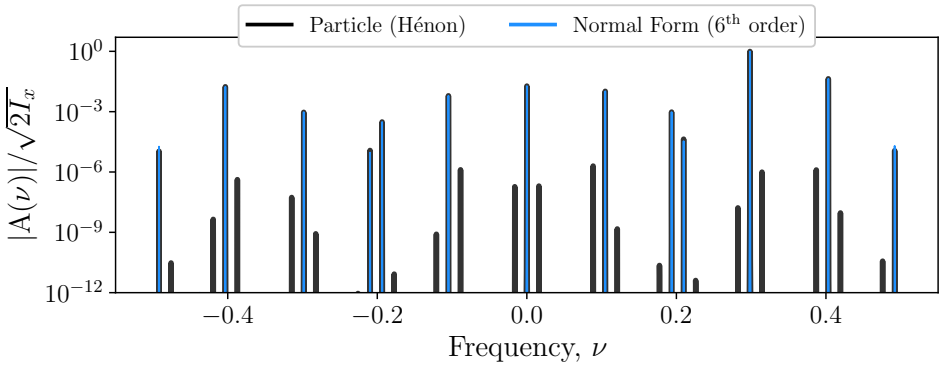

Figure 5.12: Comparison of the single-particle spectrum from the iterations of the map (tracking) or the Normal Form expansion (6^{th} order). The particle was taken from the second smallest torus next to the origin in Fig. 5.11(b). Although the topology of the torus is well-accounted for, several spectral lines are missing due to the truncation at order 6.

The *propagative* procedure mentioned earlier might not be self-evident from this simple example, since the global map can be written explicitly. That being said, in general we do not need the global map in order to find the Normal Form. Using the algebraic rules presented in Chapter 3, it becomes possible to transport $\tilde{\mathbf{\Psi}}$ and evaluate the dephasing condition on an arbitrary map by sequentially applying the operators (element-by-element, using PYTORI [3]). This is what was used here, even for the simple 2D Hénon map.

Although the Normal Form presented above provides a good description of the invariant tori, the complete particle spectrum is naturally richer (the truncation is ultimately a truncation in the spectral content). This is highlighted in Fig. 5.12, where we compare the single-particle spectrum from the Hénon map with the Normal Form expansion. For reference, the particle considered was taken from the second smallest torus next to the origin in Fig. 5.11(b). The topology of the Normal Form is accurate, but several lines are still missing in the spectrum. This observation suggests a different avenue, where one could combine both the functional strengths of the Normal Form ($\mathbf{\Psi}(\vec{I}, \vec{\Theta})$), and the practical strengths of a NAFF-based approach. The challenge of the Normal Form, indeed, lies in the determination of the coefficients, which grow in number as the truncation order is increased. Let us recall that the collapse of $\mathbf{\Psi}(\boldsymbol{\rho}) \mapsto \mathbf{\Psi}(\vec{\Theta})$ is always a straightforward operation (eq. (5.25)):

$$\tilde{A}_{\vec{n}} = \langle\, \vec{n} \,|\, \tilde{\Psi}_x \,\rangle = \sum_{jklmpq} \begin{cases} \tilde{a}_{jklmpq} \, (2I_x)^{\frac{j+k}{2}} (2I_y)^{\frac{l+m}{2}} (2I_\zeta)^{\frac{p+q}{2}} & \text{if } (j,l,p) - (k,m,q) = \vec{n} \\ 0 & \text{otherwise} \end{cases} \tag{5.41}$$

The inverse operation, however, is much more difficult. In general, the number of unknowns $\tilde{a}_{jklmpq}$ leading to any finite number of observable spectral lines $\tilde{A}_{\vec{n}}$ leads to an undetermined system of equations. That being said, using a few different particles with various actions $\vec{I}$, one could lift this limitation and obtain and overdetermined system of linear equations for $\tilde{a}_{jklmpq}$. This approach could be a practical route to a numerical Normal Form — and, crucially, a way to extend normal-form ideas to 6D, where purely analytic constructions are often impractical.

CHAPTER 6

Conclusion

6.1 Closing Remarks

The motivation for this work stemmed from a persistent difficulty to understand non-linear beam dynamics in a natural and effective way. Although the advanced theoretical tools available — such as Resonance Driving Terms and Normal Form analysis — are undeniably powerful, they are often disconnected from the intuitive (and pedagogically accessible) language of linear optics. This gap between advanced theory and basic intuition makes it difficult to reconcile our understanding of the motion when going beyond the Courant-Snyder regimes into non-linear ones. Inspired by the works of É. Forest, A. Bazzani, J. Laskar, and A. Chao, this dissertation explored a new perspective intended to reconnect the Courant-Snyder tradition with a complete six-dimensional description of non-linear motion.

A striking observation, in more advanced theories, is the overwhelming reliance on perturbative constructions. Coupling is often framed as an error spoiling an otherwise ideal FODO cell. Frequencies are ambiguously referred to as either "bare tunes" or "eigentunes", which can be misinterpreted as a *resonance*, or even attributed to non-linear phenomena. Resonance Driving Terms (in the form of *exact* RDTs or *combined* RDTs or n^{th} *order* RDTs) then appear as perturbative corrections which tend to obscure the underlying geometry. Even the so-called action, supposedly invariant, becomes a perturbation of the Courant–Snyder invariant and is eventually replaced by empirical quantities measured in restricted subspaces of the full six-dimensional phase space.

While we recognize the value of perturbative approaches, this work sought to establish a description of non-linear motion exempt from perturbative artifacts, in hope of deepening our understanding of beam dynamics.

6.1.1 A 6-dimensional framework

The notion of Hamiltonian flow proved to be a particularly natural concept for accelerator physics: we design beam pipes, where particles flow through magnetic elements, undergoing a sequence of symplectic transformations that globally define the map of the system. Building upon this, the framework makes use of the general quasiperiodic expansions found in advanced theories — and in the seminal works of Laskar, Forest, and Poincaré. This allows us to visually represent the tori on which particles are confined. This topological interpretation restores the action as a measurable area, both geometrically and numerically, and places the particle spectrum at the center of the theory.

Naturally, the present work lays only the foundations for a truly comprehensive six-dimensional description. The intricate interplay between longitudinal and transverse degrees of freedom, such as synchro-betatron coupling and chromatic effects, was discussed primarily in the context of drifts. However, a full exploration of these coupling effects from a topological standpoint remains to be done. Nevertheless, the results obtained for the LHC demonstrate that six-dimensional motion can indeed be reconstructed and studied within this formalism — a necessary first step towards a deeper understanding of longitudinal stability in real machines. In this sense, the formalism serves as both a conceptual and computational bridge between abstract Hamiltonian theory and measurable accelerator observables.

6.1.2 A tracking-oriented approach

Tracking codes such as XSUITE can simulate the long-term evolution of particles through billions of turns with remarkable precision. Yet the theoretical interpretation of these results often remains fragmented, largely due to their conceptual difference from the intuitive Courant–Snyder picture. One of the aims of this dissertation was to provide a theoretical framework that renders tracking results mathematically intelligible and provide an account of complex observables such as the particle spectra. More than being a mere convenient numerical solution, this approach is grounded in the fundamental limitations of Hamiltonian mechanics. We have shown that the Baker–Campbell–Hausdorff formula leaves us with only two options: to integrate an exact Hamiltonian (a hopeless task, as É. Forest remarked) or to integrate a sequence of elementary transformations. The latter, although approximate with regard to the former, reflects both the physical and computational reality of tracking. Clarifying this conceptual framework is an important step in a faithful description of non-linear motion. As S. Wolfram aptly observed, "we have to live the steps; this is what makes the passage of time significant, and meaningful".

Of course, this approach remains incomplete: collective effects and statistical distributions of particles are not treated explicitly. Still, the framework provides a consistent foundation on which such extensions could be built — a bridge between the microscopic motion of single particles and the macroscopic collective behaviour of beams. This work still remains to be done.

6.1.3 A stability-based study

The entire dissertation revolved around the concept of stability. What was shown is our capacity to describe and quantify regular motion through the geometry of KAM tori. In doing so, we deliberately avoided discussing complex phenomena such as resonances or chaos; choosing instead to focus first on what could be known and computed with precision. Although resonances can be naturally treated as an extension of the present formalism, chaos itself remains elusive. In this sense, the work stands on the shore of stability, away from the sea of chaos, which will need to be tackled in future work. Far from being a limitation on the scope of the work, it appears as a recognition that progress in understanding instability begins with a precise understanding of stability itself.

6.1.4 Outlook and future work

We began the dissertation with a few open questions pertaining to the nature of KAM tori. By now, at least two important ingredients should have been made clear. First, the fundamental frequencies of KAM trajectories are fixed and well-defined. Second, the six-dimensional trajectories can be described by a quasiperiodic expansion which yields the integrals of motion and allows for insightful visualization of the tori, plane by plane. Building on these foundations, several directions naturally emerge.

Emittance. Reviewing the concept of beam emittance in a six-dimensional phase space appears necessary to deepen our understanding of conservation laws in beam dynamics. This key observable bridges empirical measurements (the RMS area occupied by the beam) with theoretical considerations. A more careful analysis of the expected emittance for realistic cases, starting with linear coupled lattices [53], would be an important step towards more robust diagnostics for future machines.

Non-linear matching. Modern circular accelerators often face problems of "mismatch" when injecting beams into non-linear lattices, leading to degradation of beam quality. Exploring the process of non-linear matching — and understanding how beam distributions evolve over time — could provide insight into particle diffusion and the development of non-Gaussian distributions [27]. These questions are directly relevant for high-intensity colliders, where the control of beam halo is critical.

Dynamic Aperture. In Chapter 5, we showed a strong correlation between the non-linear residual and the dynamic aperture, suggesting that the residual could serve not only as a diagnostic tool, but also as an optimization metric. It might therefore be possible to use the KAM region to describe the region of stability, instead of relying on beam losses. Systematically exploring this connection and integrating the residual into standard design workflows could provide a powerful tool for future machines.

Experimental validation. Finally, the framework developed here has been applied exclusively to tracking simulations. Extending the analysis to experimental turn-by-turn data — using beam position monitors or other diagnostics — would provide an important validation and could enable new forms of beam-based measurements for non-linear dynamics, similar to what has been done with fixed lines [56]. In particular, connecting the visualization techniques introduced in this dissertation to resonance driving terms could open new avenues for operational optimization.

These directions share a common aim: to bridge the quasiperiodic description of motion with measurable observables used in the design and operation of realistic machines.

6.2 Summary

This dissertation proposes a way to present beam dynamics as a single coherent picture: analytic and numerical, linear and non-linear, transverse and longitudinal — all standing on equal footing. While substantial work remains to be done, the six-dimensional description introduced here offers powerful visualization methods and new tools to inspect the non-linear world beyond what was previously accessible. This work reaffirms that stability in accelerators is not restricted to linear systems, but can be rigorously studied in non-linear ones as well. Ultimately, exploiting the topological structure of phase space — building upon the corollaries of the KAM theorem — stands as a guiding principle towards a deeper understanding of beam dynamics.

References

[1] G. Iadarola, A. Abramov, P. Belanger, et al., "Xsuite: An Integrated Beam Physics Simulation Framework", in (Oct. 22, 2023), 10.18429/JACOW-HB2023-TUA2I1.

[2] P. Belanger, K. Paraschou, G. Sterbini, et al., *Nafflib: A Python Implementation of the Numerical Analysis of Fundamental Frequencies Algorithm*, https://pypi.org/project/nafflib/.

[3] P. Belanger, *Pytori: A Python Package for the Transport of Loops and Tori in Accelerator Beam Lines*, https://pypi.org/project/pytori/.

[4] A. Wolski, *Beam Dynamics in High Energy Particle Accelerators* (Imperial College Press ; Distributed by World Scientific, 2014).

[5] J. Moser, "Is the Solar System Stable?", Pauli lectures (1975).

[6] J. D. Meiss, "Symplectic Maps, Variational Principles, and Transport", Reviews of Modern Physics **64**, 795–848 (1992) 10.1103/RevModPhys.64.795.

[7] J. Laskar, *Frequency Map Analysis and Particle Accelerators*, 2003, 10.1109/PAC.2003.1288929.

[8] P. Belanger and G. Sterbini, *Numerical Evaluation of the Integrals of Motion in Particle Accelerator Tracking Codes*, 2025, 10.48550/arXiv.2503.19122.

[9] É. Forest, "Geometric Integration for Particle Accelerators", Journal of Physics A: Mathematical and General **39**, 5321–5377 (2006) 10.1088/0305-4470/39/19/S03.

[10] A. Chao, "Slim: a Formalism for Linear Coupled Systems", Chinese Physics C **33**, 115–120 (2009) 10.1088/1674-1137/33/S2/030.

[11] J. Laskar, "Introduction to Frequency Map Analysis", in *Hamiltonian Systems with Three or More Degrees of Freedom* (Springer Netherlands, 1999), 10.1007/978-94-011-4673-9_13.

[12] J. Livingood, *Principles of Cyclic Particle Accelerators* (1961).

[13] J. Laskar, C. Froeschlé, and A. Celletti, "The Measure of Chaos by the Numerical Analysis of the Fundamental Frequencies. Application to the Standard Mapping", Physica D: Nonlinear Phenomena **56**, 253–269 (1992) 10.1016/0167-2789(92)90028-L.

[14] A. Franchi, L. Farvacque, F. Ewald, et al., "First Simultaneous Measurement of Sextupolar and Octupolar Resonance Driving Terms in a Circular Accelerator from Turn-by-Turn Beam Position Monitor Data", Physical Review Special Topics - Accelerators and Beams **17**, 074001 (2014) 10.1103/PhysRevSTAB.17.074001.

[15] A. Bazzani, E. Todesco, G. Turchetti, et al., "A Normal Form Approach to the Theory of Nonlinear Betatronic Motion", Publisher: CERN, 10.5170/CERN-1994-002 (1994) 10.5170/CERN-1994-002.

[16] É. Forest, "A Hamiltonian-Free Description of Single Particle Dynamics for Hopelessly Complex Periodic Systems", Journal of Mathematical Physics **31**, 1133–1144 (1990) 10.1063/1.528795.

[17] J. D. Jackson, *Classical Electrodynamics*, 3. ed. (Wiley, 2009).

[18] G. Iadarola, *Xsuite Physics Manual*, https://xsuite.web.cern.ch (2023).

[19] J. Laskar, "Large Scale Chaos and Marginal Stability in the Solar System", Celestial Mechanics and Dynamical Astronomy **64**, 115–162 (1996) 10.1007/BF00051610.

[20] A. Chao, "Chaos in Accelerators", SLAC–PUB–8144, 10078 (1999) 10.2172/10078.

[21] G. Gallavotti, *Quasi Periodic Motions from Hipparchus to Kolmogorov*, June 28, 1999.

[22] I. C. Percival, "Chaos in Hamiltonian Systems", Proceedings of the Royal Society of London. A. Mathematical and Physical Sciences **413**, 131–143 (1987) 10.1098/rspa.1987.0105.

[23] H. Poincaré, "Sur Le Problème Des Trois Corps", Bulletin astronomique **8**, 12–24 (1891) 10.3406/bastr.1891.10419.

[24] M. Hénon, "Numerical Study of Quadratic Area-Preserving Mappings", Quarterly of Applied Mathematics **27**, 291–312 (1969) 10.1090/qam/253513.

[25] M. Hénon and C. Heiles, "The Applicability of the Third Integral of Motion: Some Numerical Experiments", The Astronomical Journal **69**, 73 (1964) 10.1086/109234.

[26] S. Wolfram, "How to Think Computationally about AI, the Universe and Everything", Stephen Wolfram Writings (2023).

[27] C. E. Montanari, "Diffusive Models and Chaos Indicators for Non-Linear Betatron Motion in Circular Hadron Accelerators", PhD thesis (2023).

[28] J. Laskar, "Frequency Analysis for Multi-Dimensional Systems. Global Dynamics and Diffusion", Physica D: Nonlinear Phenomena **67**, 257–281 (1993) 10.1016/0167-2789(93)90210-R.

[29] J. Masoliver and A. Ros, "Integrability and Chaos: The Classical Uncertainty", European Journal of Physics **32**, 431–458 (2011) 10.1088/0143-0807/32/2/016.

[30] A. Chao, "SLIM: An Early Work Revisited", EPAC (2008).

[31] C. E. Mitchell, R. D. Ryne, K. Hwang, et al., "Extracting Dynamical Frequencies from Invariants of Motion in Finite-Dimensional Nonlinear Integrable Systems", Physical Review E **103**, 062216 (2021) 10.1103/PhysRevE.103.062216.

[32] E. Courant and H. Snyder, "Theory of the Alternating-Gradient Synchrotron", Annals of Physics **3**, 1–48 (1958) 10.1016/0003-4916(58)90012-5.

[33] J. Vervaeke and J. M. Kennedy, "Metaphors in Language and Thought: Falsification and Multiple Meanings", Metaphor and Symbolic Activity **11**, 273–284 (1996) 10.1207/s15327868ms1104_3.

[34] J. Vervaeke and J. M. Kennedy, "Conceptual Metaphor and Abstract Thought", Metaphor and Symbol **19**, 213–231 (2004) 10.1207/s15327868ms1903_3.

[35] A. Chao, "Lie Algebra", in *Special Topics in Accelerator Physics* (World Scientific, Nov. 30, 2021), pp. 134–327, 10.1142/9789811253508_0004.

[36] A. J. Dragt, "An Overview of Lie Methods for Accelerator Physics", Proceedings of PAC (2013).

[37] M. Berz, *Modern Map Methods in Particle Beam Physics*, Vol. 108 (1999), 10.1016/S1076-5670(08)70227-1.

[38] M. Berz, "Differential Algebraic Description of Beam Dynamics to Very High Orders", Part. Accel. **24**, 109–124 (1989).

[39] E. Forest and R. D. Ruth, "Fourth-Order Symplectic Integration", Physica D: Nonlinear Phenomena **43**, 105–117 (1990) 10.1016/0167-2789(90)90019-L.

[40] H. Yoshida, "Construction of Higher Order Symplectic Integrators", Physics Letters A **150**, 262–268 (1990) 10.1016/0375-9601(90)90092-3.

[41] O. Gilanliogullari, B. Mustapha, and P. Snopok, *A Formalism for the Transport and Matching of Coupled Beams in Accelerators*, May 13, 2025, 10.48550/arXiv.2505.08987.

[42] A. Chao, "Phase Space Gymnastics", Proceedings of the 13th Symposium Acc. Phys., 10.18429/JACOW-SAP2017-MOCH1 (2018) 10.18429/JACOW-SAP2017-MOCH1.

[43] E. Forest, "Analytical Computation of the Smear", SSC–95, 6750681, ON: DE90014100 (1986) 10.2172/6750681.

[44] J. Bengtsson and J. Irwin, "Analytical Calculations of Smear and Tune Shift", SSC–232, 6876278, ON: DE90013770 (1990) 10.2172/6876278.

[45] M. A. Furman and S. G. Peggs, "A Standard for the Smear", SSC–N–634 (1989).

[46] P. Belanger, R. Baartman, D. Kaltchev, et al., "A Topological Approach to the Problem of Beam-Beam Compensation", Beam-Beam Workshop (2024).

[47] K. Skoufaris, S. Fartoukh, Y. Papaphilippou, et al., "Numerical Optimization of DC Wire Parameters for Mitigation of the Long Range Beam-Beam Interactions in High Luminosity Large Hadron Collider", Physical Review Accelerators and Beams **24**, 074001 (2021) 10.1103/PhysRevAccelBeams.24.074001.

[48] W. Herr, "Beam-Beam Effects in the LHC", in International Workshop on Collective Effects in Large Hadron Colliders, Vol. 50 (1995), pp. 69–81.

[49] W. Herr, X. Buffat, R. Calaga, et al., "Long-range beam–beam effects in the LHC", in Mini-Workshop on Beam–Beam Effects in Hadron Colliders (2013), 10.5170/CERN-2014-004.87.

[50] J. Koutchouk, "Correction of the long-range beam-beam effect in LHC using electromagnetic lenses", in PACS2001. Proceedings of the 2001 Particle Accelerator Conference (Cat. No.01CH37268), Vol. 3 (2001), pp. 1681–1683, 10.1109/PAC.2001.987147.

[51] F. Zimmermann, "10 Years of Wire Excitation Experiments in the CERN SPS", in Proceedings of the ICFA Mini-Workshop on Beam–Beam Effects in Hadron Colliders, Publisher: CERN (2013), 10.5170/CERN-2014-004.153.

[52] S. Fartoukh, A. Valishev, Y. Papaphilippou, et al., "Compensation of the Long-Range Beam-Beam Interactions as a Path Towards New Configurations for the High Luminosity LHC", Physical Review Special Topics - Accelerators and Beams **18**, 121001 (2015) 10.1103/PhysRevSTAB.18.121001.

[53] A. Franchi, E. Métral, and R. Tomás, "Emittance Sharing and Exchange Driven by Linear Betatron Coupling in Circular Accelerators", Physical Review Special Topics - Accelerators and Beams **10**, 064003 (2007) 10.1103/PhysRevSTAB.10.064003.

[54] R. T. S. Garcia, "Direct Measurement of Resonance Driving Terms in the Super Proton Synchrotron (SPS) of CERN using Beam Position Monitors", PhD thesis (2003).

[55] D. E. Veres, A. Bazzani, F. Capoani, et al., "Xnlbd: a New Python Package for the Analysis of Non-linear Beam Dynamics Phenomena", Journal of Physics: Conference Series **3094**, 012038 (2025) 10.1088/1742-6596/3094/1/012038.

[56] H. Bartosik, G. Franchetti, and F. Schmidt, "Observation of Fixed Lines Induced by a Nonlinear Resonance in the Cern Super Proton Synchrotron", Nature Physics **20**, 928–933 (2024) 10.1038/s41567-023-02338-3.

Publications

Paper I

JACoW Publishing: IPAC 2023

BEAM-BEAM LONG-RANGE WIRE COMPENSATORS IN LHC RUN 3*

P. Bélanger†,1, R. Baartman, D. Kaltchev, TRIUMF, Vancouver, Canada
G. Sterbini, CERN, Geneva, Switzerland
[1] also at University of British Columbia, Vancouver, Canada.

Abstract

Beam-beam effects are known to undermine the performance of the LHC during proton-proton collisions. In order to enhance the luminosity production and increase the tolerance of the working point of the machine after the High Luminosity upgrade of the LHC, it is relevant to study the possibility of using current-carrying wires to compensate long-range beam-beam effects. Following proof of principle studies in LHC Run 2, beam-beam wire compensators embedded in the collimators of the LHC are used in standard operation since the start of Run 3. In this paper, a figure of merit quantifying the efficiency of luminosity production is introduced and measurements from LHC Run 3 are presented. Bunch-by-bunch data is used to demonstrate the successful compensation of beam-beam effects in the LHC.

INTRODUCTION

In circular colliders, the non-linear electromagnetic interaction between two colliding beams significantly perturbs the beam dynamics, which is known as the beam-beam (BB) effect [1]. For high beam intensity and small beam-beam separation (or small crossing angle), beam-beam effects are known to become an important limiting factor for luminosity production [2]. In the Large Hadron Collider (LHC) the two beams share a common beam pipe around the interaction points (IPs), where several proton bunches collide based on a specific filling scheme. The head-on (HO) interactions, when two bunches collide, are necessary for luminosity production. On the contrary, long-range (LR) interactions take place on both sides of the IPs, where the beams are separated by several transverse sigmas. These interactions, akin to multipolar errors, occur several times (≈ 40) per IP for each bunch and strongly contribute to the tune-spread, eventually leading to the development of instabilities, proton losses and the reduction of dynamic aperture [3–5].

Following a proposal to use current-carrying wires to compensate BBLR interactions [6], beam-beam compensation wires (BBCW) were first installed in the SPS [7] and eventually in the LHC [8], alongside theoretical progress regarding the optimal compensation scheme to adopt [9]. In 2018, the first results of BBCW operation in the LHC were recorded in a machine development experiment [10, 11]. This proof-of-principle study allowed using the BBCW prototypes in standard operation during the first months of LHC Run 3, an essential step in order to gather operational experience for future BBCW operation in HL-LHC.

* Work supported by the High Luminosity Large Hadron Collider project. The authors would like to thank the Machine Development team, the LHC Operation team as well as the HL-LHC Management for their support.
† pbelanger@triumf.ca or philippe.belanger@cern.ch

In this paper, the burn-off efficiency is introduced as a novel figure of merit to discuss luminosity production in the LHC, and experimental BB compensation results from Run 3 are presented. Results from a follow-up study to the aforementioned machine development experiment are presented and compared to operational observations of successful BB compensation. The bunch-by-bunch signature of BB-driven losses is also presented and discussed.

WIRE COMPENSATORS IN RUN 3

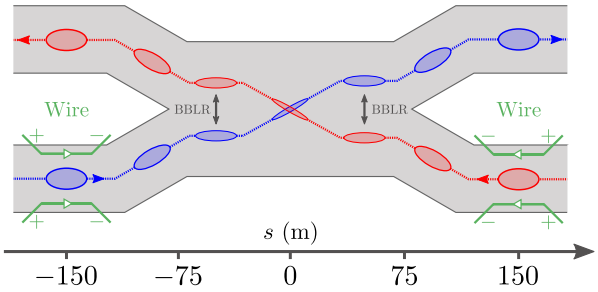

Figure 1: BBCW layout for LHC Run 3 around IP1 and IP5.

The wire compensators for LHC Run 3 (2022) are BBCW prototypes, comprised of 2 copper wires per beam and per IP around IP1 and IP5 (ATLAS and CMS), as depicted schematically in Fig. 1. The wires are lying in the crossing plane of each IP, vertically and horizontally, for IP1 and IP5 respectively. To facilitate the ad hoc movement of the wires as well as the machine protection requirements of such devices, the BBCW prototypes are embedded directly in the jaw of the tertiary collimators of the collimation system [8]. Since the condition for optimal compensation (β_x/β_y aspect ratio, beam-wire distance, etc.) are not met with this in-jaw BBCW installation, the wires are installed in pairs, on both sides of the beam. This allows to compensate the BBLR leading order effect, which is an octupole-like tune-spread [9]. The limitations of the present BBCW prototypes have been under review since the start of Run 3 and could be addressed in the HL-LHC era via the installation of standalone BBCW assemblies at specific locations on both sides of the IPs [12].

BBCW Commissioning

At the end of 2022, the BBCW were commissioned to be used during regular LHC operation, alongside the intensity ramp-up of the machine. The commissioning consisted mainly in validating the 5$^{\text{th}}$ axis alignment of the BBCW using the collimator alignment system and to implement a tune feed-forward system to compensate the quadrupole-like tune-shift caused by the wires. This was done using the trim

quadrupoles on both sides of each IP. Following a successful commissioning period of about two weeks, the wires were routinely used at the end of regular proton-proton physics fills with constant β^* of 30 cm, once a satisfying level of integrated luminosity had been cumulated for the fill. The BBCW were used for several hours over more than 60 fills, where the main objective was to study the impact on the beam and to optimise the orchestration of BBCW operation during the regular LHC cycle. In total, 6 beam dumps were related to BBCW operation: 4 of them related to an excessive leakage current (earth fault) from the power supply, showing a clear weakness of the present in-jaw prototypes. No beam dumps have been related to beam instabilities caused by the operation of the wires. Following the earth fault dumps, the BBCW of Beam 2 were successfully repaired to be used for the rest of Run 3. However, the BBCW of Beam 1 are no longer operational. As such, the rest of the paper will focus exclusively on Beam 2 BBCW operation.

FIGURE OF MERIT FOR LUMINOSITY

A common figure of merit used to quantify the condition of the LHC is the lifetime of the beam. It provides important information for the LHC as a storage ring, but does not inform about the luminosity production of the collider. Instead, it is more appropriate to define the instantaneous burn-off efficiency η, following:

$$\eta \equiv \left[\frac{dN}{dt}\right]_{\text{bo}} \Big/ \left[\frac{dN}{dt}\right]_{\text{total}} = \frac{\sigma_{\text{pp}}\mathcal{L}}{\sigma_{\text{pp}}\mathcal{L} + R_\ell N} \tag{1}$$

where $\left[\frac{dN}{dt}\right]_{\text{total}}$ and $\left[\frac{dN}{dt}\right]_{\text{bo}}$ are the total and burn-off losses, N is the beam intensity, $\mathcal{L} = \sum_{\text{IPs}} \mathcal{L}_{\text{IP}}$ is the total luminosity of the collider, R_ℓ is the loss rate from non-burn-off losses and $\sigma_{\text{pp}} = 80$ mb is the accepted value for the cross section of proton-proton collisions at 7 TeV. The efficiency is similar to the effective cross section $\sigma_{\text{eff}} = \frac{1}{\mathcal{L}}\left[\sigma_{\text{pp}}\mathcal{L} + R_\ell N\right]$ used in previous work [10, 11]. One can note that $\eta = \sigma_{\text{pp}}/\sigma_{\text{eff}}$. To optimise luminosity production, a well-behaved machine needs to lose most of its protons to collisions, i.e. $\eta \to 1$. Assuming small R_ℓ over a short period of time compared to the length, T, of luminosity production for a fill, one can show that the relative gain in integrated luminosity, G, scales with the integral of $\eta(t)$, or more precisely:

$$G \sim -r_0 \left[\frac{r_0 T + 2}{r_0 T + 1}\right] \cdot \int_0^T \left(\frac{1}{\eta} - 1\right) dt \tag{2}$$

where $r_0 = \sigma_{\text{pp}}\mathcal{L}_0/N_0$ is a constant which depends on the initial conditions (with units of s^{-1}). Alternatively, one can see that $\left(\frac{1}{\eta} - 1\right) = \frac{R_\ell N}{\sigma_{\text{pp}}\mathcal{L}}$ corresponds to the luminosity-normalized losses of the machine. For example, if $\eta = 0.5$ for 30 minutes in typical LHC conditions ($N_0 = 2400 \cdot 1.3 \times 10^{11}$ p$^+$ and $\mathcal{L}_0 = 2 \times (2.2 \times 10^{34}$ Hz/cm^2)), the change in integrated luminosity is $G \sim -3$ % for $T = 10$ h. Hence, the experimental efficiency is to be discussed on the basis of its deviation from $\eta = 1$ over a certain period of time.

EXPERIMENTAL RESULTS

Building up on a previous study from 2018 [10] and following the successful use of BBCW in standard LHC operation in 2022, a dedicated machine development experiment was realized to study BB compensation in a beam-beam dominated regime. For this experiment (fill 8348), the bunch intensity was increased, the crossing angle was reduced, and the filling scheme was modified to mitigate electron cloud formation by colliding isolated trains [13]. The beam parameters used for the machine development (MD) experiment are summarized in Table 1 and compared to a typical operational case. Fill 8120 was chosen as a case study for standard operation since it is representative of the general observations from the first months of operation in Run 3.

Table 1: LHC conditions for the machine development experiment and the operational fill at the start of Run 3.

Parameter		**MD**	**Operational Fill**	
Wire current	I_{w}	350	350	(A)
Wire pos. IP1|IP5	d_{w}	9.2 | 12.4	9.2 | 12.4	(mm)
Beam Energy	E	6.8	6.8	(TeV)
Bunch intensity	N_b	1.4×10^{11}	1.0×10^{11}	(p$^+$/b)
Beta at the IP	β^*	30	30	(cm)
Half-crossing	$\theta_c/2$	130 – 160	160	(µrad)
Num. of bunches	n_b	158	2413	
Bunches per train		48	48	

During the machine development experiment, the half-crossing angle was reduced in steps, from 160 µrad to 130 µrad. Meanwhile, the BBCW of IP1 and IP5 were cycled together to their maximum current of 350 A. The filling pattern was chosen such that isolated trains of 48 bunches were colliding exclusively in IP1 and IP5. The measured burn-off efficiency for Beam 2 is reported in Fig. 2 on a bunch-by-bunch basis. Calibrated diamond beam loss monitors (dBLMs) [14] were used to evaluate the $R_\ell N$ term of eq. (1) and the bunch-by-bunch luminosity was taken from the ATLAS/CMS measurements. From the color code, one can see that the efficiency scales with the effective number of BBLR interactions, used to quantify the BB strength experienced by the different bunches of a train. This quantity is discussed in more details in the following section, alongside the interpretation of the results.

Figure 2 also shows the clear reduction of the efficiency with the crossing angle, as expected due to the scaling of BB effects with beam-beam separation. One can see that the efficiency tends to slowly improve over time on a time scale of about 30 – 60 min. With every cycle of the BBCW, the efficiency improves instantaneously to reach 0.95 and returns to its prior state when the BBCW are powered-off. Moreover, the variation between the bunches of a train is dramatically reduced when the wire compensators are powered: bunches with a high number of BBLR encounters reach a similar efficiency as the other bunches. A similar behaviour is observed

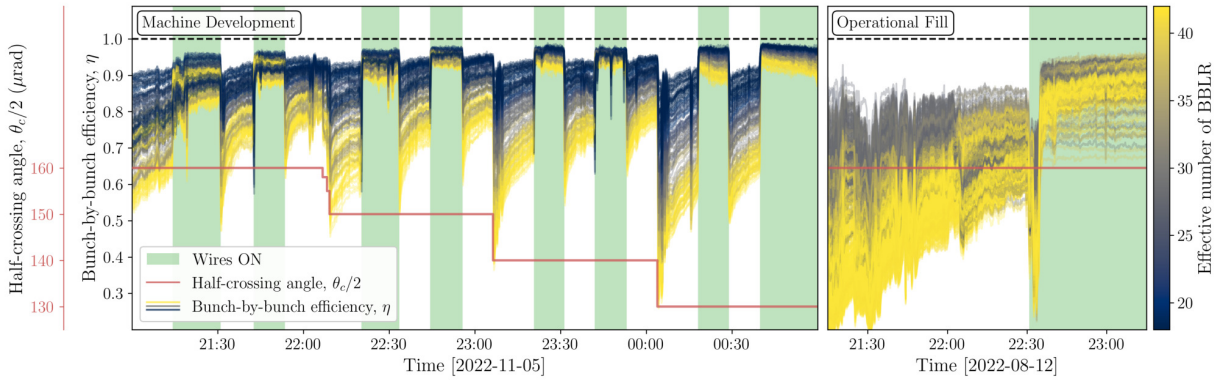

Figure 2: Bunch-by-bunch efficiency measured during the machine development study, fill 8348, and the operational fill 8120. The effective number of BBLR interactions is shown with the color code. The powering of the BBCW is shown with the green areas and the half-crossing angle is shown in red. All axes are using the same scales for both plots.

with the operational case study, albeit with more variability in the bunch-by-bunch response. The difference in clarity of the signal is attributed to the filling pattern of the operational case. Indeed, contrarily to the MD, the operational case included series of 5 trains of 48 bunches. With such a filling pattern, bunches from successive trains interact together in both IPs via BBLR interactions and electron-cloud build-up along the trains. This situation is fundamentally different from the machine development experiment, where isolated trains were used to mitigate electron-clouds.

Bunch-by-Bunch Signature

The relationship between beam-beam effect and beam losses is not straightforward. For this reason, it is relevant to consider the variation of efficiency (or losses) between different bunches of a given train, hereby referred to as the bunch-by-bunch signature. Indeed, despite the complexity of the experimental observations and the experimental unknowns, the relative behaviour within a train can be studied in detail. To quantify the BB strength, the area $\mathcal{A}$ (in tune space) of the octupole-like tune-spread experienced by a given bunch due to all long-range encounters is used. One can define the effective number of BBLR encounters, $n_{\mathrm{LR}}^{\mathrm{eff}}$, to be proportional to $\mathcal{A}$ following:

$$n_{\mathrm{LR}}^{\mathrm{eff}} = \mathcal{A} \cdot \left[n_{\mathrm{LR}}^{\mathrm{mid}} \middle/ \mathcal{A}^{\mathrm{mid}} \right] \tag{3}$$

where $n_{\mathrm{LR}}^{\mathrm{mid}}$ is the number of long-range encounters experienced by the middle bunch of the train and $\mathcal{A}^{\mathrm{mid}}$ is the octupole-like tune-spread area for that bunch. In Fig. 3, experimental observations are compared to the expected signature for $n_{\mathrm{LR}}^{\mathrm{eff}}$ assuming that $\mathcal{A}$ is an adequate indicator of BB strength. As one can see from the machine development data, important experimental features of the bunch-by-bunch signature are seen before (a plateau) and around the middle (local maxima) of the train. Similar observations have also been reported in the past [5], but have not yet been fully explained.

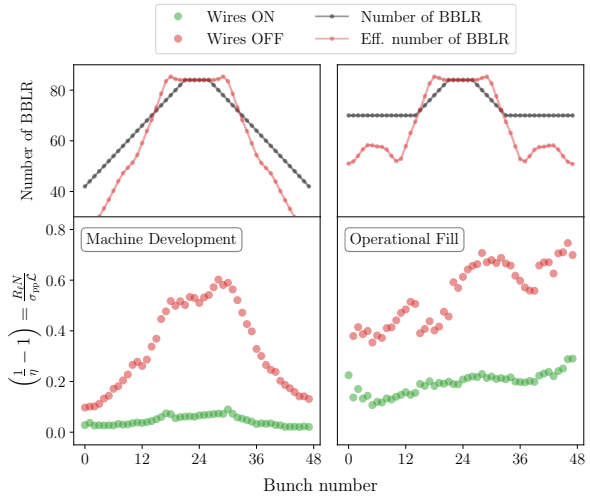

Figure 3: Bunch-by-bunch normalized losses measured during the machine development study, fill 8348, and the operational fill 8120. The red and green dots show the average losses 5 min before and 5 min after powering-on the BBCW.

SUMMARY

This paper presents experimental results from Run 3, showing a successful compensation of the BB effect using BBCW prototypes in the LHC. A novel figure of merit quantifying the efficiency of luminosity production is presented. Using this metric, results from a machine development study in a beam-beam dominated regime are presented, showing clear BB compensation. The results are compared to an operational fill, in which a compensation is also observed, despite the presence of important electron-cloud effects. Finally, the bunch-by-bunch signature of beam losses along a train is presented and compared to the area of BB-related tune-spread in tune space. It is believed that the visible features of the bunch-by-bunch signature could be exploited in the future, due to their intrinsic link to the BB effect.

REFERENCES

[1] W. Herr and T. Pieloni, "Beam-beam effects," in *CAS - CERN Accelerator School: Advanced Accelerator Physics*, 2014, pp. 431–459. doi:10.5170/CERN-2014-009.431

[2] Y. Papaphilippou and F. Zimmermann, "Weak-strong beam-beam simulations for the large hadron collider," *Phys. Rev. Spec. Top. Accel Beams*, vol. 2, no. 10, p. 104 001, 1999. doi:10.1103/PhysRevSTAB.2.104001

[3] K. Skoufaris et al., "Numerical optimization of DC wire parameters for mitigation of the long range beam-beam interactions in high luminosity large hadron collider," *Phys. Rev. Accel. Beams*, vol. 24, no. 7, p. 074 001, 2021. doi:10.1103/PhysRevAccelBeams.24.074001

[4] W. Herr, "Beam-beam effects in the LHC," in *International Workshop on Collective Effects in Large Hadron Colliders*, vol. 50, 1995, pp. 69–81. https://cds.cern.ch/record/272882

[5] W. Herr et al., "Long-range beam–beam effects in the LHC," in *Mini-Workshop on Beam–Beam Effects in Hadron Colliders*, 2013. doi:10.5170/CERN-2014-004.87

[6] J.-P. Koutchouk, "Correction of the Long-Range Beam-Beam Effect in LHC Using Electro-Magnetic Lenses," in *Proc. PAC'01*, Chicago, IL, USA, Jun. 2001. https://jacow.org/p01/papers/TPPH012.pdf

[7] F. Zimmermann, "10 years of wire excitation experiments in the CERN SPS," in *Proc. of the ICFA Mini-Workshop on Beam–Beam Effects in Hadron Colliders*, 2013. doi:10.5170/CERN-2014-004.153

[8] A. Rossi et al., "Progress with Long-Range Beam-Beam Compensation Studies for High Luminosity LHC," in *Proc. IPAC'17*, Copenhagen, Denmark, May 2017, pp. 2358–2361. doi:10.18429/JACoW-IPAC2017-TUPVA115

[9] S. Fartoukh, A. Valishev, Y. Papaphilippou, and D. Shatilov, "Compensation of the long-range beam-beam interactions as a path towards new configurations for the high luminosity LHC," *Phys. Rev. Spec. Top. Accel Beams*, vol. 18, no. 12, p. 121 001, 2015. doi:10.1103/PhysRevSTAB.18.121001

[10] G. Sterbini et al., "First Results of the Compensation of the Beam-Beam Effect with DC Wires in the LHC," in *Proc. IPAC'19*, Melbourne, Australia, May 2019, pp. 2262–2265. doi:10.18429/JACoW-IPAC2019-WEYYPLM3

[11] A. Poyet et al., "First experimental evidence of a beam-beam long-range compensation using wires in the large hadron collider," 2023. doi:10.48550/arXiv.2203.08066

[12] G. Sterbini, A. Rossi, A. Bertarelli, A. Poyet, P. Belanger, and Y. Papaphilippou, "Potential and constraints of a beam-beam wire compensator in the HL-LHC era," presented at IPAC'23, Venice, Italy, May 2023, paper WEPL103, this conference.

[13] G. Iadarola et al., "Progress in Mastering Electron Clouds at the Large Hadron Collider," in *Proc. IPAC'21*, Campinas, Brazil, May 2021, pp. 1273–1278. doi:10.18429/JACoW-IPAC2021-TUXA03

[14] S. M. Vigo et al., "Beam Loss Signal Calibration for the LHC Diamond Detectors During Run 2," in *Proc. IBIC'21*, Pohang, Korea, 2021, pp. 290–293. doi:10.18429/JACoW-IBIC2021-TUPP33

Paper II

JACoW Publishing: IPAC 2024

BUNCH-BY-BUNCH SIMULATIONS OF BEAM-BEAM DRIVEN PARTICLE LOSSES IN THE LHC*

P. Bélanger†,1, R. Baartman, D. Kaltchev, TRIUMF, Vancouver, Canada
G. Iadarola, G. Sterbini, CERN, Geneva, Switzerland
[1] also at University of British Columbia, Vancouver, Canada

Abstract

Recent experimental measurements in the Large Hadron Collider (LHC) have shown a clear correlation between beam-beam resonance driving terms and beam losses, with a characteristic bunch-by-bunch signature. This observation creates interesting conditions to study diffusive processes. Over the past few decades, early chaos indicators, frequency map analysis and dynamic aperture studies have been commonly used to study particle stability in circular machines. However, the underlying mechanisms driving particles to large amplitudes in the presence of high order resonances is still an open question. Leveraging on years of development on particle tracking tools, this paper presents full-fledged 6-dimensional bunch-by-bunch beam loss simulations in the LHC. The computed loss rates are shown to be in agreement with experimental observations from LHC Run 3.

INTRODUCTION

Maximizing the beam lifetime is a critical task for the optimal operation of storage rings and circular colliders like the Large Hadron Collider (LHC). In recent years, particle stability in circular machines has been extensively studied with chaos indicators, frequency map analysis and dynamic aperture studies [1]. However, the underlying mechanisms driving particles to large amplitudes in presence of high order resonances is still an open question [2, 3]. No simple model exists to describe the effect of beam perturbations on the slow loss of particles over time. This conceptual gap can be attributed, on one hand, to the fundamental limitations in fully describing chaotic systems via closed form equations outside of particle tracking codes [4], and on the other hand, to the extensive computational resources required to study a system like the LHC over any meaningful period of time. Indeed, a realistic scenario would need to include 10^{14} particles tracked over several tens of thousands of accelerator components for 10^4 turns in order to study a single second of LHC operation. To understand the steady state losses taking place after hours of operation, the number of turns would need to be increased by three orders of magnitude. That being said, following decades of progress in the development of symplectic particle tracking codes [5] and the modernization of computational tools, more complete simulations are now within reach.

* Work supported by the High Luminosity Large Hadron Collider project. The authors would like to thank the Machine Development team, the LHC Operation team as well as the HL-LHC Management for their support.
† philippe.belanger@cern.ch

In principle, diffusive models offer a promising avenue to describe slow particle losses over long periods of time by describing the behaviour of an ensemble of particles directly. Such models have already been fitted to experimental data [6, 7], but a direct correlation between diffusive parameters and the underlying machine parameters (such as the resonant driving terms (RDTs)), remains to be done [8, 9]. In this regard, realistic full-fledged beam loss simulations offer an ideal framework to validate diffusive models by having access to both the machine parameters and the ensuing beam losses. Moreover, in order to consider both the transverse and longitudinal dynamics in a complex 6-dimensional (6D) system like the LHC, full-fledged tracking simulations appear as the only solution allowing to include high-order non-linear elements without resorting to drastic approximations.

In 2022, the precise measurement of the characteristic bunch-by-bunch signature coming from the beam-beam effect was carried out in the LHC [10]. This observation offers the ideal starting point to validate full-fledged beam loss simulations, as proposed in this paper. In the following sections, beam-beam effects will be briefly introduced, the simulation tools will be explained and the resulting bunch-by-bunch losses will be presented.

BEAM-BEAM EFFECTS

Alongside electron cloud effects, the main source of nonlinearities in the LHC is the beam-beam (BB) effect, coming from the electromagnetic interaction between the two counter-rotating beams. Around the interaction points (IPs), the two beams share a common beam pipe and perturb one another. Head-On (HO) collisions take place at the center of the IPs, whereas Long-Range (LR) interactions are distributed on both sides of the IPs. These interactions, akin to multipolar errors, occur several times ($\approx$40) per IP for each bunch and strongly contribute to high-order resonances, eventually leading to the development of diffusive processes and proton losses. The beam-beam long-range (BBLR) kick can be included in tracking simulations via a weak-strong model [11], where a given (weak) bunch is subject to a static (strong) BBLR element for every BBLR encounter. Not all bunches of a train experience the same number of BBLR interactions as they cross the interaction regions (IRs), because of different encounter schedule with the bunches of the opposite beam. As a result, every bunch needs to be tracked in a different effective lattice to account for beam-beam effects.

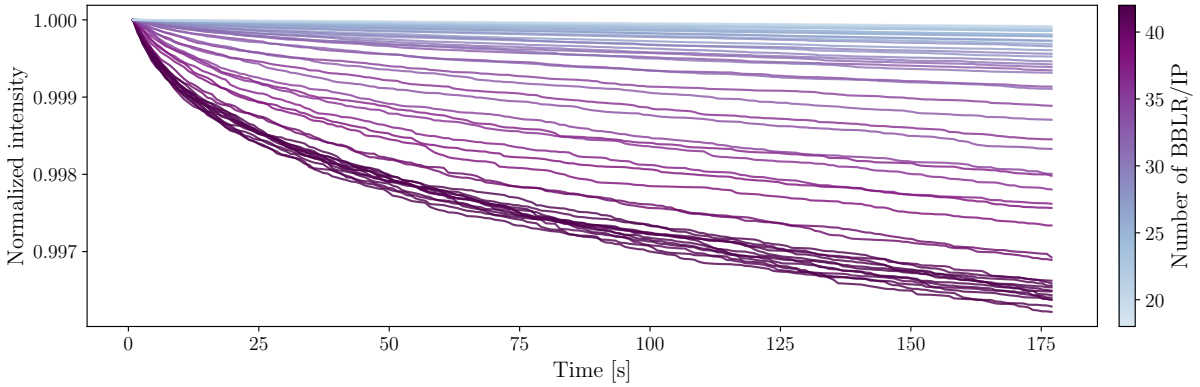

Figure 1: Evolution of the normalized intensity as a function of time for 48 bunches in the LHC, tracked for 2×10^6 turns. The particle distribution is Gaussian ($q = 1$) and the collimators are fixed at 5 σ_{nom} in all planes. The number of long-range interactions experienced by each bunch is shown with the color code.

SIMULATION STRATEGY

In the last few years, significant efforts have been made at CERN to develop and consolidate a modernized software for multi-physics simulations in particle accelerators. Xsuite [12] was developed to replace several programs (COMBI, PyHeadTail, Sixtrack, Sixtrack-lib, MAD-X, etc.) and unify them under a common framework. More importantly, it supports different computing platforms and allows the use of Graphics Processing Units (GPUs), which can be used to parallelize computations and speed up simulations by orders of magnitude [13]. By leveraging on such a tool, is it now possible to track tens of thousands of particles over a few million turns in about 15 h of computation time[1]. Despite these improvements, the sampling of a 6-dimensional phase space with a few thousand particles is extremely sparse and additional strategies need to be employed to obtain practical results, as described below. The simulation parameters, shown in Table 1, were chosen to match the LHC operational conditions from an *ad hoc* fill (Fill 8348) in order to compare the simulation results with the experimental data collected during that fill.

Table 1: Simulation Parameters, Chosen to Match Fill 8348.

Parameter		Value	Unit
Beam Energy	E	6.8	(TeV)
Bunch intensity	N_b	1.4×10^{11}	(p^+/b)
Emittance	$\varepsilon_x, \varepsilon_y$	2.0	(µm)
Beta at the IP	β^*	30	(cm)
Half-crossing	$\theta_c/2$	130	(µrad)
Octupoles	I_{oct}	430	(A)
Tune	Q_x,Q_y	(62.31, 60.32)	
Chromaticity	ΔQ_x,ΔQ_y	15	

[1] Computation done using the *NVIDIA A100 40GB GPU*

To study the bunch-by-bunch losses, a single train of 48 bunches meeting in IP1 (ATLAS experiment) and IP5 (CMS experiment) was considered. For each bunch, the encounter schedule with the other beam was computed to determine the location and the strength of the BBLR interactions to be included in the effective lattice of the bunch.

Particle Distribution

Since beam losses are computed by counting the number of particles hitting the collimators, the particle distribution considered is of prime importance and a realistic distribution needs to be used. However, typical Gaussian-like particle distributions are highly inefficient to track, since most particles are close to the origin and will survive a large number of turns. Moreover, because of the heavy computational time, repeating the simulation to test various distributions becomes impractical. In order to solve both of those problems, the particles were distributed uniformly inside the volume of a 6D hypersphere in the normalized phase space. This choice of distribution allows to sample the entire phase space as densely as possible and to later re-weight the particles with the desired probability density function in post-processing, without needing to repeat the tracking. As such, the 25,000 particles tracked for each bunch were used to sample the phase space and the final losses were inferred after resampling the hypersphere distribution with a realistic distribution (1.4×10^{11} particles) in post-processing.

Typical particle distributions in the LHC have been observed to follow the heavy-tail q-Gaussian [14, 15], for which the beam profile in a given plane follows:

$$f_{1D}(x) = \frac{e_q(-x^2/(\sigma_x^2(5-3q)))}{C_q\sqrt{\sigma_x^2(5-3q)}}, \quad \text{for } 1 \le q < 5/3,$$

where C_q is a normalization constant, σ_x^2 is the variance and $e_q(x) = \left(1 + (1-q)x\right)^{1/(1-q)}$ when $q > 1$. When $q = 1$, $e_q(x) = e^x$ and the q-Gaussian becomes a regular Gaussian

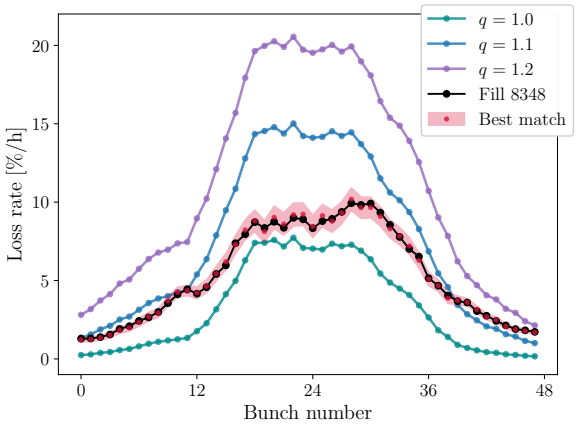

Figure 2: Bunch-by-bunch average loss rate over the full simulation window for different q-Gaussian distributions. The experimental data from Fill 8348 is shown and compared to the best match obtained when allowing q (±0.01 shaded area) to vary between the bunches.

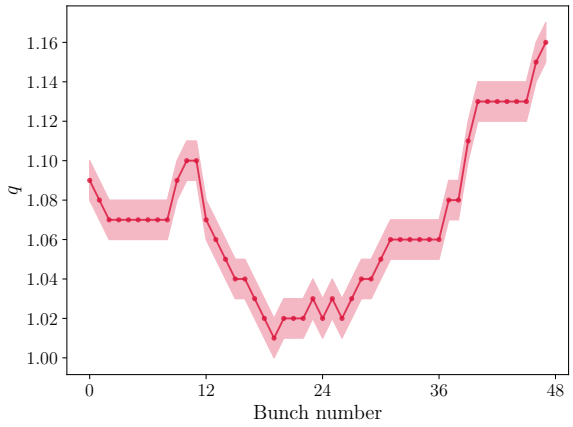

Figure 3: Bunch-by-bunch q-Gaussian parameter, q (±0.01 shaded area), for the best fit with the experimental data.

distribution. The 4D elliptically-symmetric generalization of this distribution [16] was used for the transverse plane and a 2D multivariate Gaussian was used for the longitudinal plane, assumed to be independent from the transverse one.

Beam Aperture

To compute the losses, the three primary collimators of the LHC (horizontal, vertical and skew collimators) were considered as the beam aperture. Similarly to the particle distribution, the computations were done in post-processing after tracking the particles. To do so, the maximum excursion of each phase space variable was binned every 10,000 turns and recorded for every particle, allowing to infer whether or not the particle would hit one of the three collimators, placed at an arbitrary position over time. The advantages of this method are twofold. First, the disk space required to store the data is reduced by a factor 10^4. Second the aperture can be moved over time in the transverse plane to study collimator scraping, once again in post-processing, without having to repeat the simulation. The large binning considered reduces the time resolution of the losses, which was deemed acceptable to study slow diffusive losses in the context of this paper.

BUNCH-BY-BUNCH LOSSES

After tracking the particles for each bunch, the losses were computed with the collimators at 5 σ_{nom} in each plane, where σ_{nom} is the nominal sigma value, computed with the nominal emittance of 3.5 µm. The evolution of the intensity over time is shown for each of the 48 bunches on Fig. 1 for the case of a Gaussian beam ($q = 1$). The loss rate evolves rapidly in the first few seconds of the simulation and stabilizes by the end of the time window. A longer simulation window would be preferable to model realistic beam losses accurately. One way to accelerate the process is to bring the collimators at 4 σ_{nom} for the first 10,000 turns, before retracting them to 5 σ_{nom} afterwards to measure the losses. This procedure aims at mimicking the numerous perturbations *cleaning* the beam over the several hours of typical operation. The next results were obtained following this aforementioned procedure.

In Fig. 2, the bunch-by-bunch loss rate is compared to the experimental data from Fill 8348 for different q-Gaussian distributions. Even for the most conservative distribution (6D Gaussian, $q = 1$), the results are in agreement with the experimental data, both in terms of the order of magnitude of the loss rates and in terms of the bunch-by-bunch signature. However, the precise value of the bunch-by-bunch loss rate depends on several parameters, such as the bunch-by-bunch intensity, emittance, q-value and the parameters of the bunches from the other beam. To highlight this effect, the particle distribution was allowed to vary separately for each bunch by changing the q-value, while keeping the bunch intensity and emittance constant. By doing so, the agreement with the experimental data is found to improve, and the q-value for each bunch is reported in Fig. 3. These results suggest that with all free parameters held constant between the bunches, the loss rate is underestimated for bunches with a few BBLR interactions and overestimated for bunches with numerous BBLR interactions.

SUMMARY

This paper presents simulation strategies to allow for full-fledged 6-dimensional bunch-by-bunch beam loss simulations in a complex accelerator like the LHC. As a result, it is shown that the loss rate obtained with a limited number of assumptions is in good agreement with the experimental data observed in the LHC. Moreover, by allowing the bunch distribution to vary, the agreement is improved. Such simulations can be used to study diffusive models in more details, by allowing to inspect both the machine parameters and the ensuing beam losses.

REFERENCES

[1] Y. Papaphilippou, "Detecting chaos in particle accelerators through the frequency map analysis method," en, *Chaos: An Interdisciplinary Journal of Nonlinear Science*, vol. 24, no. 2, p. 024 412, 2014. doi:10.1063/1.4884495

[2] A. Chao, "Chaos in Accelerators," en, Tech. Rep. SLAC-PUB-8144, 10078, 1999, SLAC–PUB–8144, 10 078. doi:10.2172/10078

[3] F. Galluccio and F. Schmidt, "Towards a better understanding of slow particle losses in large hadron colliders," in *AIP Conference Proceedings*, 1992, pp. 86–104. doi:10.1063/1.42298

[4] H. Zwirn and J.-P. Delahaye, "Unpredictability and Computational Irreducibility," in *Irreducibility and Computational Equivalence: 10 Years After Wolfram's A New Kind of Science*, 2013, pp. 273–295. doi:10.1007/978-3-642-35482-3_19

[5] É. Forest, "Geometric integration for particle accelerators," en, *Journal of Physics A: Mathematical and General*, vol. 39, no. 19, pp. 5321–5377, 2006. doi:10.1088/0305-4470/39/19/S03

[6] C. E. Montanari, A. Bazzani, M. Giovannozzi, A. Poyet, and G. Sterbini, "Modelling the experimental data for long-range beam-beam wire compensators at the CERN LHC with diffusive models," in *Proc. IPAC'23*, Venice, Italy, 2023, pp. 2689–2692. doi:10.18429/JACoW-IPAC2023-WEPA021

[7] C. E. Montanari, A. Bazzani, M. Giovannozzi, P. Hermes, and S. Redaelli, "Recent measurements and analyses of the beam-halo dynamics at the CERN LHC using collimator scans," in *Proc. IPAC'23*, Venice, Italy, 2023, pp. 2693–2696. doi:10.18429/JACoW-IPAC2023-WEPA022

[8] F. Zimmermann, "Emittance growth and proton beam lifetime in HERA," Other thesis, 1993.

[9] D. Kaltchev, P. Belanger, and G. Sterbini, "Analytic calculations of RDT and detuning generated by beam-beam collisions and wire correctors," in *Proc. IPAC'23*, Venice, Italy, 2023, pp. 3383–3386. doi:10.18429/JACoW-IPAC2023-WEPL116

[10] P. Belanger, R. Baartman, D. Kaltchev, and G. Sterbini, "Beam-beam long-range wire compensators in LHC Run 3," in *Proc. IPAC'23*, Venice, Italy, 2023, pp. 2789–2792. doi:10.18429/JACoW-IPAC2023-WEPA060

[11] Y. Papaphilippou and F. Zimmermann, "Weak-strong beam-beam simulations for the large hadron collider," *Phys. Rev. Spec. Top. Accel Beams*, vol. 2, no. 10, p. 104 001, 1999. doi:10.1103/PhysRevSTAB.2.104001

[12] G. Iadarola et al., "Xsuite: a flexible python toolkit for beam dynamics," presented at IPAC'24, Nashville, TN, USA, May 2024, paper WEPR56, this conference.

[13] K. Paraschou, "Studies of incoherent effects for the upgrade of the large hardon collider and detector applications," Ph.D. dissertation, Aristotle U., Thessaloniki, 2023. doi:10.26262/heal.auth.ir.348933

[14] S. Papadopoulou, F. Antoniou, T. Argyropoulos, M. Hostettler, Y. Papaphilippou, and G. Trad, "Impact of non-Gaussian beam profiles in the performance of hadron colliders," en, *Physical Review Accelerators and Beams*, vol. 23, no. 10, p. 101 004, 2020. doi:10.1103/PhysRevAccelBeams.23.101004

[15] M. A. Abed, A. A. Babaev, and L. G. Sukhikh, "Luminosity calibration by means of van-der-Meer scan for Q-Gaussian beams," en, *The European Physical Journal C*, vol. 84, no. 2, p. 122, 2024. doi:10.1140/epjc/s10052-024-12469-3

[16] E. Lamb, G. Sterbini, and H. Bartosik, "Luminosity effects due to dependent heavy-tailed beams," presented at IPAC'24, Nashville, TN, USA, May 2024, paper MOPC09, this conference.

Paper III

arXiv preprint 2025

Numerical evaluation of the integrals of motion in particle accelerator tracking codes

P. Bélanger[1,2], G. Sterbini[1]

[1] *CERN, Geneva, Switzerland*
[2] *TRIUMF, Vancouver, Canada*

(Dated: October 6, 2025)

Particle tracking codes are one of the fundamental tools used in the design and the study of complex magnetic lattices in accelerator physics. For most practical applications, non-linear lenses are included and the Courant-Snyder formalism falls short of a complete description of the motion. Likewise, when the longitudinal motion is added, synchro-betatron coupling complicates the dynamics and different formalisms are typically needed to explain the motion. In this paper, a revised formalism is proposed based on the Fourier expansion of the trajectory — known to be foundational in the KAM theorem — which naturally describes non-linear motion in 2D, 4D and 6D. After extracting the fundamental frequencies and the Fourier coefficients from tracking data, it is shown that an approximate energy manifold (an invariant torus) can be constructed from the single-particle motion. This cornerstone allows to visualize and compute the areas of the torus projections in all conjugate planes, conserved under symplectic transformations. These are the integrals of motion, ultimately expressed in terms of the Fourier coefficients. As a numerical demonstration of this formalism, the case of the 6-dimensional Large Hadron Collider (LHC) is studied. Examples from the 2D and 4D Hénon map are also provided. Even for heavily smeared and intricate non-linear motion, it is shown that invariant tori accurately describe the motion of single particles for a large region of the phase space, as suggested by the KAM theorem.

I. INTRODUCTION

Particle accelerators and storage rings such as the Large Hadron Collider (LHC) at CERN require their beam of particles to be stable for long periods of time. In the LHC, the circulating beams can be stored for dozens of hours (57 h achieved in a single fill in 2022). This corresponds to more than 10^9 revolutions around the accelerator — a number comparable to that of Earth's revolutions around the Sun over the past few billion years. As such, the 10^{14} protons of the LHC beam experience a comparable journey to that of our Solar System, *daily*. This machine therefore offers an ideal testing ground to study the stability of conservative Hamiltonian systems, historically tied to the famous *n-body problem* in celestial mechanics. In its simplest formulation, the Kepler problem, two masses orbit each other and the motion remains stable for all eternity. Adding additional masses, say by considering Jupiter alongside the Earth and the Sun, brings us into the famous three-body problem, which has no general closed-form solution. The system can then exhibits chaotic motion and the question of stability becomes a complicated one. This is what led J. Moser to ask [1]: *Is the Solar System stable?* And similarly, one could reasonably ask: *Is the LHC beam stable?*

That being said, most practical applications do not require us to know if the motion is stable for all eternity, but simply for a limited *meaningful* period of time, which lifts a lot of mathematical subtleties and opens the door for numerical methods to be used. When the single-particle motion is not stable, or *regular*, it is said to be *chaotic*, in the sense of Poincaré [1, 2], which is to say that the trajectory cannot be represented as a convergent series. Chaotic motion may appear to be random at all times, or it may appear to be regular over long periods of time before diverging [3]. If this characteristic time length is longer than the lifetime of the circulating beams, then such a trajectory might be, by all practical accounts, indistinguishable from a stable one.

In any case, the behaviour of a system as a whole is in general neither completely regular nor chaotic, but *mixed*. As demonstrated by the KAM theorem [1] (1954-1963), mixed systems always admit some regular solutions close to integrable regions of the system. This can be seen, for example, with the gaps in the rings of Saturn or the gaps in the observed frequencies of the asteroids orbiting our Sun [4]: unstable chaotic trajectories amidst stable ones. With the popularization of computational physics, both types of trajectories can be observed and studied, although the challenge presented by chaos still remains. To paraphrase S. Wolfram [5, 6]: "We've come to believe that there would be formulas to predict everything. But computational irreducibility [*e.g.*, for chaotic systems] shows us that that isn't true, and that in fact, to find out what a system will do, we have to go through the same irreducible computational steps as the system itself". As such, chaotic motion is perfectly deterministic, but the future state of the system cannot be found readily from its present state. This simple fact establishes *particle tracking* as the fundamental tool to be used in order to better our understanding of complex machines like the LHC.

By design, the magnetic lattice of storage rings is built mainly out of linear elements: dipolar and quadrupolar magnets for which the Hamiltonian admits closed-form solutions (analogous to the Kepler problem). Of course, real machines make use of higher order magnets (sextupoles, octupoles, etc.) and feature high order multipolar contributions such that the final non-linear system admits mixed solutions. Despite this complexity, the linear picture has become the standard description of accelerator physics since the work of Courant and Snyder in 1958 [7]. In fact, the Courant-Snyder theory [8] has been a cornerstone in the design, description, and operation of particle accelerators. The success of this approach is partly due to the fact that its main assumptions — that of linear and uncoupled dynamics — have proven to be excellent approximations to describe realistic stable machines.

However, as highlighted by A. Chao [9], the Courant-Snyder picture is not without weakness and fails to describe non-linear dynamics in a natural way. Indirectly, the ubiquity of this linear formalism popularized the idea that elliptical phase space topologies are to be expected in particle accelerators. With non-linear magnets present in the lattice, this formalism is of course unsatisfactory and one should instead expect the particle trajectories to follow a more complex shape, described by a more general quasiperiodic expansion (of which ellipses are only a particular case [10]). In fact, this was already well described by the epicycle theory of the Greeks, formalized in the *Almagest of Ptolemy* [11], which is to say that the motion can be decomposed into a finite number of uniform circular motions. This age-old claim still finds itself to be useful in modern times, as discussed in later sections.

On the analytic front, these ideas are not so far from the picture provided by the *normal form* approach [12], which aims at finding an approximate interpolating Hamiltonian to describe the system. In the last few decades, this framework allowed for the formulation of the so-called resonance driving terms (RDTs), which are used to describe perturbations from the linear behaviour, arising from the presence of high order multipolar terms and other spurious effects [13]. Correction schemes based on experimental measurements of resonance driving terms have had important practical results for the successful operation of the LHC. That being said, when the machine complexity is increased, far-reaching assumptions are needed for those methods to succeed, without which the analytic calculations rapidly become intractable.

One can therefore understand the interest that was put, over the years, towards the development of *symplectic* particle tracking codes [14], driven by the need to accurately investigate the complex dynamics of non-linear systems beyond the reach of analytic calculations. By numerically implementing symplectic elements [15], tracking codes can be used to build virtual machines which closely resemble the real machines being modelled and for which the single-particle physics is accurate. From there, complex phenomena such as particle diffusion or chaos can be studied via brute-force tracking of many particles over long periods of time. But as mentioned, when trying to interpret the results, the linear formalism commonly used in accelerator physics falls short of a proper description of the non-linear effects.

The present paper is set to address the aforementioned limitations. It needs to be said that no new mathematical results are presented, most of which can be found in earlier work [16]. Instead, we propose a revised formalism which allows for a deeper conceptualization and understanding of non-linear motion in particle accelerators, both for the longitudinal and the transverse motion. First, it is shown (section II) that the quasiperiodic expansion describing the time series of regular trajectories can be obtained numerically — from tracking — to a high level of accuracy. From there, the approximate energy manifold of the particles can be constructed following a simple change of variable. This topological jump (section III), in turn, allows for the visualization and the computation of an area which is conserved by the symplectic transformations of the system — the so-called integrals of motion — in 2D, 4D and 6D (section III B). Additionally, coupled motion and phase space smearing appear naturally within the context of this formalism. Finally (section IV), these concepts are applied to tracking data from the 6D LHC, where it is shown that the integrals of motion can indeed be accurately computed for a large region of the phase space.

II. THEORY & FORMALISM

The Hamiltonian flow of a conservative system (*e.g.* a non-dissipative storage ring) can be expressed via a symplectic *map*, which describes the discrete evolution from an initial set of coordinates to a final set of coordinates, some finite time later [17]. This is the essence of particle tracking codes, where single particles are transported along the accelerator and their trajectories are observed in phase space, turn after turn. It can be shown that a simple non-linear lattice made out of dipoles, quadrupoles and a single sextupole follows the well-known Hénon map [18] (see Appendix B for details of the map), which will be used for illustrative purposes in the following sections.

A. KAM Theorem

A fundamental aspect to consider for the stability of single-particle trajectory is the question of integrability. A system with n degrees of freedom (a $2n$ dimensional phase space) is said to be *integrable* if there exist n independent integrals of motion I_i, also called *actions*, which commute under the Poisson bracket $\{I_i, I_j\} = 0$ $(i, j = 1, 2, \ldots, n)$. For a realistic particle accelerator with 3 degrees of freedom, one should therefore expect to be able to find 3 integrals of motion [19] such that the Hamiltonian $\mathcal{H}$ can be written as a function of the actions only:

$$\mathcal{H}(x, p_x, y, p_y, \zeta, p_\zeta) \mapsto \mathcal{H}(I_x, I_y, I_\zeta) \tag{1}$$

In general, however, the Hamiltonian might be not integrable for all initial conditions and the system is mixed. It exhibits both regular motion, for which the series development of the trajectory converges, and chaotic motion, for which it does not. Fig. 1 shows the phase space portrait of the Hénon map, for which the two types of trajectories can be clearly identified. As mentioned by M. Hénon, regular trajectories "seem to lie exactly on a curve" [19], which takes the form of a quasiperiodic series (see following section). The KAM theorem, from Kolmogorov, Arnold and Moser, guarantees the *existence* of some of those regular trajectories for certain classes of mechanical systems [1, 3]. This is notably the case of the n-body problem, as well as restricted regions of non-integrable systems where the Hamiltonian is almost integrable (in a perturbative sense). Particle accelerators belong to this latter category. Since particle accelerators are built by adding high-order multipoles to a linear foundation of dipoles and quadrupoles, they are intrinsically designed in a perturbative fashion. Hence, the final Hamiltonian is well integrable near the closed orbit — stable, by construction — of the machine and stable KAM solutions are guaranteed to *exist*, up to some amplitude.

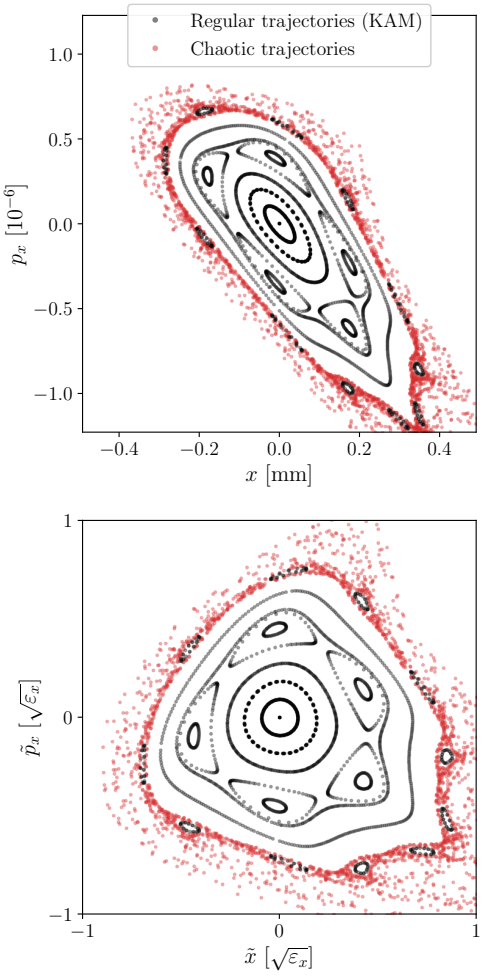

FIG. 1. Phase space portrait of the 2D Hénon map ($\mu_x = 0.2071$) in the physical phase space with $\varepsilon_x = 0.335$ nm (top plot) and the Courant-Snyder phase space (bottom plot). Both regular and chaotic trajectories can easily be identified. The KAM theorem guarantees the existence of some regular trajectories near the elliptical fixed points.

B. Choice of Coordinates

Naturally, the single-particle motion at a given s position along the ring can be described in the physical phase space $\vec{x} = (x, p_x, y, p_y, \zeta, p_\zeta)$ directly from tracking (see Appendix A for details), as shown in the top plot of Fig. 1. However, to highlight the effect of non-linearities, the coordinates can always be transformed into the Courant-Snyder (or *linearly normalized*) phase space coordinates $\vec{\tilde{x}} = (\tilde{x}, \tilde{p}_x, \tilde{y}, \tilde{p}_y, \tilde{\zeta}, \tilde{p}_\zeta)$ with the help of the W-matrix [20] using $\vec{\tilde{x}} = W^{-1}(s)\ \vec{x}$. By doing so, linear motion (*e.g.* close to the origin) takes the form of circles instead of ellipses, as shown in the bottom plot of Fig. 1. A convenient way to describe the turn-by-turn motion of a particle is to use the complex notation $\tilde{\psi}_x = \tilde{x} - i\tilde{p}_x$, combining the position and the momentum together [21]. One can then write, for 2D linear motion:

$$\tilde{\psi}_x(N) = \tilde{x} - i\tilde{p}_x = A_0\ e^{i[2\pi Q_x N]} \quad (\text{for } I_x \to 0) \tag{2}$$

where N is the turn number, $|A_0| = \sqrt{2I_x}$ is the radius of the circle in the complex plane and Q_x is the *fundamental frequency* of the particle. In the Courant-Snyder phase space, the coordinates ($\tilde{x}$, $\tilde{p}_x$, etc.) homogeneously assume units of $\sqrt{\text{m}}$. If the beam emittance is known, one can further express the coordinates in units of $\sqrt{\varepsilon}$ such that $\tilde{x} = 1\ \sqrt{\varepsilon_x} \ \mapsto \ x = 1\ \sqrt{\beta_x \varepsilon_x} = 1\ \sigma_x$, which relates to the beam size.

Regular trajectories can in principle be further simplified by going to *normal form*, $\vec{\hat{x}} = (\hat{x}, \hat{p}_x, \hat{y}, \hat{p}_y, \hat{\zeta}, \hat{p}_\zeta)$, a phase space where the motion takes the form of purely

independent rotations around a given fixed point (typically the origin) expressed in terms of the action-angle variables [12] — similar to eq.(2), but for all amplitudes. That being said, this transformation is not straightforward and cannot be done, in general, without resorting to numerical methods like the ones presented in this paper. It is nonetheless important to note that there *exists*, in principle, such a transformation which can be used to normalize the motion step-by-step, going from the physical to Courant-Snyder to normal form phase space, $(x, p_x) \mapsto (\tilde{x}, \tilde{p}_x) \mapsto (\widehat{x}, \widehat{p}_x)$, in a symplectic manner.

C. Regular Motion & Quasiperiodic Expansion

One important practical implication of the KAM theorem is to provide us with a closed-form expression to describe regular trajectories. Using the complex notation $\tilde{\psi}_x = \tilde{x} - i\tilde{p}_x$ to describe both position and momentum in the Courant-Snyder phase space, the motion in each plane can be written as three Fourier series, each made of N_h harmonics, following:

$$\begin{aligned}
\tilde{\psi}_x^{(N_h)}(N) &= \tilde{x} - i\tilde{p}_x = \sum_{k=0}^{N_h} A_k \; e^{i[2\pi(\vec{n}_k \cdot \vec{Q})N]} \\
\tilde{\psi}_y^{(N_h)}(N) &= \tilde{y} - i\tilde{p}_y = \sum_{k=0}^{N_h} B_k \; e^{i[2\pi(\vec{m}_k \cdot \vec{Q})N]} \\
\tilde{\psi}_\zeta^{(N_h)}(N) &= \tilde{\zeta} - i\tilde{p}_\zeta = \sum_{k=0}^{N_h} C_k \; e^{i[2\pi(\vec{\ell}_k \cdot \vec{Q})N]}
\end{aligned} \tag{3}$$

giving us the coordinates as a time series in N, the turn number. The spectral amplitudes A_k, B_k and C_k are complex numbers, sorted with decreasing amplitudes for increasing k. In general, this description of the motion is only an *exact* solution to the KAM problem when $N_h \to \infty$. By truncating the quasiperiodic expansion to a finite N_h, one obtains an approximate solution where the error is periodic and bounded, provided that the KAM solution exists. It is noteworthy that the series development in each plane only contains contributions from a *discrete set* of well-defined spectral lines ν_k (or frequencies, with units of turn^{-1}) [22]. For example, in the horizontal plane, $\tilde{\psi}_x$, one can write:

$$\nu_k = \vec{n}_k \cdot \vec{Q} + n_{0k}, \qquad \vec{n}_k \in \mathbb{Z}^3, \; n_{0k} \in \mathbb{Z} \tag{4}$$

where the $\vec{n}_k \cdot \vec{Q} = (n_x, n_y, n_\zeta)_k \cdot (Q_x, Q_y, Q_\zeta)$ are integer linear combinations (and so are $\vec{m}_k \cdot \vec{Q}$ and $\vec{\ell}_k \cdot \vec{Q}$) of the particle's fundamental frequencies, $\vec{Q}$, properties of the single-particle trajectory, shared between the three planes $\tilde{\psi}_x$, $\tilde{\psi}_y$ and $\tilde{\psi}_\zeta$. For the convenience of the graphical representation, the frequencies are aliased in the domain $\nu_k \in [-0.5, 0.5]$ using the additional integer n_{0k}, without loss of generality.

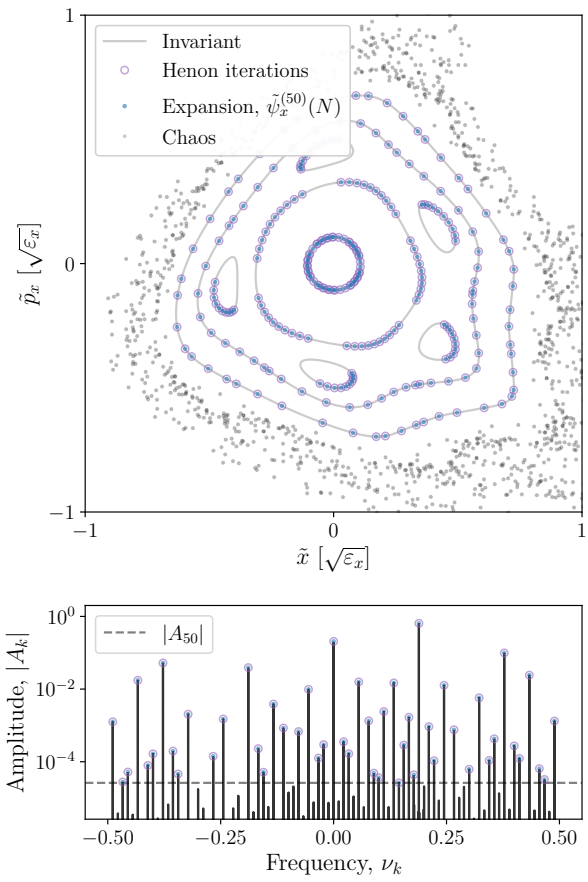

FIG. 2. Comparison of the time series obtained from the quasiperiodic expansion of eq. (3) for the 2D Hénon map ($\mu_x = 0.2071$) and the map itself, shown for the last 50 turns out of 10^5 iterations. The expansion is numerically obtained from $N_h = 50$ harmonics evaluated after 10^4 turns. The validity of the time series therefore extends outside of its evaluation window. The bottom plot shows the Fourier spectrum of the outermost stable particle from the plot above: only the discrete set of frequencies from eq. (4) are found.

In Fig. 2, the turn-by-turn position obtained from eq. (3) (truncated to $N_h = 50$ harmonics) is compared to the iterations of the Hénon map itself from which it was numerically extracted. As shown in the bottom plot, the Fourier spectrum of a regular trajectory contains a discrete set of frequencies, made out of linear combinations of the fundamental frequency — one only, for this 2D case — as stated by eq. (4). The description of the motion given by eq. (3) is an important cornerstone of the present approach, allowing for a closed-form analysis of the trajectories. One can see that the turn-by-turn position lies on an *invariant* curve, which will be introduced in the next section. The area enclosed by this loop is an integral of motion, preserved under Hamiltonian transformations.

The interest of eq. (3) lies in the fact that the Fourier expansion can be obtained numerically from a Fourier analysis or — to a better accuracy — from the Numerical Analysis of the Fundamental Frequencies (NAFF), introduced by Laskar [22]. This claim holds even for complex non-linear systems, where analytic calculations become impractical. The NAFF algorithm (see `nafflib` [23], or Appendix C [24–27]) is an iterative scheme where a windowing function is used to recover the frequencies of the signal with an accuracy that is several orders of magnitude better than a simple Fast Fourier Transform (FFT).

After finding the dominant frequency, ν_0, its contribution is subtracted from the original signal and the procedure is repeated to obtain the second dominant frequency, ν_1, and so on. By doing so, one eventually obtains the set of sorted amplitudes, A_k, and frequencies, ν_k, corresponding to the quasiperiodic expansion of eq. (3) with great accuracy for a relatively low number of turns. For the 2D Hénon map shown in Fig. 2, 10^4 turns are sufficient to get most frequencies up to machine precision, which allows to describe the time series of the quasiperiodic trajectory beyond the analysis window, say up to 10^5 turns in this particular example. Evidently, the numerical description obtained is an approximation of the real trajectory of the map.

III. ENERGY MANIFOLD

For the non-dissipative conservative case, individual particles conserve their energy and the single-particle trajectories are constrained to evolve on well-defined constant-energy surfaces, called — in phase space — *energy manifolds*. By construction, these energy manifolds are invariant under the one-turn map of the system, *i.e.* the mapping of any point from the energy manifold also belongs to the manifold itself, one turn later. This can be seen, for example in 2D, from the invariant curves of the Hénon map depicted in Fig. 2. The following sections generalize this idea to 4D and 6D systems and present a description which allows for the calculation of the integrals of motion.

A. Invariant Tori

By following a given particle (*e.g.* in Fig. 2) over many turns using eq. (3), one finds that it eventually covers the invariant curve — the energy manifold — on which it resides *densely*. Out of the quasiperiodic turn-by-turn motion emerges an underlying periodic structure. This is to say that the main argument of the quasiperiodic expansion, $2\pi\vec{Q}N \pmod{2\pi}$, smoothly and monotonically completes a full period in the process of describing the energy manifold. In fact, provided that $\vec{Q}$ does not satisfy any resonant condition [16], $\vec{p}\cdot\vec{Q} = q$ ($\vec{p} \in \mathbb{Z}^3$, $q \in \mathbb{Z}$), the energy manifold of a particle can be recovered with the simple change of variable $\vec{\Theta} = 2\pi\vec{Q}N$. By doing so, one constructs an invariant torus, $\tilde{\Psi}$, directly from the time series of eq. (3). Denoting the projections of the torus in all three planes as $\tilde{\Psi}_x$, $\tilde{\Psi}_y$ and $\tilde{\Psi}_\zeta$, one can write:

$$\begin{aligned}
\tilde{\Psi}_x^{(N_h)}(\vec{\Theta}) &= \tilde{X} - i\tilde{P}_x = \sum_{k=0}^{N_h} A_k \; e^{i[\vec{n}_k\cdot\vec{\Theta}]} \\
\tilde{\Psi}_y^{(N_h)}(\vec{\Theta}) &= \tilde{Y} - i\tilde{P}_y = \sum_{k=0}^{N_h} B_k \; e^{i[\vec{m}_k\cdot\vec{\Theta}]} \\
\tilde{\Psi}_\zeta^{(N_h)}(\vec{\Theta}) &= \tilde{Z} - i\tilde{P}_\zeta = \sum_{k=0}^{N_h} C_k \; e^{i[\vec{\ell}_k\cdot\vec{\Theta}]}
\end{aligned} \tag{5}$$

where capital letters are used to distinguish the single-particle coordinates ($\tilde{x}, \tilde{p}_x$, etc.) from the underlying topological object ($\tilde{X}, \tilde{P}_x$, etc.) on which they reside. Broadly speaking, an n-dimensional torus is a periodic structure constructed as the product of n independent circles, or periodicities such as $\vec{\Theta} = (\Theta_x, \Theta_y, \Theta_\zeta)$ [28]. The above result is therefore deeply linked to the existence of the normal form. Indeed, this particular phase space — where the motion takes the form of independent rotations — informs us that the energy manifolds of regular trajectories are topologically described by hyperdimensional tori. By going into the Courant-Snyder phase space (or even physical phase space), this claim is no less true and the topology is preserved, albeit deformed, leading to eq. (5). In the resonant case, the topology is different and needs to be appropriately described with regards to its corresponding fixed point. For example, the 5-th order resonance shown in Fig. 2 requires to consider the 5-cycle of the map (thereby lifting the resonant condition) to get a new expansion in the form of eq. (3) and construct the energy manifold with eq. (5).

As mentioned, outside of the resonant condition, a given particle eventually covers the entire surface of its invariant torus as $\Theta_j = 2\pi Q_j N$, $j \in \{x, y, \zeta\}$, varies with arbitrarily large N values, eventually covering $\Theta_j \in [0, 2\pi] \pmod{2\pi}$ densely. This can be seen, for example, from the invariant curves (1-torus) of the Hénon map depicted in Fig. 2, obtained from eq. (5) by letting $\tilde{\Psi}_y = \tilde{\Psi}_\zeta = 0$. It should be clear — at least visually — that the invariant curves $(\tilde{X}, \tilde{P}_x)$ are continuous closed loops, in contrast with the iterations of the map $(\tilde{x}, \tilde{p}_x)$ which are obtained from a stroboscopic sampling (*i.e.* $2\pi Q_x N$) of this underlying topological object. The spectral amplitudes A_k, B_k, C_k and the integer vectors $\vec{n}_k$, $\vec{m}_k$, $\vec{\ell}_k$ in eq. (5) are the same as in eq. (3). As such, the torus obtained is a numerical approximation of the *truly invariant* one ($N_h \to \infty$), obtained from — and fully consistent with — the quasiperiodic expansion of eq. (3).

For systems with more than 2 dimensions, visualizing the invariant tori requires additional care. In particular,

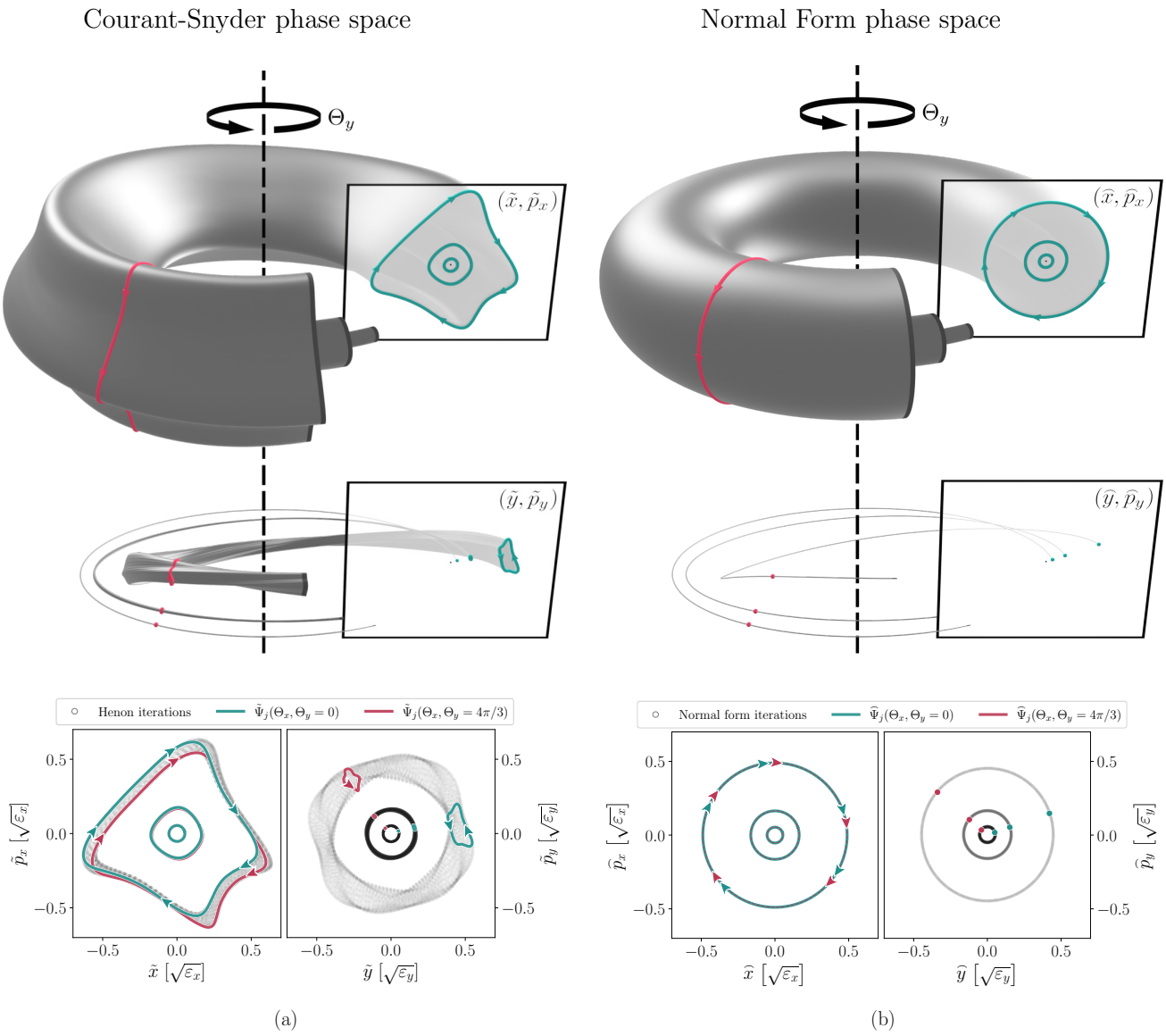

FIG. 3. Visualization of the energy manifolds $\tilde{\Psi}$ (invariant tori) from eq. (5), in grey, for 3 different particles in the 4D Hénon map with $\mu_x = 0.2465$, $\mu_y = 0.4142$ and $\rho = 0.3$ (see Appendix B for details). (a) In the Courant-Snyder phase space, $\vec{\tilde{x}}$. (b) In the normal form phase space, $\vec{\widehat{x}}$. The top plots show the projections of the invariant tori, $\tilde{\Psi}_x(\Theta_x, \Theta_y = \text{cst.})$ and $\tilde{\Psi}_y(\Theta_x, \Theta_y = \text{cst.})$, for all Θ_y. The projections of two different 4-dimensional Θ_x loops are also shown in red and green, travelled following the directional arrows. The area is positively oriented if travelled clockwise. The sum of the areas enclosed by corresponding colored loops is an invariant. The azimuthal deformation of the tori gives rise to the smearing observed in the single-particle trajectory over many turns, when plotted in the conjugate planes, as shown in the bottom plots.

non-linear coupling effects make the analysis difficult by introducing *smearing* [10] in the single-particle trajectories when observed in either the physical phase space, $\vec{x}$, or the Courant-Snyder phase space, $\vec{\tilde{x}}$, as shown in the bottom plot of Fig. 3a for the 4D Hénon map (see Appendix B for details of the map). That being said, eq. (5) offers a way to study and visualize the periodic structure of the underlying tori by letting one of the angles, say Θ_x, vary along a closed loop while fixing the other angles, here Θ_y. By doing so, the projections of the tori are obtained in both transverse planes; $\tilde{\Psi}_x(\Theta_x)$ in $(\tilde{x}, \tilde{p}_x)$ and $\tilde{\Psi}_y(\Theta_x)$ in $(\tilde{y}, \tilde{p}_y)$ for the 4D case, as illustrated in the top plot of Fig. 3a. When the single-particle trajectory is observed over many turns, both angles are densely explored following $\vec{\Theta} = 2\pi\vec{Q}N$ and the azimuthal deformation of the

tori gives rise to the smearing observed in the bottom plot. Non-linear coupling can also be observed in Fig. 3a (more evidently for the high-amplitude particle) as the non-zero area of the projection observed in the $(\tilde{y}, \tilde{p}_y)$ plane. This is to say that $\tilde{\Psi}_y$ varies as a function of Θ_x — the very definition of coupled motion.

More importantly, one can note that the sum of the areas enclosed by the loop projections $\tilde{\Psi}_x(\Theta_x)$ and $\tilde{\Psi}_y(\Theta_x)$ is one of the integrals of motion, conserved under the Hamiltonian flow. By numerically calculating this area following the procedure presented in the upcoming section, one can reconstruct the equivalent normal form tori — circular tori of equal cross-sectional area — as shown in Fig. 3b.

B. Integrals of Motion

Embedded in the very nature of a symplectic transformation is the fact that the enclosed *area* of any loop drawn in phase space is to be conserved [17]. For a $2n$-dimensional phase space, this area is the sum of the n projections, on the different conjugate planes of the system, of the $2n$-dimensional loop. In particular, by choosing a loop lying on the energy manifold of a particle — and moreover obtained from the evolution of a particular periodicity of the system, Θ_j — one obtains the Poincaré integral invariant [16, 17], defined as :

$$I_j = I_{jx} + I_{jy} + I_{j\zeta} = \frac{1}{2\pi} \oint_{\Theta_j} \left(\tilde{P}_x d\tilde{X} + \tilde{P}_y d\tilde{Y} + \tilde{P}_\zeta d\tilde{Z} \right) \quad (6)$$

with $j \in \{x, y, \zeta\}$. Following the construction of the invariant tori with eq. (5), the above integral takes a purely geometric interpretation, already represented graphically in earlier plots. In Fig. 2, $I_x = I_{xx}$ is the area enclosed by the invariant curve of a particle in the $(\tilde{x}, \tilde{p}_x)$ phase space. In Fig. 3, $I_x = I_{xx} + I_{xy}$ is the sum of the areas (identified with a common color) enclosed by the projections of a 4-dimensional Θ_x loop in the $(\tilde{x}, \tilde{p}_x)$ and $(\tilde{y}, \tilde{p}_y)$ conjugate planes. The contribution to the integral can either be positive or negative, depending on the orientation of the loop projection (positive if travelled clockwise), as indicated with the directional arrows in Fig. 3. In that example, the I_{xy} projection — which comes from non-linear coupling — is negative in sign and varies along the torus. That being said, the sum $I_x = I_{xx} + I_{xy}$ is expected to be invariant. In fact, for a general torus described by eq. (5), the result of the integral from eq. (6) can be shown to yield (see Appendix D for derivation):

$$I_j^{(N_h)} = \frac{1}{2} \sum_{k=0}^{N_h} \left(n_{j_k} |A_k|^2 + m_{j_k} |B_k|^2 + \ell_{j_k} |C_k|^2 \right) + \epsilon_j(\vec{\Theta}) \quad (7)$$

which carries a remaining $\vec{\Theta}$ dependence. For a pure KAM torus — that is, the energy manifold of a Hamiltonian system — the $\vec{\Theta}$ dependence observed in each projection is required to cancel out, which allows us to write:

$$\epsilon_j(\vec{\Theta}) = \Delta_{jx}(\vec{\Theta}) + \Delta_{jy}(\vec{\Theta}) + \Delta_{j\zeta}(\vec{\Theta}) = 0 \quad \forall \quad \vec{\Theta} \quad (8)$$

where the Δ functions describe the variation of each projection as a function of the non-integrated angles due to coupling effects, as discussed in the next section. However, in the numerical approximation of a KAM torus, it might be the case that the remainder $\epsilon_j(\vec{\Theta})$ does not exactly cancel out, which will be discussed in section III B 2. It is important to mention that the remainder $\epsilon_j(\vec{\Theta})$ being zero or not is not an artifact of the truncation itself, but rather the result of the torus being Hamiltonian or not.

This Poincaré integral, expressed in eq. (6) in terms of the Courant-Snyder variables, can equally be computed in the physical phase space or the normal form phase space. Since Θ_x, Θ_y and Θ_ζ are 3 *independent* periodicities of the torus, they describe 3 topologically independent loops, where none of the loops can be deformed continuously into each other or shrunk to zero [28]. Hence, the 3 integrals of motion obtained via eq. (6) are independent actions of the system.

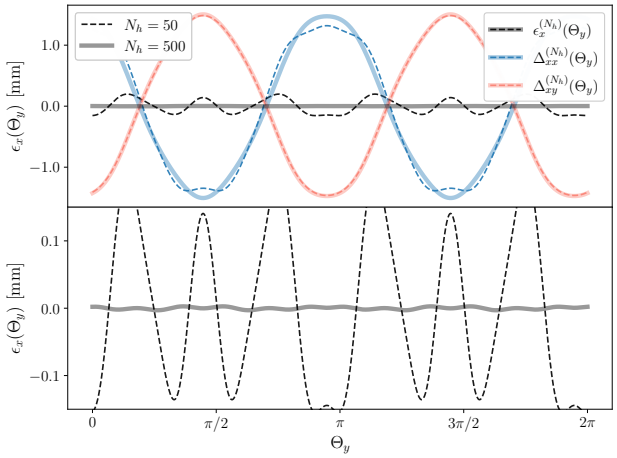

FIG. 4. Evolution of the angle-dependant terms in the partial actions, I_{xx} and I_{xy}, for the case of the 4D Hénon map (from Fig. 3a, outermost trajectory). Two truncation numbers, N_h, are shown. As $N_h \to \infty$, the sum of the angle-dependant terms goes to zero, $\epsilon_x = \Delta_{xx} + \Delta_{xy} \to 0$. With $N_h = 50$ the variations along the torus are in the order of 0.1% of the action.

1. *Angle-dependant projections*

As mentioned, the projections of a given loop in the conjugate planes of the system each carry an angular dependence, which only cancels out when the projections are summed together via eq. (6), following eq. (8). This

can be seen in the bottom plot of Fig. 3a, where the projection of the red loop in the $(\tilde{y}, \tilde{p}_y)$ plane is smaller than its green counterpart, evaluated at a different Θ_y. In fact, for a loop around Θ_j, the projections in the 3 different conjugate planes, $I_{jx} = \frac{1}{2\pi} \oint_{\Theta_j} \tilde{P}_x d\tilde{X}$, $I_{jy} = \frac{1}{2\pi} \oint_{\Theta_j} \tilde{P}_y d\tilde{Y}$ and $I_{j\zeta} = \frac{1}{2\pi} \oint_{\Theta_j} \tilde{P}_\zeta d\tilde{Z}$ take the form:

$$\begin{cases} I_{jx}^{(N_h)}(\vec{\Theta}) = \dfrac{1}{2} \displaystyle\sum_{k=0}^{N_h} n_{j_k} |A_k|^2 + \Delta_{jx}(\vec{\Theta}) \\ I_{jy}^{(N_h)}(\vec{\Theta}) = \dfrac{1}{2} \displaystyle\sum_{k=0}^{N_h} m_{j_k} |B_k|^2 + \Delta_{jy}(\vec{\Theta}) \\ I_{j\zeta}^{(N_h)}(\vec{\Theta}) = \dfrac{1}{2} \displaystyle\sum_{k=0}^{N_h} \ell_{j_k} |C_k|^2 + \Delta_{j\zeta}(\vec{\Theta}) \end{cases} \tag{9}$$

where for example:

$$\Delta_{xx}^{(N_h)}(\vec{\Theta}) = \frac{1}{2} \sum_{k=0}^{N_h} \sum_{l \neq k}^{N_h} \delta_{n_{x_k}}^{n_{x_l}} \left(n_{x_k} |A_k||A_l| \cos(\varphi_{x_k} - \varphi_{x_l}) \right) \tag{10}$$

in which δ_a^b is the Kronecker delta and $\varphi_{x_k} = n_{y_k}\Theta_y + n_{\zeta_k}\Theta_\zeta + \arg[A_k]$ is the parameter responsible for the dependence on Θ_y and Θ_ζ, the non-integrated angles. The different Δ functions are obtained from eq. (10) by permuting the plane considered, *i.e.* where $\Delta_{xx} \to \Delta_{xy} \to \Delta_{x\zeta}$ is obtained by replacing $\vec{n}_k \to \vec{m}_k \to \vec{\ell}_k$ and $A_k \to B_k \to C_k$ and so on.

The evolution of these angle-dependant terms is shown in Fig. 4 for the numerical approximation of a KAM torus obtained with different truncation numbers. The invariant torus considered is the one from the outermost particle from Fig. 3a. As one can see, the remainder $\epsilon_x(\vec{\Theta}) = \Delta_{xx}(\vec{\Theta}) + \Delta_{xy}(\vec{\Theta})$ goes to zero as the number of harmonics, N_h, is increased.

2. *Numerical evaluation*

If the closed-form expansion provided by eq. (5) holds — that is if the time series of eq. (3) accurately describes the single-particle motion and $\vec{Q}$ does not satisfy any resonant condition — then all the aforementioned quantities can be computed numerically for the torus considered, which serves as an approximation to the energy manifold of the particle. However, as shown in Fig. 4, the angular dependence of this numerical description is not guaranteed to cancel out when summing up the different projections. In such cases, the action becomes difficult to evaluate. That being said, due to the presence of the cosine in eq. (10), the average over the angles — for any Δ function — always vanishes, *i.e.* $\langle \Delta \rangle_{\vec{\Theta}} = 0$. Moreover, since the amplitude of these oscillating functions converges towards zero as the number of harmonics is increased, the average value of $I_j^{(N_h)}(\vec{\Theta})$ can be taken as an estimator of the true action for most truncation numbers. In fact, one can show that this average yields:

$$\left\langle I_j^{(N_h)} \right\rangle_{\vec{\Theta}} = \frac{1}{2} \sum_{k=0}^{N_h} \left(n_{j_k} |A_k|^2 + m_{j_k} |B_k|^2 + \ell_{j_k} |C_k|^2 \right) \tag{11}$$

which is identical to eq. (7) with $\epsilon_j(\vec{\Theta}) = 0$, the action of a pure KAM torus. From there, one can asses the numerical validity of the approximation of a given torus by writing its actions as $I_j(\vec{\Theta}) = \langle I_j \rangle_{\vec{\Theta}} + \epsilon_j(\vec{\Theta})$, separating the constant part from the angle-dependant part. Nevertheless, the estimation provided by eq. (11) should be the final quoted quantity, since it converges much faster than the remainder, $\epsilon_j(\vec{\Theta})$, when increasing the truncation number. As shown in Fig. 5, the convergence rate of this average depends on the amplitude of the particle or, more generally, on the degree of non-linearity of the lattice at the amplitude considered. The three particles taken here as examples are the ones of Fig. 3a, shown previously. For highly non-linear regimes, an infinite number of harmonics would, in principle, be required.

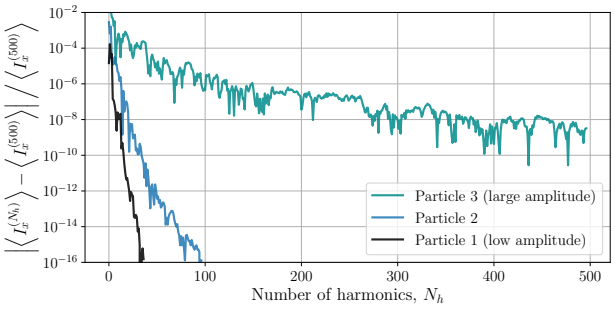

FIG. 5. Relative error of the average action $\left\langle I_x^{(N_h)} \right\rangle_{\vec{\Theta}}$ as a function of the truncation number N_h for the three particles of Fig. 3a. The convergence depends on the degree of non-linearity of the trajectory, which scales with the amplitude.

IV. APPLICATION TO THE LHC

As a final demonstration of the framework introduced in this paper, the case of the 6-dimensional LHC at top energy is studied. The lattice considered is the one used as a baseline for the High-Luminosity upgrade of the LHC (HL-LHC), including beam-beam interactions in all the interaction points of the collider. The beam parameters considered can be found in Table I.

Alongside electron cloud effects, beam-beam effects are the main source of non-linearities in the LHC, leading to important beam losses and the reduction of dynamic aperture by several sigmas [29, 30]. Due to the complex nature of these interactions, their effect on the dynamics of the beam is typically studied in the transverse plane only, after resorting to several approximations. However,

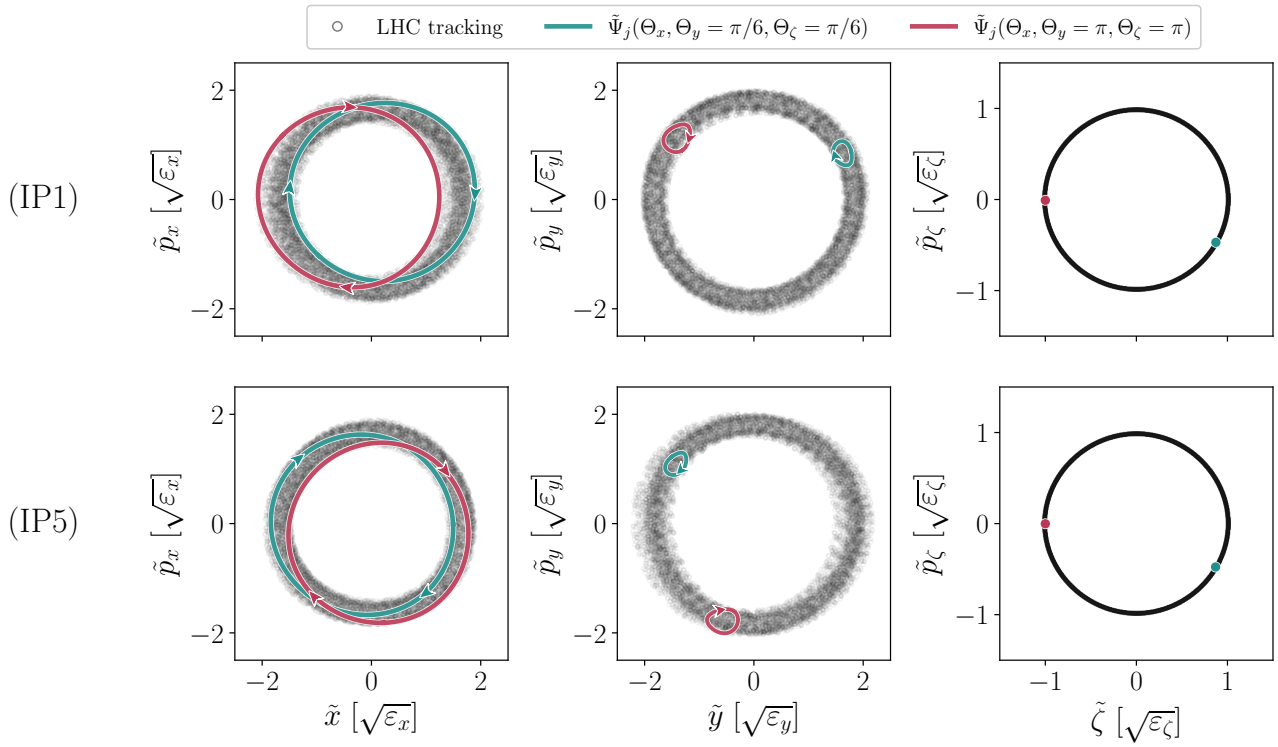

FIG. 6. Tracking results for a particle starting at $(x, y, \zeta) = (1.5\sigma_x, 2\sigma_y, 1\sigma_\zeta)$ in the LHC. The same particle is observed separately in IP1 (top) and IP5 (bottom). The turn-by-turn data is shown, as well as the projections of the corresponding torus in all three planes, $\tilde{\Psi}_x$, $\tilde{\Psi}_y$, $\tilde{\Psi}_\zeta$, looping over Θ_x. Exploring all the possible Θ_y and Θ_ζ values allows to explain the important smearing of the trajectory. The horizontal action $I_x = I_{xx} + I_{xy} + I_{x\zeta}$ is obtained from the sum of the projected areas, identified with a common color.

TABLE I. HL-LHC parameters considered.

Parameter		**Value**	**Unit**
Beam Energy	E	7.0	(TeV)
Bunch intensity	N_b	1.13×10^{11}	(p^+/b)
Norm. Emittance	$\varepsilon_x^N, \varepsilon_y^N$	2.5	(µm·rad)
Long. Emittance†	ε_ζ^N	62	(mm·rad)
Beta at the IP	β^*	15	(cm)
Half-crossing	$\theta_c/2$	250	(µrad)
Crabbing angle	θ_{cc}	−190	(µrad)
Octupoles	I_{oct}	−60	(A)
Tunes	$(Q_x, Q_y)_{\text{c.o.}}$	(62.312, 60.319)	
	$Q_{\zeta_{\text{c.o.}}}$	−0.002	
Chromaticities	$\Delta Q_{x_{\text{c.o.}}}, \Delta Q_{y_{\text{c.o.}}}$	15	

† See Appendix A for details.

using the Hirata method [20, 31], beam-beam effects can be accurately modelled in 6D tracking codes, including their impact on the longitudinal plane.

For this complex 6D case, synchro-betatron coupling effects arise and the dynamics becomes difficult to analyze. However, the system is still Hamiltonian and the formalism introduced above, mainly driven by eq. (3) and eq. (5), can still be used. Using NAFF to extract $N_h = 100$ harmonics in all three planes, the approximate tori can be constructed to evaluate the action and understand the heavily smeared single-particle trajectories observed in the tracking results. Such an example is shown in Fig. 6, where an off-momentum particle starting from $(x, y, \zeta) = (1.5\sigma_x, 2\sigma_y, 1\sigma_\zeta)$ is tracked over 10^5 turns. Slices of the corresponding torus (looping over Θ_x as an example) are shown on top of tracking data for different values of Θ_y and Θ_ζ. One can see that the turn-by-turn data can be obtained from a stroboscopic sampling ($\vec{\Theta} = 2\pi\vec{Q}N$) of this torus, turn after turn. In fact, by exploring all of the $\vec{\Theta}$ angle values, one can show that the entirety of the smeared region is eventually covered. Additionally, the horizontal action $I_x = I_{xx} + I_{xy} + I_{x\zeta}$ is obtained from the sum of the projected areas of the Θ_x loop in all three planes, identified with a common color. To show — at least visually — the effect of symplectic transformations along the machine, two independent monitors are installed, one in IP1 and one in IP5, for comparison.

The integrals of motion shall respect the defining feature of being invariant in time — turn after turn

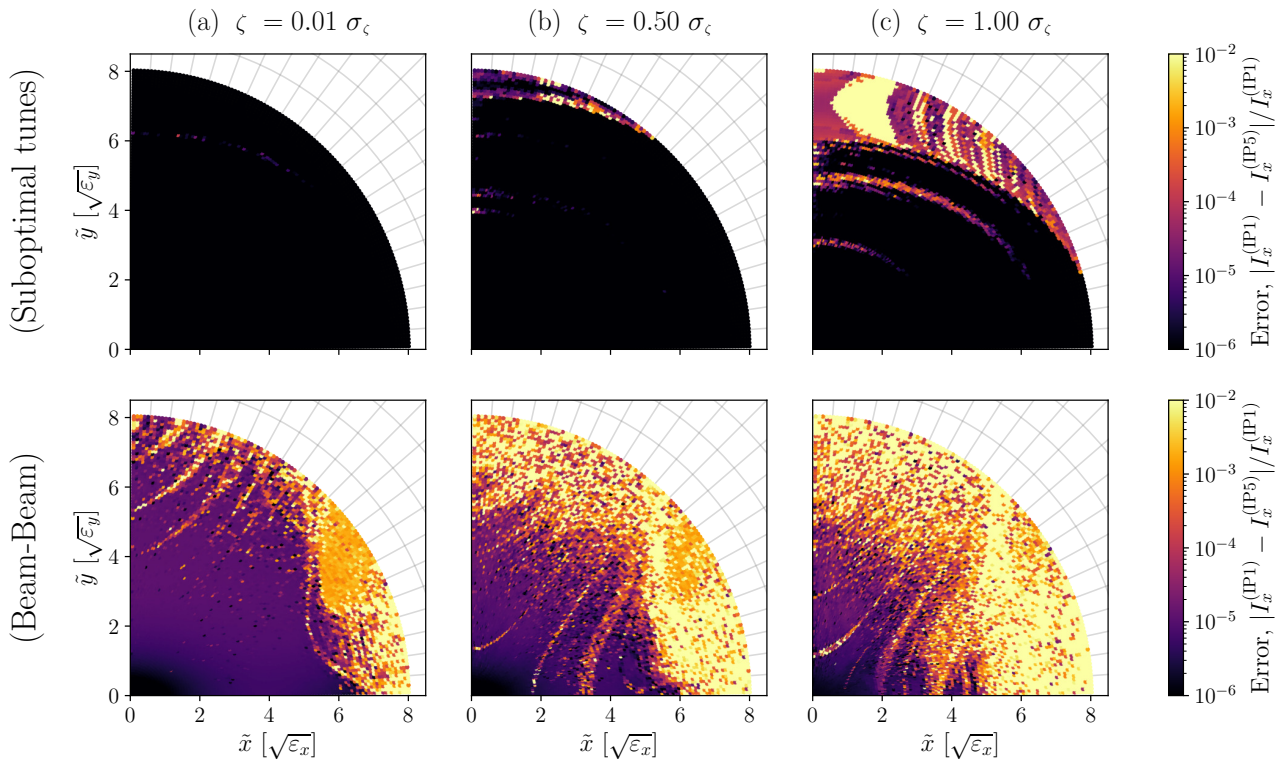

FIG. 7. Evaluation of the variation of the horizontal action, I_x, between IP1 and IP5 for two different versions of the HL-LHC lattice from Table I. (Top) A suboptimally tuned $(Q_x, Q_y)_{\text{c.o.}} = (62.315, 60.331)$ lattice without beam-beam interactions. (Bottom) The baseline HL-LHC lattice at top energy with beam-beam interactions in all IPs. Three initial off-momentum coordinates are sampled ($\zeta = \{0.01\sigma_\zeta, 0.50\sigma_\zeta, 1.00\sigma_\zeta\}$) and a dense grid of transverse initial positions is considered in each case. The presence of beam-beam interactions increases significantly the number of resonances. The trajectory of a particle taken from the rightmost bottom plot is shown in Fig. 6.

— as well as along the machine — in s. The latter form of conservation is easier to evaluate numerically since it trades computing time for memory. As such, a similar study to the one shown graphically in Fig. 6 was repeated for a dense grid of particles in the 6-dimensional phase space and the variation of the horizontal action, I_x, between IP1 and IP5 was evaluated. The results of this study are shown in Fig. 7 for two different machines based on Table I: a suboptimally tuned $(Q_x, Q_y)_{\text{c.o.}} = (62.315, 60.331)$ version of the HL-LHC baseline lattice without beam-beam (top); as well as the full HL-LHC baseline lattice including beam-beam interactions (bottom). The particles were tracked for 10^5 turns and $N_h = 100$ harmonics were extracted. It is noteworthy that a smaller number of turns could have been considered for the numerical evaluation of a simpler lattice. However, in presence of beam-beam effects, many spectral lines are introduced, which requires a higher number of turns to accurately resolve the spectrum. As an example of a simpler system, the reader is referred to the case of the 2D Hénon map, shown in Appendix F.

The suboptimally tuned case (top plots, Fig. 7) shows that the integrals of motion, evaluated numerically on the basis of eq. (11), are indeed well-preserved between the IPs. In these plots, resonance conditions appear as bright stripes where the integrals of motions cannot be properly evaluated due to the breaking of the topological condition required for eq. (5) to hold. In the bottom plots, one can see that the addition of beam-beam interactions increases significantly the number of resonances and makes the evaluation of the integrals of motion more challenging. In principle, the variation of the action between the IPs could be reduced for a large region of the phase space (purple region, $\sim 10^{-5}$ action error) by increasing the number of turns or the number of harmonics considered due to the high degree of non-linearities present in the lattice. Indeed, as shown in Fig. 6 (particle taken directly from the bottom plot of Fig. 7c), the motion in that region remains regular and is well-described by the approximate invariant torus extracted from the tracking. On the contrary, for resonant cases, such a behaviour cannot be recovered and the picture is completely different. However, the labelling of resonant cases is a subtle issue which should not be trivialized. The reader is referred

to Appendix E for additional details. As a final note, it appears that the continuity of the action is an important indicator to consider when trying to determine whether a given particle lies on a KAM torus or not, as highlighted in Appendix F.

V. SUMMARY

This paper showed that invariant tori can be constructed numerically to approximately describe the energy manifold of single-particle trajectories based on tracking data. From there, the integrals of motion can be found based on the area of the tori projections in all conjugate planes — in 2D, 4D or 6D — and computed numerically. The formalism described is based on the KAM theorem, which guarantees the existence of some regular trajectories expressed in terms of complex Fourier series. After extracting the harmonics of said series from tracking data, it is shown that the underlying topological object — an invariant torus — can be constructed. This conceptualization of the motion allows to describe coupled motion (transverse and synchro-betatron coupling) in a natural manner and accounts for the heavily smeared trajectories observed in phase space. Examples are shown based on the 2D and 4D Hénon map. As a final numerical demonstration, it is shown that the HL-LHC baseline lattice can be studied with this formalism, including beam-beam effects in 6D. This pragmatic and descriptive approach appears promising to further the understanding of non-linear motion in particle accelerators, beyond the reach of analytic calculations. In particular, the closed-form expression presented to describe invariant tori can be used to quantify non-linearities and tori deformation for compensation studies, as well as non-linear matching problems. That being said, some important challenges remain with regard to the transition from regular to resonant to chaotic motion, which was not explored in this paper.

ACKNOWLEDGMENTS

The authors would like to thank R. Baartman, T. Planche and D. Kaltchev for their help and guidance throughout the redaction of this paper. Moreover, the important contribution of K. Paraschou, through numerous discussions and arguments, needs to be highlighted. Finally, special thanks to C.E. Montanari, M. Giovannozzi and A. Bazzani for their feedback on the work.

Appendix A: Single-particle tracking

The formalism developed in this paper is intended to be general and independent of the tracking code considered. That being said, it is worth mentioning that the notation used throughout the paper is based on the Xsuite code [32], developed at CERN. Xsuite is a 6D single particle symplectic tracking code used to compute the trajectories of individual relativistic charged particles in circular accelerators. Following standard practices, the coordinates presented in Section II B correspond to deviations from the reference trajectory of a particle with speed $\beta_0 c$ and momentum P_0. The transverse canonical momenta P_x and P_y are normalized following:

$$p_x = P_x/P_0 \quad \text{and} \quad p_y = P_y/P_0 \ , \tag{A1}$$

yielding the unitless momentum considered in this paper. In the longitudinal plane, the longitudinal deviation from the reference particle, as well as the energy deviation, are considered. The coordinates (ζ, p_ζ) therefore read:

$$\zeta = s - \beta_0 ct \quad , \quad p_\zeta = \frac{1}{\beta_0^2}\frac{E - E_0}{E_0} \ . \tag{A2}$$

Just like the transverse coordinates, (ζ, p_ζ) can be transformed into the Courant-Snyder phase space to obtain $(\tilde{\zeta}, \tilde{p}_\zeta)$ with the help of the W-matrix, as discussed in Section II B. By doing so, the longitudinal motion lies on circles for small energy deviations and is ultimately limited by the RF bucket for large energy deviations, as shown in Fig. 8, which is given as an example of the metric. In the paper, the longitudinal coordinates are often given in units of σ_ζ, which coincide with the dashed lines of Fig. 8, in the Courant-Snyder phase space.

In Table I, the normalized longitudinal emittance is given in units of mm·rad, which requires clarifications. The design bucket area of the LHC is typically given as 7.9 eVs with a bunch area of 2.5 eVs, considering 2σ in both dimensions of the $(\Delta t, \Delta E)$-space. Dividing by 4π, the corresponding emittance is therefore of $\varepsilon_{\Delta t} = 0.2$ eVs. To convert this emittance to the proper units for the (ζ, p_ζ) phase space — by analogy to the transverse emittance — one needs to multiply by $\beta_0 c$ and divide by $\beta_0^2 E$ as per eq. (A2) above. Hence, normalized to $\beta_0\gamma_0$, the design value of $\varepsilon_\zeta^{\mathrm{N}}$ is $\varepsilon_\zeta^{\mathrm{N}} = \frac{\beta_0 c}{\beta_0^2 E_0}\varepsilon_{\Delta t}(\beta_0\gamma_0) = 64$ mm·rad at 7 TeV.

For additional details on the general Hamiltonian and the physics included in the Xsuite code, the reader is referred to the Xsuite manual [20].

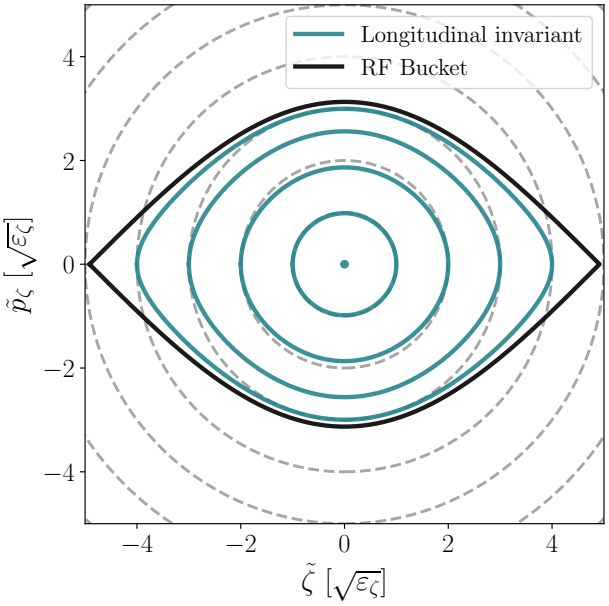

FIG. 8. Longitudinal phase space of the LHC for the Courant-Snyder coordinates $(\tilde{\zeta}, \tilde{p}_\zeta)$. The invariant curves of the Hamiltonian are shown in blue, and the separatrix (RF Bucket) is shown in black. The grey dashed lines correspond to multiples of σ_ζ, as seen in the Courant-Snyder phase space.

Appendix B: Hénon Map

The Hénon map [18] is one of the simplest model of non-integrable Hamiltonian maps which exhibits chaotic behaviour. It is an ideal mathematical tool to discuss the features of non-linear dynamics with reproducible results. Moreover, the map can be constructed from a sequence of thin magnetic elements, as discussed below.

1. 2D case

Let's consider the 2D case of a thin sextupole followed by a linear segment with phase advance μ_x and beta function β_x at its entry and exit. Using the complex notation $\tilde{\psi}_x = \tilde{x} - i\tilde{p}_x$, one can show that the one-turn map of this system can be written in closed-form in the Courant-Snyder phase space. The application of the resulting map, $\mathcal{M}_{\mathrm{H}}$, on a given complex point $\tilde{\psi}_x$ yields the new point:

$$\mathcal{M}_{\mathrm{H}}^{(2\mathrm{D})}\ \tilde{\psi}_x = e^{i[2\pi\mu_x]}\left[\tilde{\psi}_x - i\frac{a}{4}(\tilde{\psi}_x^* + \tilde{\psi}_x)^2\right] \tag{B1}$$

where $a = -\frac{1}{2}k_2\beta_x^{3/2}$ is the strength of the non-linearity as a function of the sextupole strength, k_2, and the beta function at the entrance of the linear segment. The particular case where $a = 1$ corresponds to the well studied Hénon map (which can also be obtained via a non-symplectic rescaling $\tilde{\psi}_x \to \tilde{\psi}_x/a$) [12].

2. 4D case

By extension to the previous case, the application of the very same transformations on a set of 4D coordinates $\tilde{\psi}_x = \tilde{x} - i\tilde{p}_x$ and $\tilde{\psi}_y = \tilde{y} - i\tilde{p}_y$ yields the new points:

$$\begin{cases} \mathcal{M}_{\mathrm{H}}^{(4\mathrm{D})}\ \tilde{\psi}_x = e^{i\mu_x}\left[\tilde{\psi}_x - i\frac{a}{4}\Big((\tilde{\psi}_x^* + \tilde{\psi}_x)^2 - \rho(\tilde{\psi}_y^* + \tilde{\psi}_y)^2\Big)\right] \\ \mathcal{M}_{\mathrm{H}}^{(4\mathrm{D})}\ \tilde{\psi}_y = e^{i\mu_y}\left[\tilde{\psi}_y + i\frac{a\cdot\rho}{2}(\tilde{\psi}_x^* + \tilde{\psi}_x)(\tilde{\psi}_y^* + \tilde{\psi}_y)\right] \end{cases} \tag{B2}$$

where $\rho = \beta_y/\beta_x$ and $a = -\frac{1}{2}k_2\beta_x^{3/2}$ once again. The case where $a = 1$ corresponds to the well-studied 4D Hénon map [12]. The ρ parameter is responsible for the non-linear coupling between the two planes. One can see that for $\rho = 0$ or $\tilde{\psi}_y = 0$, the 2D Hénon map is recovered in the horizontal plane for $\tilde{\psi}_x$.

Appendix C: NAFF, summary of the algorithm

Let's consider a quasiperiodic function $\psi(N)$ known over a finite time span $N \in [0, T]$. The spectral amplitude $A(\nu)$ can be computed as a function of ν (assuming continuous ν, equivalent to zero-padding FFT) following:

$$A(\nu) = \frac{1}{T}\sum_{N=0}^{T-1}\psi(N)\cdot e^{i[2\pi\nu\cdot N]}\cdot\chi_p(N) \tag{C1}$$

where the Hann window $\chi_p(N)$, of order p and centered on the dataset, is given by:

$$\chi_p(N) = \frac{2^p(p!)^2}{(2p)!}\left(1 + \cos\left(\frac{2\pi(N - T/2)}{T}\right)\right)^p \tag{C2}$$

From there, the main frequency ν_0 can be found by maximizing eq. (C1) using, for example, a Newton–Raphson method. With the windowing function of eq. (C2), ν_0 can be found with an accuracy that scales with $1/T^{2p+2}$, as compared to $1/T$ for a simple FFT [22]. The key aspect of Laskar's approach however, is to then subtract the contribution of ν_0 from the original signal, and repeat the procedure to obtain the second dominant frequency, ν_1, and so on.

Appendix D: Derivation of the integrals of motion

The Poincaré integral invariant given by eq. (6) can be separated into its projections onto the different canonical planes as discussed in section III B. We are therefore looking to compute one of these projections, *e.g.* I_{xx}, given by:

$$I_{xx} = \frac{1}{2\pi}\oint_{\Theta_x}\tilde{P}_x d\tilde{X} = \frac{1}{2\pi}\int_0^{2\pi}\left(\tilde{P}_x\frac{\partial\tilde{X}}{\partial\Theta_x}\right)d\Theta_x \tag{D1}$$

Starting from eq. (5), one can assume a set of coordinates, $(\tilde{X}, \tilde{P}_x)$, written in the complex form $\tilde{\Psi}_x = \tilde{X} - i\tilde{P}_x$ following:

$$\tilde{\Psi}_x^{(N_h)}(\vec{\Theta}) = \tilde{X} - i\tilde{P}_x = \sum_{k=0}^{N_h} A_k \; e^{i[\vec{n}_k \cdot \vec{\Theta}]} \tag{D2}$$

For any fixed Θ_y and Θ_ζ, the loop $\tilde{\Psi}_x(\Theta_x)$ thereby formed lies on the torus given by eq. (D2) — as shown graphically in Fig. 3 — for which we wish to calculate the area. To facilitate the integration over Θ_x, one can introduce the phase parameter $\varphi_{x_k} = n_{y_k}\Theta_y + n_{\zeta_k}\Theta_\zeta + \arg[A_k]$ such that:

$$\tilde{\Psi}_x^{(N_h)}(\Theta_x) = \sum_{k=0}^{N_h} |A_k| \; e^{i[n_{x_k}\Theta_x + \varphi_{x_k}]} \tag{D3}$$

Taking the real part of eq. (D3) for the position and the imaginary part for the momentum, one can directly write:

$$\begin{aligned}\tilde{P}_x \frac{\partial \tilde{X}}{\partial \Theta_x} =& \sum_{k=0}^{N_h} (-|A_k|) \sin[n_{x_k}\Theta_x + \varphi_{x_k}] \\ & \times \sum_{l=0}^{N_h} (-n_{x_l}|A_l|) \sin[n_{x_l}\Theta_x + \varphi_{x_l}]\end{aligned} \tag{D4}$$

To proceed with the integral, the following orthogonal identity can be used:

$$\begin{aligned}\int_0^{2\pi} \sin(n_{x_k}\Theta_x + \varphi_{x_k}) \sin(n_{x_l}\Theta_x + \varphi_{x_l}) d\Theta_x \\ = \pi \cos(\varphi_{x_k} - \varphi_{x_l}) \cdot \delta_{n_{x_k}}^{n_{x_l}}\end{aligned} \tag{D5}$$

where $\delta_{n_{x_k}}^{n_{x_l}} = 1$ if $n_{x_k} = n_{x_l}$ and 0 otherwise. After integration, we therefore end up with:

$$I_{xx} = \frac{1}{2} \sum_{k=0}^{N_h} \sum_{l=0}^{N_h} \delta_{n_{x_k}}^{n_{x_l}} \Big(n_{x_k} |A_k||A_l| \cos(\varphi_{x_k} - \varphi_{x_l}) \Big) \tag{D6}$$

where the summation is taken over the various spectral lines of the horizontal spectrum, $\tilde{\Psi}_x$. One can notice that the result is tied to the phase parameter φ, which depends on the non-integrated angles Θ_y and Θ_ζ. Hence, it is relevant to separate the terms that are angle-independent from the others (*i.e.* when $l = k$, $\varphi_{x_k} - \varphi_{x_l} = 0$) to expose the dependence on (Θ_y, Θ_ζ), yielding:

$$I_{xx}(\vec{\Theta}) = \frac{1}{2} \sum_{k=0}^{N_h} n_{x_k} |A_k|^2 + \Delta_{xx}(\vec{\Theta}) \tag{D7}$$

where the angle dependant part is explicitly given by:

$$\Delta_{xx}^{(N_h)} = \frac{1}{2} \sum_{k=0}^{N_h} \sum_{l \neq k}^{N_h} \delta_{n_{x_k}}^{n_{x_l}} \Big(n_{x_k} |A_k||A_l| \cos(\varphi_{x_k} - \varphi_{x_l}) \Big) \tag{D8}$$

Generalizing, the Poincaré integral invariant $I_j = I_{jx} + I_{jy} + I_{j\zeta}$ (for $j \in \{x, y, \zeta\}$) can be obtained by summing the three projections:

$$\begin{cases} I_{jx}^{(N_h)}(\vec{\Theta}) = \dfrac{1}{2} \displaystyle\sum_{k=0}^{N_h} n_{j_k} |A_k|^2 + \Delta_{jx}(\vec{\Theta}) \\ \\ I_{jy}^{(N_h)}(\vec{\Theta}) = \dfrac{1}{2} \displaystyle\sum_{k=0}^{N_h} m_{j_k} |B_k|^2 + \Delta_{jy}(\vec{\Theta}) \\ \\ I_{j\zeta}^{(N_h)}(\vec{\Theta}) = \dfrac{1}{2} \displaystyle\sum_{k=0}^{N_h} \ell_{j_k} |C_k|^2 + \Delta_{j\zeta}(\vec{\Theta}) \end{cases} \tag{D9}$$

where the different Δ functions are obtained from eq. (D8) by permuting the plane considered, *i.e.* where $\Delta_{xx} \to \Delta_{xy} \to \Delta_{x\zeta}$ is obtained by replacing $\vec{n}_k \to \vec{m}_k \to \vec{\ell}_k$ and $A_k \to B_k \to C_k$ and so on.

Appendix E: Continuity & Uniqueness

It can be shown that a given family of neighbouring KAM trajectories (a KAM region) smoothly depends on the actions, far away from resonances [22]. In fact, the Fourier expansion coefficients in each plane, as well as the single-particle fundamental frequencies, are expected to be continuous and differentiable, such that:

$$\frac{\partial A_{\vec{n}}}{\partial I_j}, \frac{\partial B_{\vec{m}}}{\partial I_j}, \frac{\partial C_{\vec{\ell}}}{\partial I_j} \text{ and } \frac{\partial \vec{Q}}{\partial I_j} \quad \text{are smooth} \tag{E1}$$

for $j \in \{x, y, \zeta\}$, where the spectral lines need to be indexed according to their corresponding integer vector ($\vec{n}$, $\vec{m}$ or $\vec{\ell}$) to be unambiguously identified, instead of sorting them by decreasing amplitude. An important consequence of eq. (E1), and in particular of the smooth evolution of $\vec{Q}$, is that if the betatron frequencies (the *tunes*) are well-defined on the closed-orbit of the machine (which is generally the case), then so are the particles fundamental frequencies in the neighbouring KAM region around the origin. To illustrate this claim, the continuity of some spectral lines (as a function of I_x) from the horizontal spectrum of the LHC is shown in Fig. 9. It can be seen that although the first synchrotron sidebands overtake the main line in terms of amplitude around $\zeta \approx 1.5\sigma_\zeta$, the continuity condition of eq. (E1) allows us to unambiguously identify the main line and its frequency (the single-particle fundamental frequency, Q_x) as being the one in continuity with the closed-orbit betatron frequency when $(x, y, \zeta) \to (0, 0, 0)$.

The labelling, or mislabelling, of the spectral lines is a subtle issue which requires careful consideration and is not to be trivialized. It is commonly assumed that the frequency of the highest spectral line, ν_0, corresponds to the fundamental frequency of the invariant torus, $\nu_0 \leftrightarrow [\nu_{(1,0,0)} = Q_x]$, which is clearly not the case

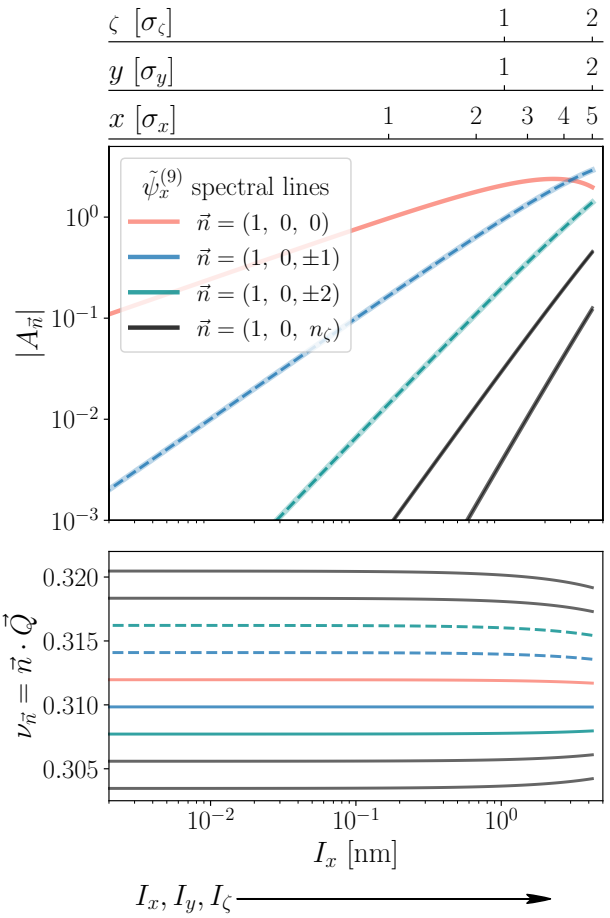

FIG. 9. Continuity of the main line and the first few synchrotron sidebands from the horizontal spectrum, $\tilde{\psi}_x^{(9)}$, for a particle moving from the origin, $(x, y, \zeta) = (0, 0, 0)$ to a high amplitude point $(x, y, \zeta) = (5\sigma_x, 2\sigma_y, 2\sigma_\zeta)$ in the LHC (see Table I for details, without beam-beam interactions). The spectral amplitudes $A_{\vec{n}}$, the fundamental frequencies $\vec{Q}$ and the harmonics $\vec{n} \cdot \vec{Q}$ are all smooth functions of the action, I_x. I_y and I_ζ are also increased as the particle is moved towards the high amplitude point. Results obtained via tracking.

in the example provided in Fig. 9 for high amplitude particles. This leads to mislabelling issues which seemingly breaks the continuity expected from eq. (E1). In fact, inspecting eq. (3) together with eq. (4) reveals that there are infinitely many possible labelling choices for the the single-particle motion which preserve the Fourier series of eq. (3). One can show [33] that the two formulations:

$$\begin{cases} \vec{Q} \\ \vec{I} \\ \{\vec{n}_k,\ \vec{m}_k,\ \vec{\ell}_k\} \end{cases} \Leftrightarrow \begin{cases} U\vec{Q} \\ (U^T)^{-1}\vec{I} \\ (U^T)^{-1}\{\vec{n}_k,\ \vec{m}_k,\ \vec{\ell}_k\} \end{cases} \tag{E2}$$

are equivalent when U is taken to be a unimodular (*i.e.* $\det U = \pm 1$) integer matrix. For example, in the case of the high amplitude particle of Fig. 9, if one identifies the sideband $Q_x + Q_\zeta$ to be the horizontal fundamental frequency, $Q_x \leftarrow Q_x + Q_\zeta$, the unimodular matrix

$$U = \begin{pmatrix} 1 & 0 & 1 \\ 0 & 1 & 0 \\ 0 & 0 & 1 \end{pmatrix}, \qquad (U^T)^{-1} = \begin{pmatrix} 1 & 0 & 0 \\ 0 & 1 & 0 \\ -1 & 0 & 1 \end{pmatrix}$$

shows that indexing the frequencies according to $(n_x, n_y, -n_x + n_\zeta)_k$, *e.g.* the line $(1, 0, 0)$ becoming $(1, 0, -1)$ and $(1, 0, 1)$ becoming $(1, 0, 0)$ and so on, yields an equivalent description of the motion through eq. (3). That being said, the three actions are also modified to become $(I_x, I_y, -I_x + I_\zeta)$, which are three new constants of the motion, different (and discontinuous) from the ones that would be expected around the origin. In the same way that the frequencies $\nu_k = \vec{n}_k \cdot \vec{Q}$ are preserved under the unimodular transformation U, one can show that the dot product:

$$\vec{I}' \cdot \vec{Q}' = \left[(U^T)^{-1}\vec{I}\right] \cdot \left[U\vec{Q}\right] = \vec{I} \cdot \vec{Q} \tag{E3}$$

is preserved, independently of the unimodular matrix U. Hence, although the mislabelling process can lead to erroneous evaluations of the individual actions, one can always use eq. (E3) to identify if the problem stems from this issue, or from the numerical evaluation itself.

To lift the equivalence condition of eq. (E2), and thereby uniquely label the spectral lines of the single-particle motion, it appears that the only robust method is to invoke the continuity of eq.(E1) by smoothly moving the particle from the origin (where labelling should be unambiguous) to the actual coordinates under study and properly identify $\vec{Q}$. Although this method is computationally demanding, it is the only one known to the authors to reliably label the spectral lines in complex systems like the LHC, with coupling in all planes. If the particle amplitude is low enough, or if the coupling is less important, one can usually retrieve the fundamental frequencies without worrying about this issue. This is the case for the results shown in Fig. 6 and Fig. 7, where the longitudinal coordinate was kept below $\zeta \leq 1\sigma_\zeta$ to avoid mislabelling problems.

Appendix F: Hénon map, integral of motion

Using the procedure described in the paper, one can evaluate the integral of motion, I_x, of the 2D Hénon map for various initial conditions in the $(\tilde{x}, \tilde{p}_x)$ plane. As shown in Fig. 10 (left), the action continuously increases with the distance from the origin. Within the resonance islands, the action is discontinuous and should instead be evaluated with regards to the appropriate fixed point, located at the center of each island. Additionally, one can assess the invariance of the integral of motion under the Hamiltonian transformation of the map, similar to

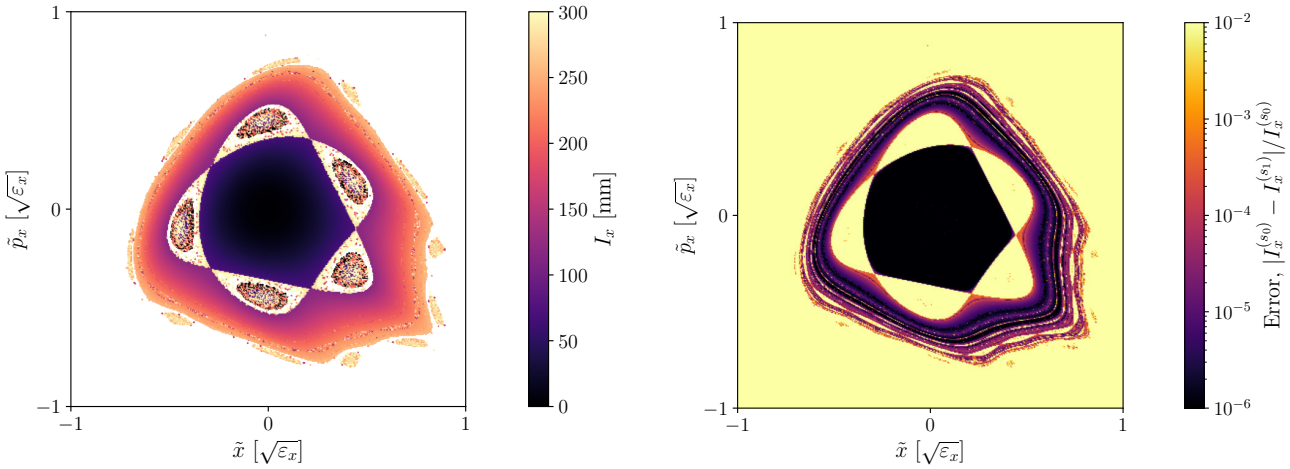

FIG. 10. Numerical evaluation of the action, I_x, using $N_h = 20$ harmonics for different initial conditions in the 2D Hénon map ($\mu_x = 0.2071$). In the right plot, the variation of the action between two observations points, s_0 and s_1, is shown. By increasing the number of harmonics N_h considered, the picture darkens and all stable tori are evaluated well-below the 10^{-6} error value.

what was done in Fig. 7 for the LHC. This can be done in time (by evaluating the integral of motion twice, after several turns), or in s, by adding additional observations points, as shown in the rightmost plot of Fig 10. To do so, the sextupolar kick of the Hénon map is split into two equal thin lenses, and the integral of motion is evaluated separately at those two locations, s_0 and s_1. If more harmonics are considered for the numerical evaluation ($N_h = 20$ here), the picture darkens and the error decreases for all initial conditions belonging to KAM tori.

[1] J. Moser, Is the solar system stable?, The Mathematical Intelligencer (1978).
[2] H. Poincaré, *Les méthodes nouvelles de la mécanique céleste.* (Paris, 1892).
[3] I. C. Percival, Chaos in hamiltonian systems, Proceedings of the Royal Society of London. A. Mathematical and Physical Sciences **413**, 131 (1987).
[4] J. Laskar, Large scale chaos and marginal stability in the solar system, Celestial Mechanics and Dynamical Astronomy (1996).
[5] S. Wolfram, How to think computationally about ai, the universe and everything, Stephen Wolfram Writings (2023).
[6] H. Zwirn and J.-P. Delahaye, Unpredictability and Computational Irreducibility, in *Irreducibility and Computational Equivalence: 10 Years After Wolfram's A New Kind of Science* (Berlin, Heidelberg, 2013) pp. 273–295.
[7] E. Courant and H. Snyder, Theory of the alternating-gradient synchrotron, Annals of Physics **3**, 1 (1958).
[8] A. Wolski, *Beam dynamics in high energy particle accelerators* (2014).
[9] A. Chao, SLIM - An Early Work Revisited, Particle accelerator. Proceedings, 11th European Conference, EPAC (2008).
[10] P. Belanger and G. Sterbini, A topological description of non-linearities in accelerator beam dynamics, (in preparation).
[11] G. Gallavotti, Quasi periodic motions from Hipparchus to Kolmogorov, arXiv:1111.4121 (1999).
[12] A. Bazzani, E. Todesco, G. Turchetti, and G. Servizi, A normal form approach to the theory of nonlinear betatronic motion 10.5170/CERN-1994-002 (1994).
[13] A. Franchi, L. Farvacque, F. Ewald, G. Le Bec, and K. Scheidt, First simultaneous measurement of sextupolar and octupolar resonance driving terms in a circular accelerator from turn-by-turn beam position monitor data, Physical Review Special Topics - Accelerators and Beams **17**, 074001 (2014).
[14] E. Forest, Geometric integration for particle accelerators, Journal of Physics A: Mathematical and General **39**, 5321 (2006).
[15] A. J. Dragt, An Overview of Lie Methods for Accelerator Physics, Proceedings of PAC (2013).
[16] A. Bazzani, L. Bongini, and G. Turchetti, Analysis of resonances by action map comparing tracking and normal forms, in *AIP Conference Proceedings* (1997).
[17] J. D. Meiss, Symplectic maps, variational principles, and transport, Reviews of Modern Physics **64**, 795 (1992).
[18] M. Hénon, Numerical study of quadratic area-preserving mappings, Quarterly of Applied Mathematics **27**, 291 (1969).
[19] M. Henon and C. Heiles, The applicability of the third integral of motion: Some numerical experiments, The Astronomical Journal **69**, 73 (1964).
[20] G. Iadarola *et al.*, *Xsuite Physics Manual* (2023) https://xsuite.web.cern.ch.
[21] R. Bartolini and F. Schmidt, Normal form via tracking or beam data, Part. Accel. **59**, 93 (1998).

[22] J. Laskar, Introduction to Frequency Map Analysis, in *Hamiltonian Systems with Three or More Degrees of Freedom*, edited by C. Simó (Springer, 1999) pp. 134–150.

[23] P. Belanger, K. Paraschou, G. Sterbini, G. Iadarola, *et al.*, nafflib: A Python Implementation of the Numerical Analysis of the Fundamental Frequencies (2024), https://pypi.org/project/nafflib/.

[24] J. Laskar, Frequency analysis for multi-dimensional systems. Global dynamics and diffusion, Physica D: Nonlinear Phenomena **67**, 257 (1993).

[25] J. Laskar, C. Froeschlé, and A. Celletti, The Measure of Chaos by the Numerical Analysis of the Fundamental Frequencies. Application to the Standard Mapping, Physica D: Nonlinear Phenomena **56**, 253 (1992).

[26] J. Laskar, Frequency map analysis and particle accelerators, in *Proceedings of the 2003 Bipolar/BiCMOS Circuits and Technology Meeting* (2003) pp. 378–382.

[27] Y. Papaphilippou, Detecting chaos in particle accelerators through the frequency map analysis method, Chaos: An Interdisciplinary Journal of Nonlinear Science **24**, 024412 (2014).

[28] J. Masoliver and A. Ros, Integrability and chaos: the classical uncertainty, European Journal of Physics **32**, 431 (2011).

[29] W. Herr and T. Pieloni, Beam-Beam Effects, in *CAS - CERN Accelerator School: Advanced Accelerator Physics* (2014) pp. 431–459.

[30] P. Belanger, R. Baartman, D. Kaltchev, G. Iadarola, and G. Sterbini, Bunch-by-bunch simulations of beam-beam driven particle losses in the LHC, IPAC24 (2024).

[31] K. Hirata, H. Moshammer, and F. Ruggiero, *A Symplectic Beam-Beam Interaction with Energy Change*, Tech. Rep. SLAC-PUB-10055, 813308 (2003).

[32] G. Iadarola *et al.*, Xsuite: An Integrated Beam Physics Simulation Framework, JACoW 10.18429/JACoW-HB2023-TUA2I1 (2024).

[33] C. E. Mitchell, R. D. Ryne, K. Hwang, S. Nagaitsev, and T. Zolkin, Extracting Dynamical Frequencies from Invariants of Motion in Finite-Dimensional Nonlinear Integrable Systems, Physical Review E **103**, 10.1103/PhysRevE.103.062216 (2021).

Paper IV

CERN Yellow Reports: Beam-Beam Workshop 2024

1 A Topological Approach to the Problem of Beam-Beam Compensation

P. Belanger[1,2], R. Baartman[1], D. Kaltchev[1], G. Sterbini[2]
[1]TRIUMF, Vancouver, Canada & [2]CERN, Geneva, Switzerland

Abstract

Beam-beam long-range interactions are known to be a strong source of non-linearities in particle colliders which can be mitigated with the help of dedicated correctors, *e.g.* by using current-carrying wires. To study this effect analytically, a normal form approach is commonly used to derive the resonance driving terms and develop suitable compensation schemes. In this paper, we propose a different approach based on a topological study of the non-linear transformation from beam-beam long-range interactions. The equivalence between long-range interactions, multipolar expansion and current-carrying wires is discussed using this formalism. Ultimately, this allows to optimize the conditions for wire compensation in HL-LHC. To support the results, we show that the proposed operational conditions also optimize the dynamic aperture and the long-term stability of the machine.

1.1 Introduction

The Large Hadron Collider (LHC) is soon to be upgraded into the High-Luminosity LHC (HL-LHC) which is planned to be operational by 2030. For this new era, the focus will be to increase the luminosity production of the machine by pushing the performance into increasingly challenging regimes. As such, addressing the problem of *compensation* to reduce non-linearities seen by the beam and improve the beam lifetime is of great importance in order to reach the targeted luminosity of the HL-LHC project.

Alongside electron cloud effects, the main source of non-linearities in the LHC (and also foreseen for HL-LHC) is the beam-beam (BB) effect, arising from the electromagnetic interaction between the two counter-rotating beams. In the interaction regions (IRs), the two beams share a common beam pipe and perturb one another. Head-On (HO) collisions take place at the interaction points (IPs), whereas Long-Range (LR) interactions are distributed on both sides of the IPs. These interactions, akin to multipolar errors, occur several times ($\approx$50) per IR for the nominal bunches and strongly contribute to the excitation of high-order resonances, eventually leading to particle diffusion, particle losses and the reduction of dynamic aperture [1–3]. A common approach to study the problem is the so-called weak-strong model [4], where a given *weak* bunch is subject to a static *strong* BBLR element for every encounter. The long-range beam-beam effect increases with the reduction of the crossing angle (needed for increased luminosity). To mitigate this problem, current-carrying wires have been proposed as a correction device to compensate the BBLR kicks [5–7]. As shown in Fig. 1, the optics of HL-LHC allows to install the beam-beam wire compensators (BBWC) in phase with all the BBLR kicks, left and right of both IP1 and IP5.

In this paper, the problem of beam-beam compensation is approached with topological arguments, where the deformation of hyperdimensional tori is used to introduce the concept of *non-linear residual* and quantify the compensation. First, a general description of beam-beam compensation is introduced to provide some context. From there, the concept of non-linear residual is presented and ultimately applied to the case of HL-LHC. We show that a wire compensator cannot be replaced by a high-order multipolar corrector package, and the optimal operational point for the wire is discussed, based on an analysis of the non-linear residual. Finally, a dynamic aperture (DA) scan is presented to support the results.

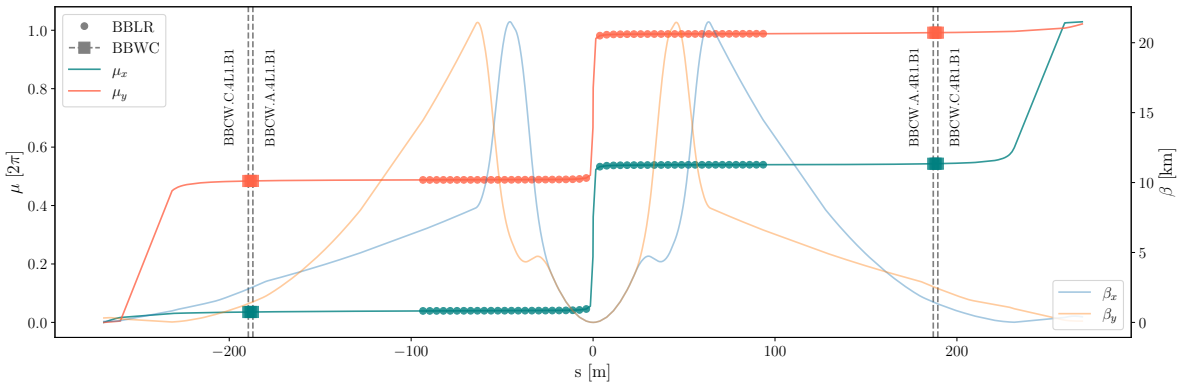

Fig. 1. HL-LHC optics around IP1 at the end of the luminosity-levelling (see Table 1). The location of the proposed wire compensators is shown with coloured squares (1 assembly of 3 modules on both sides of the IP) whereas the BBLR lenses are shown with the coloured dots. Both the BBLR and the BBWC are shown to be in phase, such that the compensation is essentially a local one.

1.2 BBWC – BBLR equivalence

In order to remain consistent with tracking codes such as Xsuite [8], a thin lattice is considered in the formulation of the problem. As shown in previous work [9], the radial integrated kick from a current-carrying wire of finite length L embedded in a drift of length L_{int} (with $L_{\text{int}} > L$) follows:

$$\Delta p_r = \int_{-\frac{L_{\text{int}}}{2}}^{\frac{L_{\text{int}}}{2}} \left(\frac{dp_r}{ds}\right) ds = -e\frac{\mu_0 I}{2\pi r}\left(\sqrt{\tfrac{1}{4}(L_{\text{int}}+L)^2+r^2} - \sqrt{\tfrac{1}{4}(L_{\text{int}}-L)^2+r^2}\right) \quad \text{(Finite wire, (1))}$$

where the integral is taken over the full length of the interaction, L_{int}. The sign of the current, I, is taken to be positive when oriented in the same direction as the weak beam. When the beam-wire distance is small compared to the length of the wire, $r \ll L$, the integration length becomes irrelevant and one retrieves the kick of an infinite wire, integrated over a length L, and given by:

$$\Delta p_r = -e\frac{\mu_0}{2\pi r}(IL) \quad \text{(Infinite wire, (2))}$$

which is a good approximation for the case of the LHC where $L \approx 1$ m and $r \approx 10$ mm. Similarly, assuming a beam of protons and neglecting the longitudinal dimension (4D transformation), the effect of a beam-beam interaction coming from a counter-rotating strong-bunch of intensity N_b, distributed over a length L_b, is to provide a radial kick in the transverse plane given by:

$$\Delta p_r = \int_{-\frac{1}{2}\frac{L_b}{2}}^{\frac{1}{2}\frac{L_b}{2}} \left(\frac{dp_r}{ds}\right) ds = e\frac{\mu_0}{2\pi r}\left(N_b \cdot (ec) \cdot \left[\frac{1+\beta^2}{2\beta}\right]\right)\left(1 - e^{-r^2/2\sigma^2}\right) \quad \text{(Beam-Beam, (3))}$$

where the length of interaction between the weak-bunch and the strong-bunch is halved since the bunches are assumed to travel in opposite directions at constant speed. We see that the beam-beam *long-range* kick (a regime where $r \gg \sigma$) is equivalent to the kick of an infinite wire powered with the equivalent current:

$$(IL)_{\text{eq}} = -N_b \cdot (ec) \cdot \left[\frac{1+\beta^2}{2\beta}\right] \quad (4)$$

where β is the relativistic velocity parameter. In the relativistic limit, one gets $(IL)_{\text{eq}} \approx -N_b \cdot (ec)$ as shown in previous work [5, 7]. Eq. (4) indicates that the wire compensator kick is completely analogous to the beam-beam kick in a *long-range* regime, and can therefore be used as a natural compensating device.

1.2.1 Multipolar expansion

One can show [7, 10] that the transverse field (B_x, B_y) from a single wire located at (x_w, y_w) in the transverse plane is the one of a pure multipole and can be written in cartesian coordinates as:

$$B_y + iB_x = -\frac{\mu_0 I}{2\pi} \sum_{n=0}^{\infty} \frac{(x+iy)^n}{(x_w + iy_w)^{n+1}} \tag{5}$$

which implies that the field contains contributions from all multipolar components. From there, following Xsuite's convention, the corresponding normal, k^+, and skew, $k^\times$, multipolar strengths for a wire compensator can be expressed as:

$$(k_n^+ L + ik_n^\times L) = -n! \left(\frac{q_0}{P_0}\frac{\mu_0}{2\pi}\right) \frac{(IL)}{(x_w + iy_w)^{n+1}} \tag{6}$$

as seen by the weak beam, where q_0 is the charge of the beam and P_0 the reference momentum. The resulting thin-lens Hamiltonian is the one of a pure multipole, *i.e.*:

$$\mathcal{H}_{\mathrm{M}} = -\frac{q_0}{P_0} A_z = \mathrm{Re}\left[\sum_{n=0}^{\infty} \frac{1}{(n+1)!}(k_n^+ + ik_n^\times)(x+iy)^{n+1}\right] \tag{7}$$

The same can be said about the BBLR kick in the long-range approximation, by virtue of eq. (4).

1.2.2 Wire compensation

In a machine such as the LHC, the linear contribution to the Hamiltonian (dipolar and quadrupolar kicks) can readily be compensated with the help of the closed-orbit feedback system and *ad hoc* quadrupolar corrections. As such, one can focus on the non-linear contributions (sextupolar kick and up) by normalizing the linear part of the motion. To do so, the *physical* phase space coordinates $\vec{x} = (x, p_x, y, p_y, \zeta, p_\zeta)$ are transformed into the *linearly normalized* phase space coordinates $\vec{\tilde{x}} = (\tilde{x}, \tilde{p}_x, \tilde{y}, \tilde{p}_y, \tilde{\zeta}, \tilde{p}_\zeta)$ with the help of the W-matrix [8] using $\vec{\tilde{x}} = W^{-1}\,\vec{x}$. Following this transformation, the normalized coordinates ($\tilde{x}$, $\tilde{p}_x$, etc.) homogeneously assume units of $\mathrm{m}^{\frac{1}{2}}$. If the beam emittance is known, one can further express the normalized coordinates in units of $\sqrt{\varepsilon}$ such that $\tilde{x} = 1\ \sqrt{\varepsilon_x} \ \mapsto\ x = 1\ \sqrt{\beta_x \varepsilon_x} = 1\ \sigma_x$, which relates to the beam size. With this change of variable, a kick in normalized space can be expressed as:

$$\begin{aligned}
\Delta\tilde{p}_x &= -L\sqrt{\beta_x} \cdot \mathrm{Re}\left[\sum_{n=2}^{\infty} \frac{1}{n!}(k_n^+ + ik_n^\times)(\sqrt{\beta_x}\,\tilde{x} + i\sqrt{\beta_y}\,\tilde{y})^n\right] \\
\Delta\tilde{p}_y &= \quad L\sqrt{\beta_y} \cdot \mathrm{Im}\left[\sum_{n=2}^{\infty} \frac{1}{n!}(k_n^+ + ik_n^\times)(\sqrt{\beta_x}\,\tilde{x} + i\sqrt{\beta_y}\,\tilde{y})^n\right]
\end{aligned} \tag{8}$$

where $n \geq 2$. Since both BBLR lenses and BBWC lenses can be modelled with the multipolar strengths of eq. (6), the ideal compensation condition would require that the sum of the kicks be zero to all orders and over the entire space. Introducing the beta-ratio $\rho = \beta_y/\beta_x$, one can show that the conditions at different orders n for a horizontal crossing (both BBLR and BBWC located in the horizontal plane) are:

$$\sum_{j\,\in\,\mathrm{BBWC}} \frac{(IL)_j \cdot (\rho_j)^m}{(\tilde{x}_j)^{n+1}} = \sum_{j\,\in\,\mathrm{BBLR}} \frac{\left[N_{b,j} \cdot (ec)\right] \cdot (\rho_j)^m}{(\tilde{x}_j)^{n+1}} \tag{9}$$

with

$$n \geq 2,\ m\ \in \begin{cases} \{0, 1, \ldots, n/2\} & \text{if } n \text{ is even} \\ \{0, 1, \ldots, (n+1)/2\} & \text{if } n \text{ is odd} \end{cases}$$

which corresponds to the sum of the contributions from all BBLR interactions and all the BBWCs used for the compensation. For a vertical crossing, the equivalent conditions are obtained by letting $\tilde{x} \to \tilde{y}$ and $\rho \to 1/\rho$. As an example, in order to compensate the octupole-like contribution, one requires that:

$$\text{(Octupole-like)} \quad n = 3 \quad \begin{cases} \displaystyle\sum_{j \in \text{BBLR}} \frac{\left[N_{b,j} \cdot (ec)\right]}{(\tilde{x}_j)^4} & - \displaystyle\sum_{j \in \text{BBWC}} \frac{(IL)_j}{(\tilde{x}_j)^4} & = 0 \\ \displaystyle\sum_{j \in \text{BBLR}} \frac{\left[N_{b,j} \cdot (ec)\right] \cdot (\rho_j)}{(\tilde{x}_j)^4} & - \displaystyle\sum_{j \in \text{BBWC}} \frac{(IL)_j \cdot (\rho_j)}{(\tilde{x}_j)^4} & = 0 \\ \displaystyle\sum_{j \in \text{BBLR}} \frac{\left[N_{b,j} \cdot (ec)\right] \cdot (\rho_j)^2}{(\tilde{x}_j)^4} & - \displaystyle\sum_{j \in \text{BBWC}} \frac{(IL)_j \cdot (\rho_j)^2}{(\tilde{x}_j)^4} & = 0 \end{cases} \tag{10}$$

Clearly, these conditions (at various n) cannot be all simultaneously satisfied unless there is a single BBWC lens used to compensated a single BBLR kick (or a sum of comparable ones). In this case, the BBWC needs to be installed at the same normalized distance $\tilde{x}_{\text{BBWC}} = \tilde{x}_{\text{BBLR}}$ and at a longitudinal location with the same beta-ratio, ρ, as the one of the long-range. For the IRs of HL-LHC (see Fig. 1), the aim is to compensate 50 BBLRs using 2 BBWC, located on the left and the right of the IPs. Because of the antisymmetric optics of the IRs, the wires have complementary beta-ratios ($\rho_L \approx 1/\rho_R$). In this case, some previous work [7] showed that the two wires should be installed symmetrically in the *physical space* and at a very specific beta-ratio ($x_L = x_R$ and $\rho_L \approx 1/\rho_R = 1/2$) in order to minimize the overall resonance driving terms (RTDs) of the lattice, or, equivalently, the residual kick provided by eq. (8).

In the following sections, we will show that a satisfactory compensation can also be achieved with the proposed location of the BBWCs for HL-LHC, shown in Fig. 1, even if the beta-ratio ($\rho_L \approx 1/\rho_R \approx 1/1.75$) is not the optimal one with the optics considered. Furthermore, we will show that the wires (left and right) can also be positioned at the same distance in *normalized space*, which brings some practical advantages in terms of implementation in the machine. To defend these points, topological arguments are used to describe the non-linear transformation from BBLR interactions.

1.3 Linearization and topological compensation

Let's consider a general transverse Hamiltonian acting at a longitudinal location s_0 and written in terms of the normalized coordinates, $\vec{\tilde{x}}$, as:

$$\tilde{\mathcal{H}}_{s_0} = \mu_x \pi(\tilde{x}^2 + \tilde{p}_x^2) + \mu_y \pi(\tilde{y}^2 + \tilde{p}_y^2) + \tilde{\mathcal{H}}_{\text{NL}}\left(\vec{\tilde{x}}\right) \tag{11}$$

where μ_x and μ_y are the linear phase advances (in units of 2π) for both planes and $\tilde{\mathcal{H}}_{\text{NL}}\left(\vec{\tilde{x}}\right)$ is a general non-linear kick. As can be shown using Lie algebra [11], if the non-linear part of this hamiltonian vanishes, then the transformation $\exp(:-\tilde{\mathcal{H}}_{s_0}:)$ corresponds to a pure rotation in both of the transverse planes, with respective rotation numbers μ_x and μ_y. On the other hand, if the non-linear part is non-zero, the corresponding transformation becomes a non-trivial deformation of the phase space, as in the case of the BBLR kick discussed earlier. Hence, we shall say that a non-linear beam line like the one of eq. (11) is said to be *compensated* if the overall transformation takes the form of a *pure rotation* in the normalized phase space with some non-trivial effective rotation numbers μ'_x and μ'_y. In other words: to compensate is to linearize, bringing the transformation back to a pure rotation.

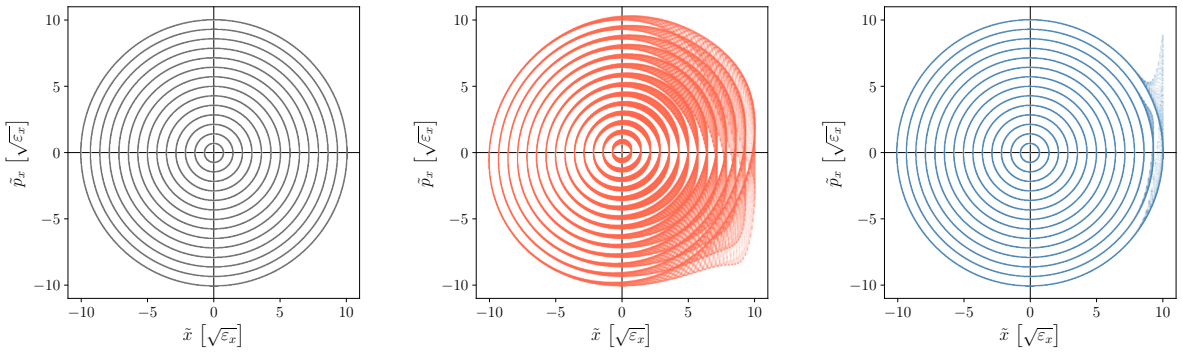

(a) Initial condition (b) After BBLR kick (c) After BBLR and BBWC kick

Fig. 2. Transformation of a series of hyperdimensional tori with the Hamiltonian of eq. (11). (a) Initial circular tori (b) Deformed tori after a single BBLR lens located at $x = 11\ \sigma_x$ (c) Compensated tori after a single BBLR lens followed by a compensating BBWC lens, also located at $x = 11\ \sigma_x$. The tori were chosen to have various horizontal amplitudes, $r_x \in [0, 10]\ \sqrt{\varepsilon_x}$, and a common non-zero vertical amplitude, $r_y = 6\ \sqrt{\varepsilon_x}$. Only the $(\tilde{X}, \tilde{P}_x)$ projections, $\tilde{\Psi}_x$, are here shown for simplicity.

In order to quantify said compensation, let's consider a hyperdimensional torus $\left\{\tilde{X}, \tilde{P}_x, \tilde{Y}, \tilde{P}_y\right\}(\Theta_x, \Theta_y)$ written in the form of quasiperiodic series [12]. In order to distinguish between the two important cases of *circular* or *deformed* tori, one can write separately:

$$\text{Circular torus} \begin{cases} \tilde{\Psi}_x = \tilde{X} - i\tilde{P}_x = \left(r_x e^{i\phi_x}\right) e^{i\Theta_x} \\ \tilde{\Psi}_y = \tilde{Y} - i\tilde{P}_y = \left(r_y e^{i\phi_y}\right) e^{i\Theta_y} \end{cases} \qquad \text{Deformed torus} \begin{cases} \tilde{\Psi}_x = \tilde{X} - i\tilde{P}_x = \sum_{k=0}^{\infty} A_k e^{i[n_{xk}\Theta_x + n_{yk}\Theta_y]} \\ \tilde{\Psi}_y = \tilde{Y} - i\tilde{P}_y = \sum_{k=0}^{\infty} B_k e^{i[m_{xk}\Theta_x + m_{yk}\Theta_y]} \end{cases} \tag{12}$$

where capital letters are used to distinguish the single-particle coordinates (*e.g.* $\tilde{x}, \tilde{p}_x$) from the topological curves (*e.g.* $\tilde{X}, \tilde{P}_x$) on which they reside. The amplitudes A_k and B_k are complex numbers with a given phase, and $\vec{n}_k = (n_{xk}, n_{yk})$ and $\vec{m}_k = (m_{xk}, m_{yk})$ are integer numbers generating various linear combinations of the angles, $\vec{\Theta} = (\Theta_x, \Theta_y)$. Evidently, the circular torus is only a specific case of the more general torus, made of a single phasor term in each plane corresponding to $\vec{n}_0 = (1, 0)$ and $\vec{m}_0 = (0, 1)$ with well defined radii, $|A_0| = r_x$ and $|B_0| = r_y$. Under the action of the transformation $\exp(:-\tilde{\mathcal{H}}_{s_0}:)$ from eq. (11), one can show that a circular torus is transformed into a deformed torus if the non-linear term $\tilde{\mathcal{H}}_{\text{NL}}(\vec{\tilde{x}})$ is present, but remains circular otherwise (albeit rotated). Hence, one can claim that a beam line is compensated if and only if it transforms a circular torus into another circular torus. Since the transformation is symplectic (and area-preserving), this implies that the two tori have the same radii, r_x and r_y, and are simply rotated. To see this effect, one can populate a circular torus like the one of eq. (12) with a few thousand *particles* (more properly conceptualized as *observation points*) and use any tracking code to see the effect of a given transformation. As a note of caution: the torus should be sampled carefully using non-commensurate angles (where the ratio Θ_x/Θ_y is irrational), in order to sample the torus densely. An example of this procedure is shown for many tori of various amplitudes in Fig. 2 for the case of a single BBLR lens and a compensated BBLR lens using a single BBWC.

1.3.1 Non-linear residual

As clearly shown in Fig. 2, the deformed tori each appear as a *smeared*[1] collection of points when projected onto a given transverse plane. Based on eq. (12), one can infer that this effect arises from the multitude of *coupled* phasors present in the quasiperiodic expansion of the deformed torus. In fact, one can show that when averaged over N densely sampled particles (observation points) from a torus, or, equivalently, over the angles Θ_x, Θ_y, the radial excursion is directly related to the underlying phasors following:

$$\lim_{N\to\infty} \left\langle \tilde{x}^2 + \tilde{p}_x^2 \right\rangle_N = \left\langle \tilde{X}^2 + \tilde{P}_x^2 \right\rangle_{\vec{\Theta}} = \left\langle \tilde{\Psi}_x \tilde{\Psi}_x^* \right\rangle_{\vec{\Theta}} = \sum_{k=0}^{\infty} \left| A_k \right|^2 \tag{13}$$

obtained from an explicit calculation of the integral:

$$\left\langle \tilde{\Psi}_x \tilde{\Psi}_x^* \right\rangle_{\vec{\Theta}} = \frac{1}{(2\pi)^2} \oint_{\Theta_x} \oint_{\Theta_y} \left[\sum_{k=0}^{\infty} A_k \, e^{i[\vec{n}_k \cdot \vec{\Theta}]} \times \sum_{j=0}^{\infty} A_j^* \, e^{-i[\vec{n}_j \cdot \vec{\Theta}]} \right] d\Theta_x d\Theta_y \tag{14}$$

which reduces to the above result by using the fact that $\oint e^{i[n\Theta]} e^{-i[m\Theta]} \, d\Theta = 2\pi \, \delta_{nm}$. This result can be directly generalized to a higher number of dimensions if need be. Interestingly, eq. (13) can be used to establish a clear difference between a circular torus for which $\tilde{x}^2 + \tilde{p}_x^2 = |A_0|^2 = r_x^2$ is a constant, and a deformed torus, for which it is not. In turn, this allows to determine whether a given torus is made of a single phasor $A_0 = r_x e^{i\phi_x}$, or of many A_k, in which case the radial excursion varies point to point.

By comparing the Courant-Snyder linear invariant, $J_x = \frac{1}{2}(\tilde{x}^2 + \tilde{p}_x^2)$, to the Poincaré non-linear invariant, I_x, one can quantify the deformation of an individual torus via the *non-linear residual*, $\mathcal{R}$, defined as:

$$\mathcal{R} \equiv \frac{\| \langle \vec{J} \rangle - \vec{I} \|}{\| \vec{I} \|} \qquad \text{with} \qquad \vec{I} = \begin{pmatrix} I_x \\ I_y \end{pmatrix} \text{ and } \langle \vec{J} \rangle = \begin{pmatrix} \langle J_x \rangle \\ \langle J_y \rangle \end{pmatrix} \tag{15}$$

where the average $\langle \vec{J} \rangle$ can be taken over the angles Θ_x, Θ_y or a collection of N particles used to sample the torus. As shown in a separate work [12], the non-linear invariants $\vec{I}$ can be evaluated numerically from tracking data in order to evaluate this deformation. By definition, the residual is $\mathcal{R} = 0$ for a circular torus, where $\langle \vec{J} \rangle = \vec{I}$, and $\mathcal{R} > 0$ otherwise, as also discussed in a separate work [13]. Although the residual is in general the property of a torus, one can equally use it to describe the deviation from linearity of a given transformation in the form of eq. (11). Let's note $\vec{\tilde{\Psi}}_{s_1} = e^{(:-\tilde{\mathcal{H}}_{s_0}:)} \, \vec{\tilde{\Psi}}_{s_0}$ the transformation of $(\tilde{\Psi}_x, \tilde{\Psi}_y)$ from s_0 to s_1. If $\vec{\tilde{\Psi}}_{s_0}$ is taken to be a circular torus, then the deformations generated on $\vec{\tilde{\Psi}}_{s_1}$ become a direct measure of the non-linearities of the transformation. Since the invariants at s_0 are known to be $\vec{I}_{s_0} = (I_x, I_y)_{s_0} = \frac{1}{2}(r_x^2, r_y^2)$ by construction (and are, by definition, *invariant* under any transformation) one can explicitly write the non-linear residual of the transformation as:

$$\mathcal{R}_{s_0 \to s_1} = \sqrt{\frac{\left(\langle J_x \rangle - I_x\right)^2 + \left(\langle J_y \rangle - I_y\right)^2}{{I_x}^2 + {I_y}^2}} = \sqrt{\frac{\left(\langle \tilde{x}^2 + \tilde{p}_x^2 \rangle_N - r_x\right)^2 + \left(\langle \tilde{y}^2 + \tilde{p}_y^2 \rangle_N - r_y\right)^2}{{r_x}^2 + {r_y}^2}} \tag{16}$$

which is an important result used for the rest of this work. The numerical procedure suggested on the basis of eq. (16) is straightforward and as follows: populate a circular torus of known radii (r_x, r_y) with N particles, track through a given segment of beam line and evaluate $\mathcal{R}_{s_0 \to s_1}$ from eq. (16) with the average taken over the N particles. In fact, this procedure was already visually illustrated in Fig. 2.

[1] The *smear* is a technical term defined in the Superconducting Super Collider (SSC) era which differs from the non-linear residual. See Ref. [13] for additional details.

1.3.2 Demonstration: multipolar compensation

Let's consider the trivial compensation case of a single BBLR kick, as previously shown in Fig. 2. Based on eq. (16), one can numerically evaluate the non-linear residual of the BBLR transformation alone, for various transverse positions in the form of $\mathcal{R}_{s_0 \to s_1}(r_x, r_y)$. The result is shown in Fig. 3(a). Far away from the center of the strong beam, the BBLR kick becomes essentially multipolar and one can hope to compensate the kick based on the expansion of eq. (6). By doing so, the non-linear residual $\mathcal{R}_{s_0 \to s_1}(r_x, r_y)$ is reduced on a wide region of transverse positions around the origin. The results are shown in Fig. 3(b, c, d), for an ideal compensation, order-by-order. One can see that the transformation (BBLR followed by multipolar compensation) is increasingly effective, as the order of the multipolar correction is increased. Finally, by considering the compensation from a wire compensator (*i.e.* a pure multipole), shown in Fig. 3(e), the non-linear residual is reduced over the entire transverse space except for the immediate vicinity of the strong beam core, where the *long-range* assumption is no longer valid (see Section 1.2). It is clear that even for the simplest case of BBLR compensation (*i.e.* a single BBLR), the BBWC is the appropriate device to consider, by virtue of the fact that it is the natural multipole counterpart of the BBLR lens.

It is noteworthy that the non-linear residual (hence the color scale of Fig. 3) is a comparative metric. Naturally, for a longer segment of beam line (*e.g.* 2 BBLR kicks), the residual would increase and there is no absolute criterion to determine what should be tolerated or not. As such, the metric should be used to compare two similar segments (*e.g.* a compensated and a non-compensated segment) to establish a relative comparison, as was done here.

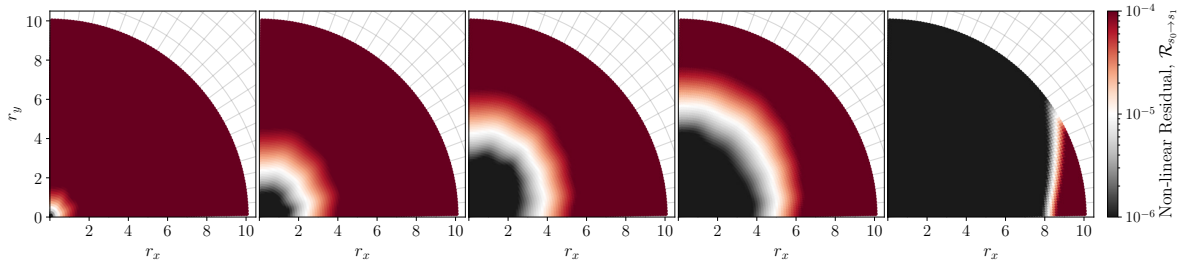

(a) No compensation (b) Sextupolar, $n \in [0, 2]$ (c) Octupolar, $n \in [0, 3]$ (d) Decapolar, $n \in [0, 4]$ (e) Wire, $n \in [0, \infty[$

Fig. 3. Non-linear residual map, $\mathcal{R}_{s_0 \to s_1}(r_x, r_y)$, for a short segment containing (a) A BBLR lens located at $x = 11\ \sigma_x$, (b, c, d) A BBLR lens followed by a multipolar compensator of increasing order, (e) A BBLR lens followed by a wire compensator. The results were obtained via tracking with the default Xsuite [8] elements (`BeamBeam2D`, `Multipole`, `Wire`) for a 7 TeV proton bunch with $N_b = 50 \cdot (2.3 \times 10^{11})$ and $\varepsilon^{\mathrm{N}}_{x,y} = 2.5\ \mu$m·rad.

1.3.3 Demonstration: flattened strong beam

As a second example, let's consider the compensation of a flattened strong beam using a single BBWC. Since the BBWC–BBLR equivalence was derived for a round beam in Section 1.2, one should not expect the same level of compensation for an elliptical beam.

Indeed, by studying the non-linear residual map $\mathcal{R}_{s_0 \to s_1}(r_x, r_y)$ for this simple case, Fig. 4 shows that the BBWC–BBLR equivalence deteriorates for elliptical beams in comparison with round ones. This is one of the many factors which can influence the overall compensation scheme for a realistic IR (alongside the beam-beam separation and the beta-ratio), as discussed in the next section for the case of HL-LHC.

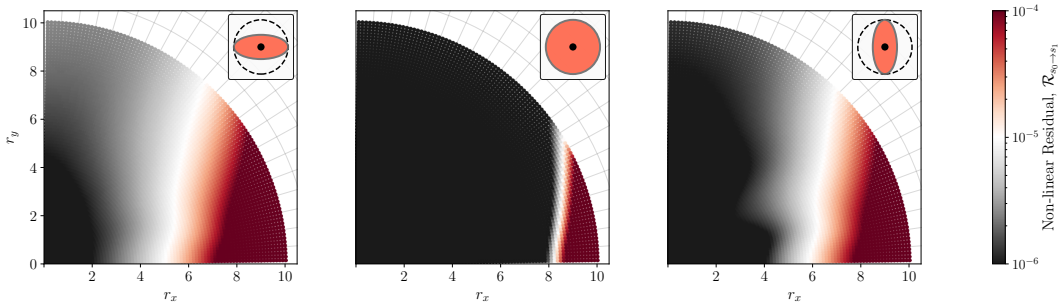

(a) Horizontal strong beam (b) Round strong beam (c) Vertical strong beam

Fig. 4. Non-linear residual map, $\mathcal{R}_{s_0 \to s_1}(r_x, r_y)$, for the BBWC compensation of a BBLR kick assuming (a) A horizontally-flat strong beam, $\sigma_x^2/\sigma_y^2 = 1/0.2$ (b) A round strong beam, $\sigma_x^2/\sigma_y^2 = 1/1$ (c) A vertically-flat strong beam, $\sigma_x^2/\sigma_y^2 = 0.2/1$. The insets show the BBWC placed at the center of the corresponding strong beam.

1.4 Application to HL-LHC

As mentioned in the introduction, a promising strategy to reach the luminosity targets of HL-LHC is to allow for the reduction of the crossing angle in both IP1 and IP5. Unfortunately, this is made challenging by the 50 BBLR interactions found in each IR. Despite being in phase, the many BBLRs are not all equivalent and cannot be perfectly reduced to a single one, due to the optics variation along the IR. From eq. (8) and eq. (9), one can see that both the BBLR separation, $\tilde{x}_j$, and the BBLR beta-ratio, $\rho = \beta_y/\beta_x$, play a significant role in the resulting kick. Moreover, as shown in Fig. 4, the beta-ratio of the strong beam also influences the quality of the compensation achievable with a simple wire compensator. In Fig. 5, an overview of the relevant parameters is shown for the 50 BBLR interactions of IR1, as well as for the proposed BBWC modules, left and right of the IP. In these conditions, no perfect solution exists and the problem of compensation becomes a problem of optimization.

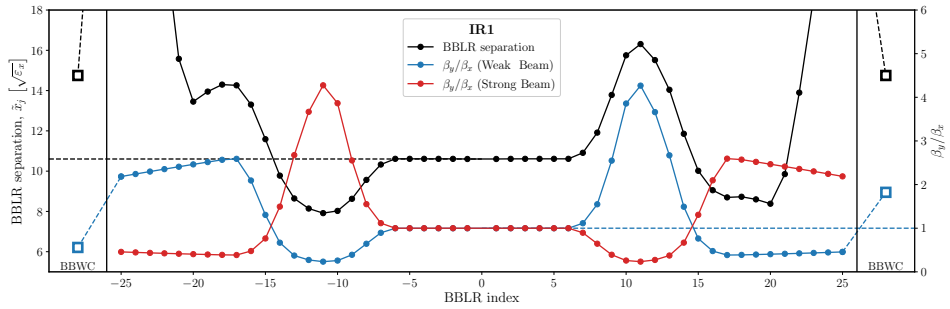

Fig. 5. Relevant HL-LHC optics parameters for the 50 BBLR interactions of IR1 with a half-crossing angle of $\theta_c/2 = 250\ \mu$rad in the horizontal plane. Close to the IP, the BBLR separation is around 10.6 σ_x and the beta-ratio is close to $\rho = \beta_y/\beta_x \approx 1$. The proposed compensation scheme requires the BBWC to be powered (at most) with 450 A·m at 14.75 σ_x from the weak beam, left and right of the IR, where $\rho_{w,L} \approx 1/1.75$ and $\rho_{w,R} \approx 1.75$.

1.4.1 Non-linear residual optimization and dynamic aperture

Outside of the framework of the present paper, it has been shown that a proper BBLR compensation scheme can be used to reduce resonances [7] and therefore push the dynamic aperture boundary beyond the 6 σ target usually considered for HL-LHC [3]. These results allow us to formulate a clear optimization problem in terms of the non-linear residual which would also improve the dynamic aperture of the machine at once.

To do so, we propose to reduce the problem to the study of the linearity of the transformation between the entry of IR1 and its exit, $\mathcal{R}_{s_0 \to s_1}(r_x, r_y) = \mathcal{R}_{\text{IR1}}(r_x, r_y)$ and aim to reduce the non-linear residual around the 6 σ boundary by varying the BBWC current and beam-wire distance. The justification for the proposed formulation is based on a few key considerations:

1. The dynamic aperture considered is mainly limited by the BBLR interactions of IR1 and IR5.
2. Due to the chosen optics, the transformation through IR1 and IR5 are analogous, such that optimizing IR1 should give the operational BBWC conditions to separately optimize IR5 as well.
3. Optimizing the linearity of the transverse transformation, $\mathcal{R}_{s_0 \to s_1}(r_x, r_y)$, around the 6 σ boundary should have a significant impact on improving the dynamic aperture of the machine as a whole.

To carry this optimization study, the machine segment between the dispersion suppressors left and right of IP1 was extracted from the full HL-LHC lattice in order to isolate IR1, as show in Fig. 1. The lattice parameters considered for the study can be found in Table 1. The current and beam-wire distance (in normalized coordinates) of the BBWCs left and right of the IP was varied and the non-linear residual was evaluated in each case. The maximum residual in the transverse plane around 6 σ ($r_x^2 + r_y^2 = ((6 \pm 0.2)\ \sqrt{\varepsilon_x})^2$) was computed for each operational condition. The results are shown in Fig. 6(a) alongside the expected sextupolar ($n = 2$) and octupolar ($n = 3$) compensation conditions from eq. (9). To understand the impacts of the non-linear residual on the long term stability of the machine, a full dynamic aperture study was also carried out, as shown in Fig. 6(b). The results indicate that minimizing the non-linear residual seems to have an important impact on the dynamic aperture of the machine. Based on this optimization study, the proposed compensation scheme would be to power the wires with their design current value of 450 A·m, at 14.75 σ_x from the beam, or closer.

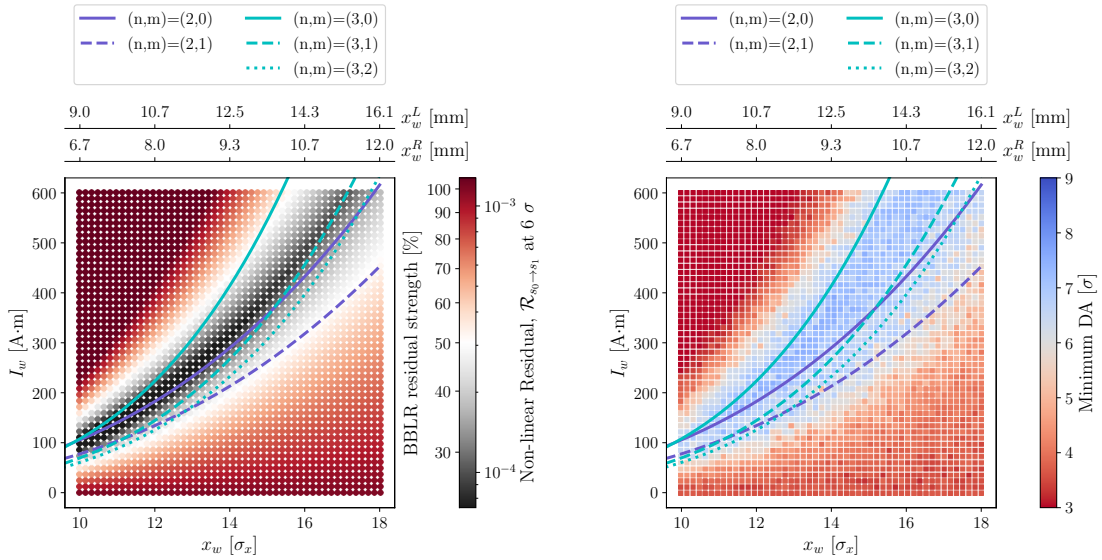

(a) Non-linear residual, IR1

(b) DA, full lattice

Fig. 6. Optimal BBWC operational condition in terms of current, I_w, and beam-wire distance, x_w, for the baseline lattice of HL-LHC (Table 1). (a) Non-linear residual at 6 σ from IR1 alone. (b) Dynamic aperture of the full lattice after 10^6 turns for $\Delta p/p = 2.7 \times 10^{-4}$ off-momentum particles. The sextupolar ($n = 2$) and octupolar ($n = 3$) compensation conditions from eq. (9) are shown in both cases and can serve as a visual guide for comparison.

Table 1. HL-LHC parameters considered for the dynamic aperture scan, Fig. 6(b).

Parameter		**Value**	**Unit**
Beam Energy	E	7.0	(TeV)
Bunch intensity	N_b	1.13×10^{11}	(p^+/b)
Norm. Emittance	$\varepsilon_x^{\mathrm{N}}, \varepsilon_y^{\mathrm{N}}$	2.5	(μm·rad)
Beta at the IP	β^*	15	(cm)
Half-crossing	$\theta_c/2$	250	(μrad)
Crabbing angle	θ_{cc}	-190	(μrad)
Octupoles	I_{oct}	-60	(A)
Tune	Q_x,Q_y	$(62.320, 60.325)$	
Chromaticity	ΔQ_x,ΔQ_y	15	

To give some additional insight into the absolute metric of the non-linear residual, $\mathcal{R}_{\mathrm{IR1}}(r_x, r_y)$ was also computed without BBWC compensation, but with artificially reduced BBLR strength in order to measure the corresponding non-linear residual. The results are shown on the left side of the color bar of Fig. 6(a). The residual corresponding to a reduction of the BBLR strength by 50% was made to line up with the middle of the color bar (white). Hence, the region inside the white lines of Fig. 6(a) corresponds to a compensation of more than 50% of the BBLR strength, which seems sufficient to have a significant gain in dynamic aperture, as show in Fig. 6(b). This observation is particularly interesting to discuss the case of PACMAN bunches [3], which typically see only half of the BBLR interactions and therefore would be completely compensated around the white areas of Fig. 6(a), but not *overcompensated*, resulting in a gain of dynamic aperture for both nominal bunches and PACMAN bunches. Finally, in order to account for the small differences between the global optimum of Fig. 6(a) and Fig. 6(b), one can refer to the few approximations mentioned at the start of Section 1.4.1.

1.5 Summary

In this paper, the problem of beam-beam compensation is addressed with the help of topological arguments. An overview of the equivalence between long-range interactions and current-carrying wires is presented and general compensation considerations are introduced. By looking at the deformation of hyperdimensional tori, the non-linear residual is introduced as a relative metric of non-linearity. This allows to clearly show the differences between a low-order multipolar compensator and a wire compensator (multipole of infinite order), as well as the differences between round strong beams and flattened strong beams. Finally, the non-linear residual is used to study the optimal compensation scheme for HL-LHC by varying both the wire current and beam-wire distance. The results are found to be in agreement with dynamic aperture studies and suggest to power the wires with 450 A·m at 14.75 σ_x from the beam or closer.

1.6 Acknowledgements

The author would like to thank K. Paraschou (CERN) and T. Planche (TRIUMF) for fruitful discussions on the subject.

References

[1] W. Herr, "Beam-beam effects in the LHC", International Workshop on Collective Effects in Large Hadron Colliders (1995), https://inspirehep.net/literature/381737.

[2] W. Herr, X. Buffat, R. Calaga, R. Giachino, G. Papotti *et al.* "Long-Range Beam-Beam Effects in the LHC", ICFA Mini-Workshop on Beam-Beam Effects in Hadron Colliders (2013), https://doi.org/10.5170/CERN-2014-004.87.

[3] K. Skoufaris, S. Fartoukh, Y. Papaphilippou, A. Poyet, A. Rossi, G. Sterbini, and D. Kaltchev, "Numerical optimization of DC wire parameters for mitigation of the long range beam-beam interactions in High Luminosity Large Hadron Collider", PRAB (2021), https://doi.org/10.1103/PhysRevAccelBeams.24.074001

[4] Y. Papaphilippou and F. Zimmermann, "Weak-strong beam-beam simulations for the Large Hadron Collider", PRAB (1999), https://doi.org/10.1103/PhysRevSTAB.2.104001

[5] J. P. Koutchouk, "Correction of the long-range beam-beam effect in LHC using electro-magnetic lenses", PACS (2001), https://doi.org/10.1109/PAC.2001.987147

[6] F. Zimmermann, "10 Years of wire excitation experiments in the CERN SPS", ICFA Mini-Workshop on Beam-Beam Effects in Hadron Colliders (2013), https://doi.org/10.5170/CERN-2014-004.153

[7] S. Fartoukh, A. Valishev, Y. Papaphilippou and D. Shatilov, "Compensation of the long-range beam-beam interactions as a path towards new configurations for the high luminosity LHC", PRAB (2015), https://doi.org/10.1103/PhysRevSTAB.18.121001

[8] G. Iadarola, A. Abramov, P. Belanger, X. Buffat, R. De Maria *et al.* "Xsuite: An Integrated Beam Physics Simulation Framework", HB2023 (2024), https://doi.org/10.18429/JACoW-HB2023-TUA2I1.

[9] A.S. Patapenka, R. De Maria, Y. Papaphilippou, and A. Valishev, "Simulations in Support of Wire Beam-Beam Compensation Experiment at the LHC", NAPAC'16 (2016), https://doi.org/10.18429/JACoW-NAPAC2016-TUPOB17

[10] A. Wolski, "Beam dynamics in high energy particle accelerators", ICP (2014), https://doi.org/10.1142/p899

[11] A. Chao, "Special Topics in Accelerator Physics: Lie Algebra Technique for nonlinear Dynamics", SLAC-PUB (2012), https://www.slac.stanford.edu/~achao/lecturenotes.html

[12] P. Belanger and G. Sterbini, "Numerical evaluation of the integrals of motion for non-linear trajectories in particle accelerator tracking codes", arXiv (2024, in preparation), https://arxiv.org/search/physics?searchtype=author&query=Belanger,+P

[13] P. Belanger and G. Sterbini, "A topological description of non-linearities in accelerator beam dynamics", arXiv (2024, in preparation), https://arxiv.org/search/physics?searchtype=author&query=Belanger,+P

Paper V

JACoW Publishing: HIAT 2025

THE BEAM DYNAMICS CASE OF BEAM-BEAM WIRE COMPENSATORS FOR THE HL-LHC ERA

P. Bélanger*,[1], R. Baartman, D. Kaltchev, TRIUMF, Vancouver, Canada
G. Sterbini, CERN, Geneva, Switzerland
[1] also at University of British Columbia, Vancouver, Canada

Abstract

Beam-beam long-range interactions are known to be a strong source of non-linearities in hadron colliders, undermining the performance of the Large Hadron Collider (LHC) during proton-proton collisions. In order to enhance the luminosity production of the machine and increase the tolerance of the working point after the High Luminosity upgrade of the LHC (HL-LHC), dedicated correctors such as beam-beam wire compensators can be used. In this paper, the beam dynamics of this compensation problem is studied in details, ultimately showing that the linearity of the machine can be significantly improved throughout the beam core — and up to several sigmas — leading to an improvement of the dynamic aperture. This conclusion is shown to be supported by analytic calculations, simulation studies, as well as experimental results presented in earlier work. With the proposed approach, wire compensators can be positioned according to the collimation settings, simplifying their implementation in the machine for the HL-LHC era.

INTRODUCTION

The Large Hadron Collider (LHC) is soon to be upgraded into the High-Luminosity LHC (HL-LHC) which is planned to be operational by 2030. For this new era, the focus will be to increase the luminosity production of the machine by pushing the operational scenarios into increasingly challenging regimes. As such, controlling the non-linearities of the lattice and improving the beam lifetime is critical to reach the target of the HL-LHC project. Alongside electron clouds, the main source of non-linearities in the LHC is the beam-beam (BB) effect, arising from the electromagnetic interaction between the two counter-rotating beams. In the interaction regions (IRs), the two beams share a common beam pipe and perturb one another. Head-On (HO) collisions take place at the interaction points (IPs), whereas Long-Range (LR) interactions are distributed on both sides of the IPs. These interactions, akin to strong multipolar errors, occur several times (≈50) per IR for the nominal bunches and contribute to the excitation of high-order resonances, eventually leading to particle diffusion, particle losses and the reduction of dynamic aperture [1–3].

To mitigate this problem, current-carrying wires have been proposed as a correction device to compensate the BBLR kicks [4–6]. As shown in Fig. 1, these so-called beam-beam wire compensators (BBWCs) need to be installed after the separation dipoles in order to act separately on the two beams, which travel in opposite directions.

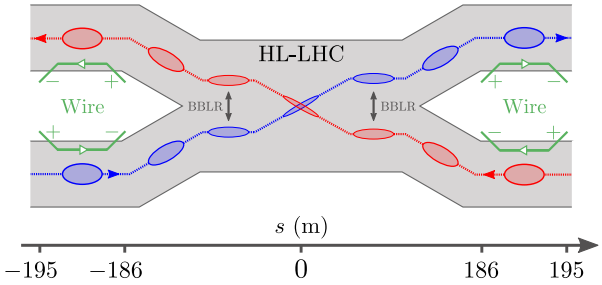

Figure 1: BBCW layout for HL-LHC around IP1 and IP5.

Table 1: HL-LHC Parameters (End of Lumi-Levelling)

Parameter		Value	Unit
Beam Energy	E	7.0	(TeV)
Bunch intensity	N_b	1.13×10^{11}	(p^+/b)
Norm. Emittance	$\varepsilon_x^N, \varepsilon_y^N$	2.5	(μm·rad)
Beta at the IP	β^*	15	(cm)
Half-crossing	$\theta_c/2$	250	(μrad)
Crabbing angle	θ_{cc}	−190	(μrad)
Octupoles	I_{oct}	−60	(A)
Chromaticity	$\Delta Q_x, \Delta Q_y$	15	

The Maxwellian equivalence between current-carrying wires and beams of charged particles has been well-established theoretically by several authors over the last few decades [4, 6, 7]. On the experimental front, successful beam-beam compensation was recently demonstrated in the LHC during dedicated machine development experiments [8, 9] as well as regular LHC operation [9]. However, the integration of a full-scale compensation system in the machine for the HL-LHC era — the first of its kind — requires additional considerations to optimize the effects on the beam dynamics, as discussed below.

In this paper, the linearity of the IRs is studied with and without BBWCs at various amplitudes using the non-linear residual, which will be introduced. This method complements the usual resonance driving terms (RDTs) approach, while reducing the complexity of the analysis by directly using generic tracking codes to reach its conclusions. To support the results, dynamic aperture scans are presented.

* philippe.belanger@cern.ch

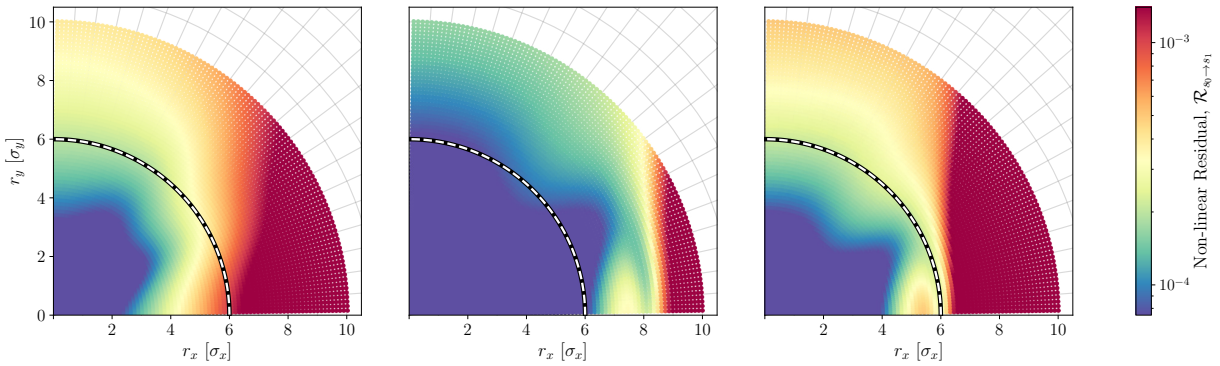

(a) Baseline, BBCW OFF (b) Baseline, BBCW ON (c) Levelling ($\theta_c/2 = 190$ µm), BBCW ON

Figure 2: Non-linear residual, $\mathcal{R}$, through IR1 for various amplitudes, (r_x, r_y), in HL-LHC. (a) Without BBWCs. (b) With BBWCs at 15 σ and 400 A·m. (c) After reducing the crossing angle, with BBWCs at 12 σ and 400 A·m.

EQUIVALENCE PRINCIPLE

In the transverse plane (4D), the beam-beam kick from a gaussian bunch of protons with size σ is purely radial and scales with the radial distance, r, following:

$$\Delta p_r = -e\frac{\mu_0}{2\pi r}\,(IL)_{\text{eq}} \times \left(1 - e^{-r^2/2\sigma^2}\right)\,, \qquad (1)$$

where $(IL)_{\text{eq}} = -N_b \cdot (ec) \cdot \left[(1+\beta^2)/(2\beta)\right]$ is the equivalent current for a bunch of intensity N_b traveling with a relativistic velocity parameter β. One can see that the beam-beam *long-range* kick (a regime where $r \gg \sigma$) is equivalent to the kick of an infinite wire powered with the equivalent current $(IL)_{\text{eq}}$. In turn, it can be shown that the magnetic field of an infinite wire is the one of a pure multipole, exciting contributions from all multipolar components [10]. As such, the effect on the beam dynamics scales with the beta functions (β_x, β_y) at the location of the kick and depends on the beta ratio, $\rho = \beta_y/\beta_x$.

In principle, any single BBLR kick can be naturally compensated using a dedicated BBWC installed in phase at the appropriate beta ratio ($\rho_{\text{BBLR}} = \rho_{\text{BBWC}}$) and at the appropriate distance from the beam. That being said, the HL-LHC lattice contains many BBLRs distributed over the IRs (≈50, with varying beta ratios), and only 2 BBWCs located after the separation dipoles on each sides of the IRs. This specific compensation scheme, introduced and thoroughly studied in earlier work [6], makes use of the antisymmetric optics of the IRs to reduce the number of BBWCs required. Indeed, with the phase advance between the BBLRs being negligible and the antisymmetric optics of HL-LHC (left to right, $\rho_{\text{L}} = 1/\rho_{\text{R}}$), it has been shown that the overall RDTs of the lattice could be optimally compensated using only a pair of wires. Since the beam-beam separation is symmetric on both sides of the IPs, it is moreover required that the BBWCs be placed symmetrically on both sides of the IPs to reach the optimal compensation.

This equivalence principle — reducing 50 BBLRs to 2 BBWCs — is an important feature of the problem. However, departing from the optimal compensation scheme suggested in earlier work [6], this paper is set to demonstrate that a satisfactory compensation can also be achieved over a wide range of operational parameters. In particular, it will be shown that the 2 BBWCs need not be installed symmetrically on both sides of the IPs, but can instead be installed at a similar normalized distance (in units of σ_x and σ_y). This choice of implementation could, in principle, facilitate the integration of the devices in the machine (in terms of machine protection), ensuring that the requirements of the HL-LHC collimation hierarchy are safely met.

COMPENSATION AND LINEARIZATION

Phase Space Rotation

Let's consider a general transverse Hamiltonian (4D) acting between the longitudinal locations s_0 and s_1 and written in terms of the normalized Courant-Snyder coordinates, $\vec{\tilde{x}}$, following:

$$\tilde{\mathcal{H}}_{s_0\to s_1} = \mu_x\pi(\tilde{x}^2 + \tilde{p}_x^2) + \mu_y\pi(\tilde{y}^2 + \tilde{p}_y^2) + \tilde{\mathcal{H}}_{\text{NL}}(\vec{\tilde{x}})\,, \quad (2)$$

where μ_x and μ_y are the linear phase advances (in units of 2π) for both planes and $\tilde{\mathcal{H}}_{\text{NL}}(\vec{\tilde{x}})$ is a general non-linear term. As can be shown from Lie algebra [11, 12], the transformation $\exp\left(:-\tilde{\mathcal{H}}_{s_0\to s_1}\Delta s:\right)$ corresponds to a pure rotation in both the $(\tilde{x}, \tilde{p}_x)$ and the $(\tilde{y}, \tilde{p}_y)$ phase spaces if the non-linear part of the Hamiltonian, $\tilde{\mathcal{H}}_{\text{NL}}(\vec{\tilde{x}})$, vanishes. On the other hand, with the non-linear term being non-zero, the corresponding transformation becomes a non-trivial deformation of the phase space. This is namely the case, *e.g.*, for the IRs of HL-LHC, when BBLR kicks are considered. It is possible, however, to combine non-linear lenses in such a way that the non-linear term vanishes or reduces to an additional linear term. Hence, we shall say that a non-linear beam line like the one of eq. (2) is *compensated* if the overall transformation

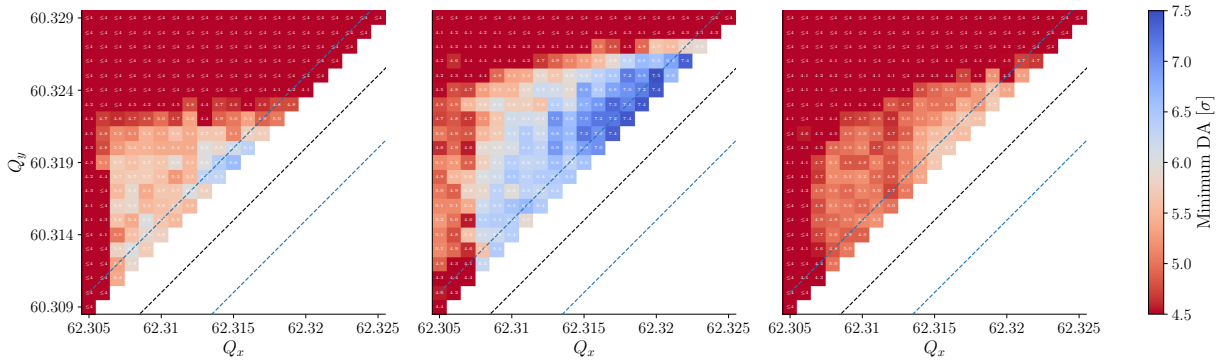

(a) Baseline, BBCW OFF (b) Baseline, BBCW ON (c) Levelling ($\theta_c/2 = 190$ µm), BBCW ON

Figure 3: Dynamic aperture scans over various working points, (Q_x, Q_y), for HL-LHC. (a) Without BBWCs. (b) With BBWCs at 14.75 σ and 450 A·m. (c) After reducing the crossing angle, with BBWCs at 13 σ and 450 A·m.

takes the form of a pure rotation in the Courant-Snyder phase space with some non-trivial effective rotation numbers μ'_x and μ'_y. In other words: to compensate is to linearize, bringing the transformation back to a pure rotation.

Non-Linear Residual

This particular framing of the problem makes it clear that the linearity of a beam line can be measured by evaluating how the corresponding transformation, $\exp\left(:-\tilde{\mathcal{H}}_{s_0\to s_1}\Delta s:\right)$, departs from a pure rotation. As shown in a separate work [12], this can be achieved by comparing the Courant-Snyder linear invariant, $J_x = \frac{1}{2}(\tilde{x}^2+\tilde{p}_x^2)$, to the Poincaré non-linear invariant [13], I_x, via the *non-linear residual*, $\mathcal{R}$, defined as:

$$\mathcal{R} \equiv \frac{\|\langle\vec{J}\,\rangle - \vec{I}\,\|}{\|\,\vec{I}\,\|} \quad \text{with } \vec{I} = \begin{pmatrix} I_x \\ I_y \end{pmatrix} \text{ and } \langle\vec{J}\,\rangle = \begin{pmatrix} \langle J_x\rangle \\ \langle J_y\rangle \end{pmatrix}, \quad (3)$$

where the average $\langle\vec{J}\,\rangle$ is taken over N particles uniformly distributed over 4-dimensional tori, allowing to cover all possible phases in both planes, ϕ_x and ϕ_y. This figure of merit can be evaluated directly from tracking data to quantify the non-linear deformation. To do so, particles are placed at fixed radial amplitudes (r_x, r_y) in the Courant-Snyder phase space $((\tilde{x}, \tilde{p}_x)$ and $(\tilde{y}, \tilde{p}_y))$ with various phases (ϕ_x, ϕ_y) and tracked through the beam line. By symplecticity, the projected areas $(I_x, I_y) = \frac{1}{2}(r_x^2, r_y^2)$ are preserved throughout the beam line but the radial excursions, $\frac{1}{2}\left\langle\tilde{x}^2 + \tilde{p}_x^2\right\rangle$ and $\frac{1}{2}\left\langle\tilde{y}^2 + \tilde{p}_y^2\right\rangle$ are not, due to non-linear deformations. Hence, the non-linear residual can be ultimately evaluated following:

$$\mathcal{R}_{s_0\to s_1} = \sqrt{\frac{\left(\left\langle\tilde{x}^2 + \tilde{p}_x^2\right\rangle - r_x\right)^2 + \left(\left\langle\tilde{y}^2 + \tilde{p}_y^2\right\rangle - r_y\right)^2}{{r_x}^2 + {r_y}^2}}, \quad (4)$$

at various amplitudes. By definition, the residual vanishes ($\mathcal{R} = 0$) for a pure rotation and is strictly positive ($\mathcal{R} > 0$) otherwise.

BBLR COMPENSATION IN HL-LHC

In Fig. 2, the linearity of a section of the HL-LHC lattice (IR1) is evaluated for the baseline configuration of the machine at the end-of-levelling. One can see that without BBWCs (Fig. 2(a)), the lattice becomes highly non-linear around the 6 σ line. With compensation (Fig. 2(b)), the level of linearity originally found only in the core of the beam is pushed beyond the 6 σ line, showing a successful compensation of the BBLR kicks. Finally, it is also shown that BBWCs can allow to reduce the crossing angle further into the levelling process (Fig. 2(c)) while preserving a similar non-linear residual to that of the baseline configuration.

Contrarily to typical RDT-based approaches, the non-linear residual allows to visualize the effect of non-linearities at various amplitudes, while providing a comparative metric to asses the quality of the compensation. As such, one can conclude that a satisfactory compensation is obtained in IR1 — despite the non-optimal compensation scheme considered — as shown in Fig. 2(b). To validate these claims, dynamic aperture scans were performed for each configuration, as shown in Fig. 3. One can see that the DA is significantly improved (reaching the HL-LHC target of 6 σ) for a wide variety of working points when powering the BBWCs.

SUMMARY

This paper presents a revised compensation scheme for beam-beam wire compensators in the HL-LHC era, allowing the wires to be positioned at the same normalized distance on both sides of the IPs. By studying the non-linear residual over IR1, it is shown that BBWCs can significantly improve the stability of the beam dynamics over a wide region of the transverse plane, making the machine sufficiently linear, beyond the 6 σ line. To support this claim, dynamic aperture scans are provided, showing an improved range of possible working points for HL-LHC.

REFERENCES

[1] K. Skoufaris et al., "Numerical optimization of dc wire parameters for mitigation of the long range beam-beam interactions in High Luminosity Large Hadron Collider," *Phys. Rev. Accel. Beams*, vol. 24, no. 7, p. 074 001, 2021. doi:10.1103/PhysRevAccelBeams.24.074001

[2] W. Herr, "Beam-beam effects in the LHC," International Workshop on Collective Effects in Large Hadron Colliders, 1995. https://inspirehep.net/literature/381737

[3] W. Herr, X. Buffat, R. Calaga, R. Giachino, G. Papotti, et al., "Long-range beam-beam effects in the LHC," ICFA Mini-Workshop on Beam-Beam Effects in Hadron Colliders, 2013. doi:10.5170/CERN-2014-004.87

[4] J. P. Koutchouk, "Correction of the long-range beam-beam effect in LHC using electro-magnetic lenses," Proceedings of PAC 2001, 2001. doi:10.1109/PAC.2001.987147

[5] F. Zimmermann, "10 years of wire excitation experiments in the CERN SPS," ICFA Mini-Workshop on Beam-Beam Effects in Hadron Colliders, 2013. doi:10.5170/CERN-2014-004.153

[6] S. Fartoukh, A. Valishev, Y. Papaphilippou, and D. Shatilov, "Compensation of the long-range beam-beam interactions as a path towards new configurations for the high luminosity LHC," *Phys. Rev. ST Accel. Beams*, vol. 18, no. 12, p. 121 001, 2015. doi:10.1103/PhysRevSTAB.18.121001

[7] Y. Papaphilippou and F. Zimmermann, "Weak-strong beam-beam simulations for the Large Hadron Collider," *Phys. Rev. ST Accel. Beams*, vol. 2, no. 10, p. 104 001, 1999. doi:10.1103/PhysRevSTAB.2.104001

[8] G. Sterbini et al., "First results of the compensation of the beam-beam effect with dc wires in the LHC," in *Proceedings of IPAC'19*, Melbourne, Australia, May 2019, pp. 2262–2265. doi:10.18429/JACoW-IPAC2019-WEYYPLM3

[9] P. Belanger, R. Baartman, D. Kaltchev, and G. Sterbini, "Beam-beam long-range wire compensators in LHC Run 3," in *Proceedings of IPAC'23*, Venice, Italy, Sep. 2023. doi:10.18429/JACoW-IPAC2023-WEPA060

[10] P. Belanger, R. Baartman, D. Kaltchev, and G. Sterbini, "A topological approach to the problem of beam-beam compensation," in *Proceedings of BB24 (in preparation)*, 2024.

[11] A. Chao, "Special topics in accelerator physics: Lie algebra technique for nonlinear dynamics," SLAC, Tech. Rep. SLAC-PUB, 2012. https://www.slac.stanford.edu/~achao/lecturenotes.html

[12] P. Belanger and G. Sterbini. "A topological description of accelerator beam dynamics." (in preparation), https://arxiv.org/search/physics?searchtype=author&query=Belanger,+P

[13] P. Belanger and G. Sterbini. "Numerical evaluation of the integrals of motion in particle accelerator tracking codes," https://arxiv.org/abs/2503.19122

Abstract

The stability of particle motion is a central concern of beam dynamics for the optimal design of particle accelerators. Linear effects are generally well under control, allowing us to store beams for more than 50 hours in machines like the Large Hadron Collider, at CERN. Non-linear effects, on the other hand, introduce complications that must be controlled to enhance the region of stable motion. In such complex systems, the emergence of chaos forces us to integrate the motion element-by-element to study the complete picture of beam dynamics. This establishes particle tracking as a fundamental tool required to probe non-linear effects. Yet despite the successes of the field, the ubiquity of the linear picture leads to a framework which often appears fragmented. In this respect, this dissertation proposes a formalism which can naturally describe linear, non-linear, analytic and numerical experiments alike using a self-consistent framework. To do so, we take an epicycle approach (in the spirit of the ancient Greeks) and place a general quasiperiodic expansion as the central object of study.

Critically, this choice ensures close contact with empirical observables and enables a detailed spectral analysis of the particle's motion. After providing a visual interpretation of KAM tori, we show how the integrals of motion can be recovered for arbitrary Hamiltonian flows, including fully coupled six-dimensional systems such as the LHC. Using Lie algebraic methods, we investigate the transport and deformation of these tori, establishing a foundation for describing coupled linear motion as a stepping stone toward a more complete non-linear treatment. Although closed-form solutions remain generally inaccessible, we demonstrate that the compensation of non-linear effects can be rigorously studied through the non-linear residual, a quantity shown to correlate strongly with dynamic aperture. Ultimately, the framework connects naturally with the Normal Form approach, which relies on the same quasiperiodic expansions.

TRIUMF | UBC | CERN